AGH University of Science and Technology
Faculty of Physics and Applied Computer Science

Doctoral dissertation

Szymon Kulis

Development of prototype luminosity detector modules for future experiments on linear colliders

Supervisor: **Dr hab. inż. Marek Idzik**

Cracow, December 2012

Declaration of the author of this dissertation:
Aware of legal responsibility for making untrue statements I hereby declare that I have written this dissertation myself and all the contents of the dissertation have been obtained by legal means.

(mgr inż. Szymon Kulis)

Declaration of the dissertation Supervisor:
This dissertation is ready to be reviewed.

(dr hab. inż. Marek Idzik)

Acknowledgements

It is a pleasure to thank those who made this dissertation possible, especially my supervisor dr hab. inż. Marek Idzik for his thoughtful guidance, autonomy and trust in the conducted research, providing all resources necessary for my research, an enormous patience, a constant motivation, and time spent on the discussions and providing invaluable advice.

I would like to thank my friends from the Nuclear Electronics and Radiation Detection Group, especially Krzysztof Swietek, Tomasz Fiutowski, Domnik Przyborowski, who designed ASICs used for the module construction.

I would like to show my gratitude to prof. Wolfang Lohmann, the FCAL Colaboration spokesmen, for entrusting very responsible tasks to me.

Many thanks to all my colleagues from the FCAL Collaboration, especially for Leszek Zawiejski, Hans Henshel, Wolfgang Lange, Wojciech Wierba, Krzysztof Oliwa, Eryk Kielar, Jerzy Kotuła, Szymon Moszczyński, Bogdan Pawlik, for enormous number of valuable discussions and help at various moments.

Special thanks to Adrian Matoga for the help with the firmware and software development for the detector module and to Przemysław Terlecki and Piotr Wiącek for assistance during the module assembly.

I also wish to thank Joanna Borkowska for revising English in my manuscript and many accurate comments.

The performed works would not have been possible without the financial support from the Polish Ministry of Science and Higher Education obtained within the framework of MC-PAD FP7 project.

Lastly, and most importantly, I wish to thank my fiancée Izabela and my parents, Natalia and Krzysztof. Without their support this dissertation would not have been possible. To them I dedicate this dissertation.

Streszczenie

Najbliższa przyszłość może się okazać jednym z najbardziej owocnych okresów Fizyki dla zrozumienia podstawowych składników materii i praw natury. Niedawno uruchomiony Wielki Zderzacz Hadronów (ang. Large Hadron Collider) zbiera ogromne ilości danych. Najprawdopodobniej zebrane dane pozwolą wyjaśnić pochodzenie masy, poprzez mechanizm Higgsa, a możne nawet ujawnią nowe informacje na temat ciemnej materii czy ciemnej energii. Prawie na pewno Model Standardowy (ang. Standard Model), opisujący nasze wyobrażenia na temat świata cząstek elementarnych, zostanie rozszerzony lub zastąpiony przez bardziej ogólną teorię.

W celu precyzyjnego badania nowych zjawisk niezbędny stanie się dużo prostszy niż proton-proton system zderzeń, umożliwiający przeprowadzenie dokładniejszych pomiarów i analiz. Obecnie prowadzone są dwa duże międzynarodowe projekty, mające na celu przygotowanie zderzacza leptonów: Międzynarodowy Zderzacz Liniowy (ang. International Linear Collider) oraz Kompaktowy Zderzacz Liniowy w CERN (ang. Compact Linear Collider at CERN). Zasadniczą cechą odróżniającą te dwa projekty jest technologia przyspieszania elektronów i pozytonów, a przez to maksymalna energia dostępna w środku masy podczas zderzenia. Koncepcja systemów detekcyjnych dla obu eksperymentów jest bardzo podobna i bazuje na bardzo precyzyjnym śledzeniu wszystkich generacji kolejnych cząstek w detektorze (ang. particle flow). Projektom związanym ze zderzaczami liniowymi towarzyszy wiele interesujących wyzwań związanych zarówno z fizyką cząstek elementarnych, jak również rozwojem technologii akceleratorowych i detektorowych.

Prace rozwojowo-badawcze (ang. Research and Development) skupiające się na budowie prototypów detektorów i elementów akceleratora rozpoczęto wiele lat temu. Pomimo iż decyzja o finansowaniu projektu zderzacza liniowego jeszcze nie zapadła, liczba fizyków i inżynierów z całego świata, pracujących nad zagadnieniami związanymi ze zderzaczami liniowymi, przekracza kilka tysięcy. Katedra Oddziaływań i Detekcji Cząstek, Akademii Górniczo Hutniczej w Krakowie, we współpracy z grupą naukową z Instytutu Fizyki Jądrowej PAN, jest zaangażowana w konstrukcję detektora LumiCal, jednego z detektorów na potrzeby przyszłych eksperymentów na zderzaczach liniowych. Detektor LumiCal będzie odpowiedzialny za precyzyjny pomiar świetlności eksperymentu. Prace te prowadzone są w ramach współpracy FCAL – międzynarodowej kolaboracji zajmującej się rozwojem technologii na potrzeby specjalistycznych kalorymetrów w przedniej części przyszłych detektorów na zderzaczach elektronów i pozytonów. Główną działalnością grupy z AGH jest rozwój modułów detektora, a w szczególności dedykowanej dla nich elektroniki odczytu. Zaproponowana architektura odczytu detektora zawiera układy elektroniki front-end, układy przetworników analogowo-cyfrowych (ang. Analog-to-Digital Converter) oraz cyfrowych koncentratorów danych, zlokalizowanych bezpośrednio przy sensorze promieniowania. Autor rozprawy wierzy iż, korzystając z postępu obserwowanego w rozwoju obecnych technologii półprzewodnikowych, możliwym jest zbudowanie takiego wysoce-zintegrowanego i wydajnego systemu detekcyjnego.

Głównym przedmiotem tej rozprawy jest projekt i weryfikacja poprawnego działania prototypowego modułu detektora LumiCal. Rozprawa prezentuje szereg prac przeprowadzonych przez autora, poczynając od prac koncepcyjnych nad architekturą detektora, poprzez kolejne fazy badań i projektowania, kończąc na wynikach otrzymanych podczas pomiarów kompletnego modułu detektora na wiązce testowej. Większość tekstu rozprawy koncentruje się bezpośrednio na pracy autora, jednakże dla zachowania kompletności, cała tematyka związana ze zderzaczami

liniowymi w ogólności, oraz detektorem LumiCal w szczególności, została poglądowo zaprezentowana.

Pierwszy rozdział tej rozprawy prezentuje zagadnienia związane z liniowymi akceleratorami elektronów i pozytonów. Ich rola w naszym rozumieniu budowy materii, jak również możliwości odkrywania Nowej Fizyki, jest przedstawiona. Omówiono główne wyzwania stojące przed kolaboracjami badawczo-rozwojowymi (R&D) zajmującymi się rozwojem technologii akceleratorowych i detektorowych, a następnie zaprezentowano planowane rozwiązania. Praca szczegółowo omawia detektory przedniej części eksperymentu (ang. Forward Region), gdzie zlokalizowane są dwa specjalistyczne kalorymetry. Detektor LumiCal jest odpowiedzialny za precyzyjny pomiar świetlności, podczas gdy BeamCal jest odpowiedzialny za szybką estymację świetlności w celu umożliwienia kontrolowania wiązki. Dodatkowo, oba detektory poprawiają hermetyczność całego systemu, umożliwiając wykrywanie wysoko energetycznych elektronów, opuszczających punkt interakcji pod bardzo małymi kontami. Architektura odczytu detektora LumiCal została zaproponowana bazując na wymaganiach dla detektora, określonych na podstawie planowanego programu fizycznego i dokładnych studiów symulacyjnych. Autor aktywnie uczestniczył w dyskusjach i wyborze optymalnej architektury odczytu dla detektora LumiCal [48, 115].

Ekstrakcja sygnału z sensorów promieniowania, jak również techniki jej późniejszego przetwarzania zostały omówione w rozdziale drugim. Poza ogólnie uznanymi metodami pomiaru czasu i amplitudy zdarzenia, została zaproponowana nowatorska implementacja, bazująca na cyfrowym przetwarzaniu sygnału (ang. Digital Signal Processing). Omówiona została implementacja cyfrowego filtru dekonwolucyjnego do ekstrakcji informacji o czasie i amplitudzie. Zależności opisujące wpływ różnych warunków eksperymentalnych (t.j. częstotliwość próbkowania, rozdzielczość przetwornika ADC, amplituda sygnału) na wydajność odzyskiwania informacji o czasie i amplitudzie zostały podane oraz przedyskutowane [116].

Przed rozpoczęciem prac nad konstrukcją modułu detektora, istotnym czynnikiem było dokładne zbadanie komponentów mających zostać użytych przy jego konstrukcji. Jest to konieczne aby zbudować wysoko wydajny system, jak również aby uniknąć nieprzewidzianego zachowania modułu po jego integracji. Autor pracy był odpowiedzialny za przygotowanie stanowisk pomiarowych (ang. test setup) umożliwiających precyzyjne pomiary układów elektroniki front-end, jak również rodziny przetworników ADC, wykonanych jako dedykowane układy scalone (ang. Application Specific Integrated Circuit) a zaprojektowany przez zespół badawczy z AGH. Stanowiska te składały się z dedykowanych, wielowarstwowych obwodów drukowanych (ang. Multilayer Printed Circuit Board), jak również autorskiego oprogramowania. Przygotowane stanowiska pomiarowe umożliwiły autorowi wykonanie obszernych pomiarów własności prototypowych układów ASIC, których wyniki zostały wykorzystane do poprawienia kolejnych wersji układów jak również zostały opublikowane w czasopismach o zasięgu międzynarodowym [88, 89, 98, 99, 100]. Dokładny opis pracy autora nad parametryzacją omówionych układów został omówiony w rozdziale trzecim, w tym też rozdziale autor prezentuje wyniki eksperymentalne dotyczące wydajności algorytmu dekonwolucyjnego. W celu wykonania pomiarów autor zbudował stanowisko eksperymentalne, które umożliwiło mu badanie omówionego wcześniej algorytmu dla różnych paramentów (t.j. źródło sygnału czy parametry próbkowania). Dodatkowo, autor przygotował pakiet symulacyjny umożliwiający generację przebiegów czasowych dla zdarzeń odpowiadających pomiarom. Wyniki analiz dla danych pomiarowych, jak również symulacyjnych, zestawione są z przewidywaniami teoretycznymi otrzymanymi przez autora.

W czwartym rozdziale zaprezentowano architekturę oraz projekt dwóch prototypowych mo-

dułów detektora LumiCal. Pierwszy moduł, zawierający ograniczone możliwości, posiadał tylko wyjście analogowe z układów front-end, podczas gdy drugi zawierał wszystkie bloki funkcjonalne, w tym także przetworniki ADC i cyfrowe układy koncentracji danych. Autor odpowiedzialny był za wybór architektury modułu, dobór niezbędnych komponentów, jak również projekt dedykowanego wielowarstwowego obwodu drukowanego [117]. w kolejnym kroku, autor rozwinął oprogramowanie wbudowane (ang. firmware) dla układu logiki programowalnej FPGA (ang. Field-Programmable Gate Array) jak również mikrokontrolera. Stworzone oprogramowanie przetestowane zostało w symulacjach komputerowych oraz podczas działania na docelowej platformie sprzętowej. Prototypowe moduły detektora zostały przetestowane oraz zparametryzowane w laboratorium. Właściwości poszczególnych kanałów odczytowych (t.j. wzmocnienie, offset, poziom szumów) zostały zmierzone dla wszystkich trybów pracy. Obszerne testy zbierania danych w rozmaitych trybach pracy systemu, potwierdziły poprawność zaproponowanej architektury i poprawność projektu komponentów, zarówno sprzętowych, jak i programowych. Zbudowane moduły detektora świetlności wykorzystywane zostały przez współpracę FCAL podczas pomiarów na wiązce testowej. Autor rozprawy odpowiedzialny był za przygotowanie stanowisk pomiarowych a także techniczną koordynację pomiarów. Uczestniczył on również aktywnie w zbieraniu danych podczas pomiarów na testowej wiązce elektronowej DESYII w ośrodku DESY w Hamburgu. Przy użyciu omówionych modułów udało się zebrać kilka milionów przypadków.

Dane zebrane podczas pomiarów na wiązce zostały dogłębnie przeanalizowane w celu wyznaczenia parametrów zbudowanych modułów [118]. Autor rozprawy przygotował dedykowane oprogramowanie, które umożliwiło wieloaspektową analizę danych. Między innymi, badał on odpowiedź detektora na wysoko energetyczne elektrony, jednorodność odpowiedzi sensora, przesłuch pomiędzy kanałami odczytowymi (ang. crosstalk), oraz wpływ efektów związanych z indukowanymi zakłóceniami (ang. common mode noise). Przeprowadzone analizy dostarczyły wielu cennych informacji na temat poszczególnych komponentów składowych modułu, jak i modułu jako całości. Dane zebrane podczas pomiarów z absorberem, wykonanym z wolframu, umieszczonym przed modułem detektora umożliwiły wyznaczenie profilu kaskady elektromagnetycznej, jak również przyczyniły się do weryfikacji narzędzi symulacyjnych używanych do modelowania procesu kreacji kaskady elektromagnetycznej.

Autorowi udało się zrealizować wyznaczone cele pracy. Możliwość wykonania zaawansowanego systemu ekstrakcji sygnału z sensorów promieniowania oraz ich późniejszego przetwarzania za pomocą zaproponowanych rozwiązań sprzętowych i programowych, została zweryfikowana eksperymentalnie.

Zaprojektowany moduł detektora świetlności eksperymentalnie potwierdził słuszność zaproponowanej architektury odczytu. Na obecnym etapie prac, pomijając aspekt miniaturyzacji, moduł detektora spełnia wymagania stawiane detektorowi świetlności Międzynarodowego Zdarzacza Liniowego (ang. ILC). Zaprojektowany moduł jest także wszechstronny: umożliwia on między innymi stosowanie różnych trybów i częstotliwości próbkowania, obsługuje różne tryby wyzwalania, adresuje zagadnienia dynamicznego kluczowania zasilania (ang. power pulsing), jak również może być wykorzystywany z systemami akwizycji danych obecnie używanymi w społeczności związanej ze zderzaczami liniowymi. Ponadto, z wykorzystaniem zbudowanego modułu, możliwe było wykonanie prac badawczo-rozwojowych (R&D) nad wykorzystaniem cyfrowego przetwarzania sygnałów (ang. Digital Signal Processing) w celu dokonania ekstrakcji informacji o czasie i amplitudzie sygnału pochodzącego z sensora promieniowania. Taki typ przetwarzania jest bardzo obiecującym kandydatem w przypadku systemów detekcyjnych wymagających

precyzyjnej informacji o czasie i amplitudzie zdarzenia, a jednocześnie pracujących z dużą częstotliwością zdarzeń.

Podczas długiej działalności związanej z pracami badawczo-rozwojowymi, autor rozprawy zdobył unikalne doświadczenie przy budowie oraz testowaniu zaawansowanych systemów detekcji promieniowania. Jego prace związane były ze wszystkimi fazami typowego eksperymentu fizyki cząstek wysokich energii: poczynając od prac koncepcyjnych nad architekturą detektora, poprzez szczegółowe prace konstrukcyjne sprzętu, rozwój dedykowanego oprogramowania, skończywszy na analizie danych zebranych podczas pomiarów na wiązce testowej.

Contents

Introduction

The nearest future may prove to be one of the most fruitful era in Physics for understanding the basic components and laws of nature. The Large Hadron Collider (LHC) is now operating and acquiring a tremendous amount of data. Most probably the collected data will allow us to explain, through Higgs mechanism, mass origin, or even the concepts of dark matter and energy. Most likely the Standard Model, which demonstrates our understanding of the particle world, will be extended or replaced with a more general theory. For an in-depth study of new phenomena a much simpler collision system than proton-proton, allowing for more precise analysis, is needed. At present two large international projects are under development to prepare a lepton collider: the International Linear Collider (ILC) and the Compact Linear Collider at CERN (CLIC). The most important differences in both projects are related to electron-positron acceleration technology, and the maximum attainable center of mass energy. Detector concepts for both experiments are very similar and are based on high granularity particle flow approach. The linear collider projects are accomplished by a lot of various and interesting challenges concerning the physics of elementary particles and the development of accelerator and detector technologies.

Research and Development (R&D) activities focused on building detector prototypes and accelerator modules started many years ahead the planned experiment beginning. Even though the decision about founding a linear collider project has not been made so far, the number of physicist and engineers involved in linear collider R&D programs from all over the world already exceeded a few thousand. The Department of Particle Interactions and Detection Techniques AGH-UST, together with a group from IFJ PAN, are involved in building one of the detectors for linear collider, namely the LumiCal, which will perform precise luminosity measurement. These works are performed in the framework of the FCAL Collaboration – the international collaboration established to develop the technologies of special calorimeters in the very forward region of future detectors at an e^+e^- collider. At the present development stage the main contribution of the AGH-UST group is the development of detector modules, and in particular its readout electronics. The AGH-UST group proposed the architecture of the LumiCal detector readout comprising of all the main processing blocks, namely front-end electronics, analog-to-digital converter and digital data concentrator, integrated immediately by the radiation sensor. The author of this dissertation believe that considering the advancement of the present semiconductor technology, it is possible to build such highly integrated and high performing detector system.

The main objective of this dissertation is to develop and validate the prototype detector module of the LumiCal detector. However, before the module can be constructed, it is important to investigate the performance of the components designed for this module. This is indispensable to build high performing system and avoid any unexpected behavior of the complete module after integration. The dissertation presents the works executed from the first detector concept,

through all subsequent R&D stages, ending with the test beam results obtained using the complete detector module. The text of the dissertation is focused around the author's work, however a complete overview of the linear collider in general, and the LumiCal detector in particular, is also provided. The author's contributions are clearly specified in the summary of this dissertation.

In the first chapter, the linear colliders are introduced. Their role in our understanding of the basis of matter, as well as sensing for the New Physics is presented. The major challenges faced by the accelerator and the detector R&D collaborations are outlined together with possible solutions. In the very forward region of experiments planned at linear colliders, two specialized calorimeters are foreseen. A LumiCal precisely measures the luminosity, while a BeamCal is responsible for the rapid estimation of luminosity and for the control of beam parameters. The details of the very forward region are revealed and the current R&D status of the FCAL Collaboration is presented.

The signal extraction from radiation sensors and further signal processing techniques are discussed in chapter 2. Besides the commonly accepted techniques of amplitude and time measurements, a novel readout implementation, utilizing Digital Signal Processing (DSP), is proposed, and its properties are analyzed in details. The signal processing method based on the digital deconvolution filter is considered in the view of systems synchronous and asynchronous with the radiation source. The amplitude and time reconstruction performance, as well as the pile-up immunity are studied.

The architecture, design, and measurements of the LumiCal readout chain components are presented in chapter 3. A dedicated test setups prepared for their parameterization are described together with the results of extensive measurements.

Finally, the construction of two prototype detector modules is presented in chapter 4. The first module comprises of limited functionalities with analog signal output, while the second one features all functionalities including data conversion and concentration. The design considerations and performance results of these two modules are followed by the test beam results. The measurements performed at electron beam at DESY validate the LumiCal detector's readout architecture.

Chapter 1

Future High Energy Physics experiments at Linear Colliders

1.1 Linear Collider

Already in ancient Greece people were deliberating on the constitution of matter. They believed that everything was built from small and non-divisible particles called atoms. At that time the Greeks were not able to see or measure atoms directly, but they suggested that different properties of atoms were reflected in a macroscale as different objects. In the 19th century, Dmitri Mendeleev sorted all known materials according to their properties in a periodic table. By using his table, it became possible to extrapolate new elements, which at that time remained undiscovered. The first subatomic particle – a negatively charged electron – was discovered by Joseph Thomson at the end of the 19th century. Around that time, Wilhelm Conrad Röntgen and Antoine Henri Becquerel, and Pierre and Marie Curie discovered X-ray and radioactivity, respectively. Ernest Rutherford's works on scattering experiments using alpha particles led him to the conclusion that the largest fraction of an atom's mass is concentrated in a positively charged nuclei. Rutherford's collision experiments (of alpha particles with gases) enabled him to identify the nuclei of hydrogen as being composed of a proton and to state that the nuclei of atoms more complex than hydrogen consist of more than one proton.

At the beginning of the 20th century, the works of James Chadwick and, independently, Walther Bothe, identified the neutron as a neutrally charged subatomic particle, which is contained in nuclei. It was suggested that radioactive β-decay could be understood as the decay of a neutron into a proton, an electron, and an antineutrino. The neutrino was postulated by Wolfgang Pauli to ensure energy conservation in β-decay. The positron – the antiparticle of the electron – was discovered a few years later. The next revolutionary step was Albert Einstein's special theory of relativity and his postulate about the equivalence of energy and mass. It became obvious that new particles (with higher masses) can be created in high-energy collisions. The accelerators were built to accelerate particles to high energies and to bring them to collision.

Increasing energies led to discoveries of even more new particles with different properties. Because it was hard to believe that so many "elementary" particles exist, the scientists were trying to find some pattern in this collection of particles. Symmetry considerations led to formulation of a scheme called Standard Model (SM), which was able to explain the origin of a variety

of particles from only six quarks and six leptons (and theirs antiparticles) – particles that are currently considered to be the primary constituents of matter.

The SM was suggested in order to provide an explanation of fundamental interactions and to supply a description of elementary particles, which are building blocks of all observable matter in universe. The SM turned out to be a very useful tool, which allowed already known particles to be sorted and many new particles to be predicted, as it was in the case of atoms in the Mendeleev's table. However, this model is not very elegant: it has been developed on top of a set of parameters, which cannot be derived from any fundamental theory. Nevertheless, because of the synergy of several types of particle colliders – lepton-lepton (e.g. Large Electron Positron Collider (LEP)), lepton-hadron (e.g. Hadron-Electron Ring Accelerator (HERA)), and hadron-hadron (e.g. Tevatron) – it became possible to measure all parameters precisely, and to extensively test the SM. Another serious limitation of the SM results from the fact that it assumes massless particles. To overcome this limitation a Higgs mechanism, which employed the Higgs boson, was proposed as an extension of the SM. The SM lacks a description of gravitational interactions as well as any prediction of the origin and properties of dark matter and dark energy. In order to extend the SM or formulate a completely new theory on top of the SM, new experimental input is necessary.

In order to validate the proposed models and obtain insight into a new physics, the LHC machine was developed and constructed [1]. The LHC is the world's largest and highest-energy particle accelerator ever built. It is located at the site of Conseil Européen pour la Recherche Nucléaire (CERN). The LHC collides two circulating beams of protons (or heavy ions) in a 27 kilometer long underground ring. The collisions take place inside four main experiments located around the ring: A Toroidal LHC Aparatus (ATLAS), Compact Muon Solenoid (CMS), A Large Ion Collider Experiment (ALICE), and Large Hadron Collider beauty (LHCb). These experiments have been accompanied by a rich physics program that should answer most of the emerging questions, for instance, regarding the origin of mass. It should also be possible to explore physics Beyond Standard Model (BSM), such as supersymmetry or extra dimensions, because the LHC provides very high center-of-mass energy, thus being on the high-energy frontier of today.

Regardless of the fact that the LHC has a very high potential for discoveries, the high energy physics community around the world has already begun R&D on high energy lepton collider design. Many measurements may be performed in a more precise manner by a lepton-antilepton collider in which both particles are annihilated and a burst of pure energy is spent to create new particle-antiparticle pairs. In lepton machines, almost all the center-of-mass energy is available for new particle production; the experimental background is relatively simple and clean. Such a collider is being considered to be the future research facility complementary to the LHC, as it was already in the past. The W and Z_0 bosons were discovered in the Super Proton Synchrotron (SPS) proton–antiproton collider, but it was the LEP electron-postiron collider that enabled precision measurement of their properties and detailed tests of the standard electroweak theory. Two possibilities are now under consideration: electron-positron or miuon-miuon colliders. While the second may offer higher collision energy with a similar accelerator footprint to that of the electron-positron machine, the first one is much more feasible in light of engineering issues. An e^+e^- collider will allow for precision measurements to explore in detail the mechanism of electroweak symmetry breaking and the properties of physics beyond the SM, possibly found at the LHC. Two concepts of an e^+e^- linear collider are presently considered: the ILC [2, 3, 4, 5] and the CLIC [6, 7, 8].

1.1.1 Physics at Linear Colliders

Over the last 20 years, detailed studies on the motivation for an electron-positron collider have demonstrated a compelling case for it as the next collider at the energy frontier [2, 3, 4, 5, 6, 7, 8, 9]. The unique strengths of a linear collider derive from the clean experimental environment arising from e^+e^- collisions. The center-of-mass energy and initial-state polarization are precisely known and can be controlled. The background processes are many orders of magnitude lower than the Quantum Chromodynamics (QCD) background that challenge hadron collider environment.

For the last two years, LHC and its experiments ATLAS and CMS have taken a direct look at this new regime, previously beyond accelerators energy range. Thanks to them, the High Energy Physics (HEP) community witnessed a deep revolution in the middle of 2012: discovery of a new boson with mass around 125 GeV. The observation of this new particle compatible with a light Higgs boson at the LHC substantiates the physics case for a linear collider even more.

The main goals of a very rich linear collider physics program include: precise measurements of the properties of the Higgs sector; precise measurements of the interactions of top quarks, gauge bosons and new particles; research beyond the SM; and sensing a new physics through tree-level or quantum effects in very high precision observables. Research in many contexts has proven that the lepton machine will precisely determine the properties of new particles found at the LHC as well as unravel the underlying structure of the new physics.

The SM hypothesizes a new form of Terascale energy called Higgs field, which permeates the entire universe. All elementary particles acquire mass by interacting with this field. The Higgs field is responsible for breaking a fundamental electroweak force into two forces: the electromagnetic and weak forces. Possible evidence of the existence of the Higgs field is a Higgs particle, which is supposed to accompany it. The observation of a new particle compatible with a Higgs boson of mass $\sim$ 125 GeV is a major breakthrough in particle physics. Beyond doubt, it is one of the most significant discoveries in modern science, which enhances our understanding of the fundamental structure of matter and the basic laws of nature. But still, a lot of questions about properties of this particle need to be answered:

- What are the couplings of the Higgs boson to particles?
- What are the mass, width, spin, and parity of the Higgs boson?
- What is the value of the Higgs particle's self coupling?
- Is this particle a single, fundamental scalar, as in the SM, or is it only a part of a larger structure?

Some of those questions are very hard, if at all possible, to answer by a hadron machine, while a lepton collider addresses all of them through a planned comprehensive set of high-precision measurements, where the large number of Higgs bosons are going to be produced. Therefore, the linear collider can be considered as a Higgs factory where Higgs boson properties can be studied in great detail. The discovery of the signal compatible with a Higgs boson is a breakthrough in particle physics; however, it should be kept in mind that the minimal electroweak symmetry breaking mechanism of the SM without other dynamic mechanisms has theoretical shortcomings. Thus, a more complex structure of electroweak region is generally favored.

The physics program of the linear collider operating in Terascale comprises of three broad categories:

- *Refining the LHC discoveries*. Phenomena discovered at the LHC will be precisely measured in a linear collider with a clean experimental environment. This is expected to reveal the physics mechanisms behind the observed phenomena.
- *New direct searches*. The linear collider has a potential for direct discoveries complementary to the LHC. In particular, the LHC discovery potential is surpassed by the linear collider in the area of the search for color-neutral states of the new physics.
- *Discoveries through precision*. A very precise measurement of observables allows for sensitivity in resolving the fingerprints of new physics, which in many scenarios manifest themselves only in tiny deviations from the SM predictions.

All of these points are crucial for revealing the possible structure of new physics and for discriminating between different possible manifestations of BSM physics.

Higgs Physics

The Higgs mechanism is a completely new phenomenon in particle physics, and its discovery will open up an entirely new and very important area of research. The fundamental properties of the Higgs boson, such as mass and total decay width, its spin and parity quantum numbers, its couplings to fermions and gauge bosons, and its self couplings that allow one to reconstruct the scalar potential responsible for electroweak symmetry breaking, still need to be measured [9].

In the e^+e^- collider, the main production mechanisms for the Higgs particle are, as shown in Figure 1.1, the Higgs-strahlung ($e^+e^- \to HZ^0 \to f\bar{f}H$) and the W^+W^- fusion process ($e^+e^- \to \nu_e\bar{\nu}_e H$) [10]. The final state $H\nu\bar{\nu}$ is generated in both the fusion and the Higgs-strahlung process. Besides the Z^0Z^0 fusion mechanism ($e^+e^- \to e^+e^-H$), which has an order of magnitude smaller

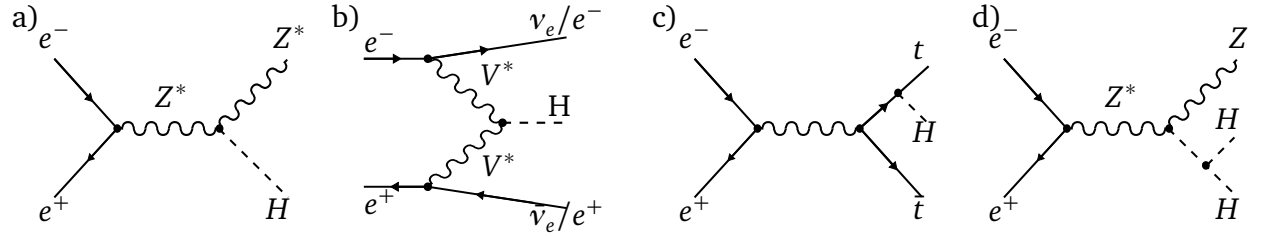

Figure 1.1: Production mechanisms of Standard Model Higgs boson: a) Higgs-strahlung process, b) W^+W^- / Z^0Z^0 fusion process, c) associated production with top quarks, d) double Higgs production in the Higgs-strahlung [7].

cross section than the twin W^+W^- fusion process, sub–leading Higgs production channels are associated with production of top quarks and double Higgs production in the Higgs-strahlung. The Higgs production cross section as a function of center-of-mass energy for Higgs mass 120 GeV is shown in Figure 1.2.

The Higgs boson decays into a large variety of channels. The main decay mode is by far the decay into $b\bar{b}$ pairs with a branching ratio of around 80% followed by the decays into $c\bar{c}$ and $\tau\bar{\tau}$

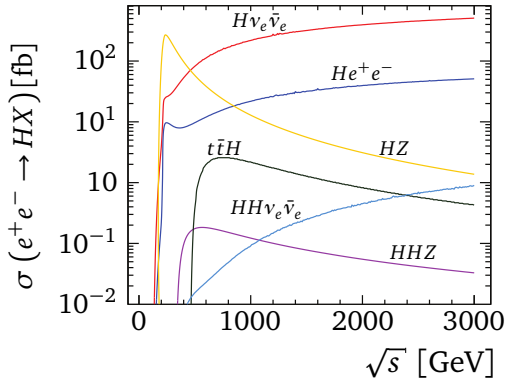

Figure 1.2: The Higgs production cross section as a function of $\sqrt{s}$ for $M_H = 120$ GeV [7].

pairs with fractions of 5%. The top-loop mediated Higgs decaying into gluons should occur at the level of 5%. In order to prove that what was observed at the LHC is actually a Higgs, it is necessary to demonstrate that its spin equals zero. The linear collider has the ability to measure the particle's spin directly by tracking the behavior of the production cross section as the collision energy is increased from the Higgs' threshold. This ability results from the fact that for electron-positron collisions the full center-of-mass energy is transferred to the final annihilation products: the particles that are created in the collision, including the Higgs. The cross section behavior (shape) near the production threshold depends on the spin, and particles of spin zero can thus easily be distinguished from those having spin 1 or spin 2. A second unique feature of the Higgs boson is that the Higgs field is responsible for the particles' masses, and therefore the Higgs boson's coupling strength is proportional to mass. Measuring how the Higgs couples to different constituent particles having different masses will not only demonstrate that this coupling relationship exists, but thanks to many collisions at the linear collider, quantitative measurements of the different coupling strengths will enable distinguishing between different models of the Higgs.

Top quark

The program, of which precision measurements in the Higgs sector are an important part, also consists of such stages or goals as establishment of a detailed profile of the top quark, study of the gauge sector with high precision, probing the dynamics of electroweak symmetry breaking mechanism, and BSM physics. The top quark, being the heaviest of the fundamental fermions observed until now, plays a very special role in the SM. Its large mass affects the prediction of many SM parameters, including the Higgs mass and the W and Z couplings, through radioactive corrections. High-precision measurements of the top quark properties and its interactions can provide for sensitivity to physics at mass scales far above the electroweak symmetry breaking masses. The top mass measurement at the hadron collider is limited because of systematic effects. The Tevatron has reached accuracy of about 1 GeV; it is probable that this number will not be significantly improved in the LHC. At the linear collider the top mass measurement is unique, since high-precision threshold mass measurement will do it. The overall precision of the top mass–better than 100 MeV–is expected to be achieved by the linear collider. Besides the extremely

precise measurement of top quark mass and width, the linear collider program contains a variety of further observables that have a high sensitivity to signatures of a new physics. The most promising is the forward-backward asymmetry in top-antitop production and the polarization of the top.

New Physics

A severe problem arises in the SM when trying to extend its validity to the Grand Unified Theory (GUT) scale: three gauge couplings of the SM do not meet at a single point and thus do not unify. A proposed Supersymmetry (SUSY) model contributes to the running of the gauge couplings to allow for their unification [11]. In addition, the SUSY solves the hierarchy problem. It assumes that for high energies (> 1 TeV) there should be a symmetry between fermions and bosons, i.e. every particle would have a heavy super-partner. The symmetry is not exact, otherwise SUSY particles would have exactly the same mass as the original particles. Supersymmetry is a well motivated scenario providing a rather complete and calculable framework of the BSM physics, including multiple new scalars and fermions of different gauge charges. The precision studies that are possible to be conducted at a linear collider could test many of the properties of the discovered particles such as values of their masses, their couplings to SM particles, or a spin. Furthermore, the precision measurement of the electroweak super-partner masses at the linear collider, combined with the measurements of strongly interacting super-partner masses at the LHC, allow us to test many ideas of the underlying organization principle for SUSY breaking. Through the results of those measurements, one gets access to a high-scale (e.g. GUT) structure of the theory.

It has been well established, mostly through astronomical measurements, that the universe must contain a sizable fraction of cold dark matter. An ideal candidate for this dark matter is a chargeless massive state χ that interacts with approximately weak gauge force strength (weakly interacting massive particle, WIMP). Several model-dependent scenarios of finding dark matter at the LHC and the linear collider exist. Most of them include cascade decays of parent particles that terminate in a stable dark matter particle candidate, which carries off missing energy. However, these missing energy signature rates strongly depend on multiple parameters of the theory and generally have little to do with the couplings directly relevant to the dark matter particle itself. A more direct and less model-dependent search for the dark matter focuses on the interaction $f\bar{f} \rightarrow \chi\chi\gamma$, where the initial-state radiated photon (or gluon) is needed to tag the event. The sensitivity to this process at the LHC is limited because of significant backgrounds. Within the clean linear collider environment, the χ mass and its major properties can be determined.

1.1.2 Machine Setup and Parameters

One of the major problems of high-energy particle accelerators is synchrotron radiation (the radiation emitted whenever charged particles change the direction of movement). To limit the effect of the resulting energy loss, the circumferences of circular machines must increase rapidly with the energy. The scaling up process of CERN's past LEP accelerator extended it to 27 km in circumference. It can be easily calculated that a circumference of thousands of kilometers would be required for an accelerator capable of accelerating an electron to the TeV energy range. For this reason, future electron–positron colliders are anticipated to be designed as linear machines.

International Linear Collider

Various laboratories were proposing electron-positron colliders with maximum center-of-mass energies of approximately one TeV, including the Stanford Linear Accelerator Center (SLAC) and the Fermi National Accelerator Laboratory (Fermilab) in the United States [12], the Deutsches Elektronen-Synchrotron (DESY) in Germany [13], and the High Energy Accelerator Research Organization (KEK) in Japan [14]. In an unprecedented milestone in HEP community, many institutes around the world involved in linear collider research and development (R&D) united in a common effort to produce a global design for International Linear Collider. The technical design and cost estimate for the ILC is based on two decades of cumulative experience of various laboratories.

The ILC is a 500 GeV center-of-mass energy high-luminosity, linear electron-positron collider, with the possibility of energy scanning. It is based on 1.3 GHz Superconducting Radio Frequency (SCRF) accelerating cavities, technology which was pioneered by the TESLA collaboration [15].

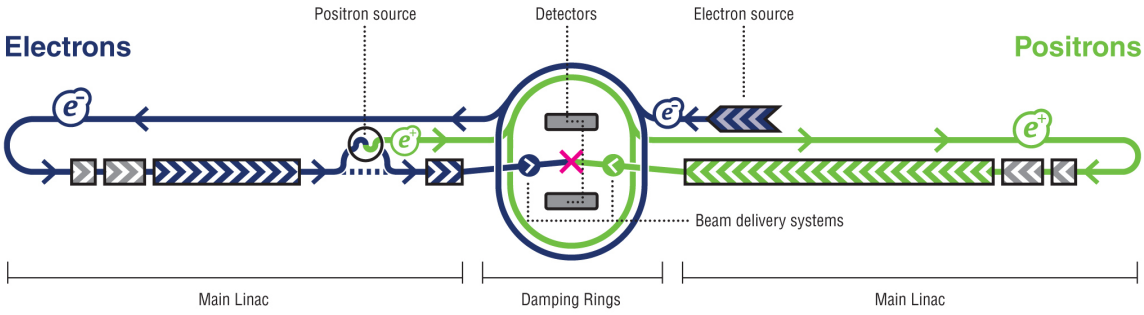

Figure 1.3: A schematic layout of the International Linear Collider [5].

A schematic view of the overall layout of the ILC is shown in Figure 1.3. The polarized *Electron source* is located on the positron linac side of the damping rings. The beam is produced by a laser illuminating a photocathode in a Direct Current (DC) gun. Bunching and pre-acceleration to 76 MeV occur in normal-conducting structures. After that, the beam is accelerated to 5 GeV in a superconducting linac. Just before injection into the damping ring, superconducting solenoids rotate the spin vector into the vertical.

The *Positron source* uses photoproduction to generate positrons. When acceleration reaches 150 GeV, the electron beam is transported through a 150 m helical undulator and returned to the electron linac. The high-energy ($\sim$ 10 MeV) photons from the undulator are directed onto a rotating 0.4 radiation-length Ti-alloy target, producing a beam of electron and positron pairs. The electrons and remaining photons are separated from the positrons and are dumped. The positrons are then accelerated up to 5 GeV and injected into the damping ring.

The ILC *damping rings*, housed in a single tunnel near the center of the site, include one electron and one positron ring (each 6.7 km long). The damping ring accepts electrons (or positrons) with large transverse and longitudinal emittances and damp to the low emittance beam required for luminosity production (by five orders of magnitude for the positron vertical

Table 1.1: Basic design parameters for the ILC [5] and the CLIC [16] accelerators.

Parameter	Unit	ILC	CLIC 500 GeV	CLIC 3 TeV
Center-of-mass energy	GeV	500	500	3000
Peak luminosity	$cm^{-2}s^{-1}$	2×10^{34}	2.3×10^{34}	5.9×10^{34}
Pulse rate	Hz	5	50	50
Pulse length (beam)	μs	~ 1000	0.177	0.156
Number of bunches per pulse		~ 3000	354	312
Bunch spacing	ns	330	0.5	0.5
Crossing angle at the IP	mrad	14	18.6	20
Particles per bunch		2×10^{10}	6.8×10^{9}	3.7×10^{9}
Accelerating gradient	MV/m	31.5	80	100
RF pulse length	ms	1.6	0.2	0.2
RF frequency	Hz	1.2	12	12
Typical beam size at IP (h × v)	nm	640×5.7	202×2.3	45×1
Number of photons per electron		1.3	1.3	2.1
Energy loss due to beamstrahlung	$\Delta E/E$	0.03	0.07	0.28
Total AC Power consumption	MW	230	271	582

emittance). It is also responsible for reducing incoming beam jitter (transverse and longitudinal) and for providing a highly stable beam. After beams are properly formed, they are transported from the damping ring to the upstream end of the linac. In the same time, polarization is rotated from the vertical to any arbitrary angle required at the Interaction Point (IP).

The two main linacs accelerate the electron and positron beams to the final beam energy of 250 GeV over a combined length of 23 km. The linacs are composed of Radio Frequency (RF) units, each of which is formed by three contiguous SCRF cryomodules containing 26 nine-cell cavities. Each RF unit has a stand-alone RF source, which includes a conventional pulse-transformer; a high-voltage (120 kV) modulator; a 10 MW multi-beam klystron; and a waveguide system that distributes the RF power to the cavities. An average accelerating gradient of 31.5 MV/m is achieved.

After acceleration, electrons and positrons are picked up by Beam Delivery System (BDS) from the exit of the high energy linacs, focused to the sizes required to meet the luminosity goals and finally brought into collision at IP. Not-collided particles (spent beams) are then transported to the main beam dumps. There is a single collision point with a 14 mrad crossing angle. There are two detectors in a common IP hall which alternately occupy the single collision point, in a "push-pull" configuration (chapter 1.2).

The total footprint of the ILC is ∼31 km. The main parameters of the ILC accelerator are presented in Table 1.1 [5]. There is also another option considered, to upgrade the ILC machine to center-of-mass energy of 1 TeV. The linacs and the beam transport lines from the damping rings would be extended by another 11 km each. Certain components in the beam delivery system would also need to be augmented or replaced.

Compact Linear Collider at CERN

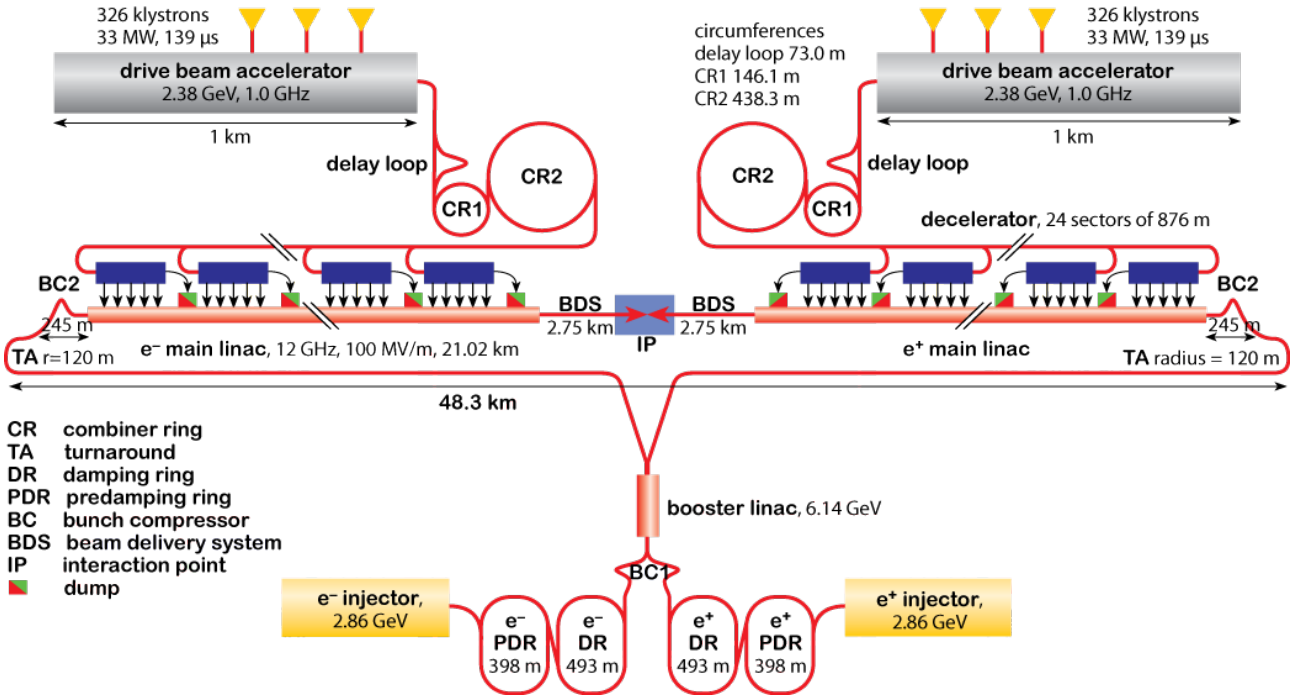

Figure 1.4: The CLIC general layout [16].

The second option currently being considered is a Compact Linear Collider (CLIC) accelerator proposed by CERN. A general layout of the CLIC, shown in Figure 1.4, is quite similar to the ILC. However, the CLIC accelerator has two key distinguishable features. The first is the operating frequency of the accelerating structures in the main linacs. To limit the length and the cost of these linacs, high accelerating fields are mandatory. Experience has shown that these can be obtained (with conventional acceleration mechanisms) only by operating at a high frequency. Therefore, the 30 GHz operation frequency has been chosen for the CLIC in order to achieve accelerating gradients as high as 100 MV/m. With such a design, a total length of 37.5 km is feasible for a 3 TeV collider.

The second interesting feature of the CLIC accelerator is the novel manner in which RF power is generated to accelerate bunches. High-intensity but low-energy “drive beams” of electrons run parallel to the main beam, and the power is extracted from these by specially designed decelerating structures. This is a particularly attractive feature because the energy for the RF power production resides in the electron beam which can be transported over long distances with very small losses. Another big advantage is that the RF power is generated locally, only where it is required. Such properties allow the transport distance from the drive linac to the main linac to be only about 60 cm. It should be noted that generation of an accelerating gradient of 100 MV/m requires the production of peak pulsed powers in the linacs of 460 MW per meter (however, the duration of the power pulse is shorter than 200 ns).

It has been envisaged that the CLIC machine would obtain a 3 TeV energy in the center-of-mass. There are, however, several reasons to consider constructing it in several stages [17]. In general, the luminosity of a given machine will drop proportionally to the energy as the energy

is decreased. For the CLIC, which is optimized for a given energy, beam stability considerations impose further limitations, and the bunch charge has to be reduced with decreasing energy. In order to maintain high luminosity, three construction stages are being considered: 500 GeV, 1.5 TeV, and 3 TeV. The main parameters of the CLIC accelerator at different energy stages are presented in Table 1.1 [16].

Even though overall layout is quite similar for both accelerators, experimental conditions at the CLIC differ from those at the ILC. In particular, the CLIC beam is composed of bunch crossings every 0.5 ns, while in the ILC bunch crossings take place every 330 ns. The short time between bunches at the CLIC means that detector systems must be able to rapidly detect and process signals generated by particles, while for the ILC each bunch crossing can be processed separately, without pileup from subsequent bunch crossings. The readout electronics for the CLIC requires time-tagging capabilities in order to assign a detection event to a particular collision. In addition, good pileup capabilities seem to be inevitable.

The choice of accelerator implementation, the ILC or the CLIC, as well as possible energy stages, will be guided mostly by the physics results obtained by the LHC experiments. In light of the most recent news from ATLAS and CMS experiments, announcing signals for relatively light boson, the ILC experiment seems to be the most probable choice because the design is almost ready and all selected technologies are already available. On the other hand, preliminary analysis performed by both experiments has shown that there is no "new physics" below 1 TeV. In the case of signals of SUSY from the LHC at energies above 1 TeV, the CLIC seems to be the only option.

1.1.3 Beam-Beam Interaction: Pinch Effect and Beamstrahlung

To increase luminosity at the future linear collider, accelerator designers increase bunch charge, thus keeping bunch size as small as possible and inducing a strong beam-beam interaction near the IP [18, 19, 20]. As soon as the bunches approach each other and start to overlap, electric charges are roughly compensated so that the electric field is canceled out while the magnetic fields, as given by the current densities, sum up. Particles inside the bunch will experience a strong Lorentz force due to the magnetic field, directed perpendicular to the beam axis, as illustrated in Figure 1.5.

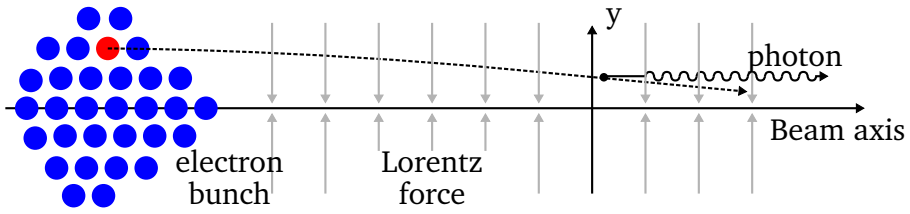

Figure 1.5: Schematic of beamstrahlung process [21].

For uniformly distributed charge densities this force is proportional to the distance of the particle from this axis. Hence, all particles with a non-zero distance to the beam axis (non-zero y in Figure 1.5) are deflected towards this axis, causing bunch compression in the x- and y-direction – the "pinch effect." The accelerated bunch particles radiate photons that are mostly collinear with the direction of the bunch motion. This phenomenon is called beamstrahlung. The

estimated number of photons generated by the beamstrahlung process per one electron for both accelerators is summarized in Table 1.1.

The large flux of beamstrahlung photons will produce e^+e^- pairs in the strong electromagnetic fields of the electron and positron bunches, both by coherent and incoherent pair creation processes [20, 22]. The coherent process consists of the interaction of the real beamstrahlung photons with the collective electromagnetic field of the opposite beam. The coherent production of e^+e^- pairs will increase the total number of colliding electrons and positrons (by up to 9% in the CLIC). The incoherent production of pairs is caused by the interaction of photons (real or virtual) with individual particles of the other beam. Most pairs are produced at a very small angle with respect to beam axis (< 10 mrad). However, depending on the motion of the produced pair with respect to beams, they may either be focused or defocused. This electromagnetic deflection may raise the transverse momentum of particles enough to travel beyond the beam pipe and become potential background in the detector active volume. The effect of deflection is much more pronounced for incoherent pairs, as they usually have lower energy and are produced at higher initial angles.

Another considered source of background in linear collider detectors are hadronic final states originating from the interaction of real and virtual photons from the colliding beams [23]. These interactions can produce particles at a large angle with respect to beam line, and become main background source in the central detector. This background process is the most distinct for the CLIC with its highest center-of-mass energy, where the predicted number of $\gamma\gamma \rightarrow$ hadron events within detector acceptance remains at the level of 3.2 per bunch crossing.

The energy spread of electron beams, as well as beam-beam effects, leads to the luminosity spectrum (also named differential luminosity). This effect is of primary importance for the 3 TeV CLIC machine, where only 35 % of luminosity will be delivered within 1 % of nominal center-of-mass energy. While the beam energy spread can be measured in an energy spectrometer upstream of the IP with sufficient accuracy, the energy loss due to beamstrahlung can only be calculated from strong field Quantum ElectroDynamics (QED) based on beam parameters. These parameters, such as beam position offset, angular rotations, or particle distribution in bunches, are changing continuously during the operation and cannot be easily directly measured. Luminosity spectrum must therefore be determined through the measurement of a physics channel. Because the luminosity spectrum is the same for all physics events, a well-known physics channel such as wide-angle Bhabha scattering is used to deduce luminosity spectrum by means of measurement [24]. Bhabha events can be precisely measured by tracking detectors and a dedicated luminosity calorimeter (chapter 1.3.3). The Monte Carlo (MC) simulation studies proved that the measurement of the differential luminosity is possible for the ILC parameters [25]. Studies on the CLIC began recently and haven't reached the final stage yet. Preliminary results, however, are encouraging [7].

1.2 Overview of Detector System

Detector systems at future linear colliders need to address a very different set of challenges compared to current state-of-the-art detectors developed for the LEP or the LHC. Linear collider detectors are not expected to suffer from high event rates, high radiation doses, or high background (with some small exceptions discussed in chapter 1.3); however, they have to fulfill

challenging demands for precision measurements and particle tracking and identification. Those requirements are led by several important physics processes.

As it was presented in chapter 1.1.1, there exists a wide range of BSM physics scenarios that define the possible goals for a future lepton collider. The accepted experimental signatures of new physics based on those models include: high multiplicity jet final states, multi-jet final states and missing energy, leptons and missing energy, heavy flavor production, or exotic final states (like non-pointing photons) [7]. On the basis of expected experimental signatures, the main detector requirements have been established by international collaboration and are presented below together with possible implementations. As detector design for future linear colliders is driven by requirements from expected physics scenarios, one has to remember that a more precise detector will result in smaller systematic errors in many measurements. Thus, it will extend the ultimate physics reach of measurements obtained by linear colliders. In addition, a more precise detector implies that the luminosity delivered by the collider will be used more efficiently, making it possible to reduce the overall operational costs and time to reach particular accuracy.

For the ILC experiment, two concepts of general purpose detectors have been established, International Large Detector (ILD) [26] and Silicon Detector (SiD) [27], based on high granularity particle flow calorimetry [28]. The concepts differ in the technologies of the sub-detectors but overall detector layout is very similar. It should be noted that the high granularity particle flow calorimetry is a relatively new concept while the energy flow and the particle flow have been used successfully by a number of collider experiments in the past. After the decay of short-lived particles created in high energy e^+e^- collisions, roughly 60% of the jet energy is carried by charged particles (mainly hadrons), around 30% by photons, and about 10% by long-lived neutral hadrons. The particle flow calorimetry requires the reconstruction of the four-vectors of all visible particles in an event. The momentum of charged particles is measured in tracking detectors with great precision, while the energy measurements for photons and neutral hadrons are obtained from the calorimeters. The jet energy is the sum of energies of individual particles, so from the point of view of event reconstruction, the sum of calorimeter energies is replaced by a complex pattern recognition problem, namely the Particle Flow reconstruction Algorithm (PFA). The detailed simulation studies of the ILC detector concepts using the PANDORA PFA have demonstrated that the jet energy resolution of approximately 3% can be achieved for jet energies in the range of 100 GeV – 1 TeV [29].

Assuming a staged approach for the CLIC, with the possibility of the initial operation at the ILC-like energies, the minimal requirements for a detector at the CLIC are same as for the ILC detectors. However, some additional requirements apply in the case of the CLIC detectors because of the planned upgrade of the center-of-mass energy and different machine environment (see chapter 1.1.2). Two detector concepts, in particular CLIC_ILD and CLIC_SiD, which are the adapted ILC detector versions, are proposed for the CLIC [7].

The design of all detectors for both experiments is driven by the requirements for excellent resolution of track momentum and jet energy measurement, excellent flavor tagging capability, and the ability to perform precision physics measurement in the presence of machine-related background (the latter applies especially to the CLIC). All detectors utilize pixelated vertex detectors, which provide a high precision vertex reconstruction, followed by sophisticated tracking detectors, optimized for high track reconstruction efficiency and excellent momentum resolution. The scheduled physics measurements rely on high quality calorimetry, so all four detector concepts have the calorimeters arranged inside the high field (3-5 T) solenoid.

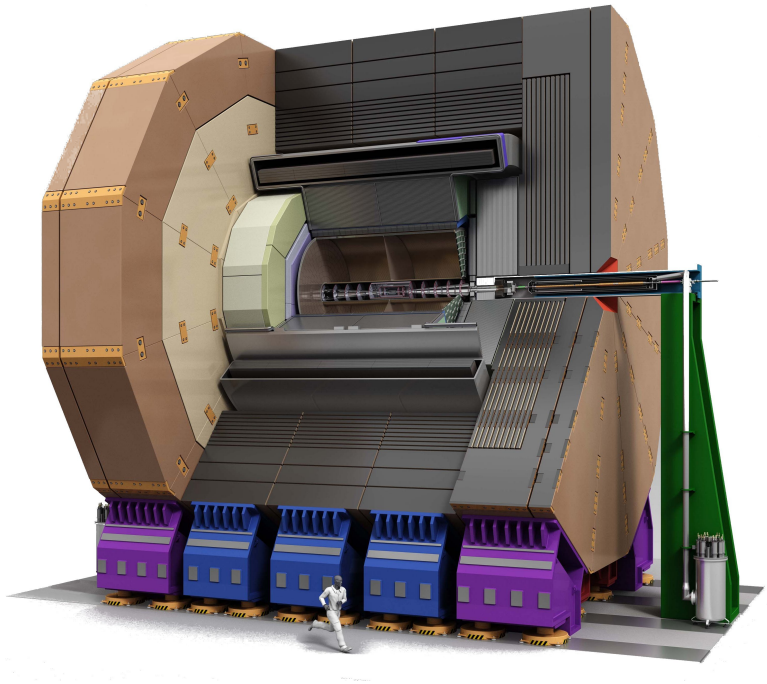

Figure 1.6: Cross section of the International Large Detector for the ILC [26].

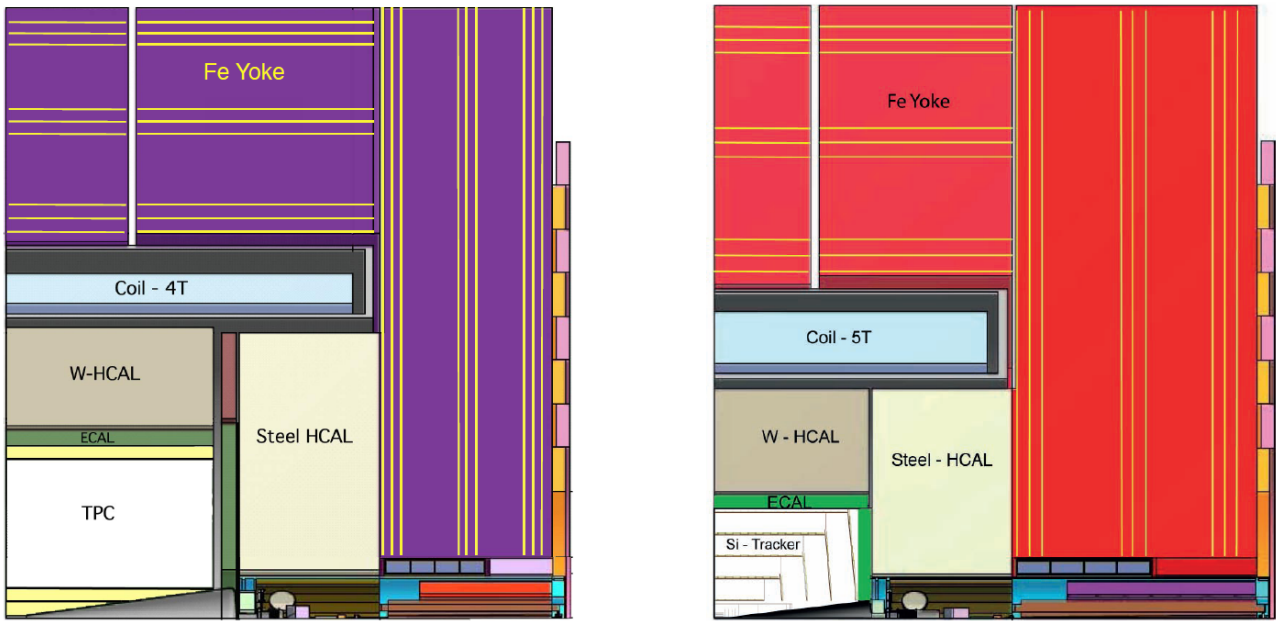

Figure 1.7: Longitudinal cross section of the top quadrant of CLIC_ILD (left) and CLIC_SiD (right) [7].

Both detectors, ILD and SiD, for the ILC and the CLIC have similar construction. As an example, a model of the ILD detector for the ILC is presented in Figure 1.6. More detailed longitudinal cross sections of the top quadrant of CLIC_ILD (left) and CLIC_SiD (right) are shown in Figure 1.7. The detector consists of a pixelated vertex detector (in the innermost region), a large volume tracker, and high granularity electromagnetic and hadronic calorimeters, all inside

a 4 T solenoid, completed by a precision muon system. In addition, two specialized calorimeters are provided in the very forward region of all experimental setups. Their development is the main subject of this dissertation, and they are described in more detail in chapter 1.3.

1.2.1 Vertex Detectors

The key element enabling the rich linear collider physics program is the Vertex Detector (VTX). A primary and secondary vertex reconstruction of unprecedented spatial resolution, minimal multiple scattering, and full geometrical coverage extending to low polar angles are required as well. Altogether, these factors impose extreme demands on the power consumption and mass budget of these detectors. The pixel VTX is placed in the center of the experiment, as it needs to be as close as possible to the beam pipe in order to obtain the best secondary vertex reconstruction. At the same time, it must safely remain (not to be blinded) outside the high occupancy caused by the background at low transverse momenta. Within the R&D framework for the ILC, several sensor technologies have been established, which proved to give the hit position resolution of 3-5 μm with pixel sizes in the 20 μm range. The ongoing activities in this field may be divided into a few major branches: the Complementary Metal-Oxide Semiconductor (CMOS) Monolithic Active Pixel Sensors (MAPS), the Silicon On Insulator (SOI), and the DEPleted Field Effect Transistor (DEPFET) solutions.

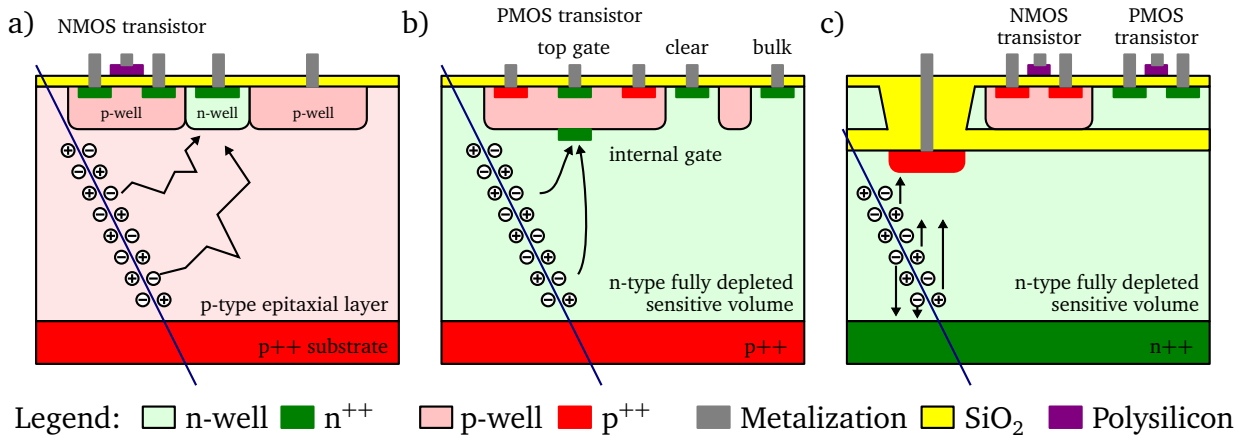

Figure 1.8: Cross section over pixel detector a) MAPS b) DEPFET c) SOI (drawings are not to scale).

The MAPS detectors [30], are made using the CMOS technology and they feature an additional epitaxial layer ranging in thickness from several micrometers to 20 micrometers, acting as a radiation sensor (see Figure 1.8a). A diode established by an n-well/p-type epitaxial layer junction is responsible for the collection of electrons liberated by the ionizing particle. The charge carriers reach the collection diodes by the thermal diffusion, and thus the MAPS detector exhibits a prolonged collection time ($\sim$ 100 ns). The difference between the doping levels of lightly doped p-type epitaxial layer and the p^{++} substrate ($\sim$ three orders of magnitude) leads to the creation of a potential barrier at the boundaries, which act like a mirror for the excess electrons. Each pixel of the MAPS detector is equipped with its own first stage signal processing electronics. The processing electronics is based only on the N-channel Metal-Oxide Semiconductor (NMOS)

transistors, that puts limitations to the complexity of the pixel level circuitry. It has already been demonstrated that MAPS detectors provide excellent single-point resolution below 2 μm (20 μm pixel pitch). The MAPS detector can be thinned down to 50 μm to reduce material budget in order to minimize the multiple scattering.

The cross section over the DEPFET detector is shown in Figure 1.8b [31]. In the DEPFET pixel concept, a first amplifying transistor is directly integrated into a high-resistivity silicon substrate. Electrons generated by ionization in the active volume are attracted by a potential minimum created underneath the transistor channel, which can be considered as an internal gate of the Field Effect Transistor (FET). The accumulated charge in the internal gate changes the transistor current. The readout is nondestructive and can be repeated several times. The removal of the signal charge and thermally generated electrons from the internal gate occurs by applying a positive voltage to the clear contact. The fully depleted bulk in the DEPFET pixel allows for short collection time and a high signal amplitude. In addition, low internal gate capacitance (of the order of 10 fF) allows for an extremely low noise operation. Moreover, DEPFETs consume very little power since the pixels are powered only during the readout. Despite all the aforementioned advantages, the major disadvantage of the DEPFET technology is its complicated and expensive fabrication process. Currently, the prototype detectors with pixel sizes of 22×30 μm^2 and matrix sizes of 64×128 pixels are fabricated on substrate as thin as 50 μm.

The cross section of the SOI [32] monolithic pixel cell is shown in Figure 1.8c. The high-resistivity, low doped n-type material of approximately 300 μm thickness constitutes the active volume of the device. An active area is depleted by applying negative voltage (with respect to n–type sensitive volume) to the p^{++} implant, creating a reversely biased p–n junction. The electronics layer is isolated from the sensor's active volume with a 1-2 μm thick Buried OXide (BOX) layer. Thus, the readout circuit can exploit both types of Metal-Oxide Semiconductor (MOS) transistors, which guarantees a much more effective functionality. The contact between the electronics layer and the p^{++} implant in the n-type sensitive volume is ensured through the bulk oxide by Vertical Interconnect Access (VIA). Since the sensor operates in a full depletion, it has a high signal amplitude and a low charge collection time, similar to the DEPFET. At present, the technology is not at a commercial standard, but the interest in it is increasing.

1.2.2 Tracking System

The tracking system is required to perform a momentum measurement of charged particles with high precision, exceeding that which has been achieved in HEP experiments thus far. The requirement for track momentum measurement at linear colliders originates from the Higgs mass determination from the Higgs-strahlung process ($e^+e^- \rightarrow ZH$). The Higgs mass can be precisely established by means of the mass distribution of the system recoiling against the pair of muons from Z decays ($Z \rightarrow \mu^+\mu^-$). However, the precision of this measurement is ultimately limited by the beam energy spread due to beamstrahlung (see chapter 1.1.3). For the resolution to be dominated by the beam energy spread, rather than detector performance, the precision of the momentum measurement needs to be $\sigma_{p_T}/p_T^2 \lesssim 5 \times 10^{-5}$ GeV^{-1} for the ILC, while for the CLIC, the requirement is even more stringent $\sigma_{p_T}/p_T^2 \lesssim 2 \times 10^{-5}$ GeV^{-1}. Similar requirements for the momentum resolution come from the considerations of BSM physics scenarios. The tracking system must cover the entire solid angle (except for the incoming and outgoing beams). The overall material budget within the tracking system should be kept as low as possible to preserve

momentum resolution, by minimizing multiple scattering. An average momentum resolution of a few 10^{-5} GeV^{-1} is desirable.

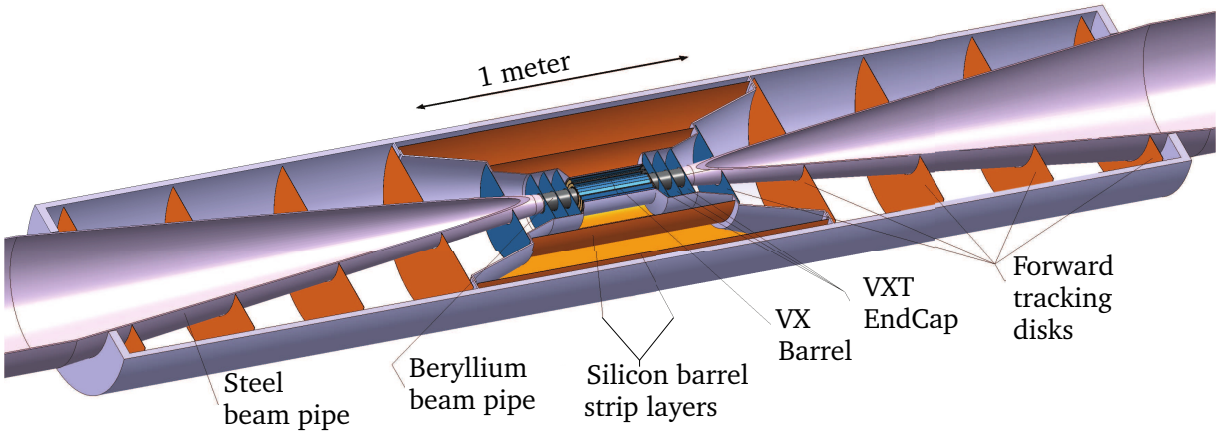

Figure 1.9: View of the inner and forward tracking region of the CLIC_ILD detector [7].

The two detector concepts have different approaches to perform momentum measurements: a Time Projection Chamber (TPC) and a silicon tracker are planned for ILD and SiD detectors, respectively. The TPC offers a highly redundant continuous tracking, efficient particle identification through dE/dx and a very little material within the active volume. However, more material needs to be present in front of the calorimeter, particularly in the forward region. In addition, track separation within dense jets and in high occupancy situations becomes very challenging, if possible at all. To provide tracking at low polar angles, the TPC needs to be supplemented by a silicon tracking system in the forward region. A view into the inner and forward tracking region of the CLIC_ILD detector is presented in Figure 1.9. The TPC in the CLIC needs to be surrounded by an additional silicon tracking layer to provide the timing and the precision space coordinates of particle entry into calorimeter.

The all-silicon solution of the SiD tracker offers an accurate space point measurement and provides precise time stamping capabilities because of a fast charge collection time. In addition, a smaller lever arm can be used because of the good spatial resolution (see Table 1.2). The tracker granularity is adjusted to deal with track separation in dense jets and with hits from the background. In contrast to ILD, the silicon tracker suffers from relatively high material density, less redundancy, and limited dE/dx information. Despite the pros and cons of both solutions, the simulation studies have demonstrated that both tracking systems are able to meet the required specifications.

1.2.3 Calorimetry System

The multi-fermion final states, which are produced in electron-positron collisions at TeV energies, give signatures with six to eight jets that are observed in the detector. The production of heavy bosons – W, Z, and Higgs – occurs in many physics channels. The main decay modes of these bosons are into hadron jets that need to be precisely measured. The particle flow approach enables demanding requirements to be satisfied; in particular, it allows W and Z bosons

to be separated on an event-by-event basis. Using the Particle Flow reconstruction Algorithm, it is possible to distinguish particles within jets and to optimize the jet energy measurement by making optimal use of the combined information from both the tracking and the calorimetry subsystems. For the jet energy range under consideration, the intrinsic calorimetric energy resolution for neutral hadrons is not of primary importance (because they appear in less than 10% of all collisions). Much more severe is the confusion during charged hadron and photon separation, when the energy deposits between charged and neutral hadrons are assigned incorrectly. Concerning this fact, the fine segmentation of the calorimeter system is mandatory. The calorimetry system is composed of an Electromagnetic Calorimeter (ECAL) surrounded by a Hadronic Calorimeter (HCAL). In addition, two specialized electromagnetic calorimeters are located in the very forward region (see chapter 1.3). They have different functions than ECAL (luminosity measurement and providing information required for fast beam tuning) so they are not considered as a part of ECAL. Since the main subject of this dissertation is the development of a luminosity calorimeter which is going to measure high energy electrons, the principles of electromagnetic interactions are presented next.

Principles of electromagnetic shower

Calorimeters are instruments made of material in which the measured particles are fully absorbed and their energy is transformed to a measurable quantity (most likely electric charge or light). The interaction (electromagnetic or strong process) of incident particle with the detector produces a shower of secondary particles having progressively degraded energy. Electromagnetic calorimeters are used to measure electrons and photons by electromagnetic interactions (bremsstrahlung, pair production).

The average energy lost by electrons in lead is shown in Figure 1.10a while the photon interaction cross section is shown in Figure 1.10b. In both figures, two regimes can be identified. At high energies, above critical energy (about $\sim$ 10 MeV for lead), electrons and positrons primarily lose energy through bremsstrahlung. In the same energy range, photon interactions produce mainly electron-positron pairs. For higher energies, those above 1 GeV, those processes become energy independent. However, below the critical energy, electrons lose energy mainly by ionization, although other processes (Møller scattering, Bhabha scattering, or positron annihilation) contribute as well. The photon interaction cross section is dominated in this range by the photoelectric effect and Compton scattering (Rayleigh scattering and photo-nuclear absorption contribute as well but are not shown in the Figure). The critical energy E_c is usually defined as the energy at which the electron ionization losses and bremsstrahlung losses become equal. As a result, electrons and photons with sufficiently high energy ($>$ 100 MeV), traveling through a block of material, most likely produce photons (by bremsstrahlung) or secondary electrons and positrons (by pair production), respectively. The generated secondary particles produce the next generation of particles through the same mechanisms. The number of particles in such a process increases exponentially until the energy of electrons drops below a critical energy, where energy is dissipated mainly by ionization end excitation. The characteristic amount of matter traversed by interacting high-energy particles is called the radiation length X_0. The radiation length is the mean distance over which an electron energy drops to $1/e$ because of bremsstrahlung and 7/9 of the mean free path for pair production by a high-energy photon.

The longitudinal shower development is governed by the high-energy part of the cascade,

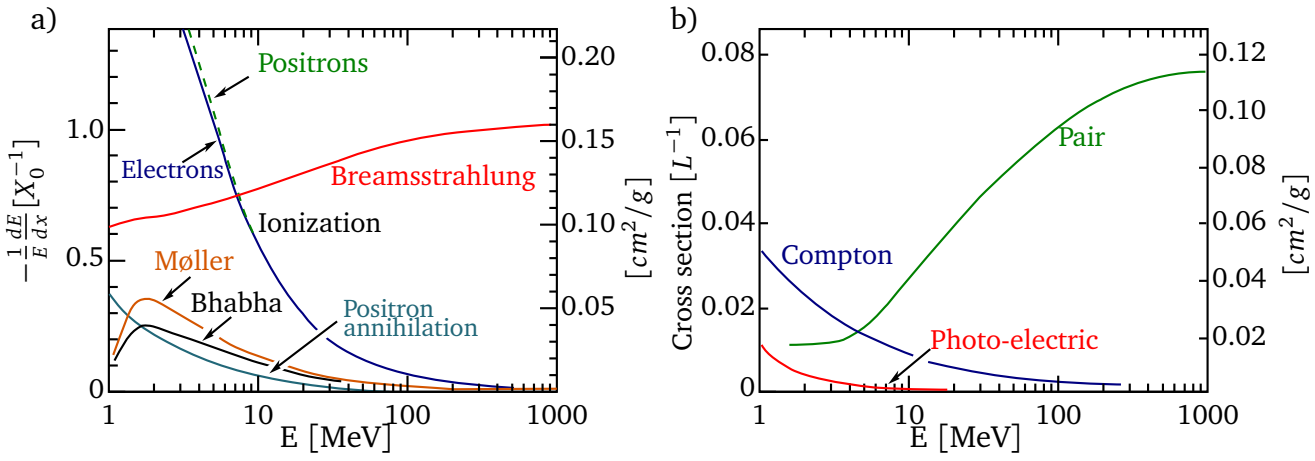

Figure 1.10: a) Fractional energy lost in lead by electrons and positrons as a function of energy [33]. b) Photon interaction cross section in lead as a function of energy [34].

and therefore scales as the radiation length of the material. Because of exponential growth of electromagnetic shower, the length of the calorimeter necessary to fully absorb the initial particle together with all secondary particles is proportional to the logarithm of the initial energy.

Most secondary particles have momentum directed parallel to the incoming particle. However, due to multiple scattering of electrons and positrons away from the shower axis, the transverse size of electromagnetic cascade is increased. The transverse development of electromagnetic showers scales fairly accurately with the Molière radius, R_M, given by:

$$R_M = X_0 \frac{E_s}{E_c} \ , \tag{1.1}$$

where $E_s \approx 21$ MeV. For the considered calorimeters in a very forward region, the Molière radius is expected to be around 14 mm. On average, only 10% of the electromagnetic shower lies outside a cylinder with radius R_M.

The calorimeters can consist of a single block of material just to give information about the energy of incoming particle. Most usually, scintillator crystals are used to transform the dissipated energy into a light pulse, which can be precisely measured at the edges of the crystal. When the information about position and direction of the particle is necessary, the calorimeter is segmented. It consists of high-Z absorber layers (responsible for shower development) interspersed by sensor layers (registering signals from charged particles). Such a calorimeter is called a sampling calorimeter. The sensors absorb only a small part of the dissipated energy so they can be similar to those used for tracking detectors. In order to determine the energy of showering particles, the integrated deposited energy in the detector has to be multiplied by a calibration factor. Because the energy deposited in sensor layers is usually only a small fraction of total particle energy, the deposited energy fluctuates. The energy measurement uncertainty can be parameterized as [34]:

$$\frac{\Delta E}{E} = \frac{a}{\sqrt{E}} \oplus b \oplus \frac{c}{E} \ , \tag{1.2}$$

where E is the mean deposited energy and ΔE is a standard deviation of the energy measurement. The symbol $\oplus$ represents addition in quadrature. The stochastic term a takes into account

fluctuations of the shower, sampling fraction, photoelectron statistics, etc. The term b represents detector non-uniformity and calibration, which is energy independent. Electronic noise, represented by c, usually contributes the least, so it can be neglected.

Electromagnetic Calorimeter

The role of the ECAL is primarily to individually measure photon energies and early parts of showers initiated by hadrons. However, photons as well as charged hadrons may be located close to each other; the most relevant feature of ECAL is therefore its very fine segmentation. In order to allow the separation of electromagnetic showers from each other, lateral segmentation is a crucial parameter. Regarding the absorber, tungsten is the material of choice for the ECAL in both detector concepts, while one- and two-sensor technologies are considered for the SiD and the ILD, respectively. The silicon pad sensor is a common option for both concepts. The second sensor option for the ILC are scintillator strips coupled to photon sensors for detecting the scintillation light. For each sensor technology, the readout electronics is embedded into sensitive layers. There are currently two Application Specific Integrated Circuit (ASIC) R&D programs within the ILC context: KPiX [27] and SPIROC/SKIROC [35]. The relative energy resolution as a function of beam energy obtained during the testbeam for both calorimeter prototypes, is shown in Figure 1.11.

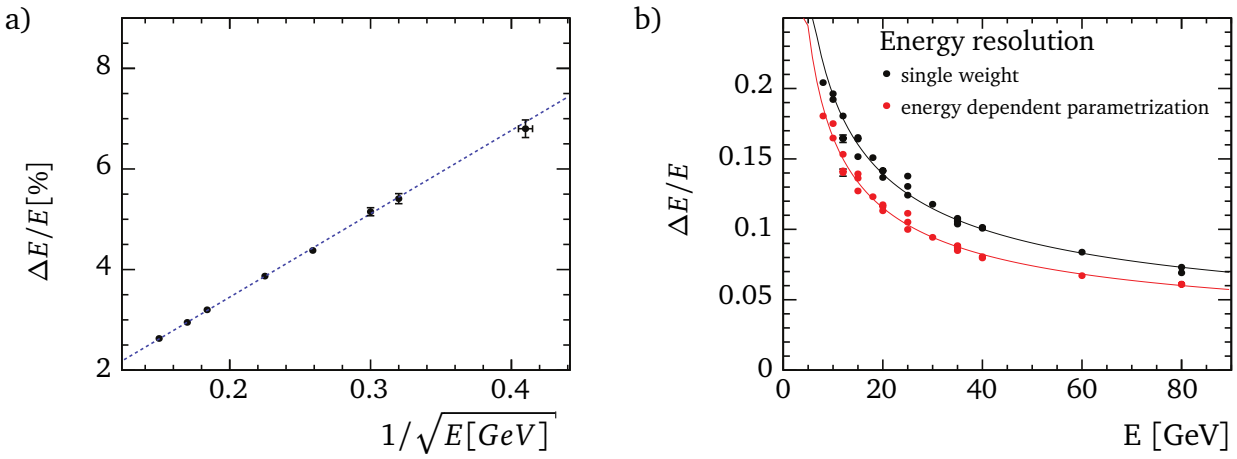

Figure 1.11: Relative energy resolution as a function of a beam energy obtained during test beam with the CALICE a) silicon ECAL prototype b) ECAL plus analog HCAL information combined for pions [36].

Hadronic Calorimeter

The HCAL is mainly responsible for measuring uncharged hadrons. It is conceived of as a sampling calorimeter with tungsten and stainless steel as an absorber and scintillator tiles (analog HCAL) or gaseous sensors (digital HCAL) as an active medium. Stainless steel has been chosen because of its mechanical and calorimetric properties. To keep the CLIC's detector barrel radius at similar level as that of the ILC, some parts of the HCAL are made of denser tungsten. Similarly to the ECAL, the active layers of the hadron calorimeter need to have a very fine longitudinal and transverse segmentation. This allows particles to be tracked through the calorimeter with

high accuracy, allowing for separation of neighboring showers. One option for the active layers are 3×3 cm^2 scintillating tiles being read by a multipixel Silicon Photo Multiplier (SiPM). Another possible option is a Resistive Plate Chamber (RPC) with 1×1 cm^2 readout pads. While the scintillator approach delivers analog output, the RPC are either digital or semi-digital (a few thresholds).

Performance studies, as well as technological prototyping of both calorimeters, are currently conducted by a worldwide CALICE Collaboration. Several realistic ECAL and HCAL prototypes have been developed and tested by CALICE [37, 38].

1.2.4 Muon System

Many interesting physics processes at the linear collider contain muons in the final state. Muon identification with high efficiency is therefore an important requirement for the detector system. In order to enhance the muon identification capability of the detector, the iron yoke is instrumented with track sensitive chambers. There are two sensor technologies under consideration: glass RPC or scintillators. Precise momentum measurement can be only achieved by an excellent tracking system. Muons have to traverse large amount of dense material before they reach the yoke; therefore, the muon system can contribute much in improving momentum measurement. The most important task is to efficiently connect tracks from the inner detector with tracks in the muon system, in order to properly reconstruct muons. In addition to its muon tagging capability, the very first layers of the muon system can act as a tail catcher for showers exiting the HCAL.

The muon system is made of nine instrumented active layers embedded into an iron yoke. Each layer is divided into 40×30 mm^2 cells. Simulation studies showed that for isolated muons with a polar angle greater than 10 mrad and energies of more than 7.5 GeV, the efficiency exceeds 99%. For events with higher multiplicity, the efficiency drops to 90%.

1.2.5 Detector Readout and Data Acquisition System

The requirements for detector's electronic readout at future linear collider are dictated by the need for high precision measurement and are related to the beam structure. Interesting high energy e^+e^- collisions are expected to be rare, while the beam-induced background level (see chapter 1.1.3) makes many additional particles traverse the detector, especially at low polar angles, in this way increasing cell occupancies. In order to precisely measure the physics events, sufficient separation between physics and background hits must be secured. In linear collider accelerators, the electrons and positrons will be delivered to experiments in trains of bunches followed by a long pause. A simplified time diagram is shown in Figure 1.12.

The time separation between bunch crossings is $\sim$ 330 ns at the ILC and, much more challenging from the readout point of view, 0.5 ns at the CLIC. However, the bunch train lasts only 156 ns at the CLIC while 1 ms at the ILC. Therefore, the experiments are designed to work without a traditional high-level trigger system. Each bunch crossing is recorded. A selection of events is performed by a software trigger during the offline data analysis. Such a solution ensures very high efficiency and sensitivity to any type of new physics but at the same time imposes greater requirements on the front-end electronics of each sub-detector. The high granularity of the subdetectors (millions of channels) and $\sim$ 3000 bunches in the ILC ($\sim$ 312 bunches in the CLIC) enforces elevated requirements concerning data links. The substantial throughput of these links

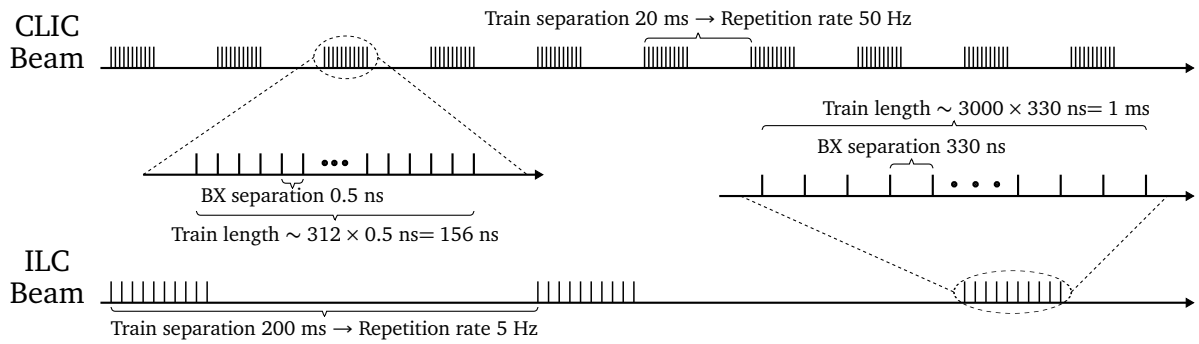

Figure 1.12: The simplified time diagram of the beam structure at the ILC and the CLIC.

is necessary to read the detector data before the next bunch train. The detector front-end needs to provide zero suppression and as much data compression as possible.

The high granularity of the detector forces multiplexing of data from many channels into a few links going out of the detector (see Figure 1.13). It is mandatory to avoid a large number of readout cables as well as to reduce dead material and gaps in the detector. The proposed data acquisition system architecture [39], adapted for forward region calorimeters, is shown in Figure 1.13. The event data collected from readout ASIC's by a Detetcor InterFace (DIF), are sent through the next level of data concentration – Data Concentrator Card (DCC) and Link Data Agregator (LDA) – to the Off Detector Receiver (ODR), which is built as a component of the Data Acquisition System Personal Computer (DAQ PC). The Clock & Control Card (CCC) is responsible for delivering information about machine operation (bunch clock, train start signal) to all sub-components.

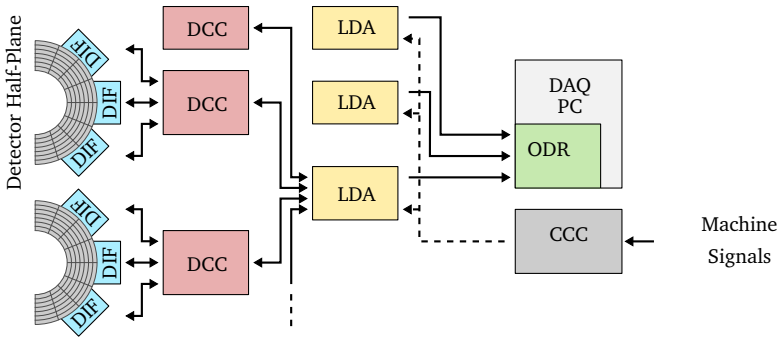

Figure 1.13: The data acquisition system architecture for forward region calorimeters. Legend: Off Detector Receiver (ODR), Data Concentrator Card (DCC), Clock & Control Card (CCC), Link Data Agregator (LDA), Detetcor InterFace (DIF) [39].

The power management for readout electronics is crucial in view of the high precision requirements and the large number of channels. Large power dissipation in the front-end electronics would result in a heavy cooling system, which would have negative impact on detector performance. The progress of microelectronic technologies has resulted in lower power voltages that reduce power dissipation in comparison with today's large experiments. This advantage is, however, counterbalanced by the huge channel count and increasingly complex front-end features.

Since the bunch structure has a very low duty cycle of 0.5% at the ILC and even less at the CLIC, the average power consumption can be significantly reduced by turning power on only when it is needed.

The radiation level for electronic readout, expected in the linear collider environment is typically a factor of 10^4 lower than at the LHC, so for most of the sub-detectors it is not treated as a challenging aspect.

1.2.6 Detectors Summary

The conceptual design of detectors has reached a rather mature state, and has not changed significantly since it was first proposed. Over the past few years, a significant progress has been made to transfer the conceptual design into a real, technically understood, and confirmed design. A summary of the key parameters of the ILC and the CLIC detector concepts is presented in Table 1.2.

Besides the great potential for the linear collider physics program, made possible by the detectors and technologies developed by the detector community, one should keep in mind that the impact of these works is very real even nowadays [40]. The high performing technologies developed for vertex detector at the ILC were already utilized by a number of different collaborations. The DEPFET detector was used by BELLE-II collaboration at the KEK b-factory [41]. The MIMOSA-26 sensor was used by the whole HEP community in high precision tracking telescopes at testbeam lines [42]. It was also chosen for the heavy flavor tracker of the STAR experiment at RICH at Brookhaven [43]. A simulation and analysis framework developed for TPC at the ILC was used to build the near detectors for the T2K experiment [44]. The hallmark of a linear collider detector – a fine-grained calorimeter – has already been recognized in the field of medical imaging for Proton Computed Tomography (pCT) [45]. The HARDROC chip, originally designed as readout electronics for the hadronic calorimeter at the ILC is currently being deployed in a handheld perioperative gamma Tumor Resection Camera [46]. The extremely radiation hard sensors, developed by FCAL collaboration for BeamCal detector (described in chapter 1.3.2), were utilized to build the fast beam condition monitor of the CMS experiment for the LHC [47]. All this confirms that the detector R&D programs have a significant and positive impact on the field of particle physics and beyond.

1.3 Forward region

In the very forward region, two specialized calorimeters are foreseen. A LumiCal precisely measures the luminosity, while a BeamCal is responsible for the rapid estimation of luminosity and for the control of beam parameters [48]. In addition, both detectors significantly improve the hermeticity of the detector, extending the acceptance range to very small polar angles. An additional detector, the pair-monitor, which is placed just in front of the BeamCal, is foreseen to support beam-tuning. The design and R&D effort of the forward region for linear colliders is being elaborated by a worldwide FCAL collaboration [49], of which the author of this doctoral dissertation is a member.

A schematic diagram of the very forward region of the ILD detector for the ILC experiment is shown in Figure 1.14. Both detectors are composed of two cylindrical sensor-tungsten elec-

Table 1.2: Key parameters of the ILC and the CLIC detector concepts [7] (B stands for barrel. E stands for Endcap).

Concept	Unit	ILD	CLIC_ILD	SiD	CLIC_SiD
VTX					
Inner Radius	mm	16	31	14	27
Barrel layers			6 (3 double layers)		5
Forward disks			6 (3 double layers)		7
Tracker					
Inner Radius	mm		329 (TPC) 165(Si)		230
Technology B / E		TPC/Silicon	TPC/Silicon	Silicon	Silicon
Max samples B / E			227 / 5		5 / 4
ECAL					
Absorber		Tungsten	Tungsten	Tungsten	Tungsten
Inner Radius	m	1.8	1.8	1.3	1.3
Δr	mm	172	172	135	135
Sampling Layers	- × mm	20 × 2.1	20 × 2.1	20 × 2.7	20 × 2.5
		+ 9 × 4.2	+20 × 4.2	+ 10 × 5.4	+ 10 × 5
HCAL					
Absorber B/E		Fe	W/Fe	Fe	W/Fe
λ_I		5.5	7.5	4.8	7.5
Solenoid					
Field	T	3.5	4	5	5
Free Bore	m	3.3	3.4	2.6	2.7
Length	m	8.0	8.3	6.0	6.5
Overall Dimensions					
Size [H x L]	m	14.0 × 13.2	14.0 × 12.8	12.0 × 11.2	14.0 × 12.8
Weight	tons		12 200		12 500

tromagnetic sampling calorimeters, centered on the outgoing beam on each side of IP. The calorimeters are composed of two half-cylinders in order to permit their installation around the beam-pipe. The distance between two adjacent tungsten plates is kept to 1 mm to approach the smallest possible Molière radius. The small Molière radius ensures veto capabilities for the BeamCal even at small polar angles, which is essential to suppress background events in new-particle searches where the signature is a large missing energy. In the LumiCal, on the other hand, a small Molière radius is necessary to precisely reconstruct the angle of Bhabha scattered electron and positron. Another, no less important function of forward calorimeters is to shield the inner tracking detectors from back-scattered particles induced by beamstrahlung pairs hitting the downstream beam-pipe and magnets.

A comparison of the main geometrical parameters for the ILD at the ILC and the CLIC_ILD detector concepts is summarized in Table 1.3. Each calorimeter is composed of 30 and 40 tung-

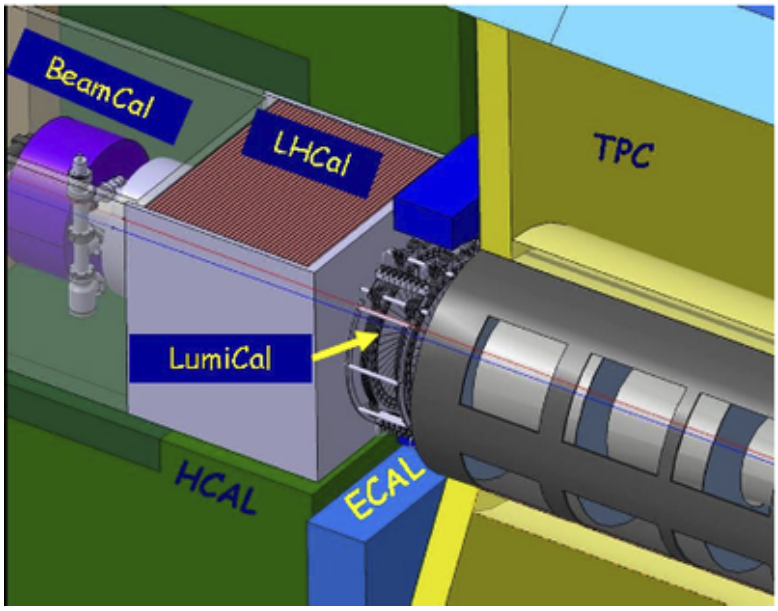

Figure 1.14: The very Forward Region of the ILD detector. (ECAL and HCAL denote the electromagnetic and hadronic calorimeter, TPC is for Time Projection Chamber). The interaction point is to the right of the plot [48].

Table 1.3: Comparison of the LumiCal and the BeamCal at the ILC and the CLIC, based on the example of the ILD detector concept [7].

		Unit	ILC	CLIC_ILD
LumiCal	geometrical acceptance	mrad	31-77	38-110
	fiducial acceptance	mrad	41-67	44-80
	z (start)	mm	2450	2654
	number of layers (W + Si)		30	40
BeamCal	geometrical acceptance	mrad	5-40	10-40
	z (start)	mm	3600	3281
	number of layers (W + Sensor)		30	40
	graphite layer thickness	mm	100	100

sten absorber plates, interspersed with sensor layers in the ILC and the CLIC, respectively. An increased number of plates in the CLIC with respect to the ILC is related to maximum energy to be measured. Every absorber layer is 3.5 mm thick, which corresponds to approximately one radiation length. The detectors' opening angles in the CLIC were adapted to reduce to a manageable level the amount of beam-induced background observed in the detectors.

1.3.1 Principles of Luminosity Measurement

Luminosity, $\mathscr{L}$, is a key parameter that describes the performance of HEP accelerators. Knowing its value, one can calculate the number of particular events per second N_{ev} produced in collisions:

$$N_{ev} = \sigma \mathscr{L} \ , \tag{1.3}$$

where σ is the process cross section. Accelerator luminosity is related to beam parameters according to the following formula:

$$\mathscr{L} = \frac{N_b^2 n_b f_r \gamma}{4\pi\epsilon_n \beta} F(\phi p) \ , \tag{1.4}$$

where f_r is the number of collisions per second, γ is the relativistic Lorentz factor, ϵ_n is the normalized transverse emittance, β is the beta function at the collision point, and finally, N_b is the number of particles per one bunch. Although the luminosity can be estimated using formula (1.4), it needs to be precisely measured in a final experiment to decrease systematic uncertainties in measurements of physical processes. The requirement for high precision measurement of the luminosity is given by a number of recorded events of the lowest cross-sectional process, which is going to be measured in an experiment (neglecting other uncertainties).

To measure experiment's luminosity, a well-understood process in which cross section can be precisely calculated has been chosen. For a number of electron-positron colliders, Bhabha scattering has been used as a gauge process to monitor the luminosity. The elastic Bhabha scattering process $e^-e^+ \to e^-e^+$ is shown in Figure 1.15.

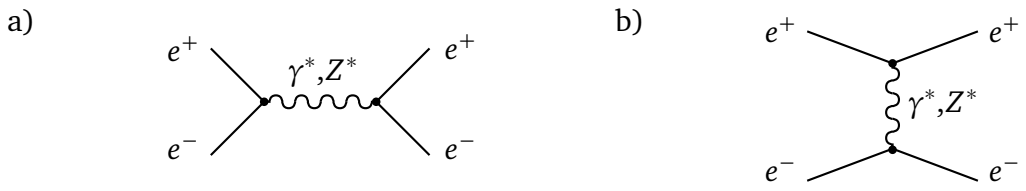

Figure 1.15: A Feynman diagram of the a) s-channel and b) t-channel elastic Bhabha scattering.

The differential cross section of Bhabha scattering, $d\sigma_B/d\theta$, can be precisely calculated from theory [50, 51, 52, 53]. If only leading order diagrams are considered, it can be presented as:

$$\frac{d\sigma_B}{d\theta} = \frac{2\pi\alpha_{em}^2}{s} \frac{\sin\theta}{sin^4(\theta/2)} \approx \frac{32\pi\alpha_{em}^2}{s} \frac{1}{\theta^3} \ , \tag{1.5}$$

where θ is the polar angle of the scattered electron with respect to the beam and α_{em} is a fine-structure constant. For a fixed θ-range, the integrated luminosity $\mathscr{L}_{int}$ can be measured by counting Bhabha events as:

$$\mathscr{L}_{int} = \frac{N_b}{\sigma_B} \ , \tag{1.6}$$

where N_B is number of observed events and σ_B is an integral of the differential cross section, eq. (1.5), over the whole θ-range. When neglecting θ_{max} dependence, it can be approximated by:

$$\sigma_B = \int_{\theta_{min}}^{\theta_{max}} \frac{d\sigma_B}{d\theta} d\theta \approx \frac{\pi\alpha_{em}^2}{s} \frac{1}{\theta_{min}^2} \ . \tag{1.7}$$

The cross section for Bhabha events falls as $1/\theta^3$ according to (1.5), so the luminosity error as a function of the polar angle bias, $\Delta\theta$, can be expressed as:

$$\frac{\Delta\mathscr{L}_{int}}{\mathscr{L}_{int}} = \frac{2\Delta\theta}{\theta_{min}} \ . \tag{1.8}$$

The polar angle bias and the minimal polar bound of the fiducial volume, θ_{min}, are the two most important parameters that affect the precision of the luminosity measurement. For the given precision of θ measurement, formula (1.8) leads to the conclusion that larger θ_{min} results in smaller uncertainties in luminosity measurements. The position of the inner radius of the detector on a μm precision level, and the distance between its two arms within 500 μm are obligatory in order to measure the luminosity precisely. However, one has to keep in mind that luminosity measurement is a counting experiment. The relative statistical error stemming from equation (1.6) is therefore proportional to $1/\sqrt{N_b}$. If the value of θ_{min} is excessive, it leads to imprecision in luminosity measurement which is mostly caused by statistical fluctuations.

1.3.2 BeamCal Detector

The BeamCal is positioned just outside the beam-pipe. As was described in chapter 1.1.3, for the considered beam energies, a new phenomenon, the beamstrahlung will appear. A fraction of photons, radiated by high-energy electrons and positrons, converts in the Coulomb field of the bunch particles creating low energy e^+e^- pairs. A large fraction of these pairs will deposit their energy in BeamCal. Distribution of these depositions is very useful for a bunch-by-bunch estimate of beam parameters as well as for a rapid estimation of luminosity. Another important role of BeamCal is to ensure a high-energy electron detection capability, even at small polar angles, to provide veto mechanism in new physics searches. The sensors of the BeamCal are structured into pads of about 8×8 mm^2 in size, thus allowing for maximum electron detection efficiency. The distribution of the energy deposited by beamstrahlung pairs after one bunch crossing in the sensors of the BeamCal in the ILC is shown in Figure 1.16a. Superimposed is the deposition of a single high-energy electron (red spot on the right side).

The expected energy depositions will lead to huge radiation doses in the BeamCal sensors. The dose in the BeamCal sensor per year as a function of radial distance from the beam axis is presented in Figure 1.16b. In sensors located close to the beam pipe (the lowest polar angles) the absorbed dose approaches about one MGy per year. Hence, radiation hard sensors are essential for proper operation of the BeamCal.

The challenge of the BeamCal is to find a radiation resistant sensor that tolerates about one MGy of dose per year. Several sensor materials have been carefully studied by FCAL collaboration. Irradiations were performed using a 10 MeV electron beam at the S-DALINAC accelerator [54] at different intensities, corresponding to dose rates between 20 and 200 kGy/h. A Chemical Vapor Deposition (CVD) diamond sensor demonstrated [55] the ability to operate properly up to 7 MGy. Since large area CVD diamond sensors are extremely expensive, they may be used only at the innermost part of the BeamCal. At larger radii, GaAs sensors appear to be a promising option [56].

Since the occupancy in the BeamCal is relatively large, each sensor cell must be read out after each bunch crossing to avoid pileups. A special ASIC has therefore been developed that matches

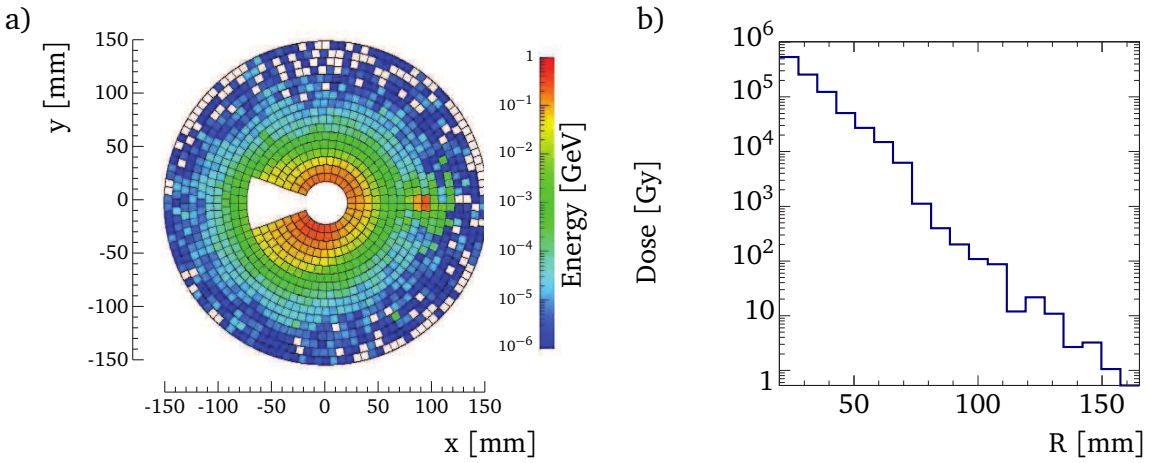

Figure 1.16: a) The distribution of the energy deposited by beamstrahlung pairs after one bunch crossing in the sensors of the BeamCal in the ILC. Superimposed is the deposition of a single high-energy electron (red spot on the right side). The white area in the center allows space for the beam-pipes. b) The dose in BeamCal sensors per year as a function of the radial distance from the beam [48].

the timing of the ILC bunches [57]. The readout chain is composed of a charge sensitive amplifier, a shaping circuit, and an Analog-to-Digital Converter (ADC) (signal processing is described in more detail in chapter 2). The readout ASIC features a fast feedback adder, capable of providing a low-latency information about integrated energy depositions in all channels, for beam diagnostics purposes. First prototypes of the BeamCal readout ASIC have been manufactured and successfully tested.

1.3.3 LumiCal Detector

A dedicated luminosity detector, LumiCal, is foreseen to measure the integrated luminosity by counting Bhabha events. A basic experimental selection of Bhabha events is obtained by requiring the coincidence of an electron and a positron in a back-to-back topology and with polar angles within acceptance volume of the calorimeter (where electromagnetic shower is fully contained) and energies larger than 0.8 of nominal beam energy. To match the physics benchmarks, an accuracy of better than 10^{-3} is needed at a center-of-mass energy of 500 GeV [27]. For the GigaZ option, where the machine is tuned to operate at center-of-mass energies around the Z boson mass, an accuracy of 10^{-4} is required [58]. The main error of luminosity measurement comes from measurements of electrons at low polar angles (see chapter 1.3.1). To meet the requested accuracies, a highly precise device is necessary, with particularly challenging requirements arising from the particle polar angle reconstruction.

A mechanical design of the LumiCal detector barrel for ILD detector is shown in Figure 1.17a [59]. The 30 tungsten absorber disks are assembled together in a mechanical frame stabilized by steel rods. Hence, as very precise polar angle measurement of electrons and positrons is needed, sensor layers are divided azimuthally into 48 segments and then each segment is divided into 64 radial pads. Such segmentation results in 3072 channels per layer and almost 100 thousand in the entire detector barrel. The 300 μm thick silicon sensors tiles, comprising of 4 segments (256 sensor pads), are fixed on the tungsten and connected via a kapton fanout to the front-end

a) b)

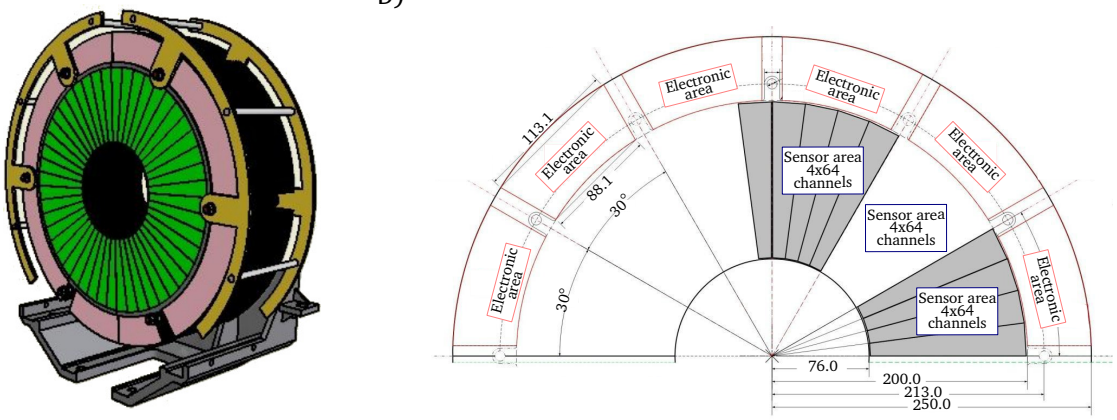

Figure 1.17: a) A drawing of the LumiCal detector at the ILC [59]. b) A half-plane layout of the LumiCal detector (all dimensions in millimeters) [60].

electronics placed at the outer radius, as shown in Figure 1.17b. Considering a huge number of channels as well as constrains for power consumption and available area, dedicated ASICs are needed to process information from the radiation sensors.

The energy deposition in each sensor pad is recorded by the dedicated readout electronics and a reconstruction of the shower is performed. The position of an electromagnetic shower on each LumiCal plane is reconstructed by computing a weighted average of the energy deposits in individual pads. The weight, W_i, of a given pad is proportional to the energy deposited in this pad E_i, according to $W_i = max\{0, \xi + ln(E_i/E_{tot})\}$, where E_{tot} is a total shower energy, and ξ is a constant [61]. Having the shower center position at each plane, the coefficients of a best straight line passing through all planes are calculated. Since the LumiCal is considered as a precision device, special care is taken to secure mechanical stability and position control. The LumiCal barrel model was simulated using a Finite Element Method (FEM). The maximum vertical calorimeter displacement induced by its weight has been estimated at the level of 20 μm. The tungsten plate deformation is estimated to be 25 μm for a temperature difference of 1° K. To meet requirements for the precision of particle measurements at lowest polar angles, the sensor position needs to be controlled to better than 40μm. Other critical quantities are the distance between the two calorimeter barrels and their position with respect to beam axis, where the requested precision should be at a level of 500 μm. To meet this requirement, a laser-based position monitoring system was proposed [62] to precisely measure all aforementioned distances.

The proposed mechanical design was implemented in a GEANT4 simulation framework. Shower development processes were carefully simulated and the geometry was optimized to achieve the best performance. Figure 1.18a presents two normalized distributions: the number of shower particles and the deposited energy as a function of the layer number, for shower generated by 250 GeV electron. The energy deposited in silicon sensors is proportional to the number of charged shower particles. Both distributions peak around the 10th layer. With 30 radiation lengths of tungsten absorber in total, high energy electrons and photons deposit almost all of their energy in the detector. The relative energy resolution (given as a term in equation (1.2)) for electrons located inside the fiducial volume of the LumiCal is estimated to be $0.21\sqrt{GeV}$. The expected range of energy depositions in a single pad covers few orders of magnitude. The mini-

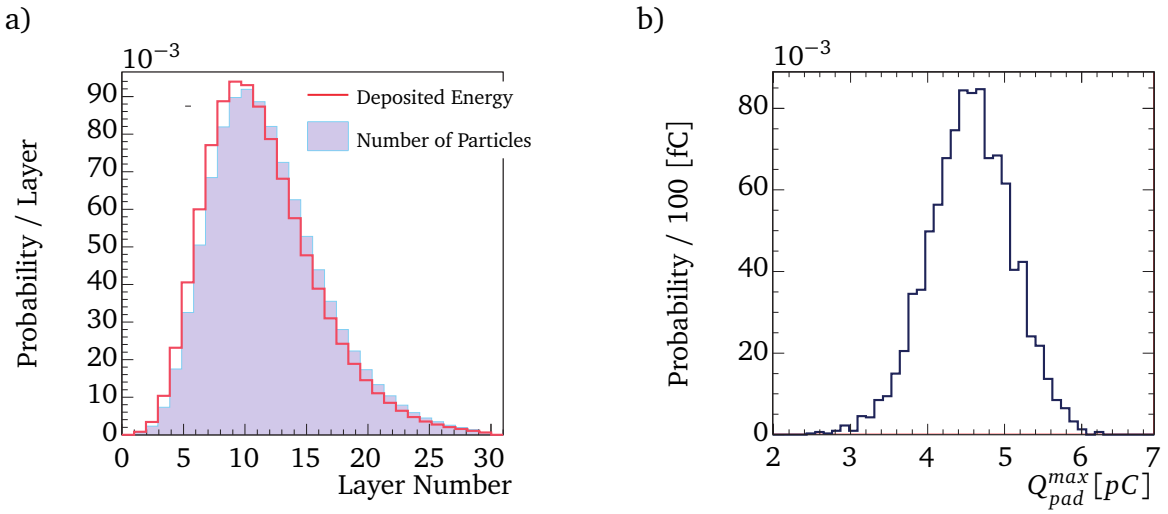

Figure 1.18: a) Normalized distributions of the number of shower particles and of the energy deposited in the silicon sensors of LumiCal as a function of the layer. Electron showers of 250 GeV were simulated [63]. b) Normalized distribution of the maximal charge collected in a single pad per shower, Q_{pad}^{max}, for 250 GeV electron showers [48].

mum charge deposition can be as small as this released by Minimum Ionizing Particle (MIP). On the other hand, the charge deposited in a single sensor cell near the shower maximum is expected to be orders of magnitude higher. The normalized distribution of maximal charge collected in a single pad, Q_{pad}^{max}, for a 250 GeV electron shower is shown in Figure 1.18b. The maximum charge slightly exceeds 6 pC, while about 95 % of the distribution stays below 5.4 pC.

The design of the LumiCal readout electronics was developed for the proposed detector architecture. The detector readout chain is composed of a charge sensitive amplifier, a shaping circuit, an ADC, and a Data Acquisition System (DAQ) system. Since the development of the LumiCal detector prototype is the main subject of this dissertation, it is described in more detail in the following chapters.

Chapter 2

Extraction of information from radiation sensors

Processing a signal from radiation sensor is a very challenging task, especially in a high energy physics experiment. A set of demanding requirements needs to be fulfilled by radiation sensors and the attached readout electronics, in order to build higher performance detectors, necessary to move the physics program beyond the frontiers of the current knowledge. The readout electronics has to process signals generated by very low charges deposited by radiation in sensor's active volume, therefore low noise operation is of primary importance. However, it is also not unusual, especially in calorimetry, to have energy depositions covering several orders of magnitude. High radiation levels set the next requirement for radiation resistance of components placed inside the detector. High luminosity experiments provide a very high event rate, so the readout system needs to be very fast in order to distinguish and precisely measure subsequent events. The requirement for high spatial resolving capabilities of detectors leads to high granulation of sensor volume, which implicates a large number of readout channels. The large number of channels imposes a very strict requirement on the power dissipated in a single channel. Large power dissipation in the front-end electronics would result in large masses and volumes for cooling systems and power delivery cables, which would have a negative impact on the detector performance. The detector produces a huge continuous stream of data, therefore the Data Acquisition System needs to be very reliable and able to work in a stable manner over a long time. Last but not least, there exist some purely economical constrains that need to be addressed when calculating the cost of detector to restrict an overall project budget.

None of the existing detector technologies is optimal with respect to all above mentioned requirements. Therefore, modern particle physics experiments commonly use very large multi-component detector systems (see chapter 1.2). Such a detector system integrates various sub-detectors, utilizing different technologies and offering different features. With the existing concepts and technologies it is usually difficult, if possible at all, to meet the challenging requirements for future experiments set by the physics scenarios. Because of that, Research and Development (R&D) programs are necessary to establish new detector/readout technologies.

The readout electronics processes signals from radiation sensors to measure: the energy released by radiation, the time of signal occurrence, and the position where the radiation hit the sensor. Depending on particular application, the requirements for precision of these measurements are different, therefore a number of measurement techniques has been developed. The highlight of selected methods is presented in this chapter.

2.1 Radiation Sensors

Interaction of particles with matter and energy deposition distribution

Since subatomic particles are far too small to be observed through purely visual means, therefore different mechanisms are used in order to detect such particles and their properties. The material which absorbs part of radiation energy to allow its detection is called a radiation sensor. The sensor translates the energy deposited by traversing particles into electric signals, which can be read out and precisely measured. For detector design and commissioning, it is essential to estimate how much energy is deposited by a particle inside the traversed sensor volume. Moderately relativistic charged particles (except electrons), lose energy in matter primarily by ionization. The mean rate of energy loss due to ionization, usually named 'stopping power', is calculated by the relativistic version of the Bethe-Bloch equation [64] as:

$$-\frac{dE}{dx} = z^2 \frac{4\pi N_A r_e^2 m_e c^2 Z}{A} \cdot \frac{1}{\beta^2} \cdot \left[\ln\left(\frac{2m_e c^2 \beta^2 \gamma^2 T_{max}}{I^2} \right) - \beta^2 - \frac{\delta}{2} \right], \tag{2.1}$$

where z is the charge of incident particle, Z is atomic number of the medium, A is atomic mass of the medium, N_A is Avogadro's number, r_e is classical electron radius, m_e is rest mass of the electron, c is speed of light, I is the mean excitation energy of the medium, δ is density effect correction to ionization energy loss, T_{max} is maximum kinetic energy which can be imparted to a free electron in single collision. The quantity $(dE/dx)\delta x$ is the mean energy loss via interaction with electrons in the layer of a medium with thickness δx. The stopping power for electrons is a bit more complicated because of quantum mechanical interferences with the final state electrons; however, it exhibits the same general properties as for the other particles. Figure 2.1 shows

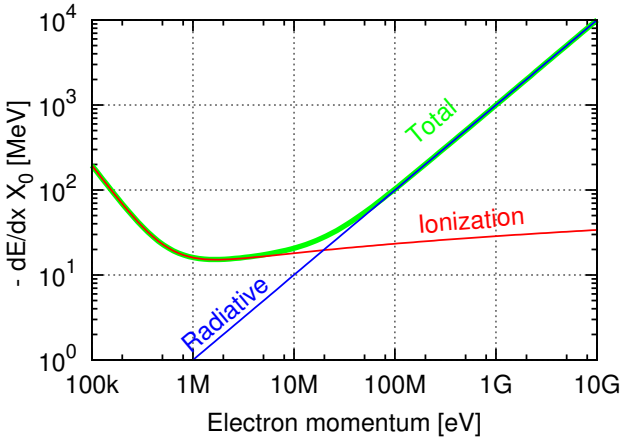

Figure 2.1: Stopping power $(-dE/dx)$ for electrons in silicon as a function of electrons momentum.

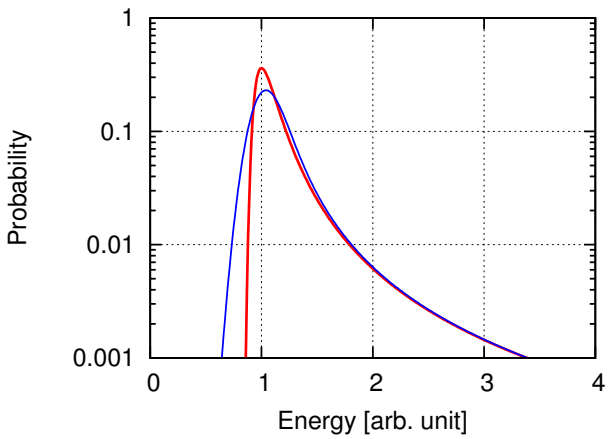

Figure 2.2: The Landau probability density function for energy loss straggling(red). The Landau convoluted with Gaussian probability density function (blue).

the ionization stopping power of an electron in silicon as a function of electron's energy. The minimum is set for energy slightly higher than 1 MeV. An electron with such kinetic energy acts

as Minimum Ionizing Particle (MIP). One may see that for energies greater than 1 MeV the energy dependence is very weak and an average energy loss by ionization reaches 20 MeV per radiation length.

The ionization process occurring during the passage of fast charged particles through matter has a statistical nature. As a result, fluctuations of energy loss (ΔE) in absorber are observed. The average number of electron-hole pairs J, is related to ΔE by the expression $J = \Delta E/P$, where P is a proportionality factor. The P factor is assumed to be constant for the given material type, but this assumption has never been proven theoretically. For silicon, P equals 3.68 eV. The probability function $f(\Delta E)$ is usually called energy loss distribution or straggling function. Only for a thick sensor layer $[(dE/dx)\delta x \gg T_{max}]$ the distribution tends to Gaussian. For finite δx, there are large fluctuations in the actual energy loss. The distribution is skewed toward high values (the Landau tail) with respect to Gaussian. The large fluctuations in the energy loss result from small number of collisions involving large energy transfers.

For an impinging particle with energy E_0 the probability to lose the energy $\Delta E = E_0 - E(d_s)$ when passing through a material block of thickness d_s fluctuates. The probability density function, $f(\Delta E, d_s)$, calculated by Landau [65] can be represented as:

$$f(\Delta E, d_s) = \frac{1}{\xi}\varphi(\lambda), \tag{2.2}$$

$$\varphi(\lambda) = \frac{1}{2\pi i}\int_{-\infty}^{+\infty} e^{u\ln u+\lambda u}du, \quad \xi = \frac{z^2e^2}{2r_e\beta^2}\frac{N_A}{A}\rho Z d_s, \quad \lambda = \Delta E - \xi(\ln\xi + 1 - \gamma_E), \tag{2.3}$$

where ξ is the average energy loss of a particle of energy E_0 penetrating an absorber of thickness d_s, as estimated from formula (2.1), and γ_E is the Euler constant. An example distribution presenting Landau probability density function (cross-section) is shown in red in Figure 2.2. Subsequently, Vavilov derived an improved solution, omitting the assumption about average energy loss [66]. Further corrections to the theory, which account for the fact that electrons in the material are not free, were proposed by Bichsel [67]. All these corrections, as well as additional noise present in the readout chain, lead to extension of the distribution. The observed energy spectrum can be calculated as a convolution of the Landau distribution (2.2) with a normal distribution (see the blue curve in Figure 2.2). The most important parameter of Landau distribution is its Most Probable Value (MPV) (one in Figure 2.2). The MPV is usually taken as a signal level and referred to just as a signal.

The detectors based on silicon sensors measure the energy deposited in the active volume, not the energy lost. The energy deposited by a particle passing through a sensor material is usually smaller than the energy lost by this particle. Bremsstrahlung processes lead to production of photons which can leave the material without interaction, carrying a sizable fraction of the energy. Some of the energy lost by the primary particle is transferred to secondary electrons – δ-electrons. These electrons also deposit a part of their energy and might then leave the detector. All these secondary particles will travel furthermore in almost all directions, forming a rather complex sequence of interactions. The detailed MC simulations performed in GEANT4 showed that MPV of energy deposition for 500 GeV electron in 300 μm thick silicon sensor is 4.1 fC [68], which is in a very good agreement with the presented first order approximation.

Sensors

Various materials can serve as radiation sensor: semiconductors, scintillators or gases. The ionization sensors are the devices measuring the ionization produced when an incident charged particle traverses the sensor. The primary generated charges must be kept from immediate recombining, this is usually done by applying a sufficiently high electric field generated by a voltage source across the sensor. The charges are separated and set in motion by the electric field. A movement of charges is observed as a current flow in external readout electronics circuitry. A simplified sensor model and its equivalent diagram are presented in Figures 2.3a and 2.3b.

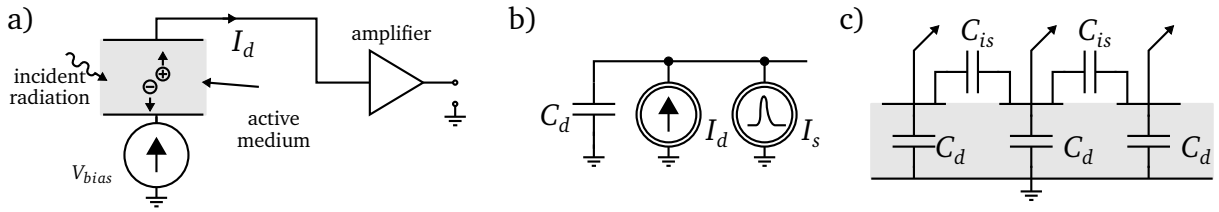

Figure 2.3: a) Simplified model of radiation sensor and amplifier. b) Equivalent circuit diagram of a sensor. c) Model of multichannel sensor.

The information about energy deposition, crucial for spectroscopy applications, is represented by the total charge carried by the current pulse. A rising current edge can be used to extract the information about the time of radiation. The location of particle interaction is delimited by the position and geometry of the sensor where the signal was observed. To extract this information, a specialized readout electronics is used.

From readout electronics point of view, a sensor can be characterized by parameters like: capacitance C_d, internal gain, pulse shape I_s, and leakage current I_d (see Figure 2.3b). Sensors with internal gain, typically gas (Gas Electron Multiplier (GEM), Micro-MEsh Gaseous Structure (Micromegas), straw tubes), provide large charge, usually in the range of pC, while typical solid state sensors (silicon, diamond, germanium) produce charge in fC range as a response to charged particle. The detector capacitance, related mostly to the geometry of the sensor, can vary from 0.1 pF (for small semiconductor pixel sensors) up to 1 nF for big ionization chambers.

The spatial resolving capability of the sensor is mostly related to its active medium size. In order to improve spatial resolution of the detector, the sensor's active medium is usually segmented into smaller volumes. Very good spatial resolutions can be achieved by such sensors. Depending on the size and the geometry of the segmentation, a single planar sensor element is called a pixel, a pad or a strip. Such a sensor needs a multichannel readout electronics. However, in a segmented sensor coupling capacitances exist between neighbor channels (see Figure 2.3c). Depending on sensor geometry the inter-strip capacitance C_{is} may be even larger than the sensor's C_d (microstrip, pixels). These capacitances have a negative impact on overall system performance, which leads to signal sharing in between pads, called the crosstalk.

Silicon semiconductor sensors

In the recent decades, solid state ionization chamber sensors based on semiconductor technology have commonly prevailed in high-energy experiments due to their reliability, availability and flex-

ible applications. A most common semiconductor sensor utilizes reversely biased p^+-n junction for radiation detection. The diode is reversely biased so that the depletion zone – the sensitive volume – covers the whole diode volume. A particle traversing through this volume generates electron-hole pairs by energy loss due to ionization. These charges drift in the electric field towards the respective electrodes, causing a signal current, which flows in the external circuit.

The depleted junction volume is free of mobile charge and thus forms a capacitor, bounded by the contacts on both sides. Its capacitance, for highly asymmetrical junction, with an acceptor doping concentration N_a, much greater than donor doping concentration N_d, can be estimated as [69]:

$$C_d = A\sqrt{\frac{\epsilon\epsilon_0 q N_d}{2(V_b + V_{bias})}}, \tag{2.4}$$

where V_b is built-in voltage, V_{bias} external biasing voltage, A area of the junction, N_d donor concentration, ϵ_0 vacuum dielectric constant, ϵ silicon dielectric constant and q electron charge. For bias voltages, $V_{bias} \gg V_b$, the capacitance decreases with a square root of bias voltage $C_d \propto 1/\sqrt{V_{bias}}$. The external biasing circuitry is responsible for providing high enough voltage V_{bias} to extend sensor's active volume to the whole sensor volume and generate strong electric field required to effectively collect the charge generated by incoming radiation. The bias voltage necessary to extend the depletion zone throughout the entire sensor thickness w is called the full depletion voltage V_{dep}, and can be calculated as [69]:

$$V_{dep} = \frac{q N_d w^2}{2\epsilon\epsilon_0} \ . \tag{2.5}$$

When the depletion zone occupies the whole sensor volume, the sensor capacitance is determined by a purely geometrical dimensions $C_d = \epsilon\epsilon_0 A/w$.

The current induced by the motion of charge deposited by incident radiation can be precisely determined according to the Ramo theorem [70, 71]. In most applications, the particular shape of the current pulse is not as important as pulse duration. For sensors working in over bias condition ($V_{bias} > V_{dep}$) the time necessary to collect holes and electrons can be calculated as [69]:

$$T_p = \frac{w^2}{2\mu_p V_{idep}} log\left(\frac{V_{bias} + V_{idep}}{V_b - V_{idep}}\right), \tag{2.6}$$

and

$$T_e = \frac{w^2}{2\mu_e V_{idep}} log\left(\frac{V_{bias} + V_{idep}}{V_b - V_{idep}}\right), \tag{2.7}$$

respectively. In the above formulas, V_{idep} is defined as the internal depletion voltage $V_{idep} \equiv V_{dep} + V_{bi}$, while μ_e and μ_p represent mobilities of electrons and holes in silicon. The high value of voltage bias results in a higher velocity of charge carriers and thus in shorter collection time.

Apart from charge carriers generated by incident radiation, there always exists a portion of charge carriers generated by thermal excitation. These charges compose leakage current, which is continuous in time and which demotes the overall system noise performance. The current induced in sensor is sensed by electronic circuitry attached to it. There are two ways of connecting the sensor to its readout electronics: Direct Current (DC) coupling and through a coupling capacitor, called Alternating Current (AC) coupling. The DC-coupled sensors have a

few advantages in comparison to AC-coupled sensors: lack of coupling capacitance eliminates additional time constant, which is unwanted for sensor operating in high rate environments. For integrated AC-coupled sensors, coupling capacitance is usually realized as an oxide layer placed on p^+ implants. This layer causes problems with reliability and breakdowns, which may occur under high radiation conditions. The process required to produce AC-coupled sensors is more complicated, in comparison to DC-coupled sensors, which makes those sensors less cost-effective. However, DC-coupled devices introduce sensor leakage current directly to readout electronics. This issue becomes of primary importance after irradiation, when the value of the leakage current is raised by orders of magnitude.

The modern semiconductor technology enables production of make very thin sensors and realization of segmented electrodes in order to enhance the information about the position of the impinging particle. In most practical applications silicon sensor thickness is between a few tens of μm up to a few hundred of μm. These boundaries are imposed by the capabilities of production technologies available today. It is worth noticing that thicker silicon sensors provide greater charge deposition, have longer charge collection time and manifest lower capacitance comparing to thin devices.

2.2 Preamplifier

The pulse shape corresponding to movement of the charge deposited in the sensor's active volume depends slightly on particle type, particle trajectory and crossing points with respect to readout electrodes. As a result, the pulses from the sensor vary in their shape and in their delays with respect to the passage of particle. For many applications, especially calorimetry, the most important information is the total energy deposited by the particle. Therefore the readout electronics usually integrates the deposited charge with the time constant much longer than the duration of current pulse originating from the sensor. If the time constant of readout electronics circuit is much greater than the charge collection time, the sensor current pulse may be approximated by delta function, i.e. $I_s(t) \simeq Q_{in}\delta(t)$. If this is not true, a ballistic deficit effect occurs, i.e. the front-end electronics output signal is stretched in time and has lower amplitude, thus degrading the amplitude resolution of the system. To decrease the impact of this effect, higher sensor bias voltage may be applied in order to obtain shorter pulses.

The preamplifier works usually in charge sensitive mode. The main function of preamplifier is to form a voltage step at its output with the amplitude directly proportional to the charge carried by the current pulse as a response to incoming radiation. In this configuration, the amplifier with transfer function of $-K_v(s)$, forms an integrator with feedback capacitor C_f (see Figure 2.4). The charge gain can be determined as:

$$K_q = \frac{V_{CSA}}{Q_{in}} = \frac{1}{C_f + \frac{C_f + C_d}{K_v}} \overset{K_v \gg 1}{\simeq} \frac{1}{C_f} \ . \tag{2.8}$$

The signal charge Q_{in} is distributed between the sensor capacitance C_d and the effective input capacitance of the preamplifier ($\sim K_v C_f$). If the gain of the amplifier is high, the effective input capacitance of the preamplifier dominates, and therefore the charge gain is almost completely independent from the sensor capacitance and the gain of amplifier. The overall gain is then

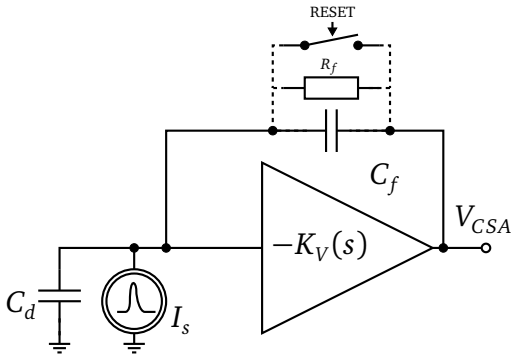

Figure 2.4: Schematic diagram of the charge sensitive preamplifier.

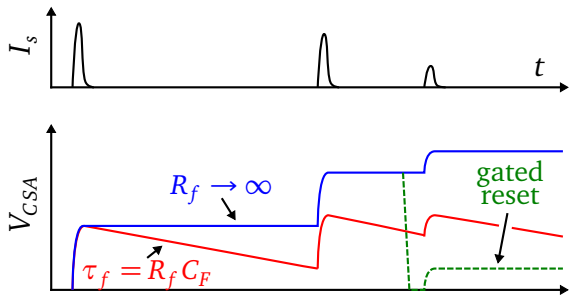

Figure 2.5: Responses of the charge sensitive preamplifier, V_{CSA}, to the current pulses, I_d, for various feedback types.

determined only by the feedback capacitance, which, in modern technologies, is stable and can be easily controlled.

One disadvantage of the charge amplifier is the fact that the output voltage signal does not return to baseline after the signal. To avoid saturation of the preamplifier output by incoming pulses, the feedback capacitance needs to be discharged (see Figure 2.5). The discharge can be achieved in two ways: continuous or discrete in time. To continuously discharge the feedback capacitor a parallel connected resistor (R_f in Figure 2.4) is used, causing the charge decay with time constant of $\tau_f = C_f R_f$. The drawback of this solution is the spurious long tail appearing at the shaper output after the pulse, enforcing the baseline change and contributing an additional noise component. However, the problem of long tail can be overcome by adding a pole-zero cancellation circuit in the following processing stages. Alternatively, a small resistance electronic switch (*RESET* in Figure 2.4) can be used, causing almost instantaneous discharge. Such a solution, called gated reset, allows a stair-like output and better noise performance, but requires an additional control logic and causes system dead time (during the reset phase).

The preamplifier gain and bandwidth are not infinite in practical implementations. A realistic transfer function of the preamplifier can be approximated by one-pole function:

$$K_v(s) = \frac{K_{v0}}{1 + s\tau_p}, \tag{2.9}$$

where K_{v0} is gain for low frequencies and τ_p is time constant of dominant pole. The limited gain results in a decreased charge gain for increasing sensor capacitances. The finite bandwidth causes an increase of the rise time with the sensor capacitance. An important design choice is the value of feedback capacitance. It should be small enough to provide high gain. On the other hand, the small value of feedback capacitance limits the highest input charge which can be processed without saturating of the preamplifier that has limited supply voltages.

2.2.1 Noise processing

The intrinsic noise of readout electronics places a lower bound on the detectable signal level and leads to uncertainty in the time and the amplitude extraction of the incoming radiation. Taking

into account that the preamplifier has a very high gain, it can be safely assumed that the major contribution to the system noise comes from the first amplifying stage. This implies that the noise optimization of the first stage is fundamental.

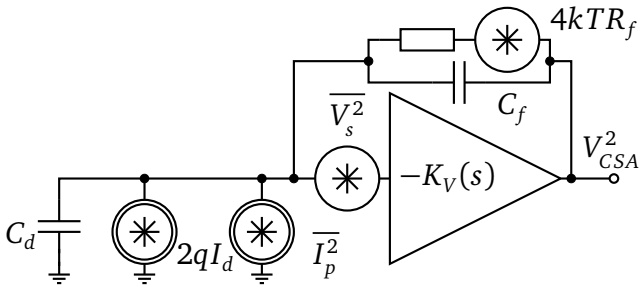

Figure 2.6: Equivalent noise diagram of readout chain. The radiation sensor is represented by its capacitance C_d and noise source of leakage current I_d. The realistic amplifier is replaced by a noiseless amplifier with transmittance $-K_v(s)$ and two equivalent noise sources: the parallel current noise $\overline{I_p^2}$ and the series voltage noise $\overline{V_s^2}$.

The equivalent noise diagram of the detector readout chain with a charge sensitive preamplifier is shown in Figure 2.6. The radiation sensor is represented by its capacitance C_d and current shot noise source $2qI_d$, which is associated with sensor's leakage current I_d and bias network. The realistic amplifier is replaced by a noiseless amplifier with transmittance $-K_v(s)$ and two equivalent input noise sources: the parallel current noise $\overline{I_p^2}$ and the series voltage noise $\overline{V_s^2}$. The thermal series noise of feedback resistor $4kTR_f$ can be transformed to parallel noise using Norton-Thevenin theory with noise spectrum density of $4kT/R_f$.

The power spectrum of the noise $\overline{v_{CSA}^2/df}$ at the preamplifier output can be calculated as [72]:

$$\frac{\overline{v_{CSA}^2}}{df} = \left[b + \frac{A_f}{f}\right]\left[\frac{K_{v0}(C_f + C_d)}{C_f(K_{v0}+1)+C_d)}\right]^2 + \frac{a}{f^2}\left[\frac{K_{v0}}{C_f(K_{v0}+1)+C_d)}\right]^2 , \tag{2.10}$$

where a is the sum of the spectrum noise density of amplifier parallel noise ($\overline{I_p^2}$) and shot noise components originating from sensor leakage current ($2qI_d$) and feedback resistor ($4kT/R_f$):

$$a = \overline{I_p^2} + 2qI_d + 4kT/R_f \ . \tag{2.11}$$

Coefficients b and A_f in equation (2.10) represent the white noise and the $1/f$ component of series voltage noise of the amplifier:

$$\overline{V_s^2} = b + A_f/f \ . \tag{2.12}$$

Assuming high amplifier gain ($K_{v0} \gg 1$), one may interpret the noise spectra density at the output of charge sensitive preamplifier as:

$$\frac{\overline{V_{CSA}^2}}{df} \approx \left[b + \frac{A_f}{f}\right]\frac{(C_f + C_d)^2}{C_f^2} + a\frac{1}{f^2 C_f^2} \ . \tag{2.13}$$

It can be noticed that with increasing frequencies the relative importance of parallel noise (a) being integrated decreases with respect to the white part of series noise spectrum (b).

2.2.2 Crosstalk

An important parameter of the preamplifier is its input impedance Z_{in}. For a single-pole preamplifier with feedback resistor R_f, it can be calculated as a ratio of the small signal voltage signal at the preamplifier input v_{in} to the preamplifier input current i_{in}. In the operator domain the input impedance Z_{in} can be calculated as [73]:

$$Z_{in} = \frac{Z_f(s)}{1+K_v(s)} \approx \frac{Z_f(s)}{K_v(s)} = \frac{R_f(1+s\tau_p)}{K_{v0}(1+s\tau_f)} \ . \tag{2.14}$$

The value of Z_{in} has two major implications for the preamplifier operation. The input impedance, together with sensor capacitance C_d, sets a time constant of the preamplifier response. It is important to minimize the preamplifier input impedance in order to keep the preamplifier response short and independent of the sensor capacitance. A second important aspect of lowering the input impedance is related to the crosstalk of signals in neighboring channels, which is of primary importance in multichannel detector systems.

Starting from equation (2.14), one can obtain the following expression for the modulus of the input impedance as a function of angular frequency [73]:

$$|Z_{in}| = \frac{R_f\sqrt{1+\omega^2\tau_p^2}}{K_{v0}\sqrt{1+\omega^2\tau_f^2}} \ . \tag{2.15}$$

Figure 2.7 shows the preamplifier's input impedance as a function of frequency for different versions of the feedback circuit. For low frequencies, where impact of the first pole of amplifier

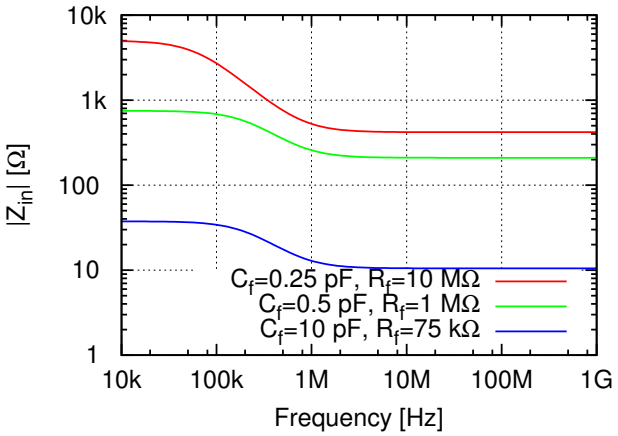

Figure 2.7: Input impedance of the charge sensitive preamplifier as a function of frequency for different feedback configurations. Amplifier gain, K_{v0} is 2000 and dominant pole is τ_p=0.2 us.

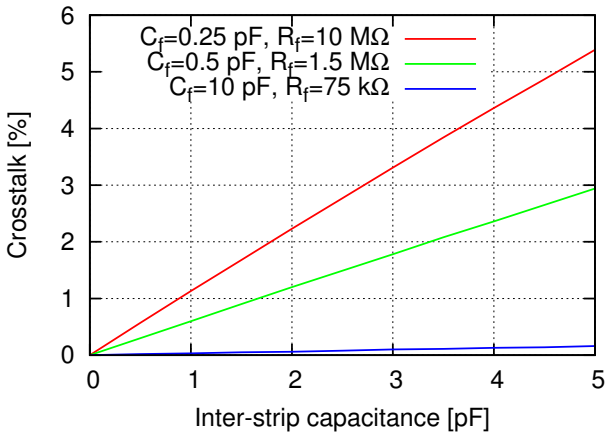

Figure 2.8: Crosstalk level as a function of inter-strip capacitance for different feedback configurations. Amplifier gain, K_{v0} is 2000, dominant pole is τ_p=0.2 us, and sensor capacitance, C_d is 5 pF.

transfer function can be be neglected, the impedance depends mostly on open loop gain and the resistor value. It can be approximated by R_f/K_{v0}. For higher frequencies, Z_{in} is determined

mainly by the value of feedback capacitance C_f and the amplifier bandwidth. It can be reduced to [73]:

$$|Z_{in}|^{\omega\to\inf} = \frac{\tau_P}{K_{v0}C_f} \ . \tag{2.16}$$

The input impedance of the preamplifier is finite if the gain K_{v0} is finite. Therefore the current induced on one sensor strip I_s, capacitively couples to the neighbors (through C_{is}) and the signal amplitude is distributed over many strips (see Figure 2.9). This effect is called crosstalk. The

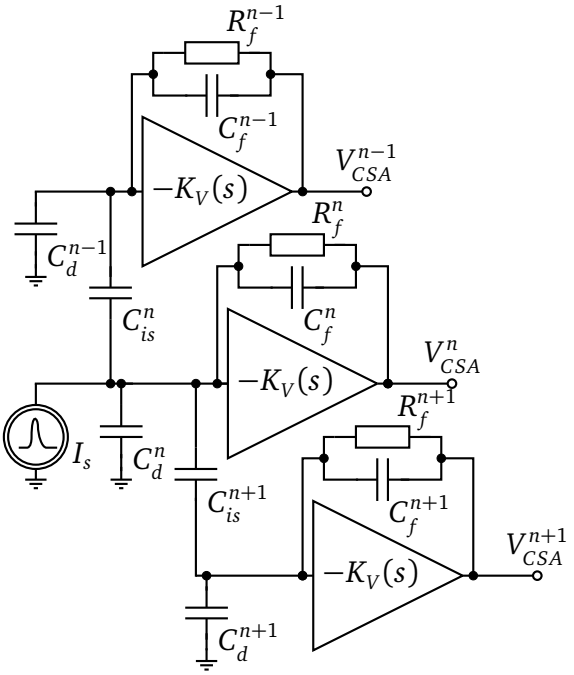

Figure 2.9: Equivalent schematic of the coupling between readout channels through the inter-strip capacitances C_{is}.

crosstalk is usually defined as the amplitude observed on neighboring channels with respect to the amplitude on channel with signal:

$$|Crosstalk(j\omega)| = \frac{\left|V_{CSA}^{n+1}(j\omega)\right|}{\left|V_{CSA}^{n}(j\omega)\right|} \times 100\% \ . \tag{2.17}$$

The crosstalk is proportional to the preamplifier input impedance. Therefore, the crosstalk strongly depends on frequency. Figure 2.8 shows the crosstalk level as a function of inter-strip capacitance for various feedback configurations. The crosstalk dependencies were calculated for 5 pF sensor capacitance and ω equal 16.6 Mrad/s – the center frequency of the shaper filter described in the next chapter. As can be expected, for the preamplifier with the lowest input impedance (highest C_f) – crosstalk is the smallest and does not exceed 0.2%. For higher impedances (lower C_f), the crosstalk is expected to remain on the level of a few percent.

The other potential source of crosstalk is related to the design of front-end ASIC. The rapid change in the net potential inside ASIC can lead to charge injection to the ASIC substrate and then to the neighbor channels. If the net is connected to elements responsible for signal processing,

like e.g. the output path, the parasitic charge transferred through the substrate appears on the neighbor channel and causes the crosstalk. In final system, contribution from the both mentioned sources of crosstalk is expected.

2.3 Shaper

In order to improve the overall Signal-to-Noise Ratio (SNR), the bandwidth of the system needs to be limited. The signal amplitude at the output of the preamplifier is high enough not to be affected by noise of the following stages. The signals are usually considered in the time domain so the filter circuits are commonly known as shapers because they change signal shape. The primary goal of the shaper circuit is pulse formation in order to improve the SNR ratio, meet the requirements of subsequent processing stages by adjusting the overall chain gain, and set the signal length to allow operation with the expected pulse rates.

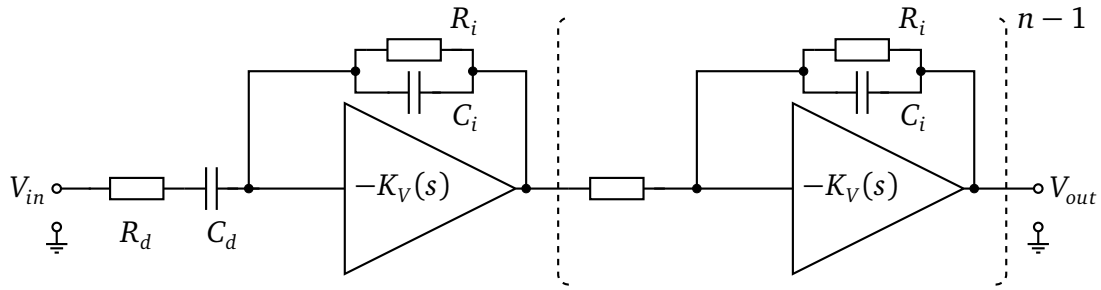

Figure 2.10: The $CR-(RC)^n$ semi-gaussian filter. Differentiating stage is followed by n integrating stages.

Conventional band-pass filters, such as $CR-(RC)^n$, called semi-Gaussian, are usually used as a trade-off between the performance, the power consumption and the simplicity of the design. A schematic diagram of $CR-(RC)^n$ shaper is shown in Figure 2.10. Such a filter can be easily implemented using a modern Very Large Scale Integration (VLSI) technology in multi-channel front-end chips. It consists of the first differentiating stage, which filters low frequency noise and determines the pulse length in time domain. It is followed by n-stages of integrators attenuating high frequency components and determining the pulse rise time. The transmittance of the n-order $CR-(RC)^n$ semi-gaussian filter, with equal differentiation and integration time constant τ, is given by the equation:

$$H(s) = \frac{K_{shp} s\tau}{(1+s\tau)^{n+1}} \ . \tag{2.18}$$

The response of the filter stimulated by Heaviside step function (from preamplifier output) can be computed as:

$$V_{shp}(t) = \frac{Q_{in}K_{shp}}{C_f}\frac{1}{n!}\left(\frac{t}{\tau}\right)^n e^{-\frac{t}{\tau}} \ . \tag{2.19}$$

The signal $V_{shp}(t)$ peaks at the time T_{peak} called the peaking time of the shaper response. For the $CR-(RC)^n$ filter it is equal to n times the filter time constant τ. The amplitude at peaking time

can be expressed as:

$$V_{max} = \frac{Q_{in}K_{shp}}{C_f}\frac{1}{n!}\left(\frac{n}{e}\right)^n . \tag{2.20}$$

In Figure 2.11a the pulse shapes described by equation (2.19) are plotted for various orders of

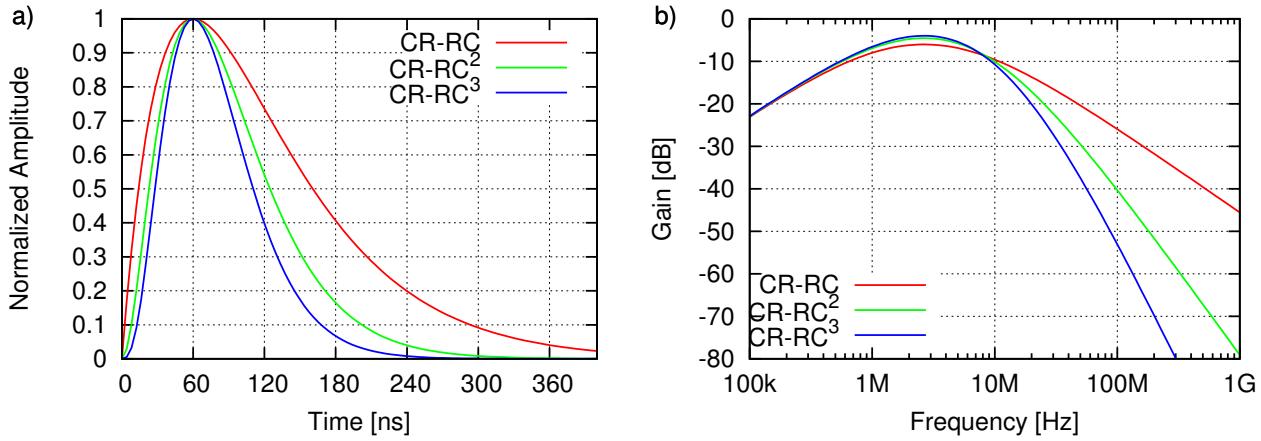

Figure 2.11: a) Responses of the shaper circuit for various order $CR-RC^n$ filters normalized to the same amplitude and peaking time (60 ns). b) Frequency characteristics of various order $CR-RC^n$ filters normalized to the same peaking time (60 ns).

the filter, keeping the same 60 ns peaking time (shaper time constant is scaled). It is expressly shown that higher order filters effectively shorten the shaper response and make it more symmetrical, improving immunity to pile-up effect and thus making the circuit capable of processing higher rate of events. Examples of the frequency characteristics for various orders of $CR-(RC)^n$ filters with the same peaking time are shown in Figure 2.11b.

2.3.1 Noise filtering

The fundamental function of the shaper is to improve the SNR. In order to study the effect of particular type of filtering on noise performance, the Equivalent Noise Charge (ENC) parameter is introduced. The ENC is defined as the amount of charge one has to inject into preamplifier input in order to get at the output a signal with the amplitude equal to the noise Root Mean Square (RMS).

The noise spectrum density at the output of preamplifier-shaper chain can be obtained by multiplying the spectral noise density at the output of the preamplifier dv^2_{CSA}/df by the square of the shaper transfer function $H(j2\pi f)$:

$$\frac{dv^2_{SHP}}{df} = \frac{dv^2_{CSA}}{df}H(j2\pi f)^2 . \tag{2.21}$$

Integration of formula 2.21 over the whole frequency range provides the value of the voltage RMS σ^2 at the processing chain output:

$$\sigma^2_{SHP} = \int_0^\infty \frac{dv^2_{SHP}}{df}df . \tag{2.22}$$

For the considered noise spectrum at the preamplifier output (2.13), the formula (2.22) can be evaluated as [72]:

$$\left(\sigma^{p}_{SHP}\right)^2 = a\frac{K^2_{shp}\tau B\left(1/2, n+1/2\right)}{4\pi C_f^2 n}, \tag{2.23}$$

$$\left(\sigma^{s}_{SHP}\right)^2 = b\left(\frac{C_d+C_f}{C_f}\right)^2 \frac{K^2_{shp} B\left(3/2, n-1/2\right) n}{4\pi\tau}, \tag{2.24}$$

$$\left(\sigma^{f}_{SHP}\right)^2 = A_f\left(\frac{C_d+C_f}{C_f}\right)^2 \frac{K^2_{shp}}{2n}, \tag{2.25}$$

for parallel, serial and 1/f noise components, respectively. In the above equations $B(x,y)$ is the beta-function. By dividing the above expressions by the signal amplitude (2.20) corresponding to one electron charge, the ENC is obtained as [72]:

$$\left(ENC^{p}_{SHP}\right)^2 = a\frac{\tau B\left(1/2, n+1/2\right)}{4\pi q^2 n}\left(\frac{n!^2 e^{2n}}{n^{2n}}\right), \tag{2.26}$$

$$\left(ENC^{s}_{SHP}\right)^2 = b\frac{\left(C_d+C_f\right)^2 B\left(3/2, n-1/2\right) n}{4\pi q^2 \tau}\left(\frac{n!^2 e^{2n}}{n^{2n}}\right), \tag{2.27}$$

$$\left(ENC^{f}_{SHP}\right)^2 = A_f\frac{\left(C_d+C_f\right)^2}{2q^2 n}\left(\frac{n!^2 e^{2n}}{n^{2n}}\right). \tag{2.28}$$

Figure 2.12 presents the relative noise level as a function of the peaking time for various shaping orders. Normalization occurs separately for parallel and serial noise levels, to the noise level at the output of CR-RC filter with peaking time equal one. It can be observed that the use of pulse shapers with larger peaking time T_{peak} limits the series noise to $\propto 1/\sqrt{T_{peak}}$. Unfortunately,

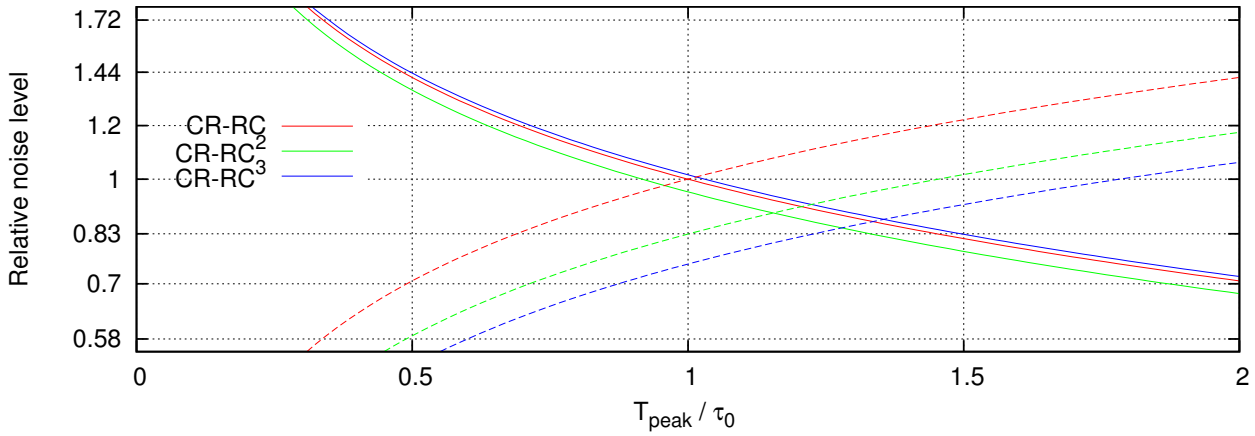

Figure 2.12: Relative serial (solid lines) and parallel (dashed lines) noise levels as a function of the peaking time for various shaping orders. Normalization occurs separately for parallel and serial noise levels, to the noise level at the output of CR-RC filter with peaking time equal to τ_0.

the contribution from the parallel noise increases with the larger peaking time of the shaper as $\propto \sqrt{T_{peak}}$. Furthermore, the higher order filter performs better when parallel noise is considered. For the serial noise, the best performance is achieved for the second order filter. The minimum noise level is obtained for the peaking time for which the parallel and serial contributions equalize. However, in many practical applications, it is not possible to use the optimal peaking time (corresponding to minimum noise level) because of additional constrains on the pulse duration. Another important conclusion which can be drawn from (2.28) is that 1/f noise is totally independent of the pulse shaper time constant and only slightly depends on the order of the shaper filter. Moreover, the 1/f component (A_f) of voltage noise is usually higher that the white noise component (b) only for frequencies below several kHz. It implicates that in very fast circuits, the contribution from $1/f$ component can be safely neglected.

The total ENC is given by the sum of the ENC contributions from individual noise sources:

$$ENC_{SHP}^2 = \left(ENC_{SHP}^p\right)^2 + \left(ENC_{SHP}^s\right)^2 + \left(ENC_{SHP}^f\right)^2 \quad . \tag{2.29}$$

2.4 Amplitude measurement

The output signal from the shaper with sufficient SNR is further processed in order to extract the event amplitude. The processing is dependent on particular application. There are two commonly used methods. In the first method, a comparator with a given discrimination level is used to check if radiation has passed through the sensor. The discriminator gives binary information (zero or one) marking the occurrence of a particle which deposited an energy exceeding the preset threshold. This mode of operation is usually called the binary architecture. Such type of architecture is applicable in experiments where spatial and/or timing information about incoming radiation is sufficient (e.g. tracking detectors). The second type of readout architecture, with analog output, provides information about the energy deposited in sensor. This type of readout is especially desired in calorimetry applications. Nowadays analog information is also used in tracking detectors in order to increase the spatial resolution by the measurement of the charge sharing between channels.

A measurement of amplitude (energy deposition) and time of incoming particle strongly depends on experimental conditions, like characteristics of radiation source. If radiation is generated periodically within a constant (known) period, e.g. in collider experiments, the information about potential interaction time can be utilized to apply synchronous sampling. In such an environment, one sample at the pulse maximum (peaking time) provides sufficient information about the energy deposition (see Figure 2.13a).

When radiation arrival time is not known a priori, the synchronous sampling cannot be applied. For asynchronous signals (e.g. a radioactive material or a continuous beam), a peak detector is often used. Schematic diagram of peak detector is shown in Figure 2.13b. Working principle of this circuit bases on charging the capacitor and instantaneous comparison of its actual voltage with the input signal. As long as the input voltage is greater than the voltage on the capacitor, it is charged through a forward biased diode. After the pulse reaches its maximum, the input voltage becomes smaller than the voltage on the capacitor. The diode is than reversely biased, which prevents the capacitor from discharge and ensures that the maximum pulse value is preserved. Once the information about the amplitude is processed, the peak detector circuit is

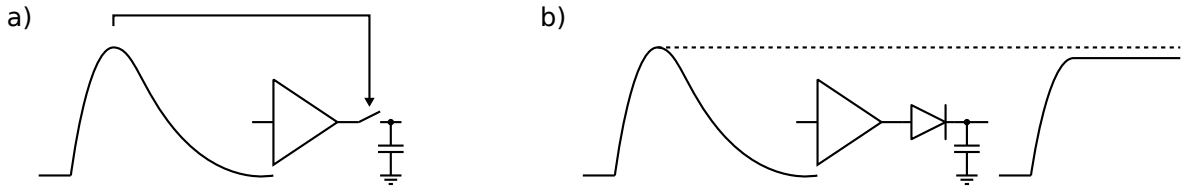

Figure 2.13: Amplitude measurements strategies. a) Synchronous signal processing using Sample & Hold circuit. b) Asynchronous signal processing with Peak Detector.

reset. The circuit reset can be performed by a transistor switch, connected parallely to the storing capacitor. In the system with peak detector, a possible event rate is limited by analog processing part. The amplitude at the shaper output has to drop below a certain level in order to accept and measure the next event.

An essential part of amplitude measurement is related to signal conversion from an analog form (usually voltage or charge) to a digital form, which can be further processed and analyzed. The Analog-to-Digital Converter (ADC) is used to perform this operation. Depending on the requirements for the conversion resolution and the conversion rate, various architectures can be used to perform the conversion. An ADC based on Wilkinson architecture is widely used in detector readout systems [74] where the time available for conversion is longer than microseconds and the good linearity is of primary importance. In systems where event rate is high, or systems which utilize a DSP, the ADC has to operate at higher speeds (a several tens of MSps). A number of ADC architectures have been recognized as well-suited for this regime of operation: flash, pipeline and Successive-Approximation-Register (SAR).

Wilkinson ADC

A schematic diagram of Wilkinson ADC is shown in Figure 2.14. The analog to digital conversion

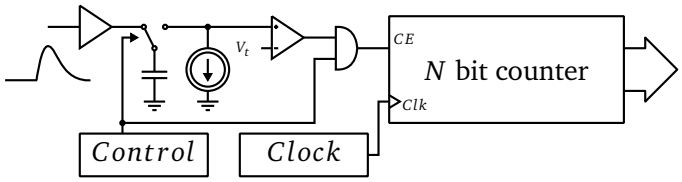

Figure 2.14: Wilkinson Analog-to-Digital Converter schematic diagram.

is performed in two phases. In the first phase, the sampling capacitor is charged either by a sample and hold circuit or by a peak detector to the maximum signal amplitude. Then the signal source is disconnected. In the next phase a constant current source is switched on and a digital counter is started. The counter is stopped when the comparator indicates that the voltage on the capacitor reached the baseline. The value stored in the counter is then proportional to the initial voltage on the capacitor. The main advantages of this architecture are: high linearity, high resolution and low power consumption. For the above reasons, it is very well adopted to multi-

channel designs. The main drawback of this type of ADC is long conversion time, proportional to sampling clock period multiplied by 2^N, where N is the number of bits.

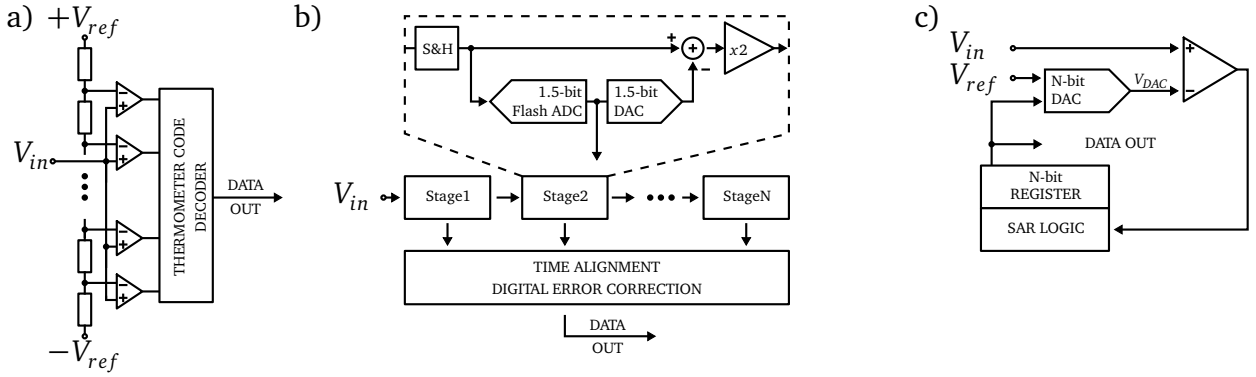

Figure 2.15: Fast ADC architectures a) flash, b) pipeline, and c) SAR.

Flash ADC

The flash ADC is composed of high-speed comparators connected in a cascade. Figure 2.15a shows a block diagram of typical flash ADC . For an N-bit converter, the circuit employs $2^N - 1$ comparators. A resistive-divider with 2^N resistors provides the reference voltages. The reference voltage for each comparator is one Least Significant Bit (LSB) greater than the reference voltage for the comparator preceding it. Each comparator produces a 1 when its analog input voltage is higher than the reference voltage applied to it. Otherwise, the comparator output is 0. The point where the code changes from ones to zeros is the point at which the input signal becomes smaller than the respective comparator reference-voltage level. This type of encoding is called thermometer code encoding. The thermometer code needs to be decoded to the binary digital output code. Such architecture requires very fast comparators with the offset lower then the expected LSB value. Otherwise, the comparator's offset could move the threshold of comparator, resulting in increasing differential nonlinearities. The high number of precise comparators usually limits the resolution of typical flash ADC to not more than 6 bits. Nevertheless, a small resolution flash ADC is often incorporated as a component of various types of ADC.

Pipeline ADC

The analog-to-digital converters based on pipeline architecture have become the most popular ADCs for sampling rates from a few MSps up to more than 100 MSps. Their resolutions range from eight bits at faster sample rates up to 16 bits at lower rates. Figure 2.15b shows a block diagram of pipeline ADC. In this diagram, the analog input V_{IN} is first sampled and held steady by a sample-and-hold (S&H), while the flash ADC in *Stage1* quantizes it to 1.5-bits (3 possible values). The 1.5-bit output is then fed to a 1.5-bit Digital-to-Analog Converter (DAC), and the DAC output is subtracted from the analog input. This residue is then multiplied by a factor of two and fed to the next stage (Stage 2). This gained-up residue continues through the pipeline, providing 1.5-bits per stage until it reaches the last ADC stage. Because the bits from each stage are determined at different points in time, all bits corresponding to the same sample need to be

time-aligned with shift registers before being fed to the digital-error-correction logic. When the stage finishes processing a sample (determining the output code and passing the residue to the next stage), it can then start processing the next sample. This pipelining action is the reason for very high throughput.

SAR ADC

The Successive-Approximation-Register analog-to-digital converters used to be the architecture of choice for medium-to-high-resolution applications with sample rates below 5 MSps. The resolution for SAR ADCs most commonly ranges from 8 to 16 bits, and these converters provide low power consumption as well as a small form factor. Most recently, due to progress in CMOS technology, achieving sample rates exceeding 100 MSps becomes feasible. As the name implies, the SAR ADC basically implements a binary search algorithm. Therefore, the internal circuitry has to run much faster than the sample rate due to the successive-approximation algorithm. Although there are many variations for implementing the SAR ADC, the basic architecture is quite simple (see Figure 2.15c). The analog input voltage V_{IN} is sampled in sample and hold circuit. To implement the binary search algorithm, the N-bit register is first set to midscale. This forces the DAC output V_{DAC}, to be $V_{ref}/2$, where V_{ref} is the reference voltage provided to the ADC. A comparison is then performed to determine if V_{IN} is smaller than, or greater than V_{DAC}. If V_{IN} is greater than V_{DAC}, the comparator output is high, and the Most Significant Bit (MSB) of the N-bit register remains at one. Conversely, if V_{IN} is smaller than V_{DAC}, the comparator output is low and the MSB of the register is cleared to logic zero. The SAR control logic then moves to the next bit down, forces that bit high, and makes another comparison. The sequence continues all the way down to the LSB. Once this is done, the conversion is complete and the N-bit digital word is available in the register. Instead of reading word register after conversion is completed, one may use single comparison result as a serial data output. A notable feature of SAR ADC is that it contains only two analog elements: comparator and DAC. This fact makes this architecture perfectly suitable for modern CMOS digital technologies. This fact makes it possible to reduce power consumption significantly.

2.5 Threshold selection for self triggering systems

In systems with a binary readout or systems with a peak detector, a discriminator is added in order to check if the signal exceeds an arbitrary preset threshold level. The positive response of the discriminator indicates that an event took place. Such type of readout system is usually called self triggering system. The front-end noise affects not only the resolution of the amplitude measurement, but also determines the minimal detectable signal level. The noise is superimposed on the baseline and some fraction of the noise pulses may cross the threshold; however a rate of such fake events drops very rapidly with the increasing threshold level. For linear circuits with noise following Gaussian distribution, the rate of noise pulses is given by Rice formula [75]:

$$f_t = \frac{f_0}{2} exp\left(-\frac{V_{TH}^2}{2\sigma_v^2}\right), \tag{2.30}$$

where f_0 is expected number of noise counts for zero discrimination threshold, V_{TH} is discrimination threshold, σ_v is root mean square of noise. From formula (2.30) one can conclude that the noise pulse rate is the highest for zero threshold. The absolute rate depends on the noise spectrum. For an ideal band-pass filter with a pass band extending from f_a to f_b the expected number of zeros per second is [75]:

$$f_0 = 2\sqrt{\frac{1}{3}\frac{f_b^3 - f_a^3}{f_b - f_a}} \quad . \tag{2.31}$$

For narrow band pass filter, like semi-gaussian CR-RC with equal differentiation and integration time constants, the ratio of cutoff frequencies $f_b/f_a = 4.5$ [69]. If the lower cutoff frequency is neglected, the expected number of noise count with zero discrimination threshold can be interpreted as:

$$f_0 \simeq 2/\sqrt{3} f_b \quad . \tag{2.32}$$

For CR-RC shaper with shaping time τ, the cutoff frequency equals $f_b = 1/4\tau$ [69]. The expected noise count rate as a function of a threshold voltage V_{TH}, normalized to the noise level σ_v, for the front-end with 60 ns peaking time is presented in Figure 2.16 (blue line).

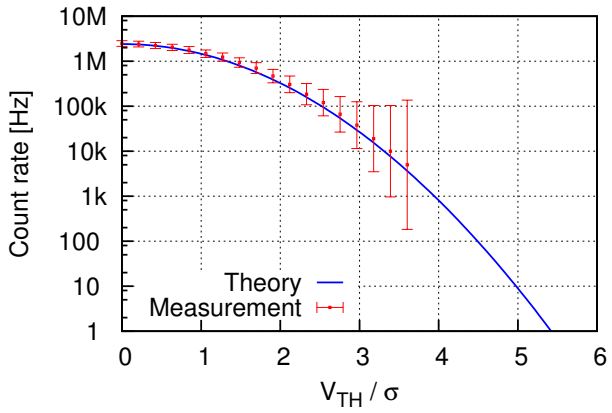

Figure 2.16: Noise count frequency as a function of the discrimination threshold to noise RMS ratio for front-end with 60 ns peaking time.

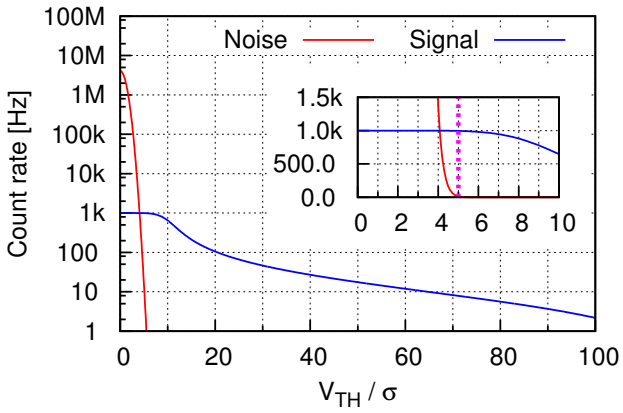

Figure 2.17: Noise count frequency and Landau signal (SNR=10) as a function of discrimination threshold and the RMS of the noise for front-end with 60 ns peaking time.

To verify if the model is correct, a measurement was performed. The experimental setup built for the deconvolution benchmarking and described in details in chapter 3.4.1 was used. The digital scope working at 2 GSps rate, collected one million of samples, within 0.5 ms. The digital discriminator followed by counter was used to perform the experiment. The measurement results (in red) are presented in Figure 2.16 on top of theoretical predictions (in blue) given by formula (2.31). The experimental results behave as expected by theory. The results are systematically slightly higher than these predicted by theory; however, the difference does not exceed a few percent. This small surplus is most probably related to simplifying assumption about the noise spectrum. The significant errors for the lowest count rates are related to the low number of counts for the high threshold value.

The discriminator threshold needs to be properly set in the final experiment in order to minimize the noise count rate. As one can read from Figure 2.16, setting the discriminator threshold to 5σ leads to mean noise count rate at 10 Hz level, while moving it above 6σ should decrease the count rate far below 1 Hz. The threshold selection is a trade-off: the threshold should be high enough to minimize the rate of fake noise pulses as well as low enough to capture the smallest interesting events. In order to optimize the readout system operation, the signal distribution as well as signal rate have to be accounted for. In silicon detector systems, the signal distribution should follow Landau distribution, as described in chapter 2.1. The threshold level can be determined based on the expected signal rate and detection reliability requirement. An expected count rate, for readout chain with the SNR of 10 and average event rate of 1 kHz is shown in Figure 2.17. For such a system, setting the threshold level to value 1/2 of signal MPV (5σ of noise) ensures that less than 0.1% of all recorded events are caused by the noise.

2.6 Time measurement

The event time is defined as the time when the response of the sensor starts. An ideal measurement of this time is not possible; nevertheless, what can be done is the measurement of an apparatus time, which is postponed to the event time. The delay time strongly depends on the measurement technique applied, but it usually can be corrected. In further discussions the event time should be taken as the apparatus time.

In detector systems one usually needs to measure the time of pulse occurrence (absolute) or the time interval between two pulses. The techniques for both types of measurements are based on the same principles. In the first phase, the analog pulse is digitized in such a way that the rising edge of the output signal marks event occurrence. In the second phase a Time-to-Digital Converter (TDC) is used to measure the time difference between rising edges of digital pulses.

The simplest, as well as the most deployed, method of pulse digitization is discrimination on the pulse leading edge (see chapter 2.5). In this method an amplitude discriminator is used to generate a logical pulse when a given (constant) threshold is exceeded by the input signal. The digital signal is then passed to the Time-to-Digital Converter (TDC), which is responsible for storing the time of rising edge occurrence. Depending on the required resolution, different techniques can be applied to perform this measurement [76, 77].

The measured signal is spread because of noise, leading to virtual expansion of the area where signal passes through the threshold level. This spread introduces an uncertainty σ_t in the time t_{TH} measurement (see Figure 2.18a). This effect is called a jitter. Assuming linear rising positive edge of the input signal $V_{shp}(t)$ (around the discrimination threshold), the time uncertainty σ_t can be expressed as:

$$\sigma_t = \frac{\sigma_{SHP}}{\frac{dv_{SHP}(t)}{dt}\Big|_{t=t_{TH}}} \quad . \tag{2.33}$$

It can be concluded from equation (2.33) that for a given noise level, the best time precision can be achieved for the threshold value set closest to the maximum steepness of the input pulse. In order to maximize steepness of the pulse rising edge, the overall pulse duration is usually decreased. The leading edge discrimination method has one major disadvantage, i.e. appearing as a significant dependence of the threshold crossing time from the input signal amplitude, which

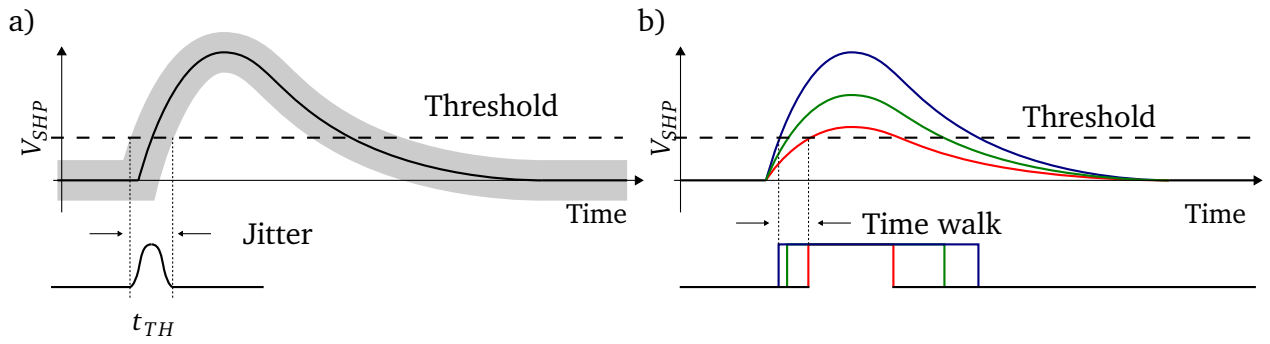

Figure 2.18: a) Jitter effect causing uncertainty in time measurement. b) Time walk effect causing amplitude dependent bias in time measurement.

is usually referred to as time walk effect. Figure 2.18b shows the impact of time walk effect on time measurement for different pulse amplitudes. As one can see, even though all signals start at the same moment, they pass the threshold after different time intervals. In systems where the amplitude of pulse is known, either by direct measurement or by Time-Over-Threshold (TOT) measurement, the time walk effect can be significantly reduced by applying the pulse-amplitude dependent time correction.

The simplest time interval measurement method utilizes an ordinary digital counter clocked with constant frequency. The time is estimated as a number of clock pulses between the start and the stop signals. This approach is limited by the speed of counter, with current technologies to about 1 GHz. Such clock speed allows for time quantization precision of about 1 ns. When a sub-nanosecond resolution is needed, a two stage interpolation time measurement is applied (see Figure 2.19). An ordinary digital counter is used for rough time estimation with $\sim$ 10 –

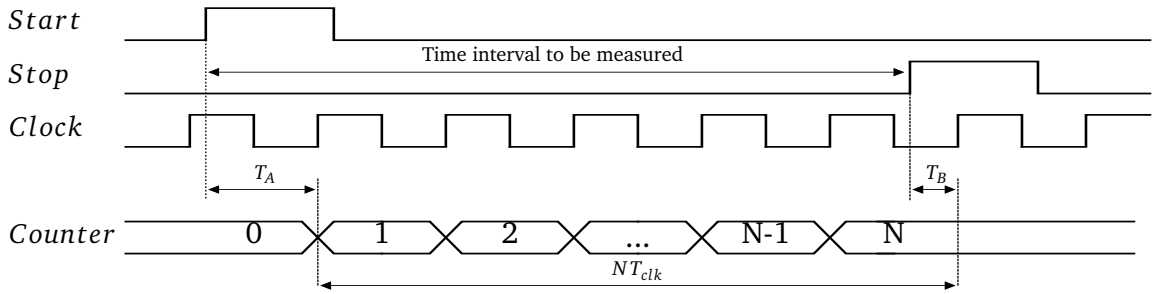

Figure 2.19: Two stage interpolation time measurement basis.

100 ns resolution (NT_{CLK} interval), while other technique is utilized for precise measurement of intervals T_A and T_B. Such an approach allows avoiding high frequency clocks and provides an excellent time resolution. The precise time measurement can be taken using Time-to-Amplitude Conversion (TAC) or clock interpolation techniques.

In the TAC technique, the time interval is converted to a voltage by charging a capacitor through a switchable constant current source I_T (see Figure 2.20a). The start pulse turns on the current source and the stop pulse turns it off. The resulting voltage on the capacitor C is $V = I_T(t_{stop} - t_{start})/C$, is then digitalized by an ADC. As a digitizer a Wilkinson ADC is

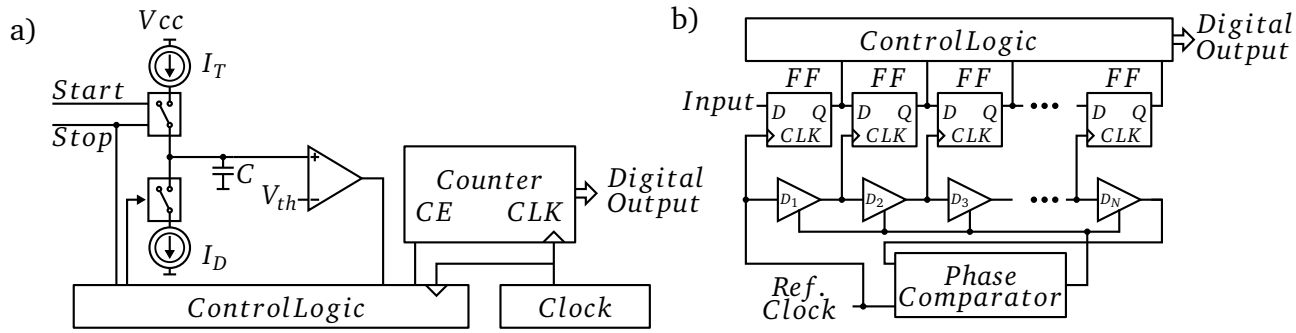

Figure 2.20: Precise time measurement techniques. a) Combination of Time-to-Amplitude Conversion with Wilkinson Analog-to-Digital Converter. The memory capacitor C is charged by the current I_T for duration $t_{stop} - t_{start}$ and subsequently discharged by current I_D being part of ADC. b) Fine digitizer using clock interpolation technique. The interpolation delays are controlled by a Delay-Locked Loop.

commonly used, because of seamless integration. It utilizes discharge current I_D, smaller than I_T, which results in time prolongation of the discharge interval with respect to the charge interval. This technique ensures high resolution, but at the expense of long dead time and poor multi-hit capability.

A block diagram of circuit utilizing clock interpolation technique is shown in Figure 2.20b. The clock period is interpolated by the delay elements (D_1, D_2, ...) – usually current-starved inverters. The delay of each inverter is fine-tuned by adjusting the current. The overall delay is stabilized by a Delay-Locked Loop (DLL) to the reference clock. This ensures very tight control against temperature or voltage variations. The interpolated clocks are then used to clock a number of Flip-Flop (FF) registers. The register outputs are passed to control logic, responsible for conversion to binary form as well as resolving multiple hits. This technique in practice is less precise than analog ramp, however, it does not have dead time and is capable to process multiple hits.

2.7 Conventional readout architecture for time and amplitude measurement

In many applications both the time and the amplitude need to be measured. As it was described in previous chapters, the time and the amplitude measurements impose different requirements on shaper circuit. To enable precise measurement of both quantities, a typical approach would be to build the system as presented in Figure 2.21. The signal originating from the radiation sensor is integrated in charge sensitive amplifier. Then two separate processing chains follow. The first one (upper in Figure 2.21) is used for amplitude processing. The shaping time is set to highest acceptable value in order to maximize the SNR (see chapter 2.4). The maximum value of the pulse is stored by the peak detector circuit and then converted to a digital form by the ADC. The second chain is optimized for time measurement. To minimize the time walk effect a fast shaper is used usually in a combination with a time walk compensation circuit. The signal is then passed to a fast discriminator. The digital discriminator's output is measured by the TDC.

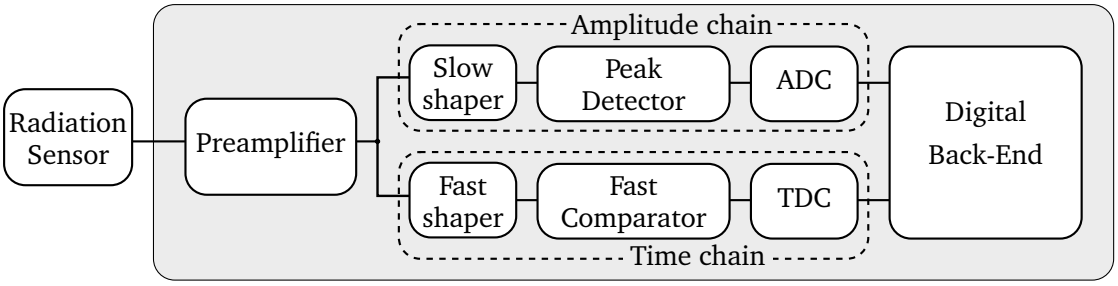

Figure 2.21: Schematic diagram of dual chain readout channel.

Usually a few interconnections are needed between the channels to ensure proper operation and synchronization of both chains. Data from the both processing chains are passed to Digital Back-End block where a logical event containing information about the time and the amplitude is built. The main disadvantages of the dual-chain readout approach are:

- large number of components to be designed and carefully optimized,
- cumulative power consumptions of all sub-blocks,
- occupied area,
- small pill-up immunity, especially because of slow amplitude-processing chain.

Another approach may be to use fast sampling ADC working continuously, and to apply digital signal processing to extract the requested information. Such readout scheme suited for high event rates, based on the deconvolution method [78], is discussed in the following section.

2.8 Advanced readout architecture for amplitude and time measurement

An attractive readout scheme for time and amplitude measurements would be to use only one processing chain (Figure 2.22), with an ADC incorporated in each channel, and to take advantage of today's high performance low power digital technology, moving the signal processing to the digital domain in the earliest possible stage. Direct digitalization of a sensor signal would be very difficult because of its small amplitude and small signal to noise ratio. The signal amplitude is greater after preamplifier, so it can be digitalized and further processed as proposed in [79, 80, 81]. With this approach a very fast ($>\sim$ 100 MSps) and high resolution ($>\sim$ 12 bit) sampling ADC is needed in order to capture precisely the rising edge of preamplifier. This approach is very attractive; however, it is not applicable in multichannel systems because of high power consumption of the ADC. The situation is changed if the signal is digitized after the shaper. The signal is slower, has higher amplitude, and Signal-to-Noise Ratio is improved. Such approach significantly reduces the requirements for the ADC in comparison to the one with digitization at the preamplifier output or the sensor directly.

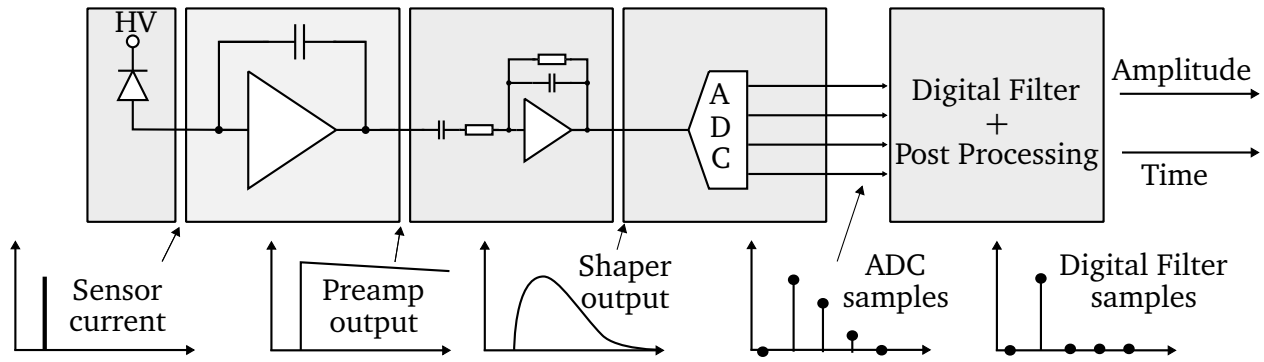

Figure 2.22: Block diagram of the proposed readout scheme.

2.8.1 Digital signal processing

Digital filters are one of the main blocks of DSP systems. These filters perform a filtering function on data by attenuating or gaining certain bands of frequencies. Several common digital filter architectures exist [82]:

- Finite Impulse Response (FIR) - Non recursive linear filter
- Infinite Impulse Response (IIR) - Recursive linear filter
- Adaptive Digital Filter - A self learning filter that adapts itself to a desired signal

The simplest, FIR filter, performs a weighted average (convolution) on a series of N data samples according to the formula:

$$s_k = \sum_{i=0}^{N-1} w_i v_{k-i} \ , \tag{2.34}$$

where s_k represents output sample, v_k represents input sample, and w_i represents weights. The filter specification is better controlled for higher order filters (higher N); however, more filter weights require more processing power to implement such a design in real time. The processing algorithm described in the following section is implemented as a FIR filter.

2.8.2 Deconvolution theory

An efficient algorithm needs to be applied on the collected signal samples in order to find and precisely measure the event pulses. The output pulse after the front-end electronics is a convolution of sensor current signal and the impulse response of the preamplifier-shaper chain. Thanks to the known pulse shape, an inverse procedure – deconvolution – can be performed in order to obtain information about the time and the amplitude of the event pulse. The deconvolution idea was proposed for use in pulse processing in High Energy Physics experiments at the beginning of the 90's [78]. It was then implemented in different versions of Analog Pipeline Voltage (APV) ASICs designed for experiments synchronous with the beam, like the CMS at the LHC, where the deconvolution was performed by an analog pulse shape processor [83]. The main goal was amplitude measurement with a good pileup rejection, plus a rough estimation of time (to identify

the beam crossings, occurring every 25 ns). In this work the deconvolution principle, besides the application in synchronous systems, is also employed in asynchronous systems to obtain precise timing information (of a few ns), good SNR, and good pileup rejection.

The deconvolution procedure can be applied to any shape in order to untangle the input signal and the impulse response of the processing chain; however, more complicated shape leads to more complicated formulas to by computed for each sample. On the other hand, the analog part of the readout chain should be as simple as possible and power efficient. The traditional CR-RC shaping fulfills these requirements and is well suited for application of deconvolution procedure in multichannel readout systems.

To cancel the effect of pulse shaping and return to the original sensor signal, a deconvolution filter with transfer function inverse to preamplifier-shaper transfer function needs to be applied. For a charge sensitive preamplifier followed by CR-RC semi-gaussian shaper, with time constant τ and transfer function given by equation (2.18), the deconvolution filter transfer function can be written as:

$$D(s) = \frac{1}{V_{sh}(s)} = (s + 1/\tau)^2 = (s - s_0)^2 \ . \tag{2.35}$$

Such transfer function cannot be easily synthesized in analog circuitry. However, the discrete time implementation of such a filter in digital domain may be obtained using the Z transform. In the pole-zero mapping technique each pole or zero (on S plane) is replaced by its mapped z position according to $z_0 = e^{s_0 T_{smp}}$, where T_{smp} is sampling period and s_0 is pole/zero position on S plane. Formula (2.35) has only two zeros, located at $s = -1/\tau$ and no poles, so it transforms to:

$$D(z) = \left(z - z_0\right)^2 = \left(z - e^{-T_{smp}/\tau}\right)^2 \ . \tag{2.36}$$

By expanding equation (2.36), one obtains:

$$D(z) = z^2 - 2e^{-T_{smp}/\tau} z + e^{-2T_{smp}/\tau} \ . \tag{2.37}$$

Because z^2 corresponds to two samples ahead, which are unknown, we may delay all samples by two, which is equivalent to multiplication by z^{-2} and achieving:

$$D(z) = 1 - 2e^{-T_{smp}/\tau} z^{-1} + e^{-2T_{smp}/\tau} z^{-2} \, , \tag{2.38}$$

where z^{-1} is a unit delay. From formula (2.38) the expression for deconvolutied filter output sample d_i at time iT_{smp} is given by:

$$d_i = Z^{-1}\left(D(z)\right) = v_i - 2e^{-T_{smp}/\tau} v_{i-1} + e^{-2T_{smp}/\tau} v_{i-2} \, , \tag{2.39}$$

where v_i is the shaper output value $V_{sh}(iT_{smp})$. Equation (2.39) can be recognized as a second order FIR filter, described by equation (2.34) where:

$$w_0 = 1, \quad w_1 = -2e^{-T_{smp}/\tau}, \quad w_2 = e^{-2T_{smp}/\tau} \ . \tag{2.40}$$

It may be noticed that the deconvolution filter for CR-RC shaper is very light, requiring only two additions and two multiplications by constant weight factors. These weights dependent only on the ratio of sampling period to shaping time.

The CR-RC pulse with amplitude A (at pulse maximum) and starting at t_0 is described by:

$$V_{sh}(t) = \frac{Ae}{\tau}(t - t_0)e^{-(t-t_0)/\tau}H(t - t_0)\,, \tag{2.41}$$

where $H(t)$ is Heaviside's step function. Without loss of generality, it can be assumed that $t_0 \in [0, T_{smp})$. A larger/smaller value of t_0 corresponds to next/previous clock period. The subsequent shaper output samples may be written as:

$$\begin{aligned}
v_{-1} &= 0\ , \\
v_0 &= 0\ , \\
v_1 &= \frac{Ae}{\tau}(T_{smp} - t_0)e^{-(T_{smp}-t_0)/\tau}\ , \\
v_2 &= \frac{Ae}{\tau}(2T_{smp} - t_0)e^{-(2T_{smp}-t_0)/\tau}\ , \\
v_{N-1} &= \frac{Ae}{\tau}((N-1)T_{smp} - t_0)e^{-((N-1)T_{smp}-t_0)/\tau}\ , \\
v_N &= \frac{Ae}{\tau}(NT_{smp} - t_0)e^{-(NT_{smp}-t_0)/\tau}\ .
\end{aligned} \tag{2.42}$$

And corresponding samples after deconvolution filter as:

$$\begin{aligned}
s_0 &= w_0v_0 + w_1v_{-1} + w_2v_{-2} = 0\ , \\
s_1 &= w_0v_1 + w_1v_0 + w_2v_{-1} = \frac{Ae}{\tau}(T_{smp} - t_0)e^{-(T_{smp}-t_0)/\tau}\ , \\
s_2 &= w_0v_2 + w_1v_1 + w_2v_0 = \frac{Ae}{\tau}(2T_{smp} - t_0)e^{-(2T_{smp}-t_0)/\tau} - \frac{Ae}{\tau}2e^{-T_{smp}/\tau}(T_{smp} - t_0)e^{-(T_{smp}-t_0)/\tau}\ , \\
s_3 &= w_0v_3 + w_1v_2 + w_2v_1 = \ldots = 0\ , \\
s_N &= w_0v_N + w_1v_{N-1} + w_2v_{N-2} = \ldots = 0\ .
\end{aligned} \tag{2.43}$$

In Figure 2.23 an example response of deconvolution filter (circles) to sampled shaper output (square) is shown. As can be concluded from (2.43), the deconvolution filter always produces zero if all three input samples v_k are on the pulse. The deconvolution formula produces non-zero output samples s_k only in the case of one or two input samples on the pulse and the rest on baseline. If the input pulse is synchronized with the sampling clock ($t_0 = 0$ in equation (2.41)), the procedure produces only one non-zero output sample (Figure 2.23a) with the amplitude s_1, directly proportional to the input pulse amplitude. In other (asynchronous) cases the filter produces two non-zero samples: s_1, s_2 (Figure 2.23b).

The ratio of non-zero samples produced by deconvolution algorithm in asynchronous mode can be written as:

$$s_2/s_1 = \frac{t_0 e^{-\frac{T_{smp}}{\tau}}}{T_{smp} - t_0}\ . \tag{2.44}$$

This ratio depends on sampling period T_{smp} , shaping time τ (which are constant), and pulse occurrence time t_0. Since the ratio does not depend on pulse amplitude and it is a monotonic

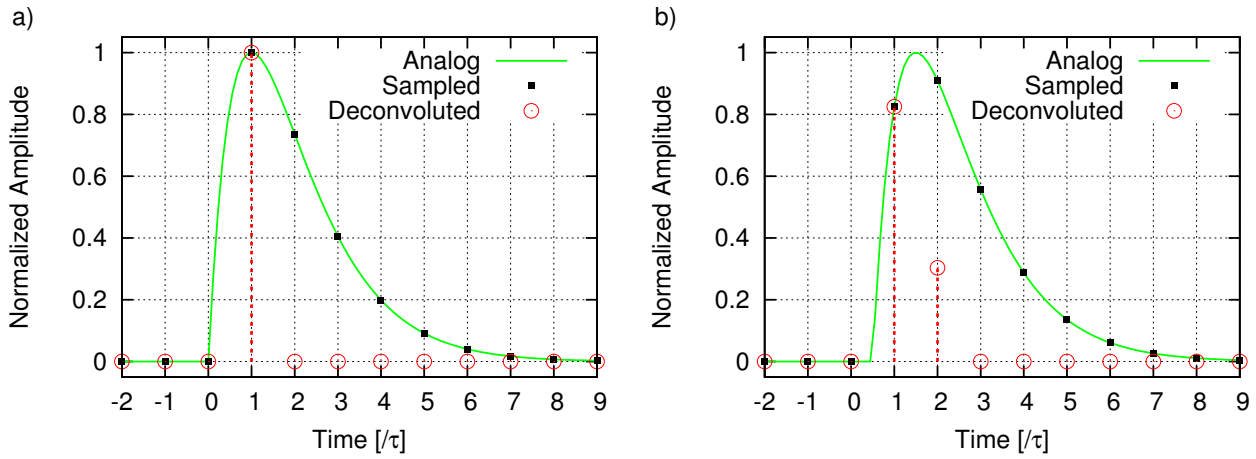

Figure 2.23: Deconvolution filter response ($T_{smp} = T_{peak} = 1, amp = 1$). a) Pulse synchronous and b) Pulse asynchronous with sampling clock.

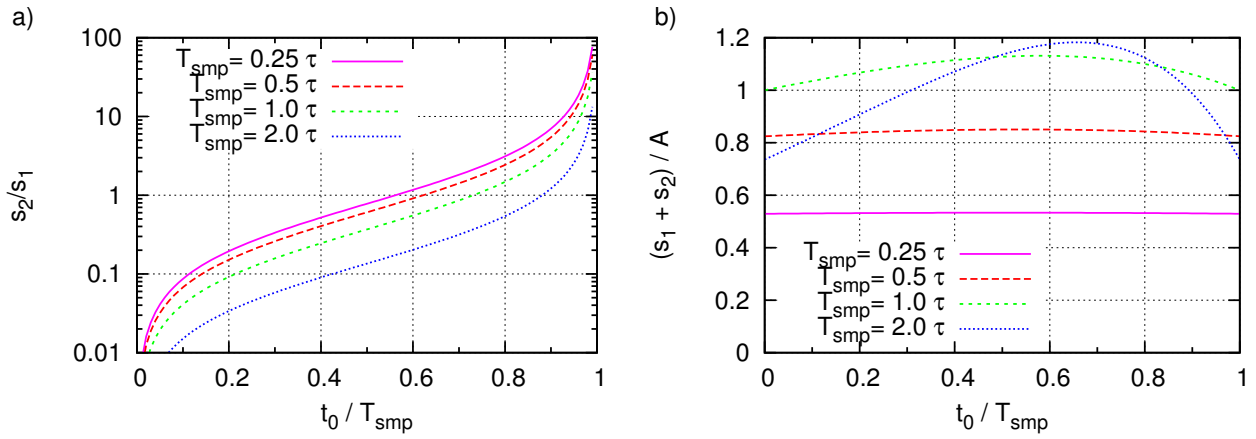

Figure 2.24: a) Ratio and b) sum of two non-zero deconvoluted samples for various sampling times T_{smp} as a function of pulse occurrence time t_0.

function of t_0 (see Figure 2.24a) the inverse function can be found:

$$t_0 = \frac{s_2/s_1 T_{smp}}{s_2/s_1 + e^{-\frac{T_{smp}}{\tau}}} \quad . \tag{2.45}$$

Formula (2.45) can be used to calculate the initial time t_0 within the proper clock period, based on the ratio of two non-zero deconvoluted samples.

The sum of two non-zero deconvoluted samples is:

$$s1 + s2 = A\frac{e^{\frac{t_0 - T_{smp} + \tau^2}{\tau}}}{\tau}\left(T_{smp} - t_0(1 - e^{\frac{T_{smp}}{\tau}})\right) \quad . \tag{2.46}$$

This sum is proportional to the input pulse amplitude A; however, it depends slightly on the pulse occurrence time t_0 (see Figure 2.24b). The time t_0 can be estimated using formula (2.45) and

then the amplitude of the input pulse can be calculated as the sum of two non-zero samples multiplied by a time dependent correction factor:

$$A = (s1 + s2)\frac{\tau e^{\frac{T_{smp} - t_0 - \tau^2}{\tau}}}{\left(T_{smp} - t_0(1 - e^{\frac{T_{smp}}{\tau}})\right)} \quad . \tag{2.47}$$

2.8.3 Impact of sampling and shaping time on deconvolution performance

To optimize the system performance, the impact of sampling time to shaping time ratio on amplitude and time resolution was studied. An example of deconvolution output for sampling period four times shorter than shaping time is illustrated in Figure 2.25a. The deconvolution filter per-

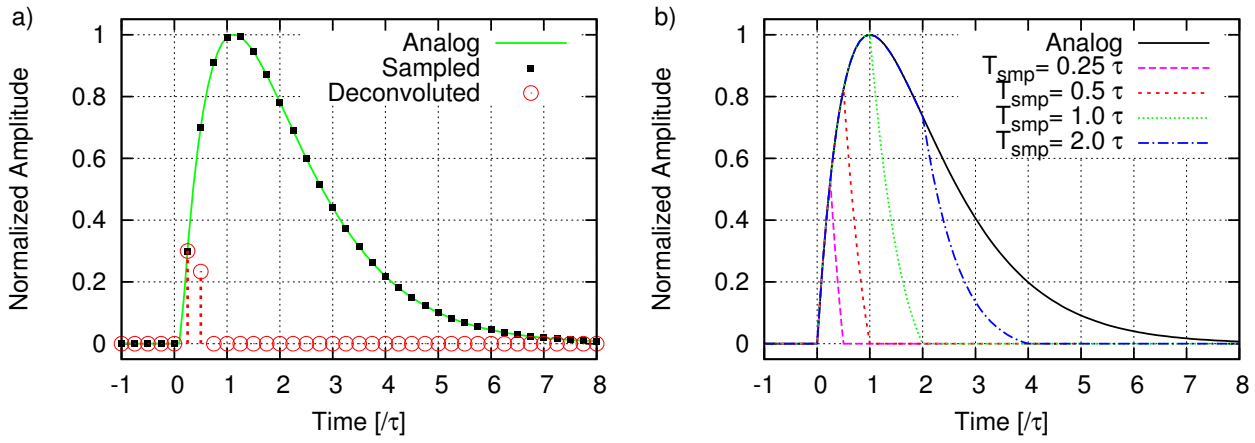

Figure 2.25: a) Response of deconvolution filter to sampled data with sampling time four times shorter than shaping time. b) Pulse shapes after deconvolution filter for different sampling times.

forms as expected, producing only two non-zero samples. However, their sum is smaller than one (check also Figure 2.24b).

In Figure 2.25b the effective pulse shapes after deconvolution for different sampling times, are presented. One needs to remember that for a single pulse such a shape is not available (for a single event there are only two non-zero samples separated by T_{smp}). This shape can be obtained for a large number of pulses with various phase differences between sampling clock and signal start (various t_0).

For different sampling time to shaping time ratios the obtained dependencies differ quantitatively but the general relationship is maintained. For sampling time equal to shaping time, in the case of synchronous sampling, the relative gain of deconvolution filter is equal to one (the value of the first non-zero sample obtained for $t_0 = 0$, see green curve in Figure 2.25b). The variation of these times brings about a change in the gain of the deconvolution filter. In order to compensate for this effect, an artificial factor of $e^{T_{smp}/\tau}/(eT_{smp})$ may be incorporated in each filter weight, transforming the weights from (2.40) into:

$$w_0 = \frac{e^{T_{smp}/\tau}}{eT_{smp}} \; , w_1 = -\frac{2}{eT_{smp}} \; , w_2 = \frac{e^{-T_{smp}/\tau}}{eT_{smp}} \quad . \tag{2.48}$$

Using the weights from (2.48) ensures unity gain only in case of synchronous sampling (see Figure 2.26a). In asynchronous case ($t_0 \neq 0$), a phase-dependent amplitude correction factor still

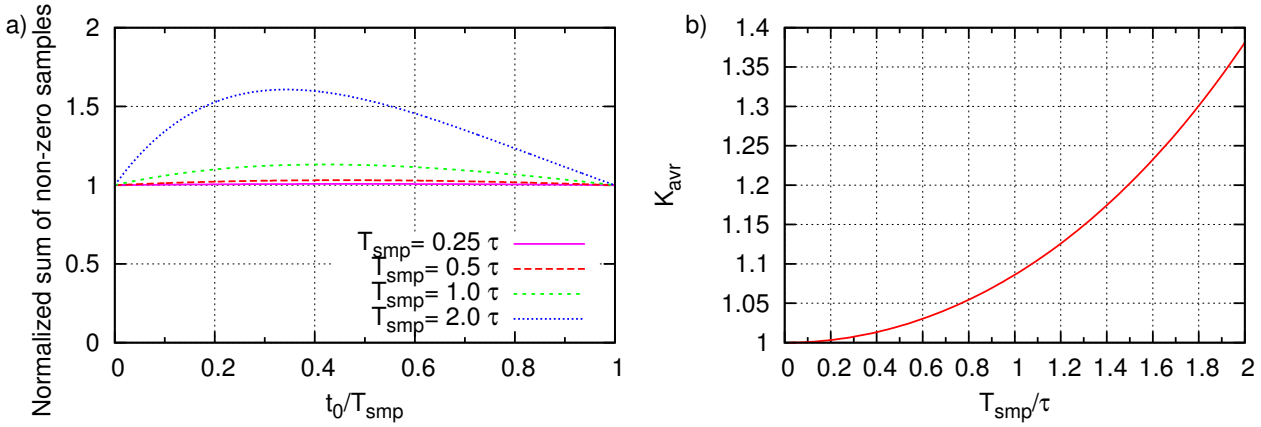

Figure 2.26: a) Normalized sum of two non-zero deconvoluted samples for different sampling times. b) Average signal gain of deconvolution filter as a function of sampling time to shaping time ratio.

needs to be applied as described in the previous section (see equation (2.47)). Assuming a flat distribution of phase difference between sampling clock and signal occurrence ($t_0 \in [0, T_{smp}]$), the average signal gain can be calculated as:

$$K_{avr} = \frac{\tau e^{\frac{\tau^2 - T_{smp}}{\tau}}}{e T_{smp}^2} \left(1 + e^{2\frac{T_{smp}}{\tau}} - 2e^{\frac{T_{smp}}{\tau}}\right) . \tag{2.49}$$

The K_{avr} as a function of sampling time to shaping time ratio is shown in Figure 2.26b. For sampling time smaller then shaping time the signal gain variation is lower than 10%.

2.8.4 Pile-up rejection capabilities

Since the deconvolution filter effectively shortens pulses, it allows for more efficient pileup resolving. In Figure 2.27a an example with two events distant by 2.5 T_{smp} is shown. Since there is one zero sample between the deconvoluted pulses, the events can be fully resolved. In general, the time separation must be grater than 3 T_{smp} (two non-zero deconvoluted samples followed by one zero) for unambiguous deconvolution. In Figure 2.27b a non-resolvable pileup is presented. Nevertheless, even in this case the deconvolution gives a signature of more than 2 non-zero subsequent samples which can be used to reject those events. To enhance pileup immunity of the readout system, the sampling frequency can be increased. Figure 2.27c presents a situation where subsequent events are separated by 0.8τ. Decreasing sampling period T_{smp} to $1/4\tau$ allows for precise measurement of both events even though they are not distinguishable from the point of view of analog input signal.

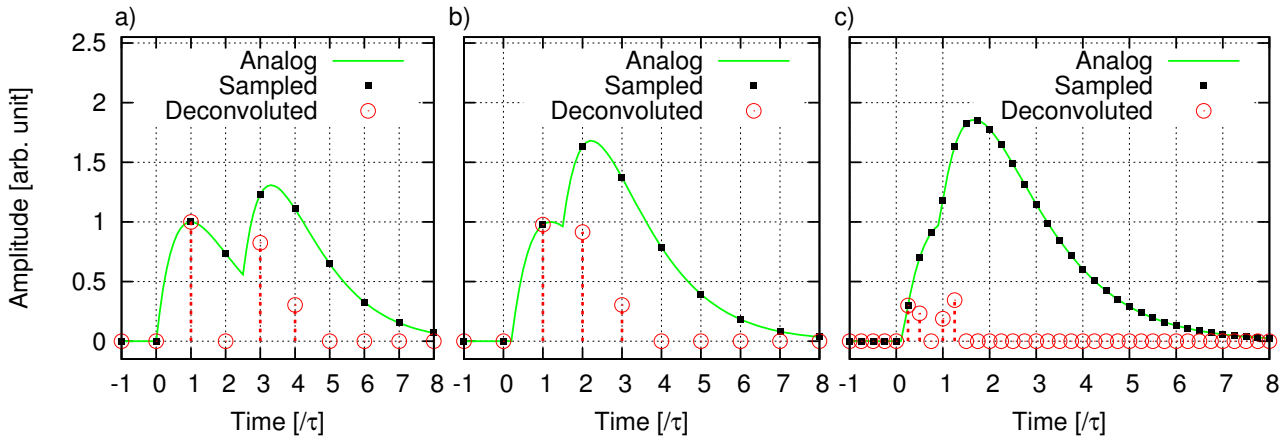

Figure 2.27: Response of deconvolution filter to a) resolvable pileup where separation between pulses is $2.5T_{smp}$ ($T_{smp} = \tau$), b) non-resolvable pileup where separation between pulses is $1.7T_{smp}$ ($T_{smp} = \tau$), c) resolvable pileup where separation between pulses is 0.8τ ($T_{smp} = 1/4\tau$) ($\tau = 1, amp = 1$ for all pulses).

2.8.5 Noise processing

The deconvolution procedure effectively changes the shape of the pulse; therefore, the noise performance is also changed. In chapter 2.3.1 the noise analysis was performed in the frequency domain. For the deconvolution filter, where the response is given in time domain, it seems more straightforward to analyze the noise performance in the time domain.

The noise as well as the signal is sampled as v_k by the ADC in discreet moments of time. To describe statistically the results after passing through any processing function $x(v_k, v_{k-1}, \ldots, v_{k-(N-1)})$ on the set of values $v_k, v_{k-1}, \ldots, v_{k-(N-1)}$ (which may be correlated), an average and variance are calculated. An estimate of the mean value of linear function x, denoted by $\overline{x}$, is obtained for the set of independent measurements as [84]:

$$\overline{x} = x(\overline{v_k}, \overline{v_{k-1}}, \ldots, \overline{v_{k-(N-1)}}) \,, \tag{2.50}$$

where $\overline{v_k}$ is the mean value of variable v_k from the measurements. To estimate the variance σ_x of the function x, one can use the formula for combined standard uncertainty of correlated input quantities [84]:

$$\sigma_x^2 = \sum_{i,j=0}^{N-1} \frac{\partial x}{\partial v_{k-i}} \frac{\partial x}{\partial v_{k-j}} cov(v_{k-i} v_{k-j}) \ . \tag{2.51}$$

In the formula (2.51) $cov(v_{k-i} v_{k-j})$ is a two-dimensional covariance between variables v_{k-i} and v_{k-j}. Because both variables v_{k-i} and v_{k-j} represent the variation of the same random variable $v(t)$, the covariance is replaced by the autocovariance – the covariance of the variable against a time-shifted version of itself. The autocovariance of function $v(t)$ is defined as:

$$cov_v(\Delta t) = \int_{-\infty}^{\infty} v(t) v(t - \Delta t) dt \tag{2.52}$$

for samples separated by time interval Δt. A normalized version of autocovariance coefficient – autocorrelation coefficient – is defined as:

$$cor_v(\Delta t) = \frac{cov_v(\Delta t)}{\int_{-\infty}^{\infty} v(t)^2 dt} = \frac{cov_v(\Delta t)}{\sigma_v^2} \ . \tag{2.53}$$

Since it is a dimension less number within the range $[-1, 1]$, it is much easier to interpret. The two samples separated by Δt are called uncorrelated if the autocorrelation coefficient equals zero. In other cases, samples are correlated. Using autocorrelation coefficient and knowing that samples v_{k-i} and v_{k-j} are separated by $T_{smp}|i-j|$ in time, one can interpret the equation (2.51) as:

$$\sigma_x^2 = \sigma_v^2 \sum_{i,j=0}^{N-1} \frac{\partial x}{\partial v_{k-i}} \frac{\partial x}{\partial v_{k-j}} cor_v(T_{smp}|i-j|) \ . \tag{2.54}$$

The mean value of a single sample s_k, described by formula (2.34), at the output of deconvolution filter according to (2.50) can be expressed as:

$$\overline{s_k} = \sum_{i=0}^{N-1} w_i \overline{v_{k-i}} \ . \tag{2.55}$$

If the mean values of all $\overline{v_i}$ distributions are equal $\overline{v_i} = \overline{v_j} = \overline{v}$ (which is usually the case in stationary systems), one may conclude that the output of deconvolution filter is proportional to the mean value of input signal $\overline{v}$. The proportionality factor is the sum of all weights. The situation is more complicated when one needs to calculate the variance of function x, due to the correlation term in the formula (2.51).

The two major types of noise sources exist in the sensor electronics: parallel and serial (see chapter 2.2.1). If the $1/f$ component of the serial noise is neglected, both noises can be represented as equivalent voltage and current white-noise sources (noise power is independent on frequency) at the input of the preamplifier. In the time domain, noise can be represented as a randomly recurring series of uniform pulses [85, 86, 87]. The frequency spectrum of the noise generated by such pulses is determined by a shape of single pulse, while the magnitude of the noise is proportional to the average rate of these pulses. The Dirac delta pulse $\delta(t)$ has white frequency spectrum and therefore the superposition of such pulses may represent the noise source with white frequency spectrum. The voltage $\delta(t)$ pulse at the preamplifier input is transferred to its output without any change in shape. Such a pulse is then processed by the shaper, and the cumulative response of the preamplifier - CR-RC shaper chain has the following form:

$$V_{SHP}^{\delta}(t) = \left(\frac{1}{\tau} e^{-t/\tau} - \frac{t}{\tau^2} e^{-t/\tau} \right) H(t) \ . \tag{2.56}$$

The current $\delta(t)$ pulse is integrated on the feedback capacitance and thus forms a step response at the preamplifier output. The spectral noise density of parallel noise at the output of the preamplifier is inversely proportional to frequency. The response of the CR-RC shaper to the step pulse equals:

$$V_{SHP}^{step}(t) = \left(\tau e^{-t/\tau} \right) H(t) \ . \tag{2.57}$$

The normalized responses of the shaper to the step and the δ functions are presented in Figure 2.28a. The total noise at the output of the preamplifier-shaper is represented by a superposition of both types of noise. The variance of the noise at the output of the considered chain is determined by average rates of the pulses. From equations (2.57) and (2.56) the autocorrelation

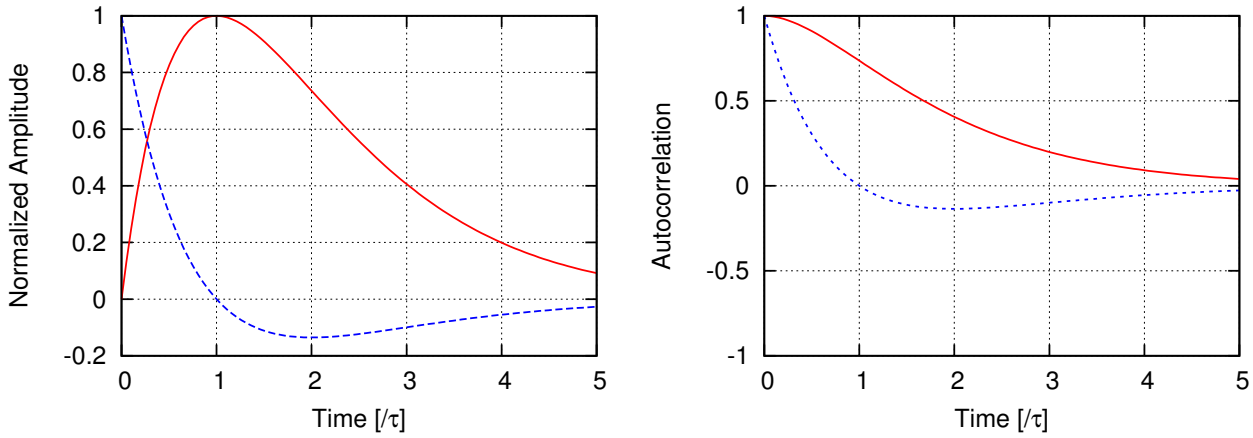

Figure 2.28: a) Normalized response of CR-RC shaper to the step (red) and the δ (blue) functions. b) Autocorrelation function for step and δ functions for CR-RC filter.

functions can be calculated as:

$$cor_{step}(\Delta t) = \left(1 + \frac{\Delta t}{\tau}\right) e^{-\Delta t/\tau} \tag{2.58}$$

and

$$cor_{\delta}(\Delta t) = \left(1 - \frac{\Delta t}{\tau}\right) e^{-\Delta t/\tau} \tag{2.59}$$

for responses to step and δ functions, respectively. The autocorrelation functions are shown in Figure 2.28b. One should notice that for $\Delta t \to 0$ autocorrelation tends to one (full correlation), while for $\Delta t \to \infty$, which corresponds to samples well separated in time, autocorrelation tends to zero, which means there is no correlation.

There is an additional consideration which needs to be accounted for if signal processing is occurs in digital domain. When the signal is transformed from analog (continuous) domain to digital (with a limited number of possible states), a quantization error is introduced for each sample [82]. Usually the quantization error is uncorrelated with the quantizer input, and so it is not autocorrelated. The quantization error has an approximately uniform distribution and stays within range [-1/2 LSB, 1/2 LSB]. On average, the quantization error has a zero mean value. Because of those properties, the quantization error is often called quantization noise. Since it is not autocorrelated, it has white frequency spectrum.

2.8.6 Amplitude reconstruction performance

Since it is assumed that all noise sources are not correlated, individual contributions to the output noise can be treated separately. The variance of a single sample caused by noise at the output of

deconvolution filter $\sigma^2_{s_k}$ can be calculated according to (2.54) as:

$$\sigma^2_{s_k} = \sigma^2_{v_k} \sum_{i,j=0}^{N-1} w_i w_j cor_{v(t)}(T_{smp}|i-j|) \ . \tag{2.60}$$

where $cor_{v(t)}(\Delta t)$ is the autocorrelation function for the noise pulses. For third order filter equation 2.60 can be expanded to:

$$\sigma^2_{s_k} = \ \sigma^2_{v_k} \left(w_0^2 + w_1^2 + w_2^2 + 2w_0 w_1 cor_v(T_{smp}) + 2w_1 w_2 cor_v(T_{smp}) + 2w_0 w_2 cor_v(2T_{smp})\right) \ . \tag{2.61}$$

By combining equations (2.58), (2.59), and (2.61), one can express the parallel and the serial noise components after the deconvolution filter as:

$$\left(\sigma^p_{dec}\right)^2 = \frac{\left(\sigma^p_{SHP}\right)^2}{T^2_{smp} e^2} \left(e^{2\frac{T_{smp}}{\tau}} - 4\frac{T_{smp}}{\tau} - e^{-2\frac{T_{smp}}{\tau}}\right) \tag{2.62}$$

and

$$\left(\sigma^s_{dec}\right)^2 = \frac{\left(\sigma^s_{SHP}\right)^2}{T^2_{smp} e^2} \left(e^{2\frac{T_{smp}}{\tau}} + 4\frac{T_{smp}}{\tau} - e^{-2\frac{T_{smp}}{\tau}}\right) \ , \tag{2.63}$$

where σ^p_{SHP} and σ^s_{SHP} are the noise components of analog system (introduced in equations (2.23) and (2.24)). Equations (2.62) and (2.63) describe the variance of a single sample at the output of deconvolution filter. These results may be used to estimate the expected noise in the synchronous system, in the case of which only one sample carries the whole information about pulse amplitude. The impact of sampling time on the noise performance is shown in Figure 2.29. The blue (red) squares represent the variance of serial (parallel) noise at the deconvolution output σ^s_{dec} (σ^p_{dec}) as a function of sampling time T_{smp} to τ ratio. The variance at deconvolution input is set to unity. The results of deconvolution processing can be compared with the noise performance obtained by changing the shaping time in the analog domain (formulas (2.26) and (2.27)) which is plotted in solid lines. The presented results for deconvolution filtering follow the behavior expected from the variation of shaping time in the analog domain. The deconvolution processing actually reduces parallel noise more than reshaping signal in the analog domain, which makes this method especially attractive in systems where a large shot noise from sensor leakage current is expected (e.g. after sensors irradiation). For sampling periods smaller than the shaping time, the deconvolution performs similarly to analog reshaping with respect to serial noise. However, for higher sampling periods, the noise value is enhanced. This behavior is caused by the fact that the information about the pulse amplitude is extracted from only one sample, not at full amplitude. For longer sampling periods, apart from sampling not full amplitude, the deconvoluted samples need to be corrected for sampling phase variation (see formula (2.49) and Figure 2.26b), which deteriorates SNR even more.

In the case of asynchronous system, the signal amplitude is obtained using formula (2.47). The formula involves also the time calculated from equation (2.45). Performing exact computation of equation (2.54) would be complex, so another approach is taken. Because time correction factor does not vary too much (less than 10% for sampling times smaller than shaping time), the approximate variance of reconstructed amplitude after deconvolution filter is calculated as a variance of the sum of deconvoluted samples $s_1 + s_2$ (obtained with weights from equation (2.48))

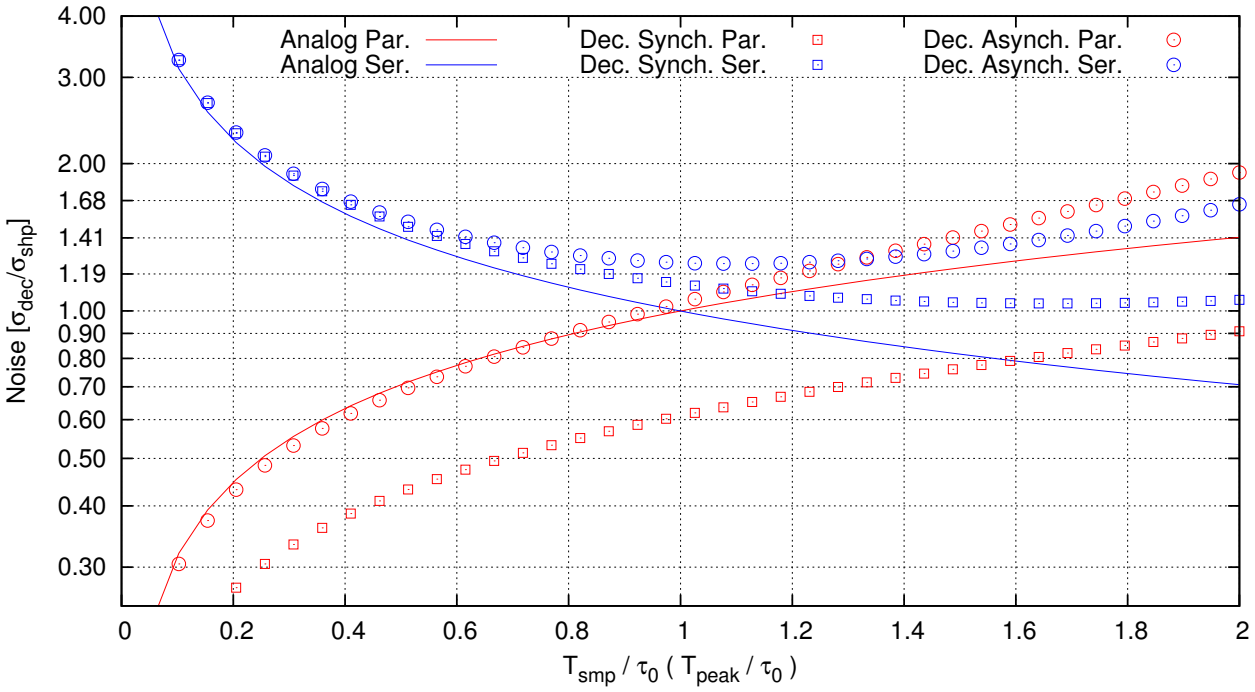

Figure 2.29: The effect of the deconvolution processing on serial (blue) and parallel (red) noise. Squares represent change in the variance of single sample (synchronous sampling). Circles represent change in reconstructed amplitude using the sum of two subsequent samples (asynchronous sampling). The solid lines show the noise level obtained for CR-RC shaper without deconvolution processing as a function of the normalized peaking time (T_{peak}/τ_0).

divided by the mean correction factor K_{avr}, for given sampling time to shaping time ratio (equation (2.49)). The results of this calculations are:

$$\left(\sigma^s_{dec}\right)^2 = \frac{2\left(\sigma^s_{SHP}\right)^2}{e^2 {T_{smp}}^2 K_{avr}(T_{smp},\tau)^2}\left(\frac{T_{smp}}{\tau}\left(4 - e^{\frac{T_{smp}}{\tau}} - e^{-\frac{T_{smp}}{\tau}}\right) + \left(e^{\frac{2T_{smp}}{\tau}} - e^{\frac{T_{smp}}{\tau}} + e^{-\frac{T_{smp}}{\tau}} - e^{\frac{-2T_{smp}}{\tau}}\right)\right) \tag{2.64}$$

and

$$\left(\sigma^p_{dec}\right)^2 = \frac{2\left(\sigma^p_{SHP}\right)^2}{e^2 {T_{smp}}^2 K_{avr}(T_{smp},\tau)^2}\left(\frac{T_{smp}}{\tau}\left(e^{\frac{T_{smp}}{\tau}} + e^{-\frac{T_{smp}}{\tau}} - 4\right) + \left(e^{\frac{2T_{smp}}{\tau}} - e^{\frac{T_{smp}}{\tau}} + e^{-\frac{T_{smp}}{\tau}} - e^{\frac{-2T_{smp}}{\tau}}\right)\right) \tag{2.65}$$

for serial and parallel noise, respectively. The impact of sampling time on noise performance in asynchronous system is shown in circles in Figure 2.29. As it can be seen, for parallel noise, the noise is increased by a factor of 1.5. This is understandable having in mind that the samples of parallel noise are highly correlated (see Figure 2.28b), especially for short time intervals. For serial noise, the effect is significantly smaller.

To estimate the overall impact of the deconvolution processing on the noise performance, the exact ratio of both mentioned noise components needs to be known. In general, it can be concluded that the deconvolution processing gives similar results as analog reshaping. More-

over, in the case of synchronous sampling the deconvolution processing outperforms the analog reshaping with respect to parallel noise processing.

2.8.7 Time resolution

The second important aspect of deconvolution algorithm is the timing resolution. In the case of the synchronous system the precise information is already known and provided as a reference clock. In the asynchronous system, the event time is obtained according to formula (2.45). The sensitivity of t_0 to the input noise is calculated using formula (2.54) as:

$$\left(\sigma^s_{t_0}\right)^2 = \frac{\tau^2\left(\sigma^s_{SHP}\right)^2}{e^2A^2}\left(\tau\left(e^{2\frac{2T_{smp}-t_0}{\tau}} - e^{\frac{-2t_0}{\tau}}\right) + 2t_0\left(e^{\frac{-2t_0}{\tau}} - 3e^{2\frac{T_{smp}-t_0}{\tau}}\right) + 2\frac{{t_0}^2}{T_{smp}}\left(e^{2\frac{T_{smp}-t_0}{\tau}} + e^{\frac{-2t_0}{\tau}}\right)\right.$$
$$\left. +4T_{smp}e^{2\frac{T_{smp}-t_0}{\tau}} + \frac{2\tau t_0}{T_{smp}}\left(e^{2\frac{T_{smp}-t_0}{\tau}} - e^{2\frac{2T_{smp}-t_0}{\tau}}\right) + \frac{\tau {t_0}^2}{{T_{smp}}^2}\left(e^{\frac{-2t_0}{\tau}} - e^{-2\frac{T_{smp}+t_0}{\tau}} + e^{2\frac{2T_{smp}-t_0}{\tau}} - e^{2\frac{T_{smp}-t_0}{\tau}}\right)\right) \tag{2.66}$$

and

$$\left(\sigma^p_{t_0}\right)^2 = \frac{\tau^2\left(\sigma^p_{SHP}\right)^2}{e^2A^2}\left(\tau\left(e^{2\frac{+2T_{smp}-t_0}{\tau}} - e^{\frac{-2t_0}{\tau}}\right) + 2\frac{\tau t_0}{T_{smp}}\left(e^{2\frac{T_{smp}-t_0}{\tau}} - e^{2\frac{2T_{smp}-t_0}{\tau}}\right) - \frac{2{t_0}^2}{T_{smp}}\left(e^{\frac{-2t_0}{\tau}} + e^{2\frac{T_{smp}-t_0}{\tau}}\right)\right.$$
$$\left. +2t_0\left(3e^{2\frac{T_{smp}-t_0}{\tau}} - e^{\frac{-2t_0}{\tau}}\right) - 4T_{smp}e^{2\frac{T_{smp}-t_0}{\tau}} + \frac{{t_0}^2\tau}{{T_{smp}}^2}\left(e^{\frac{-2t_0}{\tau}} - e^{-2\frac{T_{smp}+t_0}{\tau}} - e^{2\frac{T_{smp}-t_0}{\tau}} + e^{2\frac{2T_{smp}-t_0}{\tau}}\right)\right) \tag{2.67}$$

for the serial and parallel noise input sources, respectively. The factor $\left(\sigma_{SHP}\right)/A$ can be recognized as the inverse of SNR. The impact of the deconvolution processing on time reconstruction performance as a function of t_0 for various SNR is shown in Figure 2.30a.

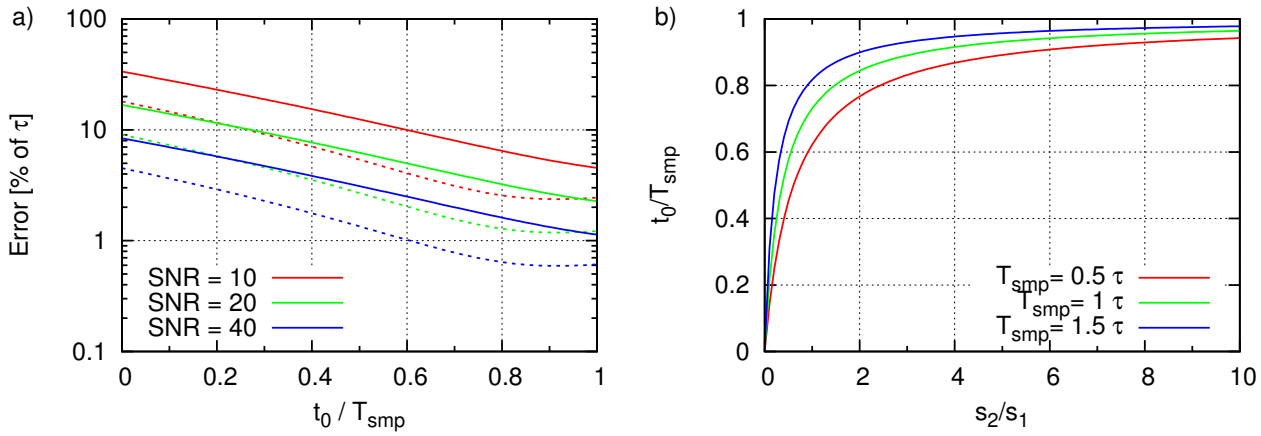

Figure 2.30: a) Time reconstruction error as a function of event appearance time t_0 for various SNR, obtained for serial (solid lines) and parallel (dashed lines) noise components. b) Reconstructed time to sampling time ratio as a function of non-zero samples ratio for various sampling times.

The time reconstruction error is not a uniform function of t_0. For small values of t_0, the s_2 to s_1 ratio is also small (Figure 2.24). This has an impact on the time $t_0(s_2/s_1)$ reconstruction from formula (2.45). The $t_0(s_2/s_1)$ is shown in Figure 2.30b; one can see that for small values of s_2/s_1 the t_0 dependence is steep, which implicates higher uncertainty.

To estimate the average time measurement error in asynchronous system (with flat distribution of t_0), formulas (2.66) and (2.67) can be integrated over the whole possible range:

$$\sigma_t^2 = \frac{1}{T_{smp}} \int_0^{T_{smp}} \sigma_{t_0}^2(t_0) dt_0 \ . \tag{2.68}$$

After calculation the final results can be obtained as:

$$(\sigma_t^s)^2 = \frac{\tau^2 \left(\sigma_{SHP}^s\right)^2}{4e^2A^2} e^{\frac{-4T_{smp}}{\tau}} \left(8\left(e^{\frac{6T_{smp}}{\tau}} - e^{\frac{2T_{smp}}{\tau}} \right) + \frac{\tau^3}{{T_{smp}}^3} \left(1 - 2e^{\frac{2T_{smp}}{\tau}} + 2e^{\frac{4T_{smp}}{\tau}} - 2e^{\frac{6T_{smp}}{\tau}} + e^{\frac{8T_{smp}}{\tau}} \right) \right.$$
$$\left. + 2\frac{\tau}{T_{smp}} \left(1 - 3e^{\frac{2T_{smp}}{\tau}} - 3e^{\frac{6T_{smp}}{\tau}} + e^{\frac{8T_{smp}}{\tau}} \right) + \frac{2\tau^2}{T_{smp}^2} \left(1 - 2e^{\frac{2T_{smp}}{\tau}} + 2e^{\frac{6T_{smp}}{\tau}} - e^{\frac{8T_{smp}}{\tau}} \right) \right) \tag{2.69}$$

and

$$(\sigma_t^p)^2 = \frac{\tau^2 \left(\sigma_{SHP}^s\right)^2}{4e^2A^2} e^{\frac{-4T_{smp}}{\tau}} \left(8\left(e^{\frac{2T_{smp}}{\tau}} - e^{\frac{6T_{smp}}{\tau}} \right) + \frac{\tau^3}{{T_{smp}}^{-3}} \left(1 - 2e^{\frac{2T_{smp}}{\tau}} + 2e^{\frac{4T_{smp}}{\tau}} - 2e^{\frac{6T_{smp}}{\tau}} + e^{\frac{8T_{smp}}{\tau}} \right) \right.$$
$$\left. + \frac{2\tau}{T_{smp}} \left(1 + 3e^{\frac{2T_{smp}}{\tau}} - 4e^{\frac{4T_{smp}}{\tau}} + 3e^{\frac{6T_{smp}}{\tau}} + e^{\frac{8T_{smp}}{\tau}} \right) + \frac{2\tau^2}{{T_{smp}}^2} \left(1 - e^{8\frac{T_{smp}}{\tau}} \right) \right) \tag{2.70}$$

for the serial and parallel noise input sources, respectively. The dependence of the average time measurement error as a function of SNR for various sampling time to shaping time ratios is shown in Figure 2.31a. The obtained time reconstruction error follows $1/SNR$ dependence.

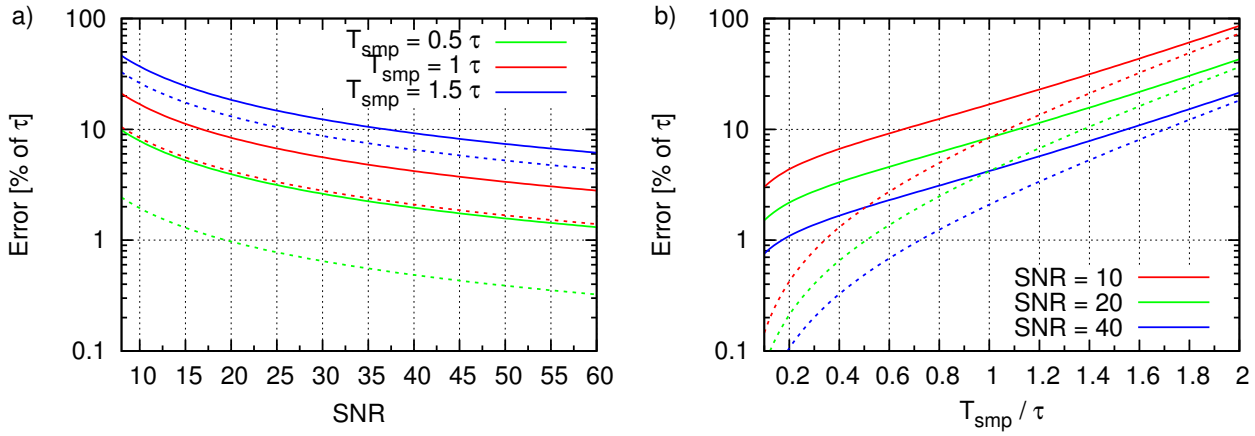

Figure 2.31: a) Time measurement error as a function of SNR for various sampling times. b) Time measurement error as a function of sampling time for various SNR (obtained for the serial (solid lines) and the parallel noise (dashed lines)).

Figure 2.31b shows the expected time reconstruction error as a function of the sampling time to shaping time ratio for various SNRs. Decreasing sampling period (increasing sampling frequency) allows reduction of errors in time measurement; for sampling time going to zero, the error of the time measurement tends to zero. The effect of the parallel noise in the presented formulas is less

pronounced than the serial noise, which is consistent with the results obtained for the amplitude reconstruction.

2.8.8 Impact of quantization noise

So far, all possibilities have been considered using not quantized values of samples. At this point an important question should be raised: what should be the minimum ADC resolution for the amplitude and the time measurement performance not being degraded by the quantization noise. Assuming that the quantization noise is not autocorrelated $cor_q(\Delta t) = \delta(t)$ (which is usually true, especially for random signals [82]), the variance of quantization noise after passing through the deconvolution filter can be calculated according to formula (2.54) as:

$$\left(\sigma^q_{sync}\right)^2 = \frac{2\left(\sigma^q\right)^2}{e^2 {T_{smp}}^2}\left(e^{\frac{-2T_{smp}}{\tau}} + 4 + e^{\frac{2T_{smp}}{\tau}}\right) \tag{2.71}$$

and

$$\left(\sigma^q_{async}\right)^2 = \frac{2\left(\sigma^q\right)^2}{e^2 {T_{smp}}^2}\left(e^{\frac{-2T_{smp}}{\tau}} + 2e^{\frac{-T_{smp}}{\tau}} + 4 - 2e^{\frac{T_{smp}}{\tau}} + e^{\frac{2T_{smp}}{\tau}}\right) \tag{2.72}$$

for synchronous and asynchronous systems, respectively. In the above formulas σ^q represents variance of quantization noise at the input of the deconvolution filter. The variance of quantization noise depends only on the quantization bin size, and in terms of LSB it can be calculated as [82]:

$$\sigma^q = \frac{1}{\sqrt{12}} LSB \ . \tag{2.73}$$

If the signal amplitude is set to A LSB and the SNR is fixed, the noise variance at the shaper output is expressed as $\sigma_{SHP} = \frac{A}{SNR} LSB$. The noise variance at the output of the deconvolution filter for individual components can be calculated using formulas (2.62), (2.63), (2.64), (2.65), (2.71), (2.72). One can calculate the amplitude for which the impact of the noise originating from the preamplifier and the quantization are equal. The dependence of the calculated amplitude as a function of sampling time to shaping time ratio is presented in Figure 2.32a. For the SNR equal 20 and sampling time to shaping time ratios greater than 0.5, the signal amplitude should have at least 6 LSB not to be dominated by quantization noise. According to expectations, for higher SNRs the required signal amplitude is higher in terms of LSB (the quantization needs to be more fine). The cumulative noise normalized to noise without quantization noise as a function of signal amplitude for various SNR is shown in Figure 2.32b. In the case when noise is dominated by serial noise and the SNR equals 20, the amplitude should have at least 15 LSB to decrease quantization noise impact to 10%. The quantization noise is not specific only for processing methods utilizing digital signal processing, it also appears in a conventional dual-chain readout where the stored pulse amplitude is digitalized by the ADC. The effect of quantization of the pulse amplitude is shown in dashed lines in Figure 2.32 as a reference. One can see, that for sampling times greater than half of the shaping time, the effect of deconvolution is negligible. Moreover, for parallel noise (which has a strong autocorrelation), the deconvolution can even reduce the requirements for the ADC.

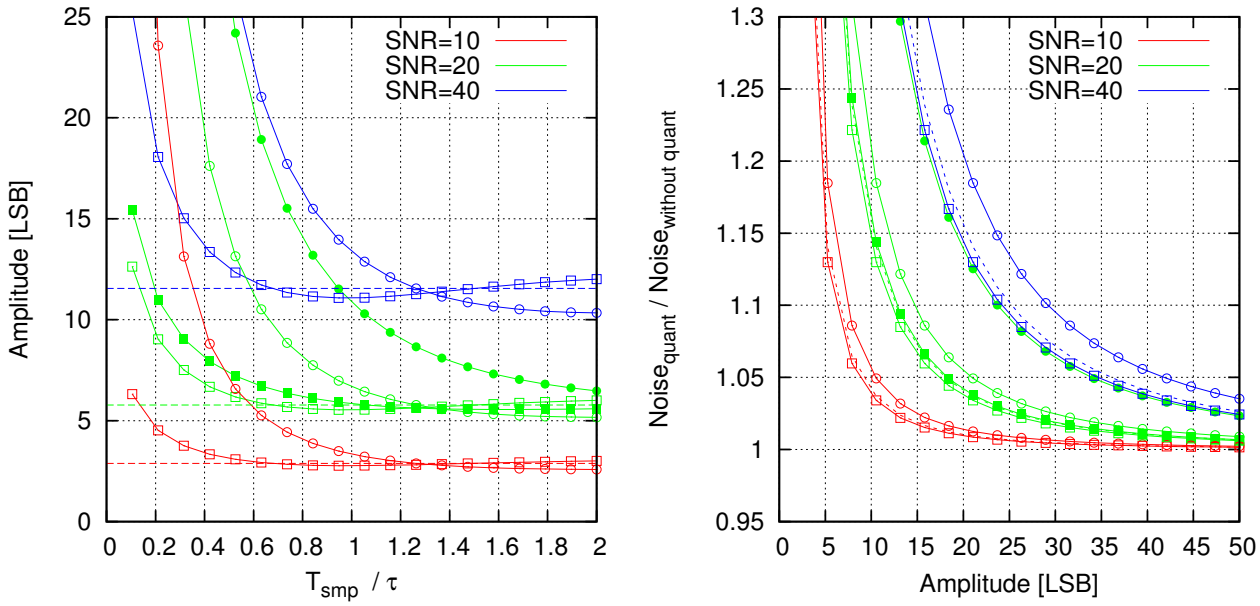

Figure 2.32: a) Signal amplitude for which contributions from the preamplifier noise and quantization noise are equal. b) Cumulative noise normalized to noise without quantization noise ($T_{smp} = \tau$). Legend: boxes represent dependence of serial noise, circles represent dependence of parallel noise, empty symbols are for asynchronous sampling, filled symbols are for synchronous sampling, dashed lines represent effect of the amplitude quantization without any DSP.

Similar calculations can be performed to estimate the impact of quantization noise on time reconstruction performance. The quantization noise translates to time measurement error according to:

$$\left(\sigma_t^q\right)^2 = \frac{\tau^2(\sigma^q)^2}{4e^2A^2} e^{\frac{-4T_{smp}}{\tau}} \left[\frac{2\tau^2}{{T_{smp}}^2}\left(1 + e^{8\frac{T_{smp}}{\tau}} + 2e^{6\frac{T_{smp}}{\tau}} + 2e^{2\frac{T_{smp}}{\tau}} - 2e^{4\frac{T_{smp}}{\tau}}\right) - \frac{2\tau}{T_{smp}}\left(1 - e^{8\frac{T_{smp}}{\tau}} - 4e^{6\frac{T_{smp}}{\tau}} + 4e^{2\frac{T_{smp}}{\tau}}\right) - \frac{\tau^3}{{T_{smp}}^3}\left(1 - e^{8\frac{T_{smp}}{\tau}}\right) \right] . \tag{2.74}$$

The signal amplitude for which the contribution to the error in time reconstruction from the preamplifier noise equals to the contribution from the quantization noise is shown in Figure 2.33a as a function of sampling time to shaping time ratio. The cumulative time reconstruction error normalized to error without quantization noise as a function of signal amplitude for various SNR is shown in Figure 2.33b. The obtained dependence is similar to the one of the amplitude reconstruction error; however, the required amplitudes are slightly higher for corresponding parameters. The presented analysis are valid only in the case when the distribution of the quantization error is flat and so the frequency spectrum is white. This requirement should be fulfilled for amplitude of pulse higher than several LSB, while for the smaller amplitudes the obtained results may be underestimated.

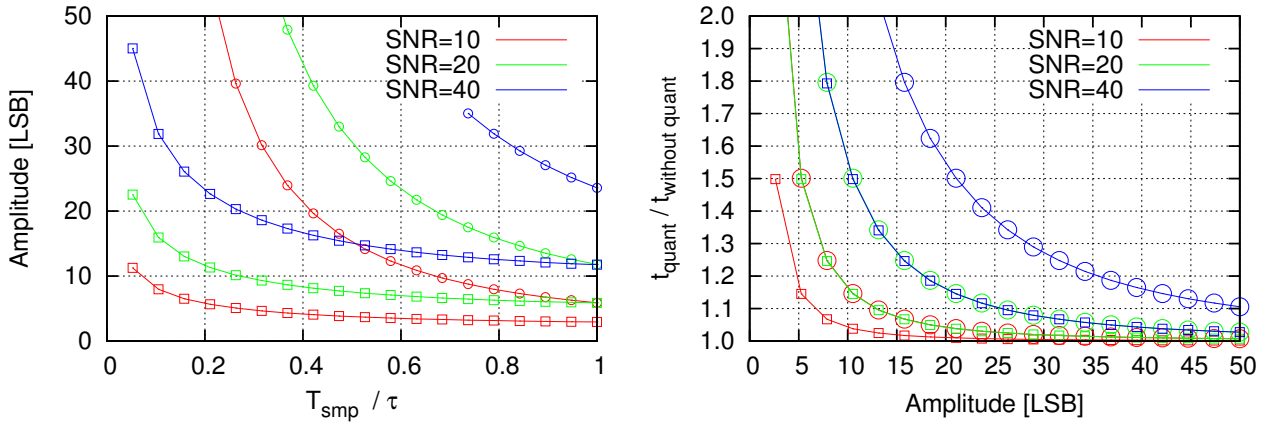

Figure 2.33: a) Signal amplitude for which the contribution to the time reconstruction error from the preamplifier noise equals to the contribution from quantization noise. b) Cumulative time reconstruction error normalized to error without quantization noise ($T_{smp} = \tau$). Legend: boxes represent dependence of serial noise, circles represent dependence of parallel noise.

2.8.9 System level considerations

In previous sections, the signal processing chain based on deconvolution filter was discussed. The performance analysis showed that the deconvolution based readout provides robust methodology for the time and amplitude measurement. Very good pile up rejection capabilities are obtained, especially in the case of oversampling. An example of the amplitude and the time reconstruction

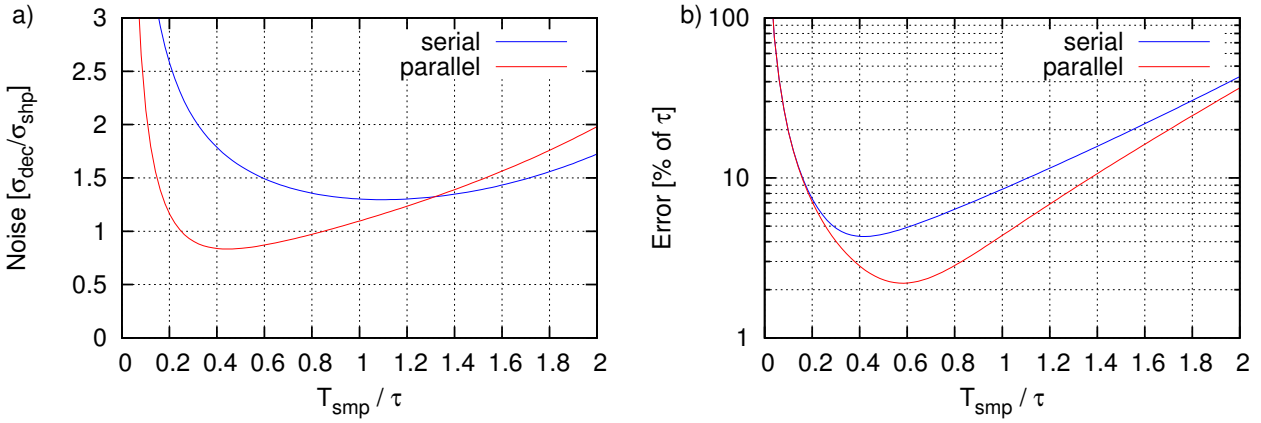

Figure 2.34: a) The effect of the deconvolution processing on the noise performance. b) Time measurement error.

performance for deconvolution algorithm (including quantization effects) applied to the output of preamplifier - CR-RC shaper chain is presented in Figure 2.34. The curves present the expected noise and time reconstruction resolution for serial and parallel noise components. The signal amplitude was set to 20 LSB and the SNR to 20. Depending on the absolute values of serial and parallel noise contributions, the best noise performance is achieved for sampling time to

shaping time ratio from 0.2 up to 1.2. The time resolution down to a few percent of shaping time is expected for sampling time equal to half of the shaping time. Further improvement of time resolution can be made by increasing the ADC resolution.

In the implementation of the deconvolution based algorithm an additional digital block is needed to detect the signal (see discussion in chapter 2.5). For synchronous systems, for which the whole information about the pulse is carried by one sample, an ordinary digital comparator can be used. When a non-zero sample is detected, the time and the amplitude become instantly known. In asynchronous systems, where the information about the pulse occupies two subsequent deconvoluted samples, one should monitor if the sum of two subsequent samples exceeds the preset threshold. When the sum of two samples exceeds the threshold level, the operations of division and summation are performed on them, as described in chapter 2.8.2. The output of these operations is used to estimate the phase and the amplitude using formulas (2.45) and (2.47), respectively. All the post-processing can be done on-line using an arithmetic unit or a Look-Up-Table (LUT). Such a post-processing unit is not necessarily found in each channel, and depending on the expected detector occupancy can be possibly shared between a number of channels. Alternatively, the post-processing can be done off-line during event building on DAQ PC. It has been verified experimentally that the noise count rate dependence on the threshold value follows the expectations from formula (2.30) and so, this formula can be used for the threshold value selection.

Another possible source of error in the time and the amplitude reconstruction is the sampling clock jitter. The sampling clock jitter influences directly the time measurement by adding uncertainty to the time instant when the sample is taken. In addition, the sampling clock jitter disturbs the amplitude measurement by deformation of pulse shape (see chapter 3.3).

In this work an application of deconvolution method to simple CR-RC shaping was considered, and it was justified by very light implementation. There are no arguments against implementation of such a procedure for more complicated signal shapes (e.g. CR-RC^n). It will certainly require a more complex algorithm (more samples to be processed), but the performance needs to be quantitatively verified.

Chapter 3

Components of LumiCal readout chain

Construction of a detector system is a multiphase process. For instance, the Application Specific Integrated Circuit (ASIC) development starts from defining requirements, taking into account the expected experimental conditions. In the next phase the detailed engineering is carried out. During this phase, the ASIC is optimized in order to meet all demanding constrains and requirements. A finished design is an input to a semiconductor factory, which is responsible for production. The delivered prototypes are then a subject of extensive testing, verification and parameterization. Only in the case when the functionality and the performance of all building blocks meet the requirements, further development of the detector module can follow (see chapter 4). The readout chain of each channel of LumiCal detector comprises of a silicon radiation sensor, a fast (60 ns peaking time) front-end [88], and a 10-bit pipeline ADC [89] sampling the signal with 25 MSps rate. In this chapter, the sensor and the ASIC prototypes developed for the LumiCal module are described, together with the measurements results.

3.1 Silicon sensors

The LumiCal geometry was optimized to meet the performance requirements for the luminosity measurement. The sensor plane is segmented into 48 sectors (in the azimuthal angle). In the polar angle, each sector is divided into 64 pads with a constant pitch of 1.8 mm and the gaps between pads of 0.1 mm. The active area extends from 80 mm (inner radius) up to 195.2 mm (outer radius) along the detector radius [90]. Because of the limitation of semiconductor technologies currently available (6-inch wafers), one sensor tail contains only four azimuthal sectors. The layout and the photograph of one tile are shown in Figure 3.1 and Figure 3.2, respectively. The sensor plane has to consist of a number of silicon tiles, as was shown in Figure 1.17b. Due to high energy depositions in the LumiCal (see chapter 1.3.3), standard 320 μm thick silicon sensors were chosen as a compromise between the capacitance and the amount of generated charge. The sensor is made from a N-type silicon, with p^+ pads with a thin aluminum metalization.

The prototypes of LumiCal sensors were designed by IFJ PAN[1], and then manufactured by Hamamatsu Photonics [91]. The prototypes were carefully parametrized by Forward Calorimeter (FCal) collaboration members in three laboratories: IFJ PAN [92], TelAviv University [93] and

[1]Institute of Nuclear Physics PAN, Cracow. More information can be found at http://www.ifj.edu.pl/.

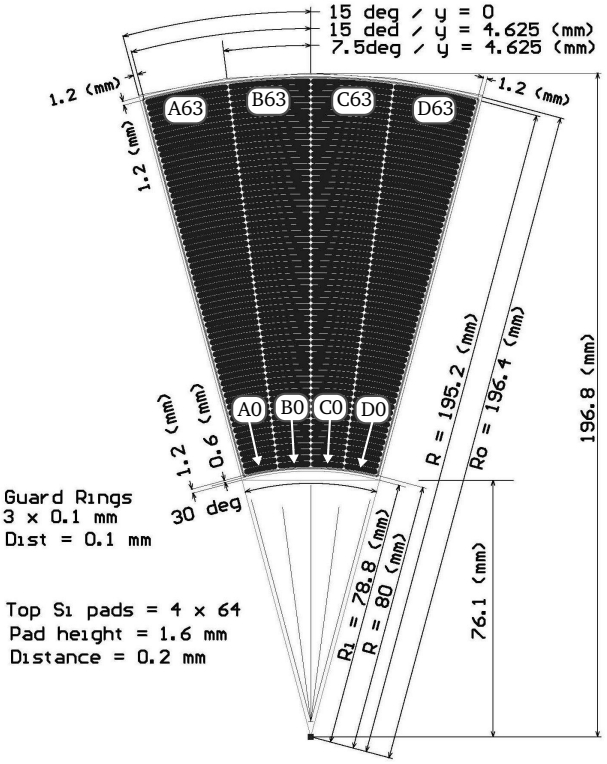

Figure 3.1: Layout of LumiCal sensor tile prototype. The sensor tile is divided in 4 sectors (A, B, C, D), each composed of 64 azimuthal pads (0 . . . 63) [90].

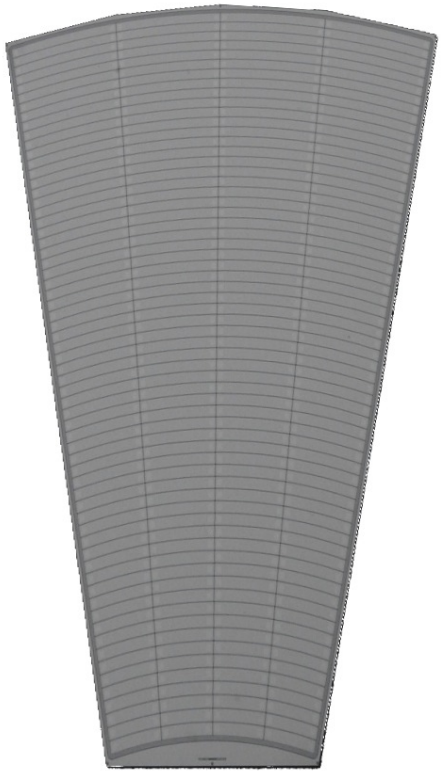

Figure 3.2: Photograph of the LumiCal silicon sensor tile prototype produced by Hamamatsu.

DESY Zeuthen [94]. The results obtained by all mentioned laboratories are in a very good agreement.

All measurements of electrical properties of the sensor were performed on the probe station in a *black box*. The *black box* guarantees separation from an incident light and it screened the device from ElectroMagnetic Interference (EMI). Figure 3.3a shows a typical dependence of a sensor capacitance on bias voltage (C-V curves) for different pads, taken with a Hewlett-Packard LCR-meter. The capacitance value as a function of pad number, obtained at 200 V bias voltage, is shown in Figure 3.3b. The measured capacitance remains on the level between 6 pF (for the smallest pads at the inner radius) and 20 pF (for the biggest pads at the outer radius). The C-V curves can be used to estimate a donor concentration and a depletion voltage of the sensor (as described in chapter 2.1). The equation (2.4) can be rewritten as:

$$\frac{1}{C_d^2} = \frac{2}{\epsilon\epsilon_0 q N_d A^2}(V_b + V_{bias}) \,. \tag{3.1}$$

A plot reflecting this relation is shown in Figure 3.3c. A rising part of the curves was used to extract the donor concentration as $10^{12} cm^{-3}$ [93]. The depletion voltage may be evaluated from $1/C^2$ curve as a point where the linear fit to the rising part crosses the value obtained for plateau (shown for B0 pad). The full depletion voltage was found to be in a range 35-50 V for all sensor pads [93].

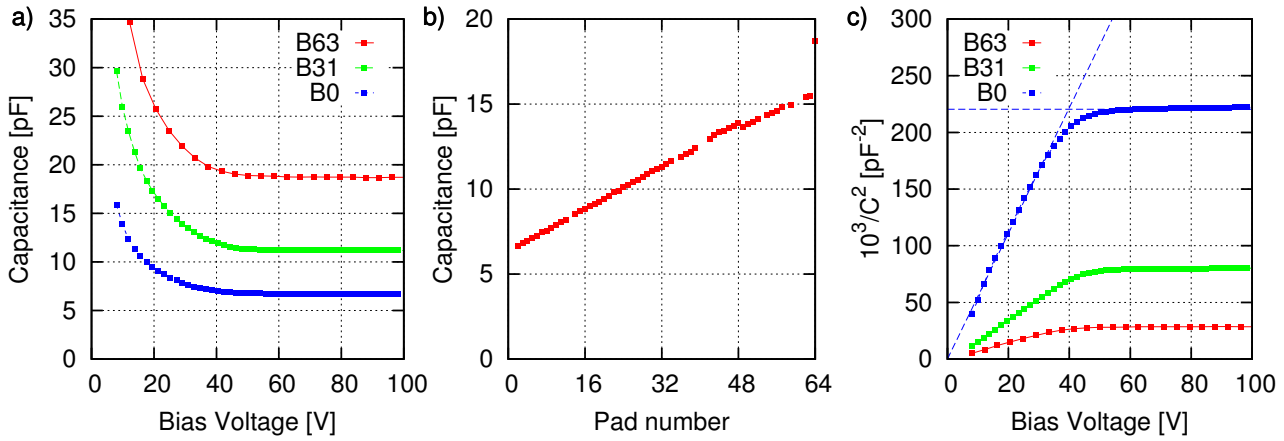

Figure 3.3: a) Sensor capacitance as a function of bias voltage. b) Pad capacitance as a function of pad number obtained for bias voltage of 200 V. c) Inverse capacitance squared as a function of bias voltage [93].

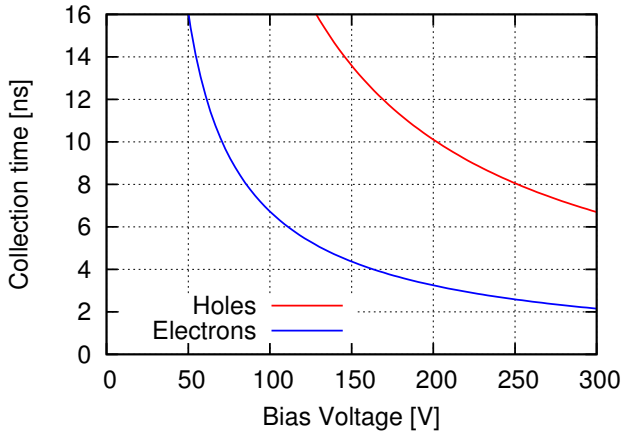

Figure 3.4: The calculated electron and holes collection times as a function of bias voltage for LumiCal sensor.

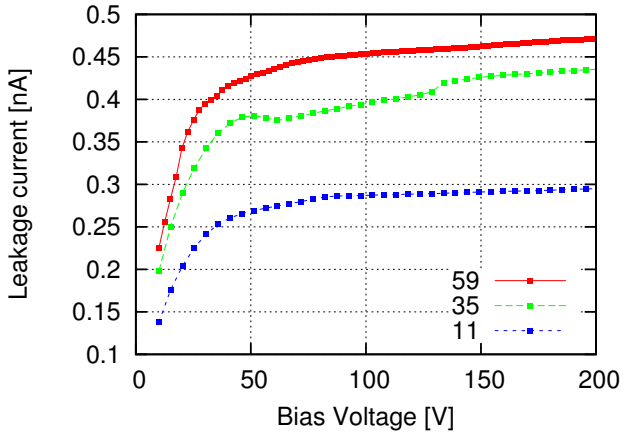

Figure 3.5: The leakage current of various LumiCal sensor pads as a function of bias voltage [93].

The approximate charge collection time for electrons and holes can be estimated for an extracted V_{dep} according to formulas (2.6) and (2.7), respectively. The obtained charge collection times as a function of the sensor bias voltage are shown in Figure 3.4. For voltages above 100 V, the electrons collection time stays below 6 ns, and can be neglected with respect to the shaping time constants in further processing chain.

The leakage current of several sensor pads as a function of the bias voltage obtained at the temperature of 17° C is shown in Figure 3.5. The current-temperature dependence was found to be almost 0.1 $nA/°C$, which significantly influenced the measurements taken in the environment without precise temperature stabilizing circuitry. Nevertheless, single pad's current remains below 1.5 nA for temperatures up to 26° C and bias voltages below 500 V [93].

3.2 Front-end ASIC

3.2.1 Front-end design

The chosen front-end architecture comprises of a charge sensitive amplifier, a Pole-Zero Cancellation (PZC) circuit and a shaper, as shown in Figure 3.6. In order to cope with large charges in the

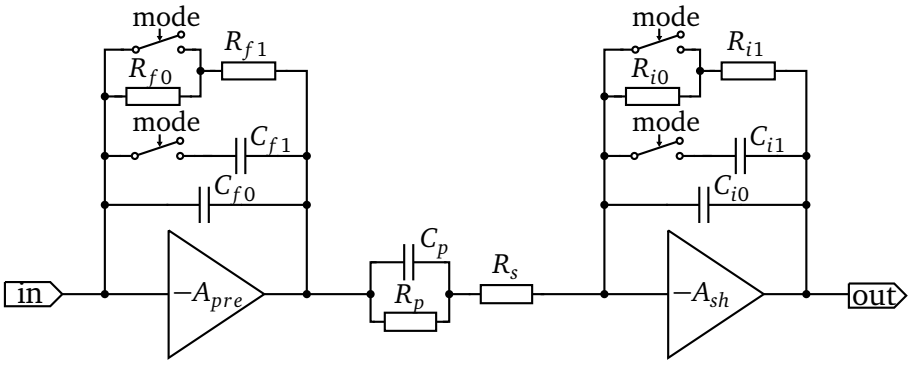

Figure 3.6: Block diagram of front-end ASIC channel.

physics mode and small ones in the calibration mode, a variable gain in both the charge amplifier and the shaper is applied. The *mode* switch in Figure 3.6 changes the effective values of the feedback circuit components R_f, C_f, R_i, C_i and therefore the transimpedance gain of the front-end ASIC is changed. The low gain (large C_f) is used for the physics mode when the front-end processes signals from large charge depositions in the sensor, while the high gain (small C_f) is used in the calibration mode when a MIP sensitivity is needed. Assuming high enough open loop gain of the preamplifier (A_{pre}) and the shaper amplifier (A_{sh}), the transfer function of this circuit is given by:

$$\frac{U_{out}(s)}{I_{in}(s)} = \frac{1}{C_f C_i R_s} \cdot \frac{s + 1/C_p R_p}{s + 1/C_f R_f} \cdot \frac{1}{(s + 1/C_i R_i)(s + 1/C_p(R_p||R_s))} \ . \tag{3.2}$$

By a proper setting of the PZC parameters ($C_f R_f = C_p R_p$) and achievement of equal shaping time constants ($C_i R_i = C_p(R_p||R_s)$), one obtains a first order shaping, equivalent to a CR–RC filter, with a peaking time $T_{peak} = C_i R_i$. Simple first order shaping is chosen as a trade-off between the noise and the power dissipation. To fulfill the timing requests regarding the pulse length, the peaking time of about 60 *ns* is chosen. Regarding the noise, the main requirement is to obtain in the calibration mode the signal to noise ratio of about 10 even for the largest sensor capacitances (which according to the old specification might be as high as 100 pF). Both of the amplifying stages (A_{pre}, A_{sh}) are designed as folded cascodes [95] with active loads, followed by source followers.

In the prototype ASIC 8 channels are implemented [88]. Four channels have been designed with passive feedback and PZC resistances R_f,R_p while the other four channels use MOS transistors in a triode region to perform this task [96]. The maximum value of passive resistance ($R_{f0} + R_{f1}$ in the calibration mode) is 1.5 MΩ, while the resistance of MOS transistors is externally controlled and may reach much higher values. In the motivation for active feedback

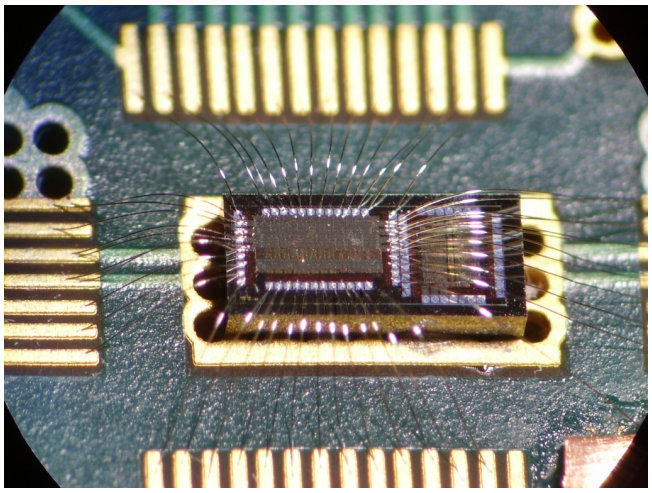

Figure 3.7: Photograph of front-end ASIC comprising of 8 channels bonded on a PCB.

implementation more important than the high resistance is the small parasitic capacitance and the possibility to compare the matching of the PZC network between active and passive solution. The value of calibration mode feedback capacitance (C_{f0}) of 0.5 pF is assigned to channels with passive resistors and 0.23 pF to channels with MOS resistors. The test capacitance (not shown in Figure 3.6) of 0.5 pF is added at the input of each channel and the test inputs are grouped separately for the odd and even channels. This allows testing the ASIC without a sensor by giving the possibility of external charge injection. The area occupied by a single channel is 630μm $\times$ 100μm. The prototype ASICs were fabricated in 0.35 μm, four–metal, two–poly CMOS technology. The photograph of bonded front-end ASIC is shown in Figure 3.7.

3.2.2 Front-end measurement results

Three prototype ASICs were bonded on the dedicated Printed Circuit Board (PCB) boards to test the front-end functionality and to measure their electrical parameters. Figure 3.8 shows the response of the front-end channel to charge injected through the input test capacitance, measured for different values of the input capacitance C_{det}. The sensor capacitance is simulated with an external capacitor. For the physics mode the results obtained for active (MOS) and passive (R_f) feedback are exactly the same and therefore only the active feedback curves are shown on the plot. It can be noticed that both, the amplitude and the peaking time ($\sim$ 60 ns), are insensitive to the value of the input capacitance in this case. In the calibration mode the amplitude and the peaking time depend on the input capacitance (C_{det}). This dependence is more pronounced for the active feedback case. This can be explained, keeping in mind that in the calibration mode the preamplifier's feedback capacitance C_f is small ($\sim$ 230 fF for MOS, $\sim$ 500 fF for R_f) and so the ratio of C_d to the effective input capacitance $A_{pre}C_{f0}$ is not negligible for the preamplifier gain of about 2000 and the input capacitance reaching 100 pF. In such a case, a fraction of the input charge is lost on the sensor capacitance and the preamplifier cannot be considered as purely charge sensitive, since C_{det} affects its transfer function. In the physics mode, where the feedback capacitance is large ($\sim$ 10 pF), the preamplifier can be considered as an ideal charge sensitive one and so no amplitude sensitivity on the input capacitance is seen. The described measurements

are in good agreement with Hspice simulations performed for both types of feedback resistors and both gain modes.

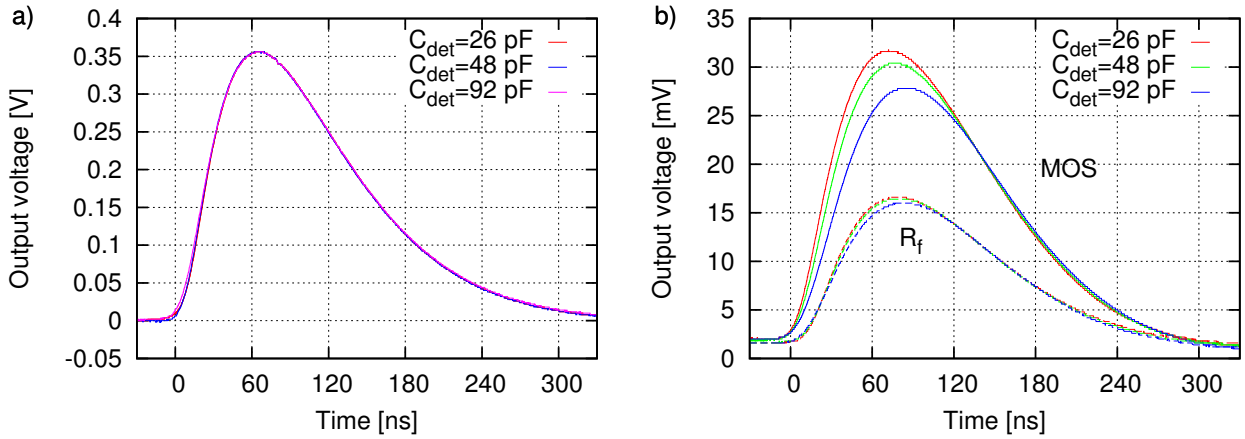

Figure 3.8: Output pulses of front-end electronics channels for various input capacitances. a) Physics mode, active feedback type ($Q_{in} = 3.3$ pC). b) Calibration mode, active (MOS) and passive (R_f) resistor feedback type ($Q_{in} = 10$ fC).

The output noise was measured using the HP3400 true RMS meter. The ENC, as a function of input capacitance is shown in Figure 3.9. The results obtained for the physics and calibration modes are shown on the same plot. Since the bandwidth of HP3400 is only about 10 MHz the numbers may be underestimated by about 20%. The measured ENC as a function of C_{det} are in agreement with simulations. In particular, in the calibration mode the SNR of 10 for the MIP is maintained for input capacitances up to about 100 pF. For the sensor geometry described in chapter 3.1, for which the sensor capacitance stays below 20 pF, the SNR for the MIP should approach 30.

In order to test the effectiveness of the PZC circuit, the front-end response was measured as a function of the rate of input pulses. To avoid input charges of both polarities, when using a square-wave test signal, the staircase test waveforms are synthesized using the Tektronix AWG2021 waveform generator. It was found that the change in amplitude reaches 2% for input rates of about 3 MHz and is quite insensitive to the input capacitance.

To estimate the crosstalk between the channels, a dedicated setup with a simple general purpose PIN diode (connected to one front-end channel) used as sensor and a laser charge injection was prepared. Using physical signals generated by light pulses in the diode allows one to exclude the possibility of additional crosstalk through the parasitic capacitances on the PCB. Such crosstalk could appear in the case of electrical charge injection through test capacitance. In the calibration mode a relatively low crosstalk is observed which is below 0.1% for the front-end with the active feedback and below 0.3% for the passive feedback. A slightly higher level in the latter case may be well explained by the large parasitic capacitance of the feedback resistance (1.5 MΩ), which occupies much larger area than the MOS transistor. Significantly higher crosstalk is observed for both front-end types in the physics mode. In case of the active feedback almost 1% crosstalk is measured while for the passive feedback it is about 1.5%. It seems that the large crosstalk can be explained by the influence of parasitic capacitance associated with the very large feedback capacitor of 10 pF.

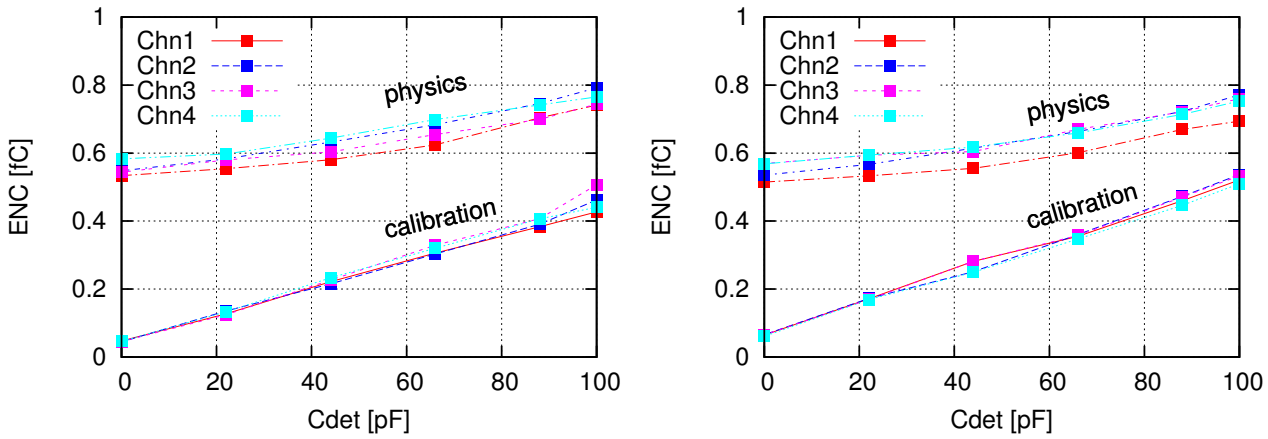

Figure 3.9: ENC measurements obtained with true RMS meter for the front-end with a) passive feedback and b) active feedback.

The power consumption of about 8.9 mW/channel is measured in accordance with the expectations from simulations. The relatively high power consumption is mainly driven by the rather old technology and the requirement of the low noise operation for very large sensor capacitances which was included in the initial specification, but can be reduced in the future. One has to remember that the average power dissipation can be significantly reduced if the power switching off between bunch trains is applied (see chapter 1.2.5). The beam train duration to beam pause ratio is around 1/200 for the ILC and even less for the CLIC. The possibility of applying power pulsing for the front-end ASIC is further investigated in chapter 4.

3.3 Analog to digital converter

3.3.1 ADC design

The LumiCal detector simulations showed that for a correct reconstruction of electromagnetic showers, Analog-to-Digital Converter (ADC) should have around 10 bits in resolution [97]. As a compromise between the speed, the area and the power consumption, the ADC was designed using the pipeline architecture (see chapter 2.4). A 1.5-bit per stage architecture is chosen because of its simplicity and immunity to the offsets in the comparator and amplifier circuits. Each channel consists of an input sample and hold circuit followed by 9 pipeline stages and digital correction circuitry.

Development of dedicated multichannel ADC has been carried out in several iterations. In the first phase the Multiplying DAC (MDAC) core was developed [98], then the full channel was assembled [89, 99]. Based on the collected experience and knowledge, a multichannel ASIC was integrated [100]. The multichannel digitizer ASIC contains 8 ADC cores, a digital serializer, a fast Low-Voltage Differential Signaling (LVDS) I/O interface, a bandgap voltage reference, a Proportional To Absolute Temperature (PTAT) sensor [101], a set of built-in biasing DACs, and a digital control unit (Figure 3.10). The flexible digital serializer has three modes of operation. In the partial serialization mode, data from one channel (10 bits) are sent to one output (8 outputs

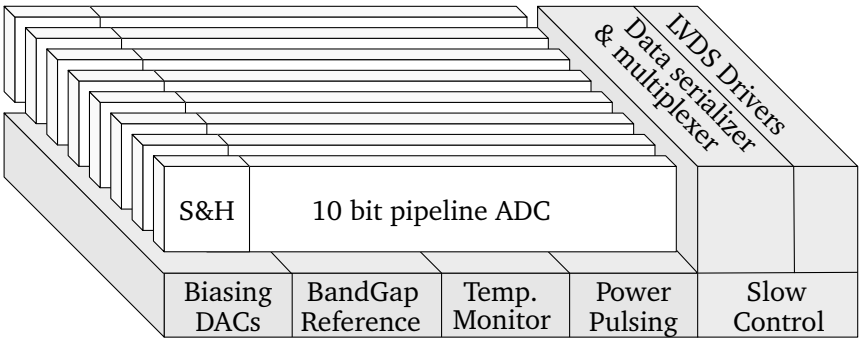

Figure 3.10: Block diagram of multichannel ADC comprising of 8 fully differential pipeline ADC cores and all peripherals.

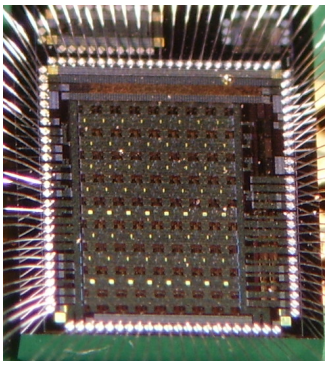

Figure 3.11: Micrograph of prototype ADC ASIC.

per ASIC). In the full serialization mode, data from 8 channels are serialized to one output. In the test mode, only one ADC core operates and each bit is sent to a separate output (10 output signals). The last mode is foreseen only for the test and debug purposes. In addition, the power switching off feature is implemented. More details about the ADC design can be found in references [98, 89, 99, 100].

All prototype ASICs were fabricated in 0.35 μm, four-metal two-poly CMOS technology. A micrograph of the multichannel ADC prototype, glued and bonded on PCB is shown in Figure 3.11. The active size of the ASIC is 3.17 $mm \times 2.59\ mm$. Eight ADC channels are placed in parallel with 200 μm pitch and are followed by the serializer and LVDS pads, while the analog and digital peripheral circuits are on the ASIC sides.

3.3.2 Test setup

In order to verify the ADC operation and measure its performance, a dedicated test setup, addressing specific features of the ASIC, is needed. To reduce the development time and ensure maximum flexibility, a setup utilizing Field-Programmable Gate Array (FPGA) technology was proposed and designed. A schematic diagram of the test setup is shown in Figure 3.12.

The Virtex-5® FXT Evaluation Kit provided by AVNET® is taken as a base. The kit includes the Virtex-5 XC5VFX30T Xilinx FPGA as the main logic unit [102]. In addition, the board provides a set of required peripherals, like: Ethernet PHYsical layer driver (PHY), flash memory, Input/Output (IO) ports and Double Data Rate (DDR) Synchronous Dynamic Random-Access Memory (SDRAM). A number of fast IO signals in various electric standards are available on a Samtec QTE high speed connector. A dedicated PCB featuring the Device Under Test (DUT) ASIC and the required supporting circuits, is designed as a mezzanine board, being plugged into FXT Evaluation Kit. A special attention needed to be paid during the PCB design. High speed differential signals were carefully routed on the PCB to match their impedances to the impedances of the receiver's inputs. In addition, track lengths were strictly controlled to ensure that all signals have the same delay. The requirement for alignment of clock signal with respect to data lines can be slightly relaxed, because of the Dynamic Phase Alignment (DPA) technique implemented in the FPGA. The clock signals with frequency lower than 120 MHz are generated

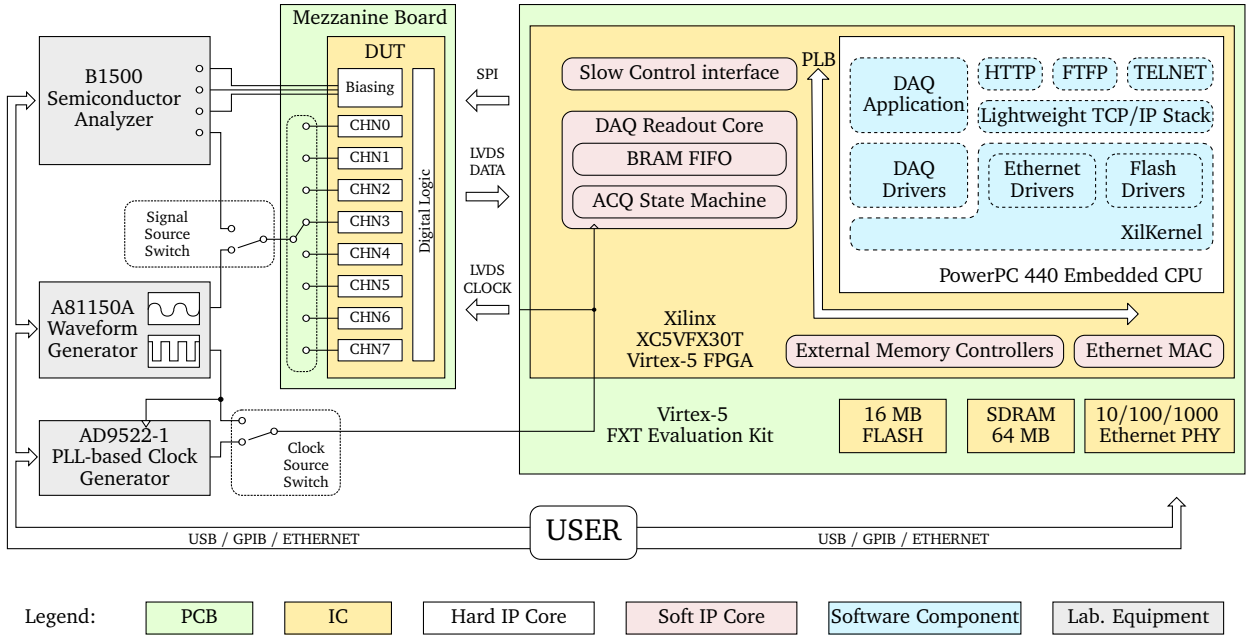

Figure 3.12: Schematic diagram of the multichannel ADC test setup.

directly by the Agilent A81150A Arbitrary Waveform Generator. To generate higher frequencies the AD9522-1 Integrated Circuit (IC) is used. The AD9522-1 provides a clock with frequency up to 800 MHz and subpicosecond jitter performance. The IC has an on-chip Phase Locked Loop (PLL) and a Voltage-Controlled Oscillator (VCO), which can be tuned from 2.27 GHz to 2.65 GHz. The output clock can be provided in LVDS standard (up to 800 MHz) or in CMOS standard (up to 250 MHz). The input signal for the tested ADC channel is provided by the Agilent B1500 Semiconductor Analyzer and the Agilent A81150A Arbitrary Waveform Generator, for static and dynamic measurements, respectively. The selection of ADC channel to be measured is done using on board *Signal Source Switch*. To allow operation with single-ended signal sources, a single-ended to differential converter based on THS4503, low distortion differential operational amplifier, is mounted on a DUT board. The utilization of the same device for the clock and the input signal generations ensures a constant ratio between theirs frequencies, even in a presence of long-term temperature drifts of the local oscillator. It is a highly desirable behavior, especially for the Fast Fourier Transfom (FFT)-based dynamic measurements. The remaining channels of B1500 device are used to provide precise voltage references and supply voltages for the DUT. The utilization of B1500 allows one to precisely set and monitor the DUT operating conditions.

To make the setup more flexible and scalable, the embedded PowerPC processor, running at 100 MHz and available on Virtex5 XC5VFX30T FPGA, is used. The dedicated peripherals, implemented as soft IP cores, are employed to preset the ADC configuration registers and to acquire the data. The peripheral cores are written in Verilog Hardware Description Language (HDL). The *Slow Control interface* peripheral writes the configuration words to the ADC ASIC over the Serial Peripheral Interface (SPI)-like bus. The *DAQ Readout* peripheral core is responsible for sampling the ADC digital data lines and saving them to an internal Block RAM (BRAM) First In, First Out (FIFO). Besides acting as a storage, the FIFO is used to pass the data between asyn-

chronous clock domains: the ADC sampling clock and the PowerPC system clock [103]. Such an architecture, with well defined IP cores, simplifies development as well as further maintenance. In addition, the blocks can be more easily migrated to the other platforms. The FPGA firmware has been developed and simulated using the ISE toolchain provided by Xilinx. The generated bit stream required to configure the FPGA logic resources is stored on the 28F128P30, 16 MB parallel flash connected to the FPGA over Byte Peripheral Interface (BPI).

Two dedicated applications have been developed to manage the whole data acquisition process. The first application works on the PowerPC. The main task of this application is to provide the remote access interface to hardware peripherals. The XilKernel is used as a Real Time Operating System (RTOS) providing a Portable Operating System Interface for Unix (POSIX) compliant layer [104]. A lightweight TCP/IP Stack (lwIP)[2] is utilized to manage network communication at a socket level. The application utilizes POSIX compatible calls in order to ensure high portability [105]. A number of lightweight services, running in separate threads, were developed to interact with a user (e.g. http, tftp, telnet). A first-level bootloader, stored directly in the FPGA BRAM, is responsible for loading the kernel and the application to the DDR SDRAM. Once the system is properly initialized, the PowerPC application waits for the remote commands.

The second application, written in the Python[3] language, runs on supervising Personal Computer (PC). It is responsible for managing the operation of all instruments. The communication with the instruments is carried by the Ethernet, the General Purpose Interface Bus (GPIB), and the Universal Serial Bus (USB) connections. Depending on the measurement to be taken, the proper sequence of operations is performed and the measurement results are stored to files.

3.3.3 ADC performance measurements

Static measurements

The static measurements were performed at various sampling frequencies and with the input voltage ramped in the range from -1 V to 1 V. To eliminate noise, the measurements were repeated several thousand times for each input voltage value.

Uniformity of gain and offset

To compare the performance of all ADC channels, the transfer curves shown in Figure 3.13a were measured for the same signal sent to all ADC inputs. As it can be seen, the transfer curves of all channels are practically the same. The gains and the offsets calculated for each channel (for two ASICs, 16 channels) are presented in the histograms shown in Figure 3.13b and 3.13c, respectively. The gain and offset dispersions were estimated to be respectively about 0.2% and 1.5 LSB, confirming the good uniformity of ADC channels.

[2] *lwIP* is a small independent implementation of the TCP/IP protocol suite. More information can be found at http://savannah.nongnu.org/projects/lwip/

[3] Python is a general-purpose, interpreted high-level programming language whose design philosophy emphasizes code readability. Python has a large and comprehensive standard library. More details can be found at http://www.python.org

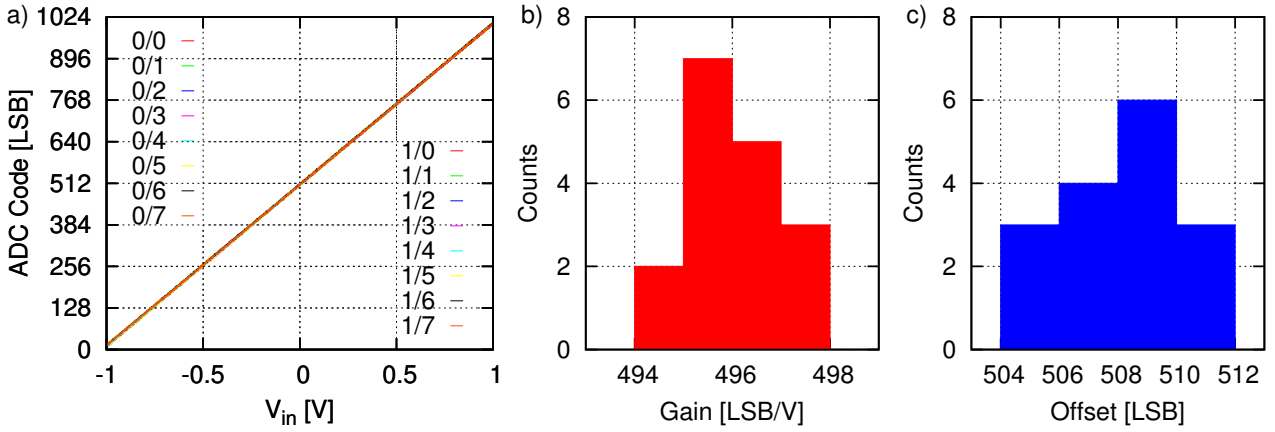

Figure 3.13: a) ADC transfer curves for 2 ASICs (16 ADC channels). Histograms of b) gain and c) offset calculated from transfer curves.

INL & DNL measurements

The ADC static performance is commonly quantified with the Integral Nonlinearity (INL) and the Differential Nonlinearity (DNL) measurements. Both parameters are obtained with the histogramming method [106]. Typical results are shown in Figure 3.14 while the maximum and RMS values of INL and DNL parameters, measured for two prototype ASICs, are presented in Figure 3.15. The worst observed parameters among 16 channels are respectively INL $\leq$0.68 LSB

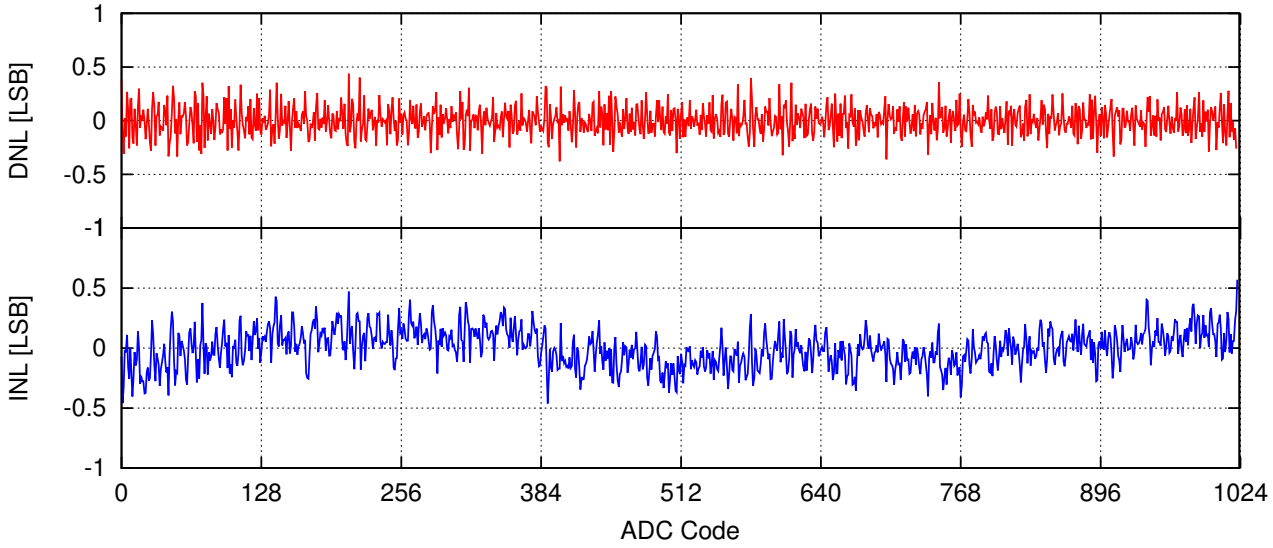

Figure 3.14: Example of INL and DNL measured at 25 MHz sampling frequency and calculated using the histogramming method

and DNL $\leq$0.62 LSB. Their average values are always below 0.2 LSB. The results confirm very good linearity and its uniformity between the channels.

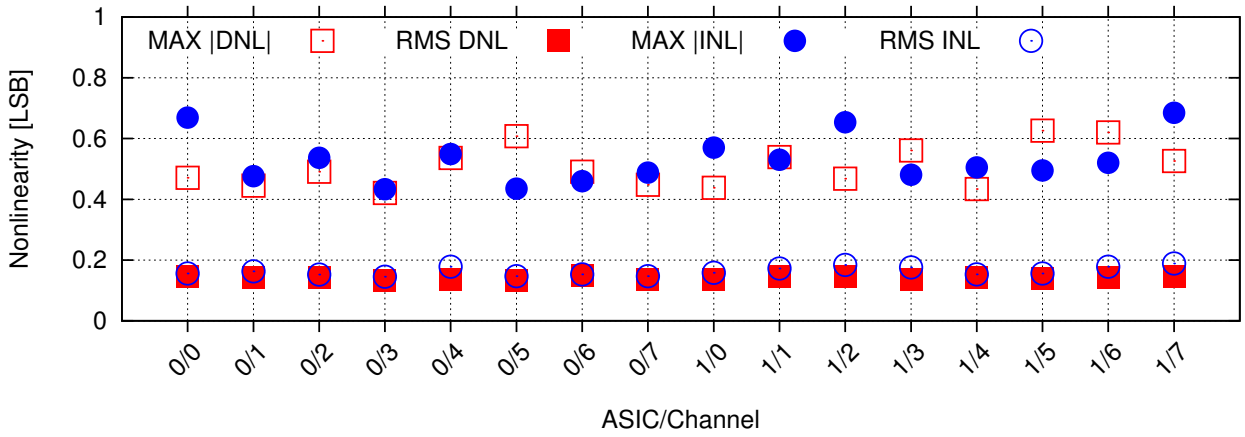

Figure 3.15: Comparison of INL and DNL measured for 2 ASICs (16 ADC channels) at 25 MHz sampling frequency.

Dynamic measurements

For the evaluation of dynamic circuit performance, FFT spectra were calculated from the measurements done with a near full-scale sinusoidal input signal [106]. An example FFT spectrum is shown in Figure 3.16. The standard ADC metrics i.e. the Signal to Non Harmonic Ratio (SNHR),

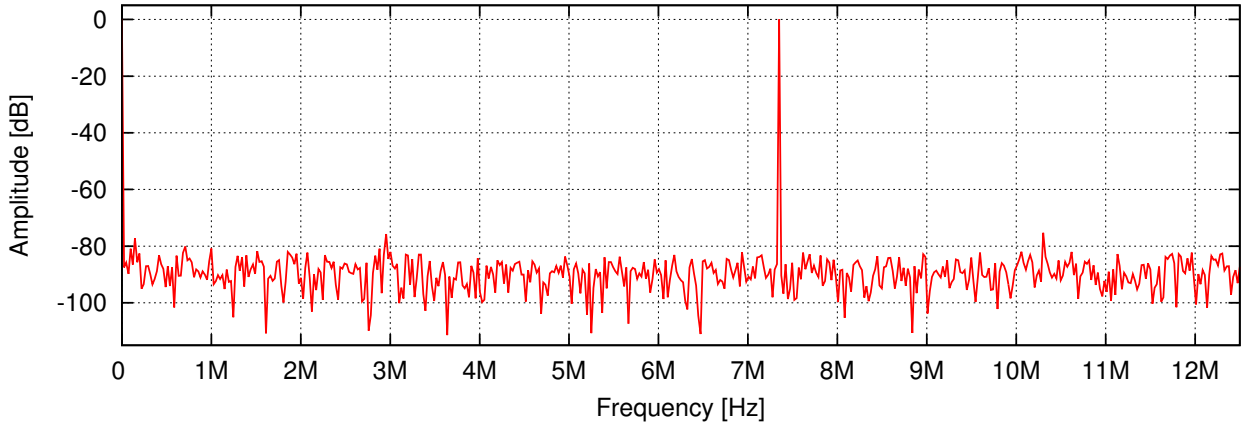

Figure 3.16: Example of FFT spectrum obtained for a near full-scale 7.3 MHz sinusoidal input signal sampled at 25 MSps.

the Total Harmonic Distortion (THD), the Spurious Free Dynamic Range (SFDR) and the Signal to Noise and Distortion Ratio (SINAD), were then calculated from the FFT output [106]. The dependence of dynamic metrics on ADC sampling frequency, measured with the input frequency 1/10 of sampling frequency, is shown in Figure 3.17. It is seen that for sampling frequencies up to about 35 MHz, the ADC performs very well, with SINAD ∼60 dB corresponding to an Effective Number Of Bits (ENOB) of about 9.7 bits. For higher frequencies the effective resolution starts to decrease slowly but the ADC keeps working at least up to 50 MHz, at which point the ENOB is about 9 bits. The measurements, performed in a test mode, showed that the ADC core allows a

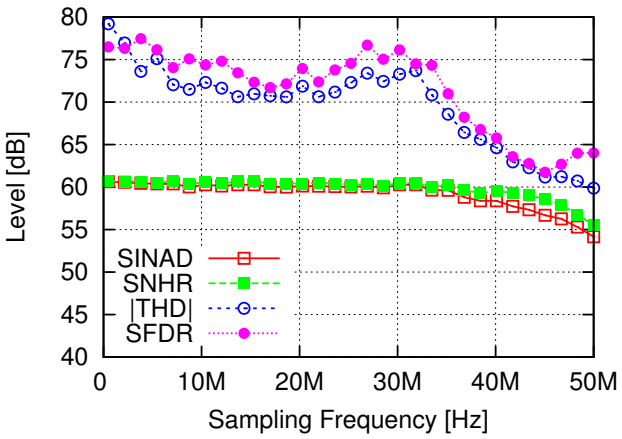

Figure 3.17: ADC dynamic performance as a function of sampling rate obtained with input signal frequency 1/10th of sampling frequency.

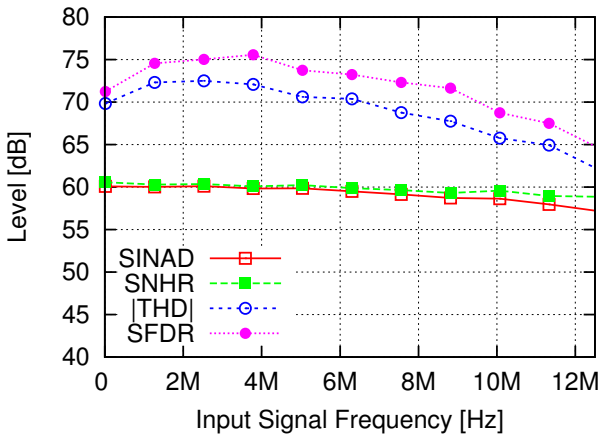

Figure 3.18: ADC performance as a function of input signal frequency at 25 MHz sampling frequency.

significantly faster operation than is possible to obtain in standard multichannel modes using the serializer. To take full advantage of ADC performance, one would need either to add zero suppression or to increase the transmission frequency in the partial serialization mode up to about 500 MHz.

The dependence of dynamic ADC metrics on input signal frequency, measured at a sampling frequency of 25 MHz, is shown in Figure 3.18. A good, almost flat, behavior with SINAD ∼60 dB (ENOB=9.7 bits) is observed up to input frequency of about 5 MHz. Above this frequency the SINAD starts to decrease slowly, reaching 58.5 dB (ENOB=9.4 bits) at 10 MHz. It is not clear whether this decrease of the SINAD should be attributed to the ADC or rather to the signal generator. According to the Agilent 81150A specifications, its harmonics deteriorate about 5 dB going from 2 MHz to 10 MHz, and this is reflected in the measurements.

Uniformity between channels

To verify the uniformity of dynamic parameters between the ADC channels, the measurements of all dynamic metrics were performed for every channel at sampling frequency of 25 MHz. The dynamic metrics obtained for all channels are shown in Figure 3.19. The average SINAD is about 60.3 dB, which corresponds to ENOB of 9.7 bits.

Crosstalk measurements

To study the crosstalk effect, a sinusoidal signal was sent to one of ADC channels, while outputs of all channels were measured. The example results of such a measurement are shown in Figure 3.20 for cases without signal and with signal on channel 3. It can be noticed that even for nearest neighbors the crosstalk signal is attenuated by 80 dB, what practically means that the effect may be neglected.

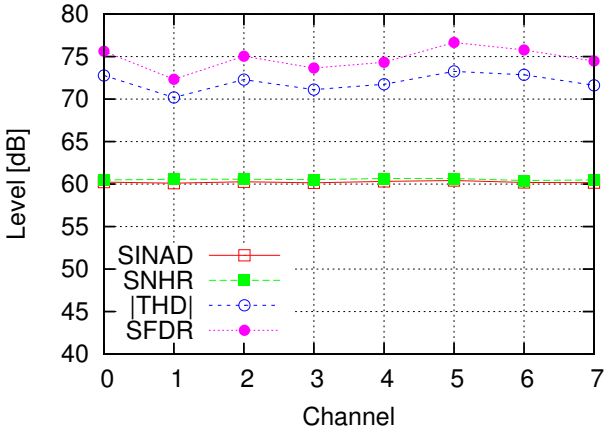

Figure 3.19: Comparison of ADC channels dynamic performance at 25 MHz sampling and 1 MHz input frequency.

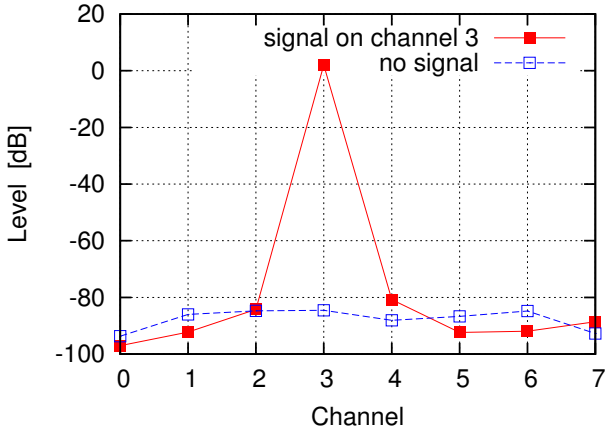

Figure 3.20: Measurement of crosstalk between ADC channels at 25 MHz sampling frequency. Solid curve is obtained for 1 MHz sine signal sent to channel number 3.

Power scaling

The power consumption of ADC core is scaled while simultaneously changing the bias currents in all ADC stages. This is done automatically by changing the setting of the internal exponential 7-bit DAC. To find the optimum bias, for each sampling frequency the minimum bias current guaranteeing the SINAD of at least 59 dB (ENOB=9.5 bits) is chosen. This conditional value is slightly lower than the resolution presented earlier, because during the optimization no particular attention was paid to filtering the ADC input signal, and therefore the obtained resolutions were worse than the actual ones. The measured power consumption of different digitizer blocks versus sampling frequency is shown in Figure 3.21 (top). In the same Figure (bottom) the power consumption normalized to single ADC channel and to 1 MSps sampling rate is shown. The main contribution to power consumption comes from the ADC cores and the serializer, and it scales linearly with sampling rate in the range, from 10 kSps to 25 MSps. The ADC consumes about 0.8 mW/channel/MSps, while the serializer consumes about 0.35 mW/channel/MSps in the partial serialization mode and about 0.85 mW/channel/MSps in the full serialization mode. The normalized total power consumption is about 1.2 mW/channel/MSps in the partial serialization mode and about 2.5 mW/channel/MSps in the full serialization mode.

An important contribution to total power dissipated by the ASIC comes from the LVDS output pads which, depending on the setting of the LVDS control DAC (adjusted accordingly to required transmission rate), may consume from 0.45 mW (∼100 kHz) to 15 mW (∼1 GHz) per pad. During the performed measurements, the power consumption per LVDS pad varied from 0.45 mW to 2.3 mW in the partial serialization mode (10 LVDS pads used) and from 1.6 mW to 2.3 mW in the full serialization mode (3 LVDS pads used). Since in the final ASIC (probably 64 channels) zero suppression will be implemented, the transmission rates, and therefore the power consumption, will be significantly smaller than for the raw data.

To check the possibility of further minimization of power consumption, the ASIC dynamic performance was verified through variation of the supply voltage. It was found that the digitizer

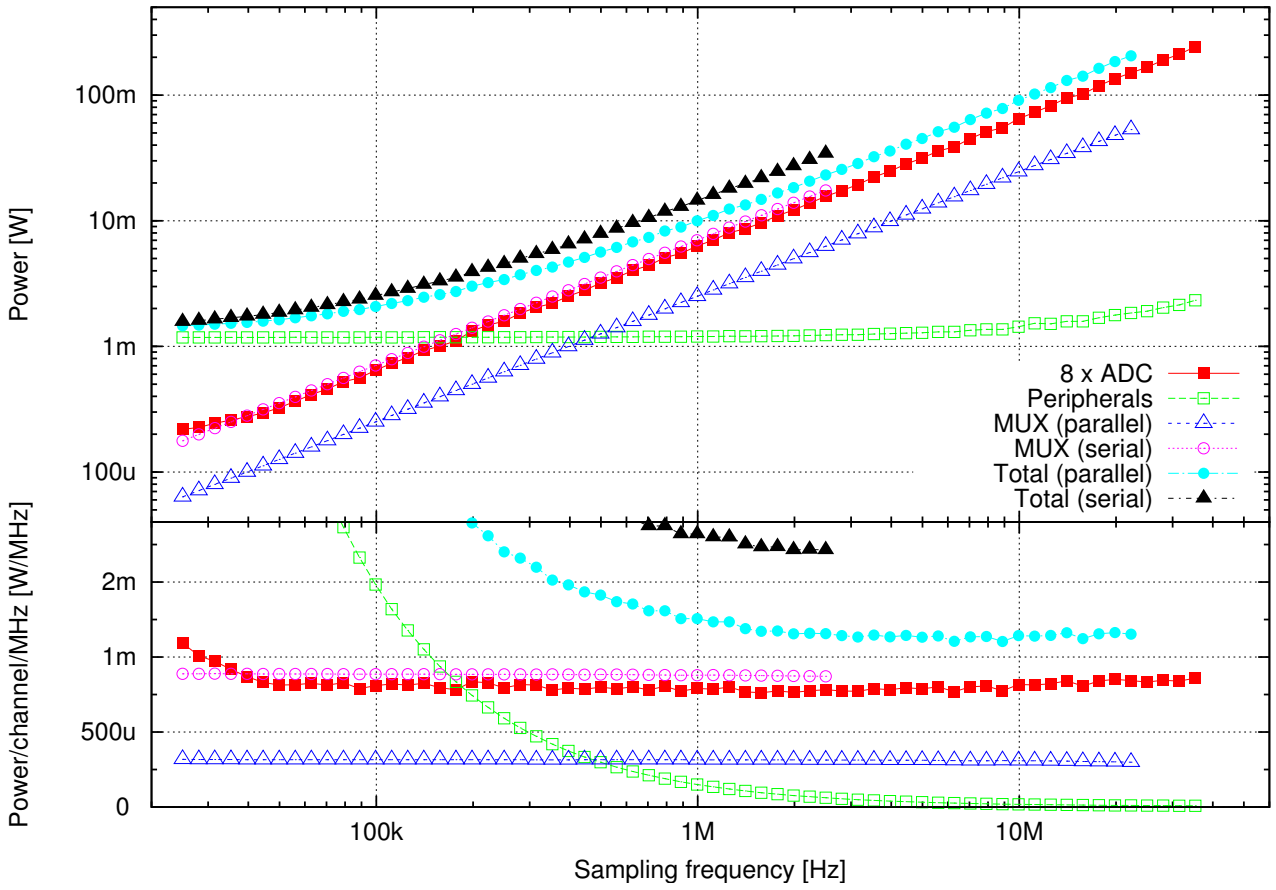

Figure 3.21: Digitizer power scaling. Power consumption (top) and power consumption per channel per MSps (bottom) is presented. The serializer power consumption (MUX) is shown for partial serialization mode (parallel) and full serialization mode (serial).

ASIC works without visible parameter deterioration from 2.5 V up to 3.5 V.

Power pulsing

As it was already pointed out in chapter 1.2.5, a very important feature which helps to limit the power consumption of detector systems in future linear colliders will be the possibility of switching off power during beam pauses. This possibility is explored by measuring the transient times necessary to return to correct ADC operation, after the ADC bias and clock is switched on. It was found that, depending on sampling frequency, between 6 and 10 clock periods are needed to restart the correct data conversion. For the ILC case (sampling period about 300 ns) it would take about 3 μs to return to proper operation, which is a negligible part of the pause (200 ms).

3.4 Performance of deconvolution based readout

A dedicated experimental framework was developed in order to benchmark the deconvolution based readout (described in chapter 2.8) and compare it with theoretical predictions. The frame-

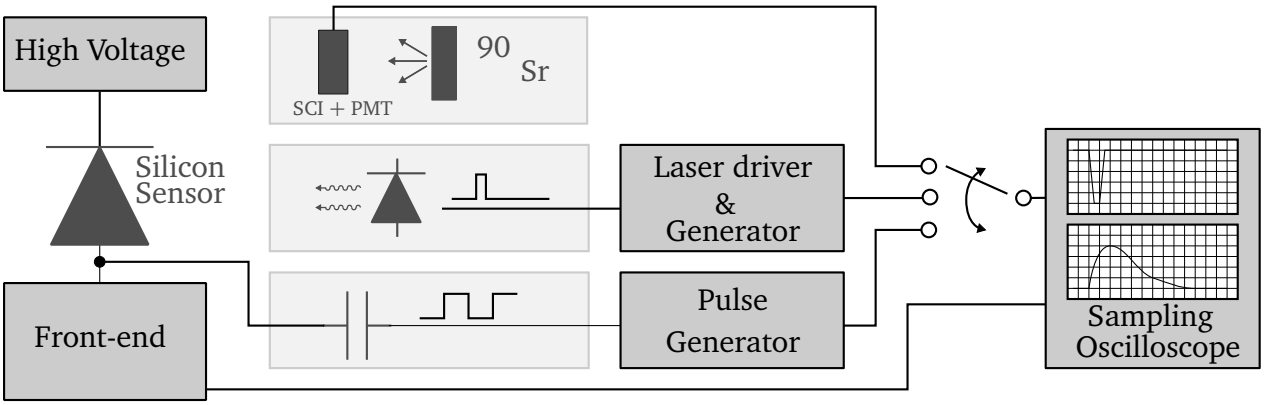

Figure 3.22: Measurement setup diagram.

work can be split to hardware and software parts. The former one allows to collect the data originating from realistic system prototype. The software part is composed of 3 modules: acquisition, MC simulations and data analysis. The acquisition part allows collection of data from the hardware part. The MC simulation module is used to generate pulses with a given shape and noise spectrum. The data analysis part processes the data originating either from the measurements or from the MC simulations. The ROOT framework[4] was used to analyze the collected data. To reduce the data volume, the measurement and the MC results were stored in compressed ROOT files. The analysis programs were written as Python scripts to ensure simple maintenance.

3.4.1 Experimental setup

The schematic diagram of the dedicated experimental setup, designed and built to verify the readout architecture based on the deconvolution algorithm, is shown in Figure 3.22. The detection system contains the silicon sensor followed by the front-end electronics described in sections 3.1 and 3.2, respectively. In the presented measurements only the results for high gain (low C_f), for which the noise effect is the highest, are discussed. The results of the same or better quality were obtained for low gain mode, for which the pulse shape is more ideal (see chapter 3.2.2). The signal from the front-end electronics output is digitalized by the MSO7104B fast digital sampling oscilloscope acting as an ADC. To generate an event, one of three different methods is used. In the first method a voltage step from the pulse generator is sent to the front-end input trough the injection capacitor. The capacitor converts a voltage step into a current pulse. A very precise time reference is available from the pulse generator; however, the whole readout chain is not tested because the sensor is not used. The second method utilizes a radioactive β source as an event generator. The PhotoMulTiplier (PMT) sensing signal from scintillator material is used to produce time reference. In this routine the whole readout chain is tested; however, three major problems exist. First, the time reference is not very precise due to a response jitter of photo

[4]The ROOT is a Data Analysis Framework that provides a set of routines with all the functionality needed to handle and analyze large amounts of data in a very efficient way. More details can be found at http://root.cern.ch.

multipliers. The second problem results from the fact that electrons from the β source have low energy, further decreased by a passage throughout the scintillator material, which entails the fact that fluctuations in the time of flight cannot be neglected. Finally, there is no precise information about the pulse amplitude (deposited energy) which could be used to benchmark the deconvolution algorithms. The most accurate, third method, utilizes a laser diode as a signal source. A very short ($\sim 100\ ps$) infra-red laser pulse with constant amplitude and very precise timing information (provided by a laser driver) is generated in this test routine. This way, the measurements performed with the laser source are considered to be the most precise.

As it was shown in Figure 2.24, the result of deconvolution processing depends on phase difference between the pulse and the sampling clock. Several approaches can be utilized to measure the sensitivity of the deconvolution performance to the phase difference between pulse and sampling clock. The most straightforward method would be to use a pulse generator – as the source of the sampling clock and the source of trigger for the event generator – this would enable fine phase tuning; however, this method is not applicable for measurements with radioactive source. To overcome this limitation, a fast sampling digital oscilloscope with at least two channels can be used. One channel digitalizes the trigger signal, coming from the pulse generator or a photomultiplier, while the second is used to digitalize the front-end output. Taking an advantage of high sampling rate (4 GSps in the described setup) and using an interpolation algorithm on digital samples, the trigger time can be measured with a precision better than 100 ps. In order to study the deconvolution performance versus sampling rate and signal phase, the sampling rate of front-end output is reduced using decimation. The decimation factor M is usually an integer or a rational fraction greater than unity. This factor multiplies the sampling period or, equivalently, divides the sampling rate. In the simplest form, for integer M, the decimation leads to retaining only every M^{th} sample while the other $M-1$ samples are disregarded. The output sample set d (sampled every $M \cdot T_{smp}$) is related with the input samples set v (sampled every T_{smp}) according to:

$$d(i) = v(i \cdot M + t_0)\,, \tag{3.3}$$

where t_0 is the initial sample. By varying t_0 value from 0 to $M-1$, M different waveforms with different phases can be achieved. The schematic diagram of the proposed procedure is shown in Figure 3.23. By using the proposed scheme with 4 GSps (T_{smp}=250 ps) oscilloscope and applying the decimation to obtain 16.6 MSps (60 ns), 240 pulses with different phases are obtained. In truly asynchronous system, no phase value should be predominant, so the phase distribution expressed in time units should have flat distribution from 0 to the sampling period T_{smp}. Because of this fact, the results of all reported measurements will be calculated as an average over all possible phase differences.

Oscilloscope with a very high sampling rate has another great advantage. It enables very precise investigation of the front-end electronics noise spectrum. An example noise spectrum at the output of the front-end chain is presented in Figure 3.24 (in red). The spectrum was obtained with FFT algorithm applied on the digital samples collected. The low frequency part of the spectrum, below 20 MHz, follows qualitatively the dependence expected from the theory (see Figure 2.11b). However, at higher frequencies some disturbances are present. The highest power is present at frequencies, 90 - 100 MHz, occupied by local radio stations. A flat spectrum above 100 MHz is related to quantization noise of the oscilloscope. An example spectrum obtained after decimation by 240, that corresponds to 16.6(6) MHz sampling rate (T_{smp}=60 ns),

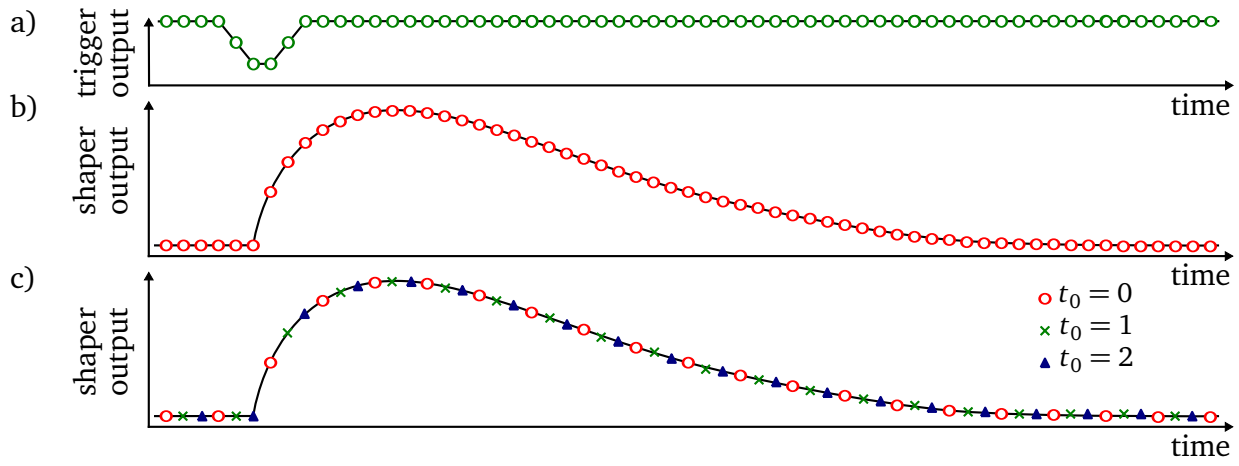

Figure 3.23: Schematic diagram of decimation procedure applied (for $M = 3$). a) Sampled trigger signal b) Sampled front-end signal c) Decimated front-end waveforms for different t_0.

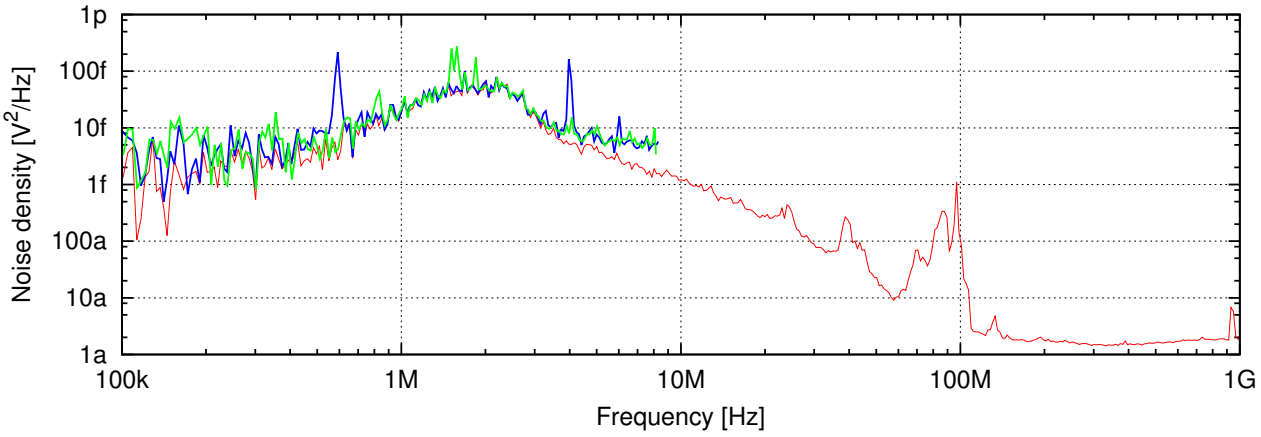

Figure 3.24: The front-end electronics noise spectrum obtained from FFT algorithm applied to samples collected at 4 GSps (red), decimated to 16.6(6) MHz a (blue), and decimated to 16.31 MHz (green).

is shown in blue in the same Figure. Because of the aliasing effect [82], the high frequencies spurs are aliased to the baseband. The strongest signals present at 96.0 MHz and 99.4 MHz in the original spectrum are aliased to 4 MHz and 0.6 MHz, respectively. For different decimation factors, the unwanted disturbances may influence the further signal processing even more. An example spectrum for decimation factor equal to 246 is shown in green. As one may see, the radio frequency disturbances are aliased directly to the center of shaper pass band, which can lead to significant errors. To neutralize the effect of these disturbances on the deconvolution algorithm, a digital low-pass FIR filter was implemented [82] and applied to the raw data, before the deconvolution procedure. The low pass filter, with cutoff frequency higher than 10 MHz, does not affect the noise spectrum of the front-end electronics; however, it effectively removes unwanted disturbances. Moreover, symmetric weights in the FIR filter ensure a constant group delay, which is crucial to preserve the original pulse shape [82]. Using the filter can be further justified by the fact that in the final experiment no such radio disturbances are expected because

of shielding.

The noise can also be investigated in the time domain by calculating the autocorrelation function, as described in chapter 2.8.5. The autocorrelation function computed for the noise signal samples acquired at the output of the preamplifier-shaper chain is shown in red in Figure 3.25. The radio frequency disturbances manifest as high frequency oscillations in the autocorrelation

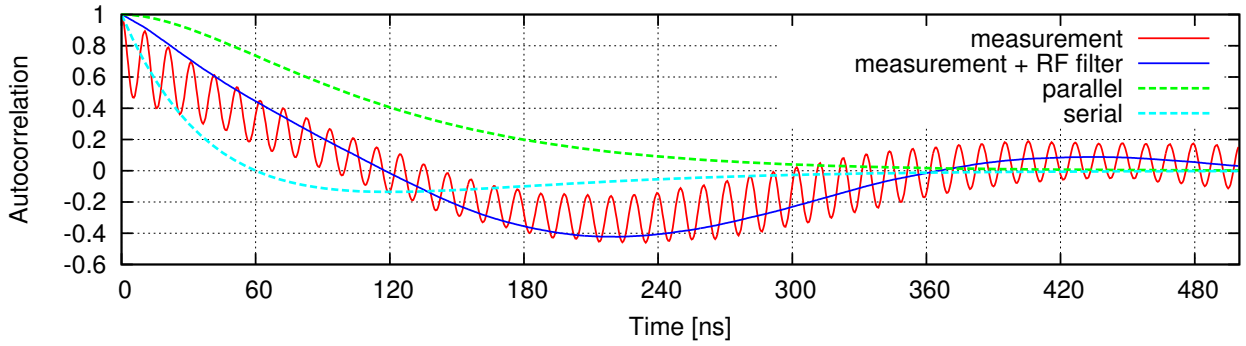

Figure 3.25: Autocorrelation function computed for the noise signal samples acquired at the output of the preamplifier-shaper chain (red and blue) and expected autocorrelation functions for pure serial and parallel noise.

function. The autocorrelation function for low-pass filtered signal is shown in blue in Figure 3.25. According to expectations, the overall shape is preserved while the oscillations are not present any longer. The expected autocorrelation functions for the cases of only serial or parallel noise presence (formulas (2.59) and 2.58)) are shown in light blue and green, respectively. The autocorrelation function calculated for the studied circuit cannot be easily decomposed to the superposition of functions for serial and parallel noise; however, the obtained dependence indicates that serial noise dominates in the circuit.

3.4.2 Monte-Carlo modeling

To understand the potential of deconvolution-based signal processing, a MC event generator was developed. To ensure the highest credibility of the generated events, the front-end signal is generated as a super-position of the pulse observed at the output of front-end ASIC (formula (2.19)) and the noise. The noise samples were carefully generated to have the same noise power density spectrum as the measured spectrum for the prototype front-end ASIC. To generate noise samples with arbitrary noise spectrum, the method proposed in [107] was used. The noise generation algorithm has multiple phases:

- a random signal $w(t)$ with white spectrum density, requested variance, and Gaussian distribution of sample values is generated,
- the Fourier transform $w(\omega)$ of the $w(t)$ signal is computed (using the FFT algorithm),
- the noise samples $s(\omega)$ (in frequency domain) are calculated as a product of the output of the Fourier transform $w(\omega)$ and the square root of the desired power density spectrum (see formula (2.18)),

- the noise samples in time domain are computed by calculating the inverse Fourier transform of the $s(\omega)$ signal.

The ADC is simulated as an ideal device, with equal quantization bins. The pulse parameters (the amplitude and the noise spectrum) as well as the ADC parameters can be changed in order to investigate their effect on the deconvolution performance. The generated events are stored in the format identical to the measured events to ensure the same data processing in both cases.

3.4.3 Results

The ADC incorporated in the used sampling oscilloscope has 8 bit resolution. To ensure the same signal processing conditions, all measurements were taken with the same oscilloscope settings. The sampling frequency was set to 4 GSps and the dynamic range to 400 mV (the corresponding LSB size is 1.56 mV). An example of the sampled time reference signal and the shaper output is shown in Figure 3.26a and 3.26b, respectively.

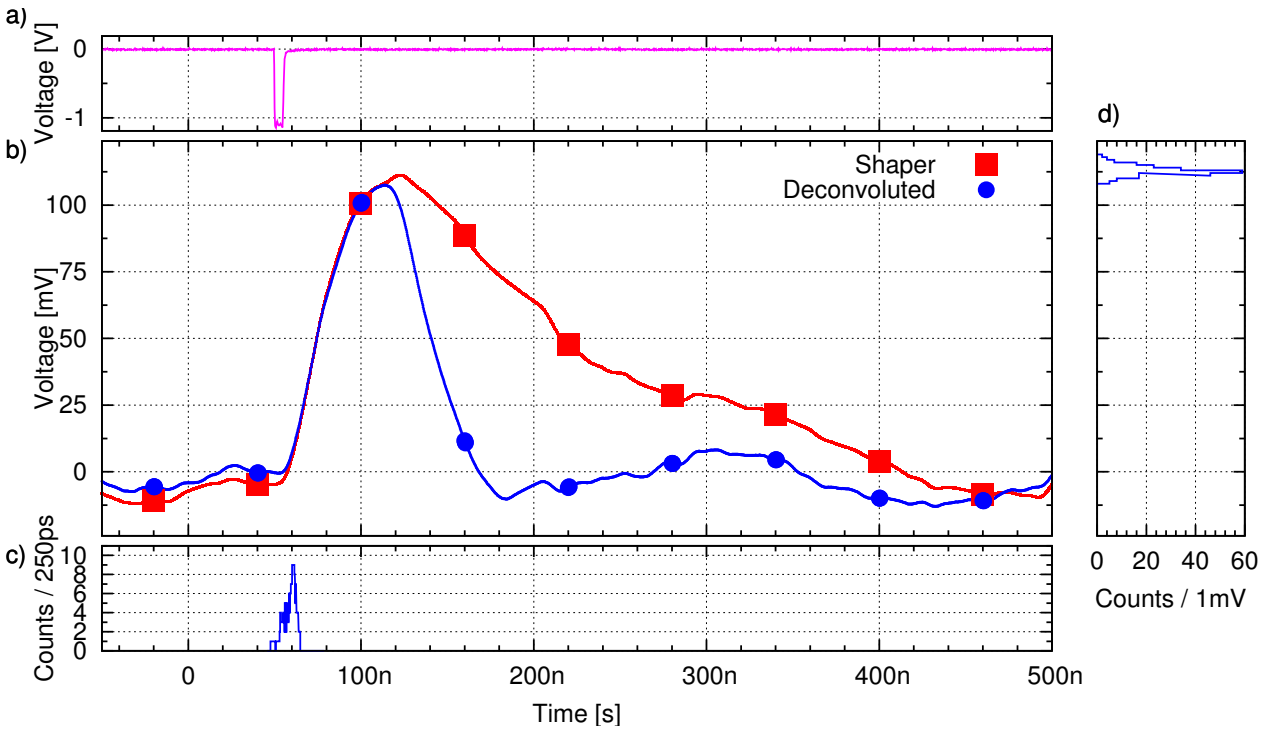

Figure 3.26: Example of a single pulse at the shaper output. a) Time reference signal b) Shaper output and deconvolution filter output c) Reconstructed time distribution d) Reconstructed amplitude distribution ($T_{smp} = T_{peak} \simeq 60$ ns).

The data collected using the oscilloscope were decimated (see equation (3.3)) to lower frequencies. An example of a waveform decimated to 16.6 MSps (1 out 240 samples) is presented in red squares. The SNR for the presented signal is around 20. The response of deconvolution filter is shown in blue in Figure 3.26b. Using the non-zero deconvoluted samples, the time and the amplitude reconstruction is performed (as described in chapter 2.8.2). The distributions of

reconstructed time and amplitude (for various T_0) are shown in Figure 3.26c and 3.26d, respectively. The distributions are not always perfect Gaussian, to describe them statistically the mean value and the RMS are used.

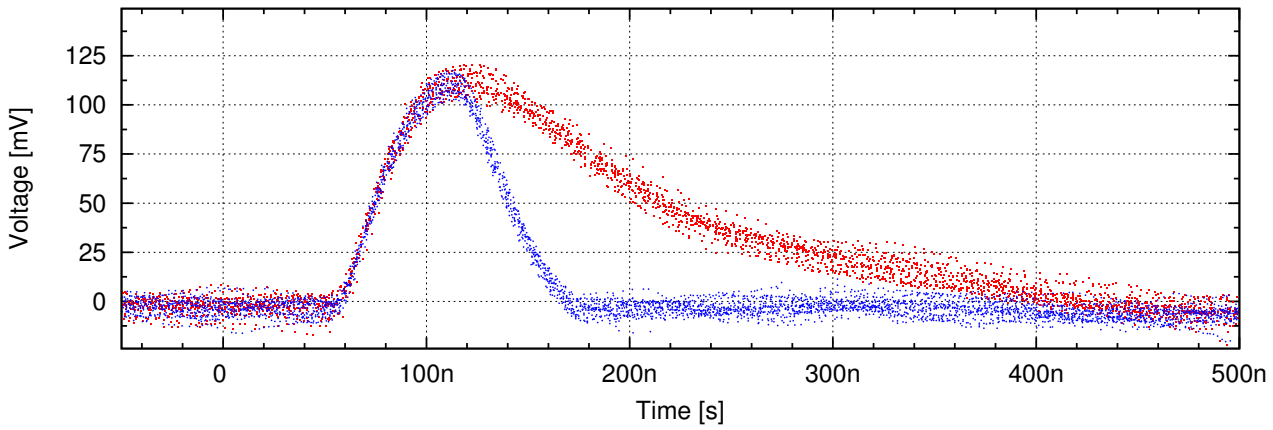

Figure 3.27: The effect of deconvolution processing (blue) on a number of different pulses for various sampling clock to signal phases (red).

The effect of deconvolution processing on a number of different pulses for various sampling clock to signal phases (T_0) is shown in Figure 3.27. The pulses were synchronized using information from the trigger channel. The pulse duration after deconvolution (blue) is shorter as expected. The spread of samples after the deconvolution is very similar to the one at the output of the shaper, what can be interpreted as no significant change in the noise.

Amplitude reconstruction performance

In Figure 3.28a the deconvolution-reconstructed amplitude as a function of input pulse amplitude is presented. The measurements were done with the laser. The reconstruction was performed for

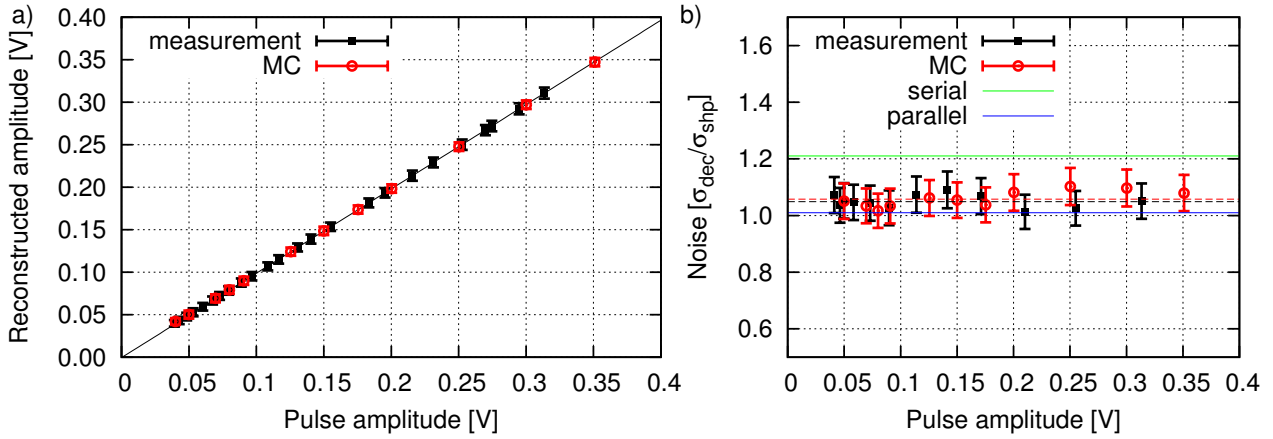

Figure 3.28: a) Reconstructed amplitude as a function of input pulse amplitude. b) Reconstructed to input noise ratio. ($T_{smp} = T_{peak} \simeq 60$ ns).

the sampling time (after decimation) equal to the peaking time (60 ns). As expected the response of the filter is linear with input signal. The deviations from linear fit remain below 0.1 %, i.e. below the measurement uncertainty. The deconvolution output noise to input noise ratio is shown in Figure 3.28b. The expected values of RMS for serial and parallel noise according to formulas (2.64) and (2.65) are shown in solid lines. The ratio stays in the range predicted by theoretical considerations for parallel and serial noise. The mean value (over all measurement points) of noise at the output of the deconvolution algorithm with respect to its input is increased by factor of 1.04, which corresponds to small degradation of the SNR. The MC simulations reproduce the measurements very well.

Time reconstruction performance

Figure 3.29a presents the reconstructed time as a function of the input SNR. As one would expect, the reconstructed time does not depend on the signal amplitude. The offset between the measurements and MC simulations is due to a constant signal propagation delay in the measurement setup (cables). The RMS of reconstructed time is shown in Figure 3.29b. The expected values of the RMS for serial and parallel noise according to formulas (2.69) and (2.70) are shown in solid lines. The shape of the measured dependence stays in good agreement with theoretical

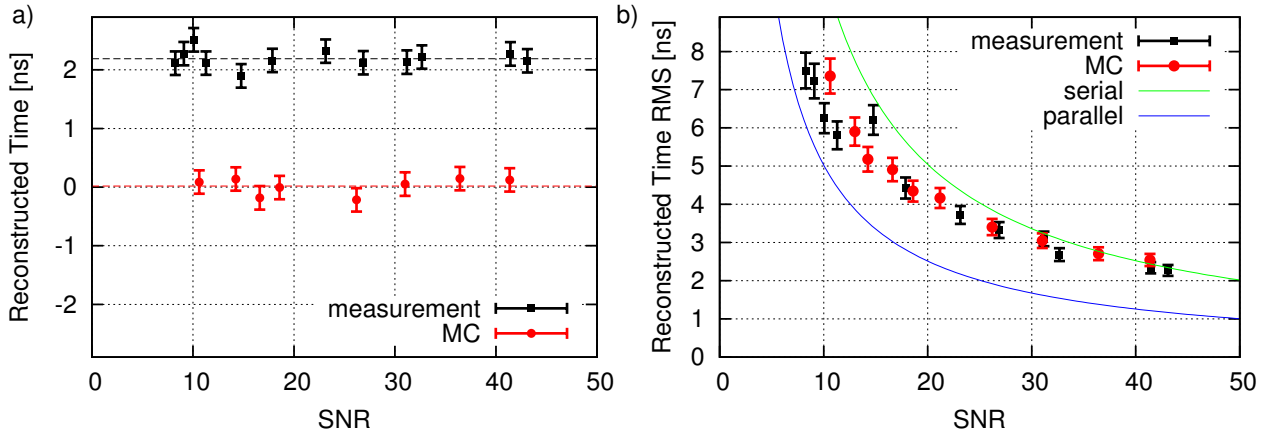

Figure 3.29: a) Reconstructed time and b) reconstructed time RMS at the output of deconvolution algorithm ($T_{smp} = T_{peak} \simeq 60$ ns).

predictions. The absolute values stay between the theoretical curves for the serial and parallel noise. The reconstructed time RMS stays below 8 ns for the SNR above 8. The time reconstruction RMS can be as small as 2 ns for the high SNR above 40. A very good agreement between the MC simulations and measurements is found in the whole range.

Sampling time impact on the algorithm performance

As it was described in chapter 2.8.6, an important parameter in the deconvolution processing is the sampling frequency. In synchronous mode, where the signal amplitude is given by only one deconvoluted sample, the RMS of deconvoluted samples translates directly to the amplitude error. The ratio of noise at deconvolution output to the shaper output as a function of sampling rate is

shown in Figure 3.30. The red curve presents the raw measurement results while the blue one

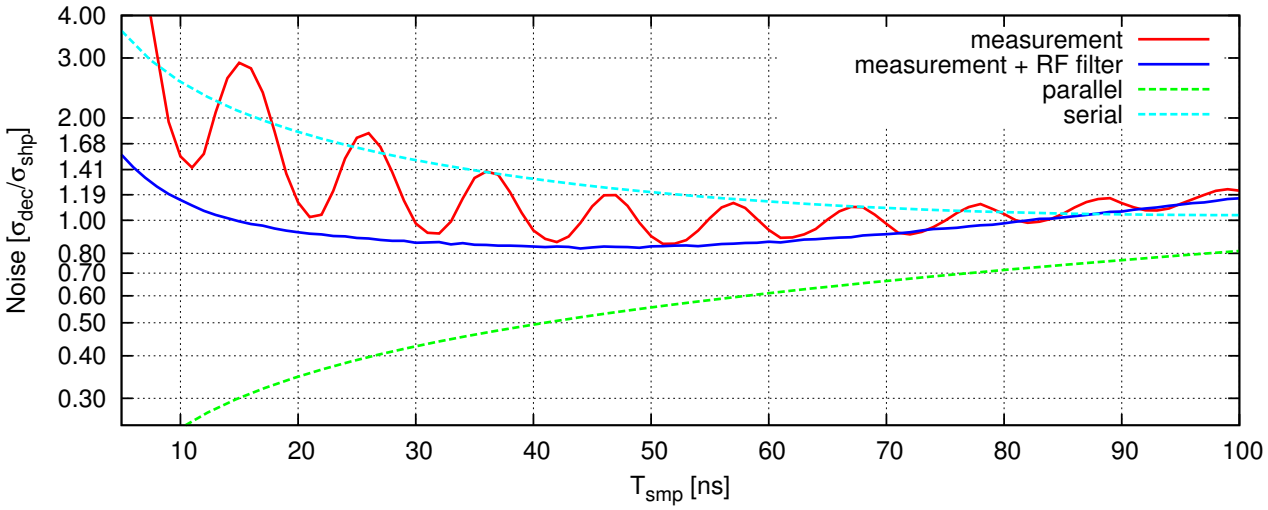

Figure 3.30: Impact of sampling frequency on the noise level ($T_{peak} \simeq 60$ ns).

shows the results obtained after RF frequencies were removed (see discussion in chapter 3.4.1). The theoretically calculated curves for the serial and parallel noise are added as a reference. One can see that RF disturbances degraded significantly the deconvolution performance. The deconvolution performed on the filtered data provides results which mostly stay between the prediction for serial and parallel noise.

To measure the impact of the deconvolution processing in asynchronous mode, the full event reconstruction was performed. The dependence of the RMS of reconstructed time on the sampling period for SNR=20 is shown in Figure 3.31a. The expected values of the RMS for serial and parallel noise are shown in solid lines. In general, very good agreement between the measurements and MC simulations is observed. For sampling periods in the range of 20-40 ns a

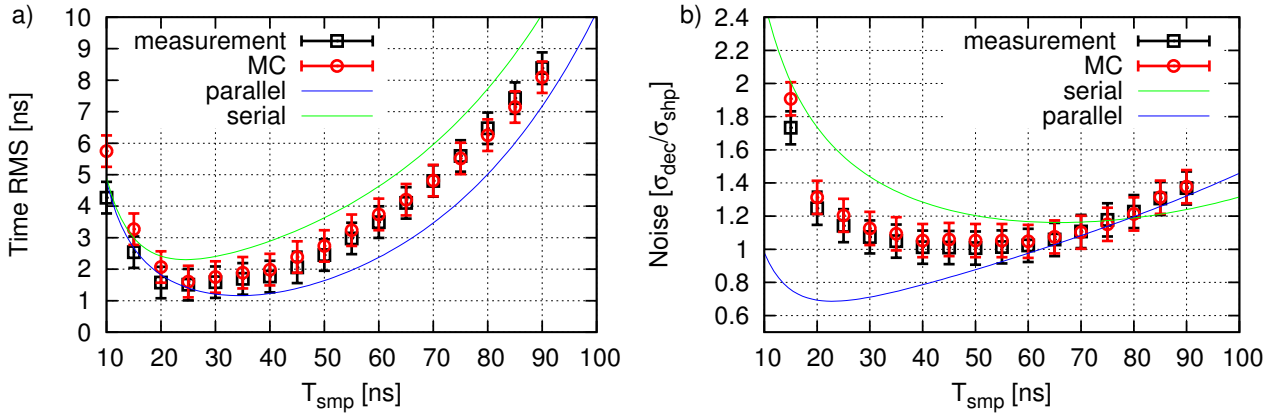

Figure 3.31: Impact of the sampling period on a) time and b) amplitude reconstruction performance for the SNR=20 and T_{peak}=60 ns.

time resolution better than 2 ns is achieved. For shorter sampling periods the time resolution is degraded by quantization noise of the ADC (see chapter 2.8.8). It is not clear whether the larger discrepancies between the measurements and MC simulation for very short sampling periods are due to non-exact noise implementation in the MC simulations or due to other reasons.

The deconvolution output to input noise ratio as a function of sampling period is shown in Figure 3.31b. The amplitude resolution depends less on the sampling period, and a plateau region is observed between 30-70 ns, for which the SNR after deconvolution is almost the same as before. For shorter sampling periods, the noise performance is worsened due to quantization noise. One has to remember that the chosen sampling frequency is always a compromise between the power consumption of the ADC and the requested system performance.

Input pulse dependence

The impact of pulse shape degradation on time reconstruction precision is presented in Figure 3.32a, which shows the dependence of time reconstruction RMS on sensor bias voltage (HV). For weak electric field in the sensor (low HV) the charge collection time increases and lengthens the current pulse (see chapter 2.1). The longer, non delta-like, current pulse from the sensor causes the ballistic deficit (see chapter 2.2), which deviates the pulse shape at the shaper output from the ideal CR-RC pulse shape. The deteriorated pulse shape causes quantitative decrease of timing resolution. For the studied bias voltage range the quantitative differences between the measured curves are rather small, of the order of 1 ns, which means that the method is moderately sensitive to the quality of the pulse shape.

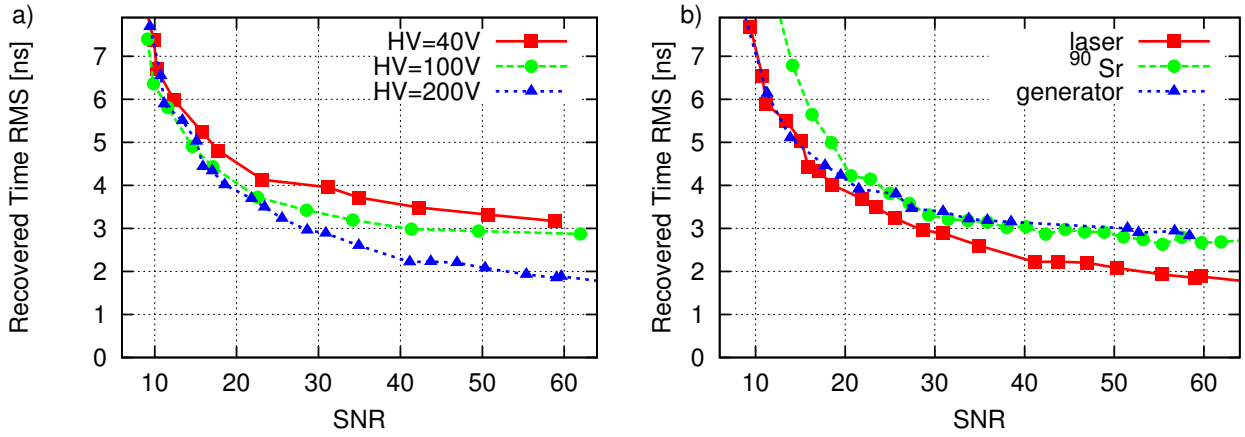

Figure 3.32: The RMS of reconstructed time for a) the various sensor bias voltages (signal generated by the laser pulses) and b) the various signal sources (sensor bias voltage 200 V). $T_{smp} = T_{peak} \simeq 60$ ns for both plots.

As a final experimental verification of the deconvolution method, the measurements of timing error are performed using different modes of pulse generation. In Figure 3.32b standard measurements with a laser source are compared to measurements performed using ^{90}Sr radioactive source and to the measurements taken with pulse generator. A good qualitative agreement of all three curves is seen. Some quantitative differences, of the order of 1 ns, may be related to: the input signal rise time and the signal reflections due to poor impedance matching of the track

carrying the test signal in the pulse generator mode; poor timing resolution of reference photomultiplier signal and non negligible time of flight of electrons for the ^{90} Sr radioactive source mode. As already explained, the measurements with the laser are considered to be the most precise.

Chapter 4

Testbeams of LumiCal detector modules

The LumiCal detector, introduced in chapter 1.3.3, is planned as a luminometer for experiments at linear colliders. Detailed studies were carried on to propose a detector architecture suitable to fulfill a set of demanding requirements and constrains of the physics program for the LumiCal detector.

To simplify the detector construction and minimize the maintenance cost, the LumiCal detector is composed of 30 (40) identical layers in the ILC (CLIC) [60]. Each layer is made of 3.5 thick tungsten plate, radiation sensor and readout electronics (see Figure 4.1). The tungsten plate acts as an energy absorber and support for the instrumentation.

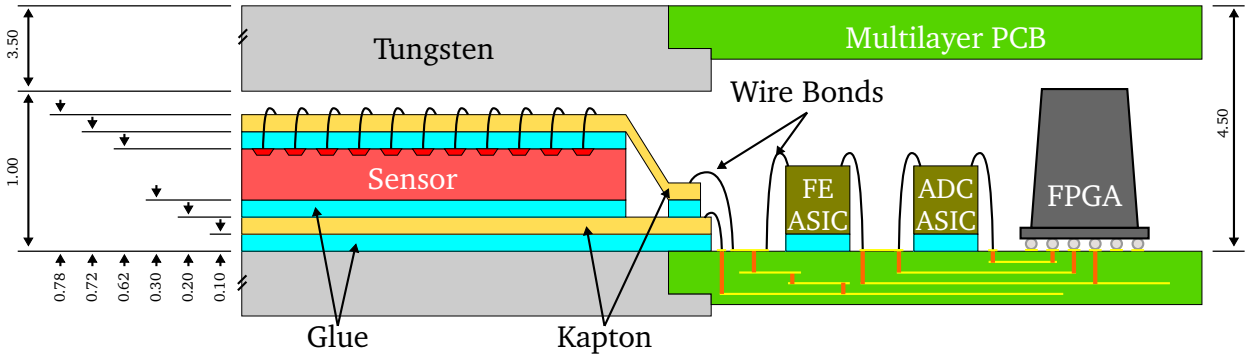

Figure 4.1: Cross section over LumiCal layer showing the connections between components (all dimensions in mm, drawing not in scale).

The kapton fanout is glued to the radiation sensor on both sides. From the bottom, high voltage is provided to bias the sensor; while on the top, the signals from the pads are carefully routed to the outer radius of the sensor where the readout electronic is placed. The front-end electronics and the first DAQ level implemented in the FPGA are placed on a dedicated multilayer PCB. Because of very limited space for the readout electronics, the naked readout ASICs (without chip carriers) are glued directly to the PCB. The connections to the sensor and to the ASICs are ensured using wire bonding technology [108].

To build the detector module, the bottom-up approach was adapted. In the first phase, all needed components, like radiation sensors and ASICs, were designed and carefully tested indi-

vidually as described in chapter 3. In the next phase the detector module was developed, and it is described in this chapter.

4.1 Analog detector module

To validate the very first part of the adopted signal processing chain, the analog detector module was designed. A dedicated multilayer PCB comprising of: silicon sensor, kapton fanout, front-end ASICs, power supply and biasing circuits, and line drivers was developed. The schematic diagram of a single readout channel is shown in Figure 4.2.

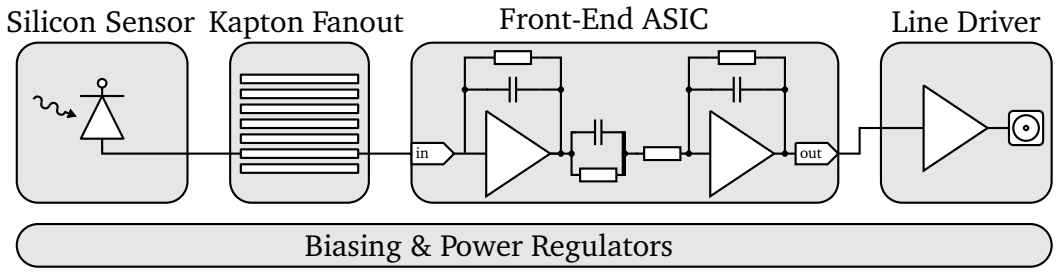

Figure 4.2: Schematic diagram of a single readout channel implemented in the analog detector module.

The sensor area on the LumiCal detector plane is divided into 12 sensor tiles, each comprising of four sectors as described in chapter 1.3.3. The sensor tile, as the smallest sensor unit produced, includes 256 separate sensor pads. For the first tests, a fraction of the single sensor tile is instrumented to validate the chain operation.

The signal generated in sensor is delivered to the front-end ASIC through the kapton fanout. For the innermost pad (at the smallest detector radius), the length of the fanout track approaches 120 mm, which leads to uncertainty about the operation of the proposed readout chain. The prototype of the kapton fanout was designed in IFJ PAN and manufactured in ITE[1]. The measurements performed at AGH-UST showed that the capacitance between the longest signal tracks (pad A0 and pad A1 in Figure 3.1) approaches 4 pF.

The signal delivered by the fanout from the sensor to the front-end ASIC (described in chapter 3.2) is amplified and shaped. The buffered front-end output is sent off the board to enable detailed studies of the chain response to radiation and test patterns. Because of the limited number of channels available in the front-end ASIC, instrumentation of all sensor pads was not possible. In order to validate the proper operation of the readout chain for the most extreme cases, a number of sensor areas were instrumented by the eight-channels ASIC prototypes. The A0-A7 pads (see Figure 3.1) located at the bottom of the sensor tile were selected as the ones with the smallest areas (and thus the lowest capacitances) and the longest fanout tracks. On the other hand, the next group of pads, B56-B63, is located at the top of the sensor tile. In this group the pads have the biggest areas and the shortest fanout tracks.

[1]Institute of Electron Technology is a major Polish research center with the primary focus on semiconductor micro- and nanotechnology. More information can be found at http://www.ite.waw.pl/en/.

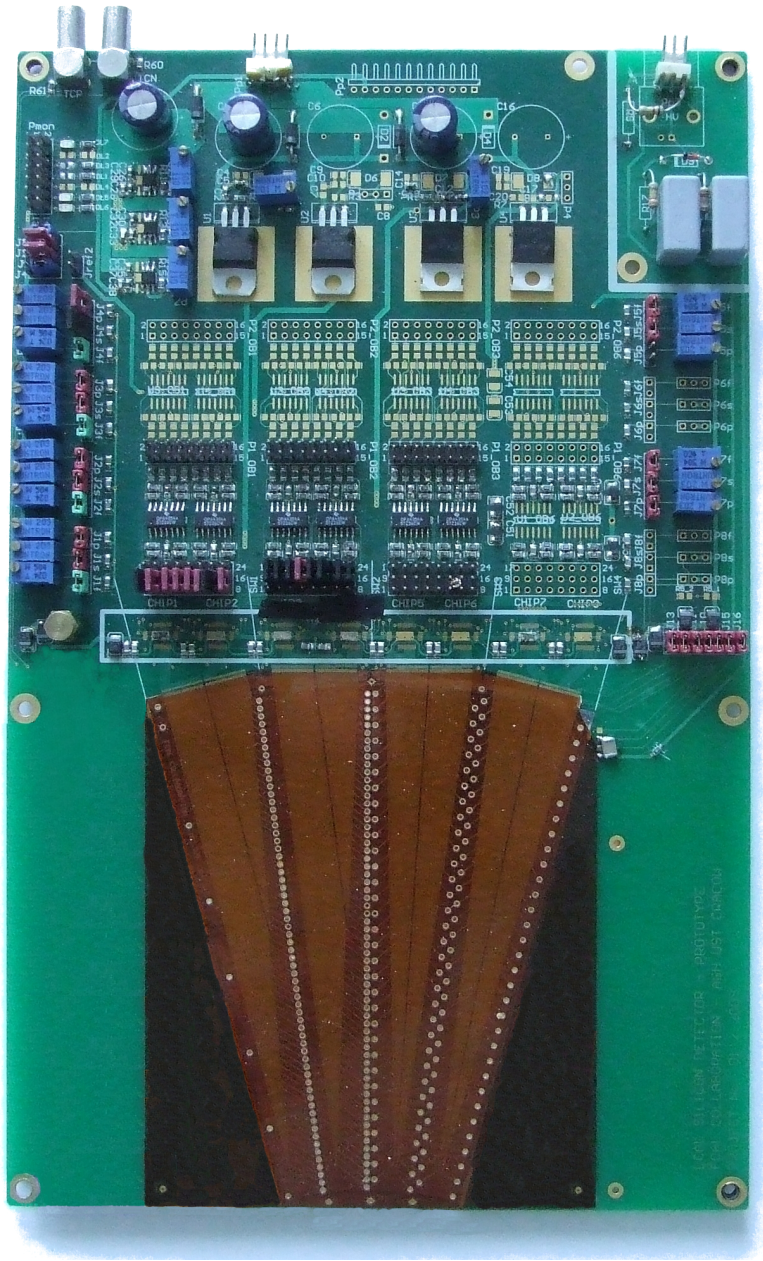

Figure 4.3: Photograph of the analog readout module. In the picture going from the bottom to the top: silicon sensor covered by kapton fanout, front-end ASICs, line drivers, voltage regulators and biasing circuits on sides.

The four-layer PCB was produced by Hatron[2] and assembled on AGH-UST. The photograph of assembled detector module is shown in Figure 4.3. The laboratory measurements performed with a pulse generator and an oscilloscope confirmed the proper operation of all channels in the front-end ASICs. The qualitative tests conducted with a ^{90}Sr radiation source proved that all sensor channels (connected to the readout) were sensitive to radiation.

[2]Hatron Electronic is a company manufacturing of high quality PCB. More information can be found at http://www.hatron.com.pl/.

4.2 Testbeams with analog detector module

4.2.1 The DESY testbeam facility

To validate the module operation under experimental conditions similar to the ones expected in future experiments, high energy electrons are necessary. A DESY II synchrotron facility, hosted at Deutsches Elektronen-Synchrotron (DESY) in Germany, is able to accelerate electrons up to several GeV, which makes this facility suitable for the testbeams. The main users of these electrons are PETRA or DORIS accelerators on the DESY site; however, three electron testbeam lines are provided for other users. The testbeam generation process is presented schematically in Figure 4.4a. Firstly, the electrons bunch is accelerated in DESY II synchrotron. A circulating beam passes through a carbon fiber, generating by the bremsstrahlung process a high-energy photon beam. The generated photons leave the synchrotron and are converted to e^-/e^+ pairs (in the pair production process) inside a metal plate (converter). The secondary electron-positron beam is spread out into a horizontal fan with a dipole magnet. The final beam available for users is cut out of this fan with a collimator. The e^- momentum is fixed by relative position of the beam pipe and collimator as well as the magnetic field provided by the electromagnet. Current in the electromagnet can be changed remotely allowing for convenient control of the particle energies delivered to the experimental area. This scheme of electron generation allows for obtaining electrons with energies ranging from 1 GeV up to around 6 GeV. For the mentioned momentum range, electrons behave like a MIP (see chapter 2.1).

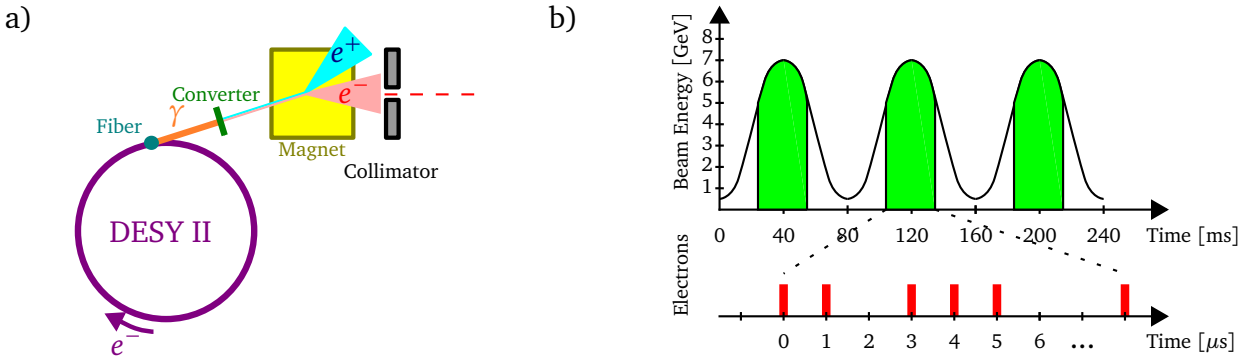

Figure 4.4: a) Testbeam generation process. b) Beam structure.

The circumference of the DESY II ring is 292.8 m, therefore the electrons traveling at a speed close to the speed of light need around 1 μs for one complete revolution. Because there is only one electron bunch in the accelerator, this period establishes the possible electron rate for the user. However, the electrons in the primary beam are accelerated and decelerated in a sinusoidal fashion with a frequency of 12.5 Hz (see Figure 4.4b). Therefore, the particles can reach the experimental area only when the momentum of electrons in the accelerated bunch is above the chosen momentum (green part in Figure 4.4b), which decreases the overall event rate. Depending on the selected particles momentum, the expected electron rate varies from several Hz up to several kHz, for the highest and the lowest energies available, respectively. while keeping the time separation of the events unchanged.

4.2.2 Testbeam setup

The schematic diagram and photograph of the experimental setup used during the testbeam measurements is shown in Figure 4.5 and Figure 4.6, respectively.

Two crossed finger scintillators (5 mm width) were placed at the setup input and one scintillator at the setup output. A compact photomultipliers were attached to the scintillators to produce electrical pulses corresponding to an act of radiation detection. A coincidence unit built on the basis of the NIM module (Nuclear Instrumentation Module) was used to combine signals from all photomultipliers in order to produce the trigger signal for all sub-detectors. Such a trigger system further limited the beam to 5×5 mm^2. A Micro Vertex Detector (MVD) developed and built by the ZEUS collaboration was used for particle tracking [109]. The telescope plane is composed of two independent fine strip detectors rotated by 90 degrees with respect to each other. It is possible to reconstruct the two dimensional position by combining the information from both planes. Three such planes placed one after the other allowed for the three dimensional particle track reconstruction. By using the particle track, it is possible to calculate the electron impact point on the face of the studied sensor plane. The dedicated DAQ system is provided to operate the telescope. The DAQ is responsible for recording the signals of all sensors strips when the trigger signal appears. Later on, the data are zero-suppressed and stored in the local telescope memory. The telescope can be controlled and the data can be accessed via an Ethernet connection.

The detector module was mounted inside a copper box. The box provided electro-magnetic screening and protection against light. The box with the detector module was mounted on a motorized X-Y table. Such configuration allowed remote control of sensor position with respect to the beam line. The analog output signals were driven out of the module and sent to an external sampling ADC v1724[3]) provided by CAEN. The ADC samples signal continuously and the data are stored in circular buffers. If an external trigger signal is present, a packet is built out of 128 samples (per each channel) and transmitted to DAQ PC over an optical link.

To ensure that both DAQ acquire the same events, a veto scheme is used. Since the telescope DAQ requires much more time to process an event (around 10 ms) than CAEN ADC, the BUSY signal generated by the telescope is used to block acceptance of new events. The data were stored in separate files, each containing approximately 50.000 events. This quantity resulted from the limitations of the telescope software. The beam energy was set to approximately 4.5 GeV. For this energy, the expected event rate should be below 1 kHz, what ensures full occupancy of the telescope DAQ and at the same time minimizes the possibility of observing two or more overlapping electrons.

4.2.3 Readout chain operation validation

An example of time responses of a single front-end channel for various energy depositions is shown in Figure 4.7. The acquisition time window was aligned to capture a part of the baseline before and after the pulse. The pulse shapes recorded for single electrons correspond very well to the signals obtained in the laboratory measurements with the pulse generator as a signal source. Moreover, the pulse shape does not depend on the pulse amplitude, as expected.

[3]v1724 is a VME module comprising 8 channels of 14 bit 100 MSps ADC. The module is provided by CAEN. More information can be found at http://www.caentechnologies.com/.

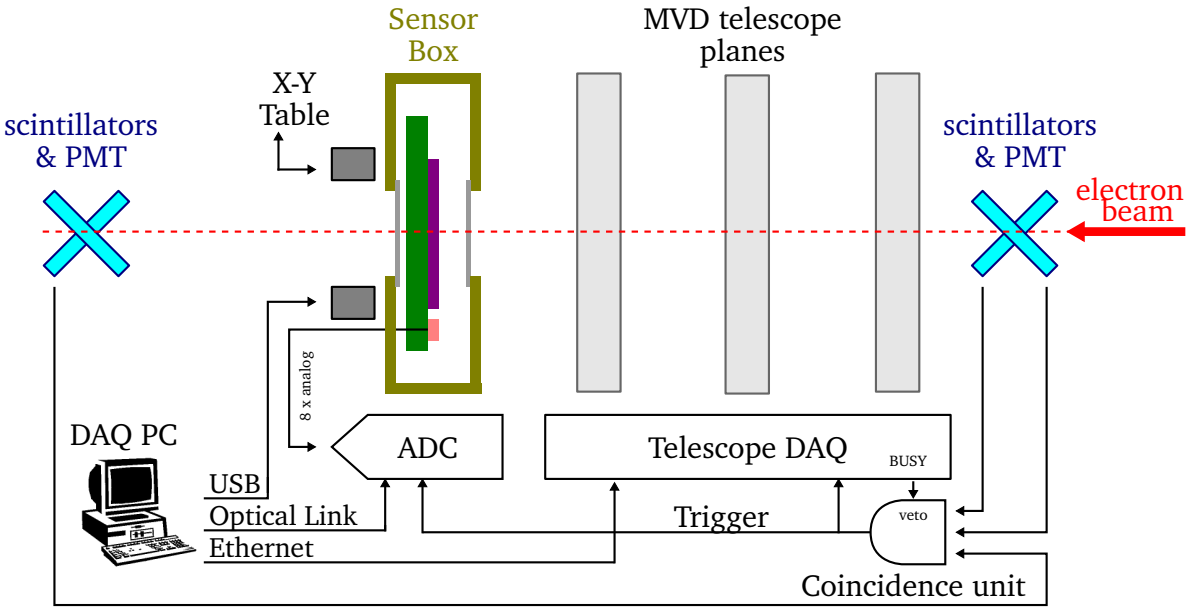

Figure 4.5: Schematic diagram of experimental setup used during analog module testbeam measurements.

Figure 4.6: Photograph of the experimental setup used during the analog module testbeam measurements.

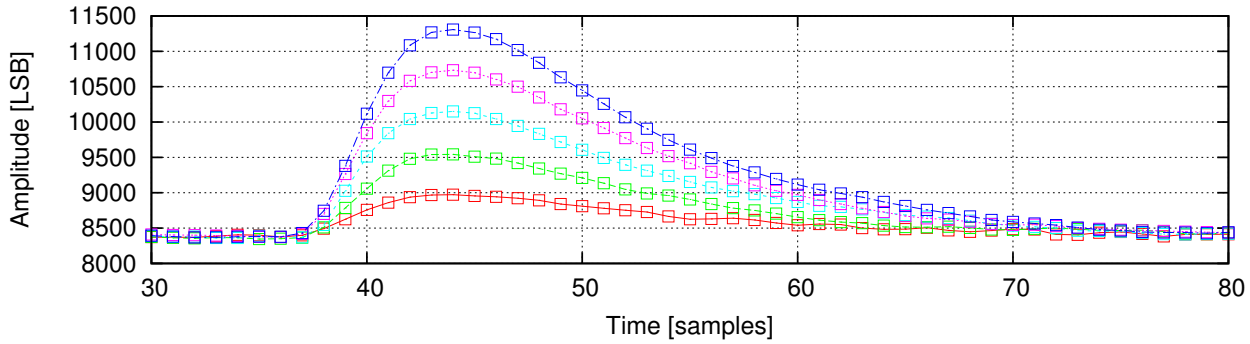

Figure 4.7: Time response of the front-end electronics channel for different energy depositions.

In the spectroscopy measurements the deposited energy is measured as a pulse height with respect to the baseline (see chapter 2.4). An average of 32 beginning samples (not containing pulse) from all events was used to estimate the baseline mean value, as well as the baseline RMS for each channel. The baseline mean value was subtracted from all samples, causing the baseline shift to the zero level. To extract information about the pulse amplitude in a similar fashion, as the one planned for the ILC, a digital peak detector was implemented in the processing software. The time information, when the peak maximum from all channels is found, is used to perform synchronous sampling on all channels. Because of the high sample rate and quite a flat top of the pulse, the error introduced by the unknown phase relation between the pulse and the sampling clock is negligible.

The distributions of pulse heights for a single channel with resistor and active feedback configurations responding to a passage of a single 4.5 GeV electron are presented in red in Figure 4.8a and Figure 4.8b, respectively. In the plot two separate peaks are visible. The left Gaussian peak,

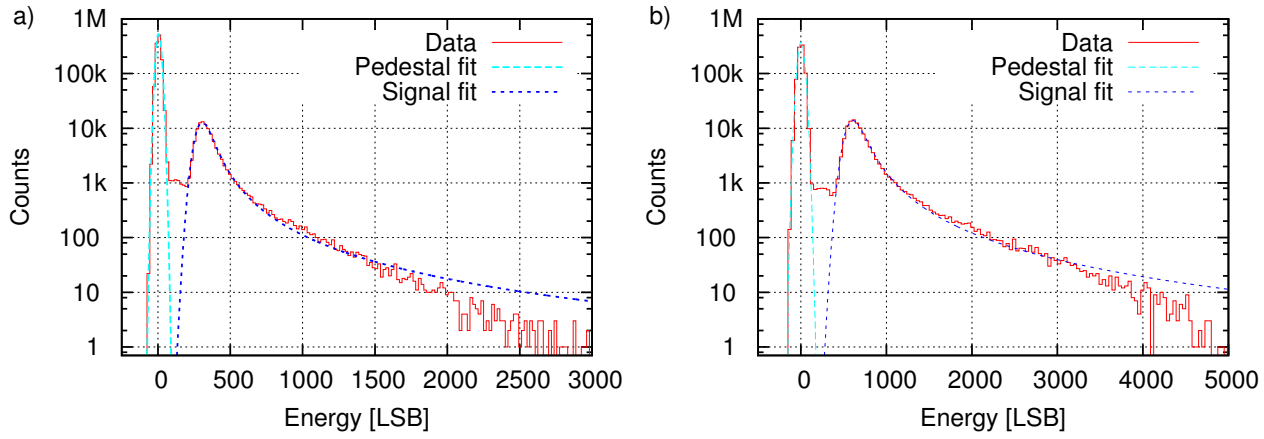

Figure 4.8: Energy deposition spectrum in a) A5 pad (passive feedback) and b) A3 pad (active feedback).

around zero value, is a pedestal, while the right peak corresponds to the signal produced by the electron. The events appear in the pedestal peak in a situation when the acquisition is triggered

and no radiation was present in the considered pad. Such a situation is expected to be frequent, having in mind that the beam is collimated to approximately 5×5 mm^2 while the single pad width is only 1.8 mm. If only the random noise is present in the system, the pedestal distribution should follow the Gaussian distribution. The width of the pedestal distribution is related mostly to the readout electronics noise. According to expectations, the observed signal energy distribution follows Landau distribution (see chapter 2.1). Fitting procedures were used to extract information about the signal and the baseline distribution. The fitted curves describe very well the measured distributions. For the high energy depositions, the measured event count is slightly lower than predicted by the theory. It can be explained by the front-end electronics saturation as explained in chapter 2.2. The points in the spectrum laying between signal and pedestal peaks are expected to be caused mainly by two effects. The first effect is related to charge sharing in between adjacent pads, resulting in decreased amplitude in a single channel. The second contribution is caused by the electromagnetic shower brought about by an incoming high energy electron in the materials in front of the studied sensor tile. In such process, small energy photons can be generated leading to small charge depositions in the sensor active volume.

The difference in the MPV of the Landau distributions obtained for the two types of feedback configurations is related to the difference in the design of the front-end ASIC (see discussion in chapter 3.2).

Estimation of channels parameters

Utilizing the measured spectra obtained for high energy electrons one can estimate the gain of the whole readout chain. The difference between the MPV of the Landau distribution and the baseline mean value can be interpreted as the readout channel gain. The SNR can be obtained by dividing the signal level by the RMS of the baseline. The results obtained for all channels are summarized in Table 4.1. The gains for channels with active feedback (MOS) are approximately

Table 4.1: Gain and Signal to Noise Ratio for different channels. Bottom pads (A0-A7) in left table. Top pads (B56-B63) in right table.

Pad	Type	Gain [LSB / MIP]	Noise [LSB]	SNR
A0	MOS	583.2	28.7	20.3
A1	MOS	572.6	27.3	21.0
A2	MOS	571.8	27.1	21.1
A3	MOS	568.8	27.1	21.0
A4	R_f	295.2	14.4	20.5
A5	R_f	294.8	14.4	20.5
A6	R_f	295.9	14.5	20.4
A7	R_f	298.7	15.2	19.7

Pad	Type	Gain [LSB / MIP]	Noise [LSB]	SNR
B56	MOS	590.1	35.1	16.8
B57	MOS	584.7	32.8	17.7
B58	MOS	587.7	33.0	17.8
B59	MOS	585.8	33.1	17.7
B60	R_f	299.9	17.5	17.2
B61	R_f	303.6	17.7	17.2
B62	R_f	301.2	17.8	16.9
B63	R_f	301.4	18.6	16.2

twice as big as for passive feedback (R_f) which is consistent with the laboratory measurements. For the same type of preamplifier feedback, the gain is quite uniform and its variations do not exceed 2%. One has to remember that this is the overall gain including the line driver gain and

the ADC conversion gain spread. The obtained SNRs for bottom pads are systematically larger than for top pads, what can be explained by the difference in sensor pad capacitance. The border channels have slightly higher gains.

Common mode disturbances

The noise level presented in Table 4.1 exceeds expectations formulated on the basis of the laboratory measurements. One of the possible reasons is an additional 'noise' pick-up by the long fanout track. Example waveforms containing disturbances are shown in Figure 4.9. As it can be observed, the baseline has similar pattern throughout all channels. To investigate it, the baseline correlation studies were conducted for various channels. In the case of a pure electronics noise, no correlation is expected between channels. In Figure 4.10 the relation of baseline value on channel A3 to baseline value on channel A1 is presented. One can notice strong positive correlation. The correlation coefficients for the bottom channels are presented in Figure 4.11a. Most of the coefficients are above 0.7, which expresses strong correlation.

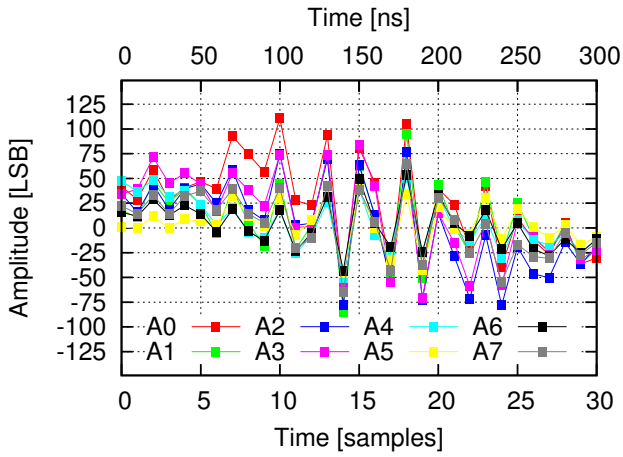

Figure 4.9: Response of front-end electronics channels to disturbance.

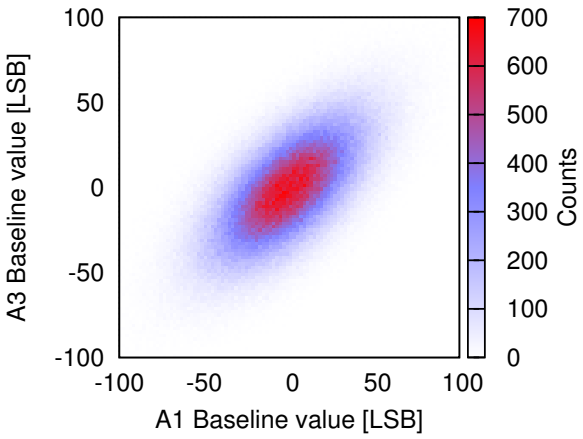

Figure 4.10: Relation of the A3 channel baseline samples to A1 baseline sample.

The overall noise level is boosted because of this additional correlated noise. One may try to estimate this contribution and subtract if from all channels. In the first attempt, the average over all channels was subtracted from each channel. The obtained correlations are presented in Figure 4.11b. The correlation level decreased, but a pattern grouping channels with the same type of feedback appeared. The primary difference between channels with different feedback networks is the gain (factor of 2). The results of applying the procedure of common mode subtraction after gain unification are shown in Figure 4.11c. The values of correlation coefficients are really small, which means that there is almost no correlation between channels. Small negative correlation can be observed for the closest neighbors, which can be caused be the crosstalk. This results lead to a conclusion that the disturbances are injected at the input of front-end preamplifier.

One needs to remember that common mode subtraction increases statistical (uncorrelated) noise to σ' according to $\sigma'^2 = \sigma^2 + \sigma^2/N$, where σ is the RMS of noise (assumed to be the same for all channels) and N is the number of channels taken to estimate the common mode. In the

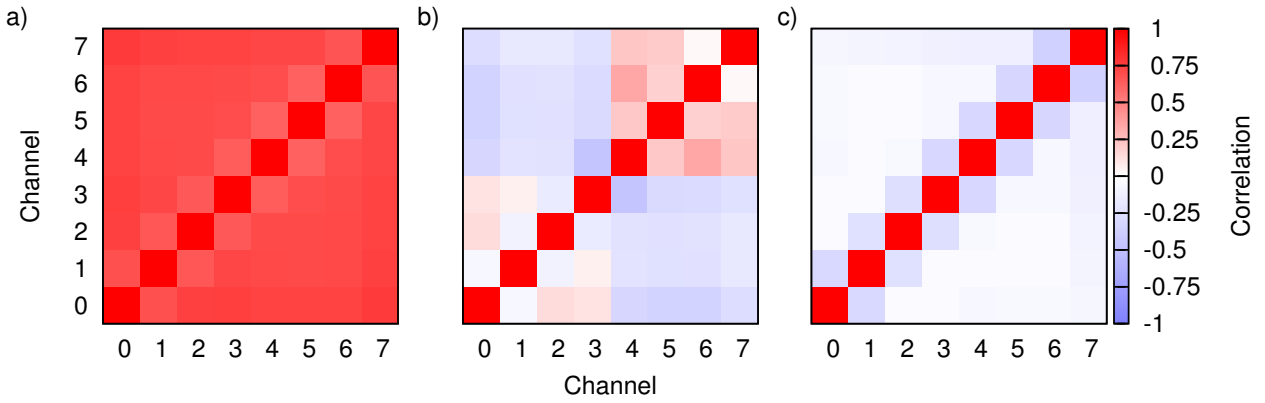

Figure 4.11: Correlation coefficient for baseline samples for bottom pads. a) Raw data. b) Common mode noise subtraction without gain unification. c) Common mode noise subtraction with gain unification.

considered experimental setup, containing only eight channels, the common mode subtraction procedure is expected to increase the uncorrelated noise level by approximately 35%.

To apply common mode subtraction to waveforms containing signals, some selection criteria need to be applied in order to determine which channels can be used for common mode estimation. The most straightforward method would to be to check whether the amplitude is below some arbitrary threshold. The detailed analysis of threshold selection was presented in chapter 2.5.

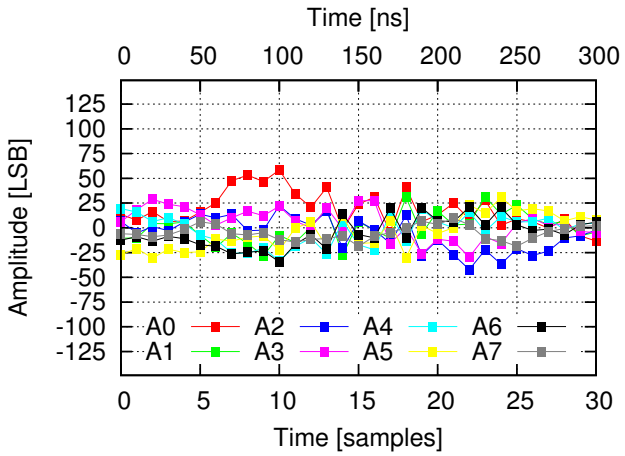

Figure 4.12: Response of front-end electronics channels to disturbance after common mode subtraction.

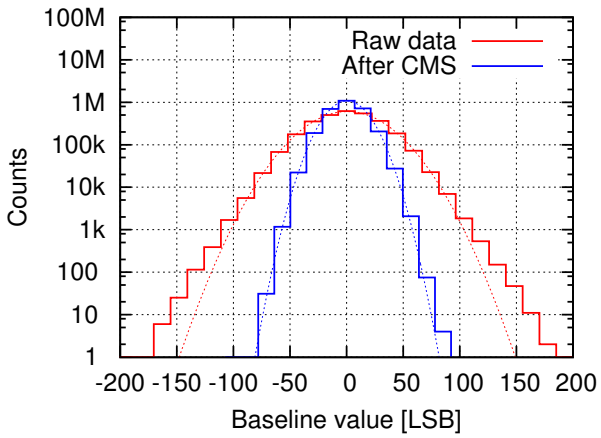

Figure 4.13: Distribution of the raw baseline samples and the baseline samples after common mode subtraction for channel A1.

The result of the common mode subtraction on the waveforms from Figure 4.9 is shown in Figure 4.12. It can be seen that the RMS of samples decreased. The distributions of the raw baseline samples and the baseline samples after common mode subtraction procedure are

shown in Figure 4.13. The mean value of both distributions is equal to zero, so the common mode subtraction does not introduce any bias in spectroscopic measurement. The width of the distribution after common mode subtraction is reduced by 42%. The distributions (especially the one after common mode subtraction) follow Gaussian distribution very well (shown in dashed lines).

4.2.4 Position reconstruction

A relativistic particle going through a thin sensor does not change the motion direction significantly. Using a telescope, it is possible to calculate a particle track in 3D space. Knowing the particle track, one can predict the impact point on the plane of the tested sensor. The *telana* software package [110] provided with the telescope, was used to perform the track reconstruction.

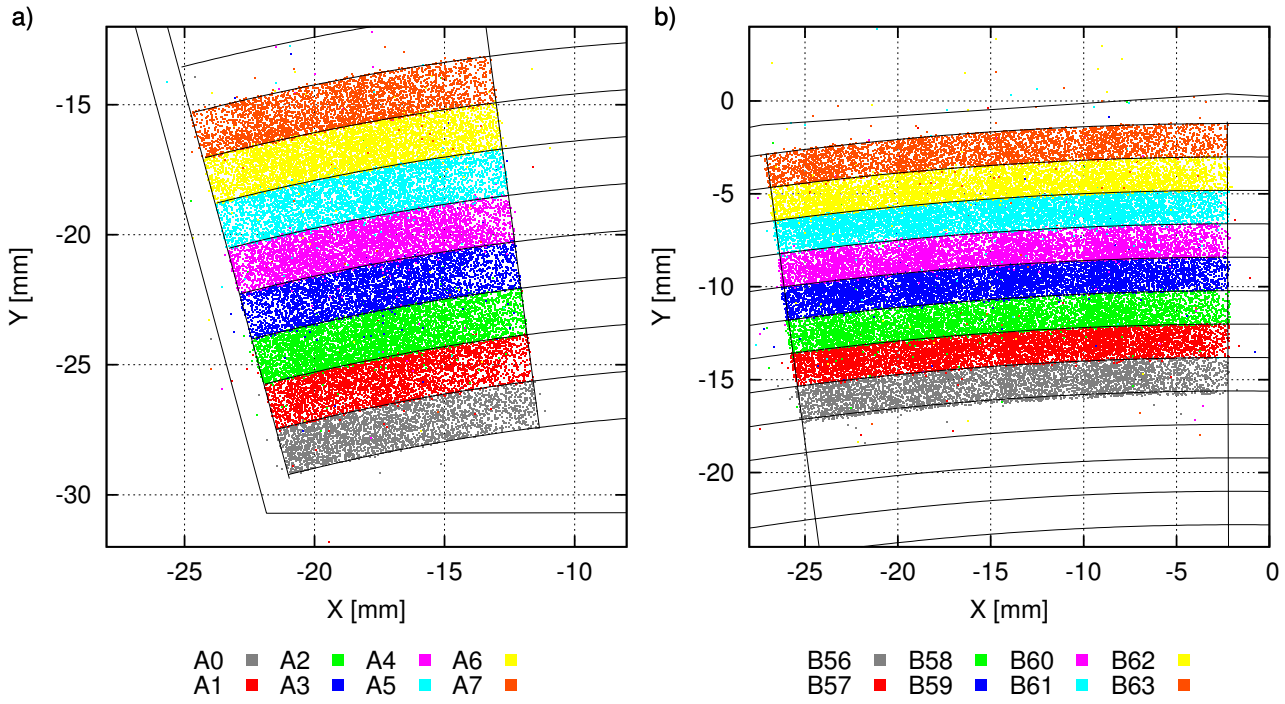

Figure 4.14: Reconstructed position of high energy electron impact point combined with the signals registered in the LumiCal sensor pads: a) bottom pads area (A0-A7) and b) top pads area (B56-B63).

In Figure 4.14 one can see the combined information from LumiCal DAQ and telescope DAQ. A colored dot is placed at the position returned by the telescope prediction when there is a signal present in a given detector channel. As one can see, the structure of the LumiCal sensor (outlined in black) is very well reflected by the reconstructed points. The overall precision of impact point prediction is limited by the resolution of the telescope sensors, as well as by multiple scattering of beam electrons that causes deviations from straight track. Due to these effects, some points lie outside the expected pad borders. To obtain the results presented in Figure 4.14, several dozens of data sets (each comprising of 50.000 events) corresponding to the different positions of the detector module with respect to the beam line needed to be analyzed and combined together (the beam was collimated to 5×5 mm^2).

4.2.5 Studies to improve signal to noise ratio

Two possible sources degrading the SNR were identified in previous chapters: common mode noise and charge sharing between the pads. By applying the common mode subtraction and setting the requirement for only one hit laying farther than 200 μm from the pad border, the spectra presented in Figure 4.15 are obtained.

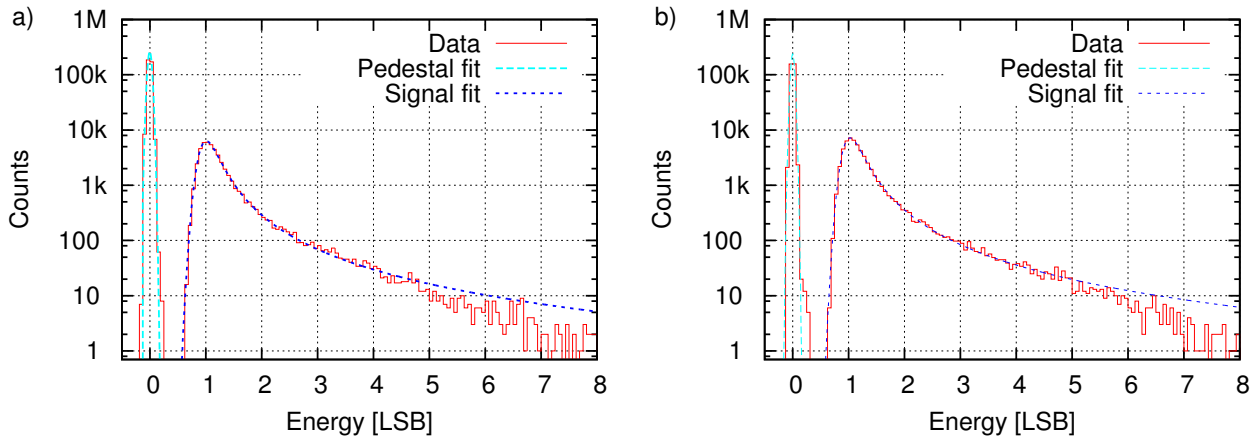

Figure 4.15: Energy deposition spectrum obtained after common mode subtraction and rejection of events with position close to pad borders in a) A5 pad (passive feedback) and b) A3 pad (active feedback).

Table 4.2: Impact of common mode subtraction on the SNR.

Pad	Type	SNR_{RAW}	SNR_{CMS}
A0	MOS	20.3	32.5
A1	MOS	21.0	31.4
A2	MOS	21.1	31.7
A3	MOS	21.0	30.9
A4	R_f	20.5	29.2
A5	R_f	20.5	28.6
A6	R_f	20.4	28.8
A7	R_f	19.7	29.2

Pad	Type	SNR_{RAW}	SNR_{CMS}
B56	MOS	16.8	33.0
B57	MOS	17.7	32.2
B58	MOS	17.8	32.6
B59	MOS	17.7	31.8
B60	R_f	17.2	30.8
B61	R_f	17.2	30.8
B62	R_f	16.9	30.5
B63	R_f	16.2	30.8

The improved SNRs are observed for all channels as presented in Table 4.2. For all channels the SNR is around 30, what correspond to ENC of approximately 0.13 fC. Having in mind that this result is contaminated at least in 35% by the contribution from the common mode subtraction procedure, the pure electronics noise remains at the level of 0.1 fC, which agrees with laboratory measurements shown in chapter 3.2.2. It is not clear why the SNR observed for the pads with higher capacitance (B56-B63) is slightly higher than for smaller pads (A0-A7), even taking into account a fanout capacitance. A possible explanation may be that sensor pad behaves as a panel antenna and this effect dominates.

4.2.6 Sensor uniformity measurements

A sensor response in calorimeter application is essential. In sandwich type calorimeters, like LumiCal, the track is reconstructed using information from several subsequent layers. The procedure of finding the center of gravity is used to estimate the impact position on each plane, and the charge collected in each sensor cell is used as a weight during the center of gravity calculation. The sensor should produce signal directly proportional to the total energy deposited in its active volume independently of particle crossing point or energy deposited, as explained in 2.1. The main effects which cause non-uniformities in signal collection are: charge diffusion during the charge collection and non-uniform electric field distribution in the area in between the strips. In theory, the detection efficiency (and charge collection) should be flat under the pad and drop immediately to zero outside the pad area.

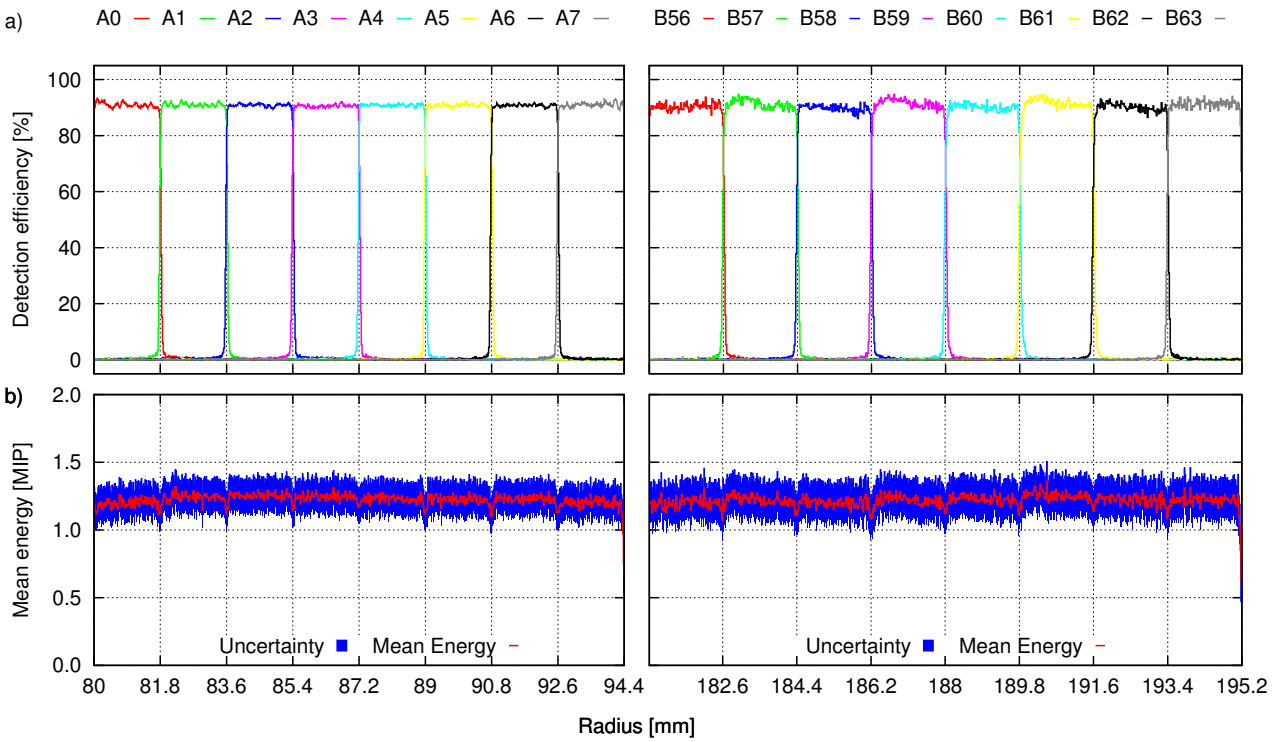

Figure 4.16: a) LumiCal sensor detection efficiency as a function of the radius. b) Mean energy deposited as a function of the radius.

The detection efficiency was calculated as the number of recorded signals above the threshold in a particular channel to the number of tracks expected to cross the sensor pad area connected to the channel. The measured detection efficiencies as a function of radial distance are presented in Figure 4.16a for all pads. The radial distance was calculated using the position obtained from the track calculated by the telescope. The pad structure is clearly reflected as 1.8 mm wide bins with flat tops. According to expectations the detection efficiency drops immediately to zero outside the pad area. The detection efficiency is lower than the expected 100%; this can be explained by the imperfect track reconstruction by the telescope (compare with Figure 4.14).

Figure 4.16b shows the average energy deposited as a function of the radius. The relatively high uncertainty of the results come from the statistics available. The flat behavior for all pads is observed. Small drops in the collected charge are visible in the area between pads, this effect can be explained by the non uniformities in the electric field in this area.

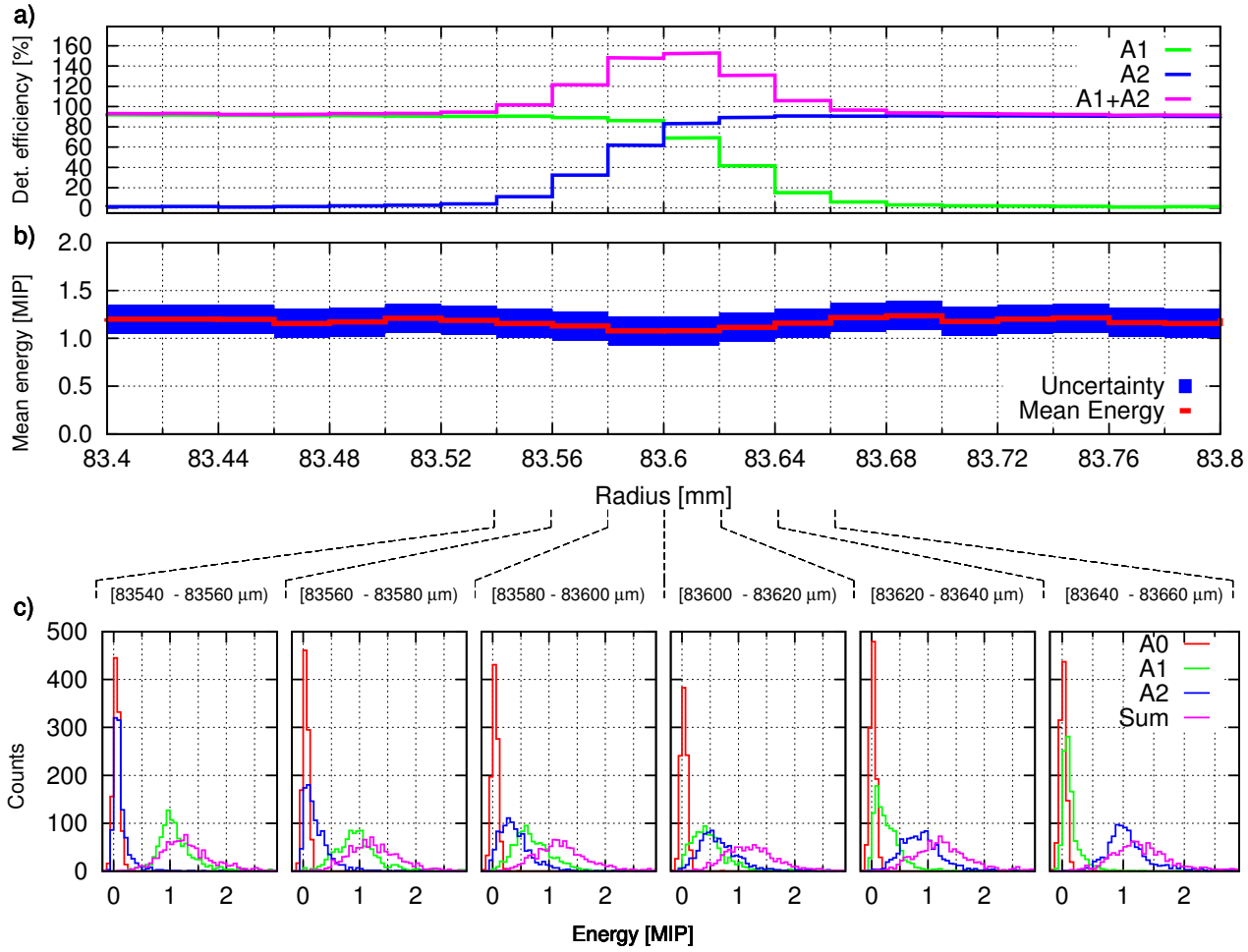

Figure 4.17: a) Detection efficiency and b) mean energy deposited as a function of the radius close to border between pads A1-A2. c) Deposited energy spectra for various radiuses close to A1-A2 border.

The detailed results obtained for regions in between pads A1 and A2 are presented in Figure 4.17 as an example. The electric charge generated by electrons hitting the sensor surface is smeared because of diffusion. In this way, the charge generated close to the border between two pads is often visible on both pads (more than 100% detection efficiency). Figure 4.17c presents the detailed energy deposition spectra for hits located close to the border between pads. One can see that the distribution of total visible energy has a constant shape, while the contributions from A1 and A2 pads interchange.

4.2.7 Crosstalk studies

The relation between signal amplitudes on neighboring pads was studied to evaluate the crosstalk level between pads. An example relation of amplitude on channel A2 to amplitude on channel A1 is shown in Figure 4.18. Every histogram entry corresponds to the recorded event with

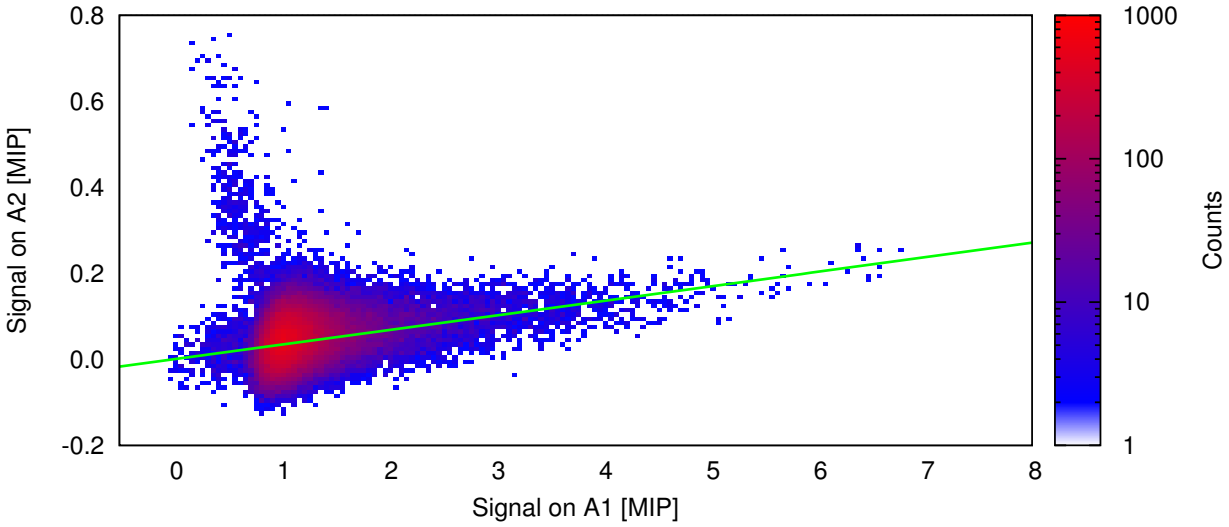

Figure 4.18: Relation of signal amplitude on A2 pad to the amplitude on channel A1 obtained for events with the reconstructed impact position inside pad A1.

reconstructed position inside the area of pad A1. In addition, only events identified to lie further than 200 μm from the pad border were used, to minimize the previously discussed effect of charge sharing. One can see the positive correlation between these amplitudes, that can be interpreted as a crosstalk. The green line represents the best linear fit. According to the definition (2.17), the slope of the line describes the crosstalk level. The A2 amplitudes above 0.3 MIP (group of hits at the top of Figure 4.18) are too high to be caused by the crosstalk. Such amplitudes are observed in cases when the signal on A1 is relatively small, which leads to the conclusion that the hit position is wrongly assigned by the telescope (real hit position is closer to the border the required 200 μm) and the high amplitude on A2 is caused by charge sharing between the pads. For the crosstalk measurement the common mode subtraction procedure was not applied. This ensures no artificially introduced biases; however, this comes at the cost of broader distributions, and therefore less precise results.

The summarized crosstalk coefficients between all channels are presented in Figure 4.19a. The significant crosstalk can be observed only between the closest neighbors. The value of the crosstalk coefficient between the closest neighbors, grouped by the feedback configuration, is shown in Figure 4.19b. According to expectations from the model described in chapter 2.2.2, the highest crosstalk is observed for pads with the longest fanout attached to it. Moreover, there is a significant difference between channels with different feedback type, which can be explained by the differences in the input impedance.

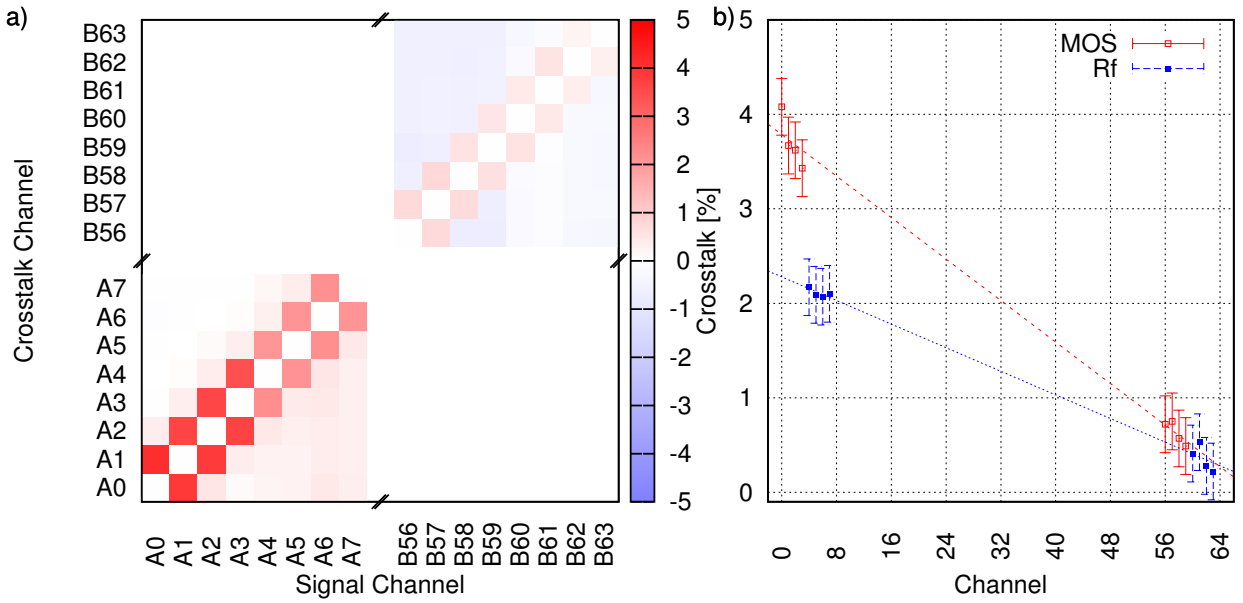

Figure 4.19: a) Measured crosstalk coefficients for groups of eight pads. b) Measured crosstalk coefficients to the closest neighbor.

4.3 Complete detector module

The analog module prototype of the LumiCal detector, described in previous chapter, validated the proper operation of the readout chain composed of silicon sensor, kapton fanout and front-end ASIC. To capture the analog waveforms, an external fast sampling ADC or a digital sampling oscilloscope were used. Due to the limited space available in the final detector, the only possible option is integration of a fast multichannel digitizer ASIC directly on the detector modules.

This chapter presents the development of a complete detector module. Besides the ADC integration into the readout chain, a detailed design of the first level DAQ is carried out. The developed DAQ system is able to effectively handle a stream of data continuously produced by the ADC. Moreover, issues specific to linear colliders, like power pulsing (see chapter 1.2.5) are addressed.

4.3.1 Architecture and design

Overview

The block diagram of the developed detector module is shown in Figure 4.20. In order to increase the system flexibility and to allow operation with different sensors (e.g. BeamCal), the signal is sent to front-end electronics through a multi-way connector. The signal is then amplified and shaped in the dedicated front-end ASIC, and digitized in the dedicated multichannel digitizer ASIC, continuously sampling the front-end output. There are four pairs of front-end and digitizer ASICs, 8 channels each, giving 32 channels in total.

To apply sampling synchronous with the beam, as planned for the experiments at the ILC, the

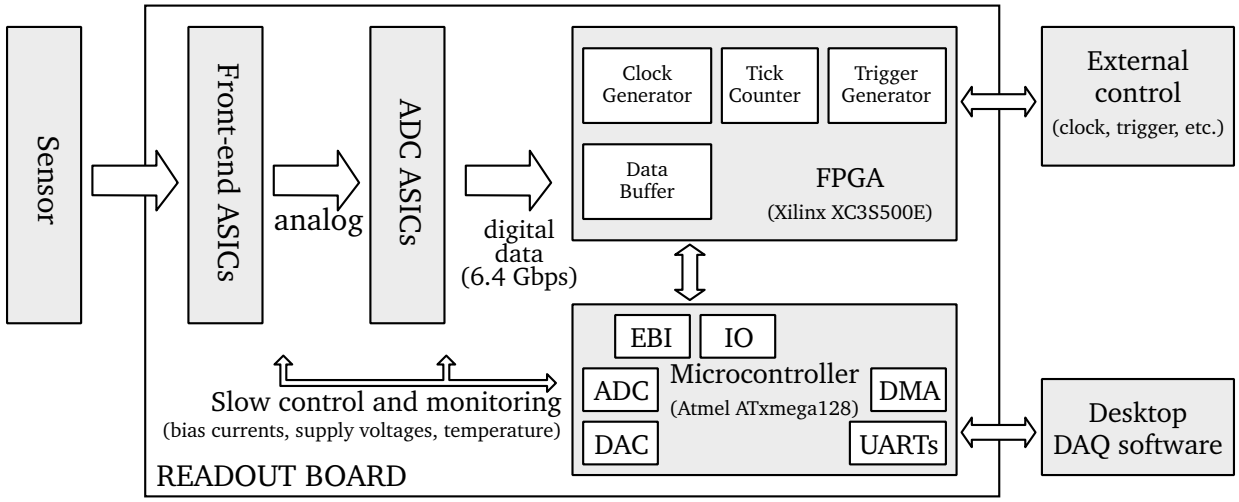

Figure 4.20: Complete detector module block diagram.

sampling rate of approximately 3 MSps would be enough (or even 1 MSps in conditions available at DESYII testbeam). For such sampling rates, the multichannel digitizer can operate in full serialization mode, where the data from all channels are transmitted over one LVDS link. Since the system should be as flexible as possible, the possibility of working with much higher sampling rates was requested. The laboratory measurements of the deconvolution-based processing showed that results close to optimal are obtained for the sampling period similar to the shaping time of the shaper. For this reason, the signal on each channel should be sampled with up to 20 MSps. Keeping in mind that the digitizer has 10-bit resolution, the raw data stream of about 6.4 Gbps is expected.

Other important readout aspects concern the trigger generation. An external trigger signal may or may not be provided to the detector module. If an external trigger is not available, the detector must generate one itself, for example by tracking the signal level and comparing it to the threshold value (see chapter 2.8.9). There are also situations, like previously described testbeam measurements of the analog detector module, in which several detectors work together, measuring different properties of the radiation emitted by a single source. It is necessary to apply a mechanism to synchronize the readout from all of them. Moreover, it is also useful to have them working with common DAQ software, to control the process and store the data in a uniform way.

The digitized data stream is continuously recorded in a buffer inside the FPGA. When a trigger condition occurs, the acquisition is interrupted and the microcontroller firmware builds an event packet and transmits it to a host PC. To fulfill high throughput requirements, the architecture of the digital part is based on a low-cost, high-density Spartan XC3500E FPGA [4] and the ATxmega128A1 microcontroller [5]. The use of the microcontroller was motivated by its

[4]Spartan XC3500E is a FPGA device provided by Xilinx Co. More information can be found at http://www.xilinx.com/.

[5]Atxmega128A1 is 8-bit microcontroller provided by Atmel Co. More information can be found at http://www.atmel.com/

analog features, namely a set of 12-bit ADCs and DACs, which were used to control and monitor the ASICs operating conditions. In addition, splitting the DAQ tasks allowed a higher data rate to be obtained by the FPGA to be utilized, and provided the user with a more convenient control interface.

FPGA hardware implementation

The FPGA firmware was modeled using Verilog HDL and subsequently synthesized in the Xilinx ISE design flow tools. It comprises the following custom Intellectual Property cores (IP Core): clock generator, data deserializers and data buffers, trigger generator, timestamping counter and microcontroller interface.

The clock generator block is responsible for providing the clock signals for the ADCs and data buffer accesses. The clock signal can be produced internally or an external clock signal may be connected and adjusted. A high-level view of the clock system tree is presented in Figure 4.21.

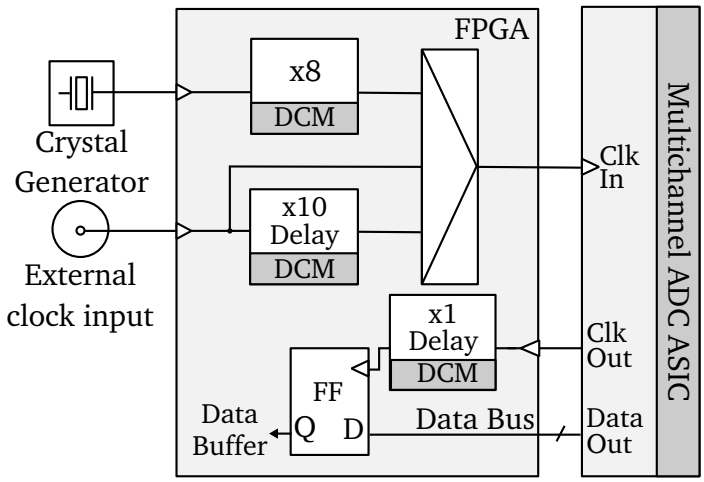

Figure 4.21: Block diagram of clocking subsystem.

The internal clock of 192 MHz is generated by multiplying by 8 the clock from the on-board 24 MHz crystal generator. To perform this operation, the Digital Clock Manager (DCM) block inside the FPGA is used. An external clock signal can be sent directly to the ADC, or it can be internally multiplied by 10. It is meant to be used for synchronous operation (with ILC-like beam, laser, pulse generator). To simplify the process of adjusting phase difference between the sampling clock and the front-end pulse, an additional configurable delay was implemented. Such solution allows for equalizing delays (e.g. from different cable lengths) in the final setup. The clock source can be dynamically changed during the operation. The clock signal delivered to the ADC is mirrored by the chip so that its phase is in a fixed relation to the digital data transmitted by the ADC. In highly-integrated system, like the described module, it is almost impossible to equalize the track lengths on PCB for all data signals. To address this issue, the phase of the clock provided by the ADC can be aligned in the DCM stage in order to find the best instant to sample the data lines. This adjustment is made once at the system startup, utilizing the digital pattern generator incorporated in each digitizer ASIC.

The deserialized data from the ADC are stored in a circular buffer and passed to comparators in the trigger generation unit. The buffer is implemented using a dual port Block RAM (BRAM), and is capable of storing up to 128 samples per channel. By taking advantage of dual port operation, it was possible to apply simultaneous write by the FPGA and read by the microcontroller.

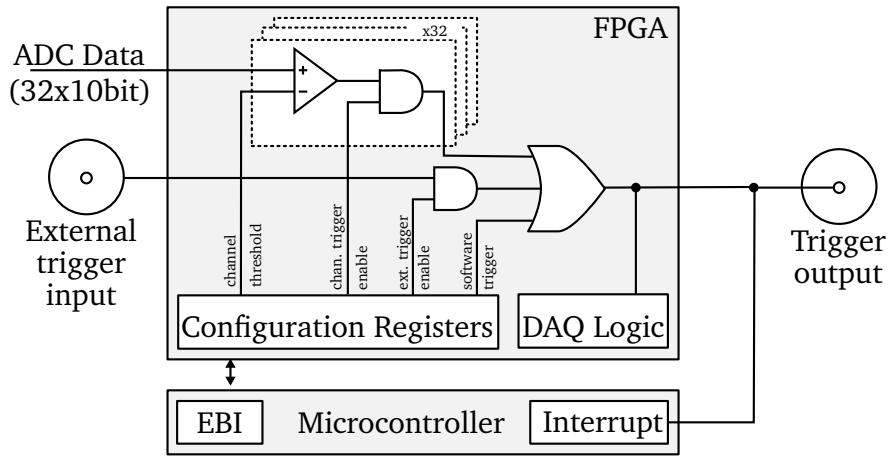

Figure 4.22: Block diagram of trigger subsystem.

The trigger generation unit, shown in Figure 4.22, generates trigger pulses based on the state of digital comparators outputs and external trigger input. The trigger can also be generated upon software request. Trigger sources can be enabled separately. The threshold values for comparators are configured individually for each channel, and the microcontroller firmware can compute the optimal threshold values based on baseline estimation.

A timestamp counter is implemented inside the FPGA to enhance the detector module with the time measurement capabilities. The timestamp counter operates at the same speed as the ADC sample rate. Each event is tagged with the value of the timestamp counter. It allows for a raw time estimation with the precision, dependent on the ADC sample rate, up to 50 ns (see chapter 2.6). This precision can be further improved by applying the deconvolution algorithm, to single nanoseconds (as described in chapter 2.8). The length of 64-bits ensures that even for the fastest sampling rates, the counter will not overflow.

The registers which control operation of all blocks described above, as well as data buffers, are accessible for the microcontroller through the External Bus Interface (EBI).

Other hardware

The possibility of running the front-end and ADC with non-continuous power dissipation is very useful feature, allowing to benefit from the beam timing structure like the one in future linear colliders. A technique based on switching off the analog bias currents and disabling the clock was adopted in the proposed system. The digitizer ASIC incorporates the dedicated circuitry and uses an external CMOS signal to control the state of its operation (see chapter 3.3). The front-end ASIC does not have such feature built in, so it had to be implemented externally with discrete components mounted on the PCB. To limit the peak current flowing to the system a 2200 μF low

Equivalent Series Resistance (ESR) storage capacitor was added (see Figure 4.23). It is followed by a Low Drop-Out (LDO) voltage regulator to ensure a stable supply voltage for the ASICs. The DACs in the ATxmega, followed by voltage-controlled current sources, are used to adjust biasing currents for the front-end ASICs.

In addition, a set of voltage and current monitors across the circuit was incorporated. The schematic diagram of the power control block is shown in Figure 4.23. The 10 mΩ shunt resistor together with Zero-Drift Series Current Shunt Monitor INA210 are used to measure current. The voltage signals corresponding to ASICs supply voltages, currents and temperature are connected to ATxmega ADC inputs via on-board analog multiplexers, controlled by ATxmega Input/Output (IO) pins. The use of 12-bit/1.5 MSps ADCs in ATxmega allows for measuring transient responses and slowly monitoring all supplies during normal physics runs. The obtained results may help in explaining possible anomalies in collected data and optionally adjust them according to the required ASICs operating conditions.

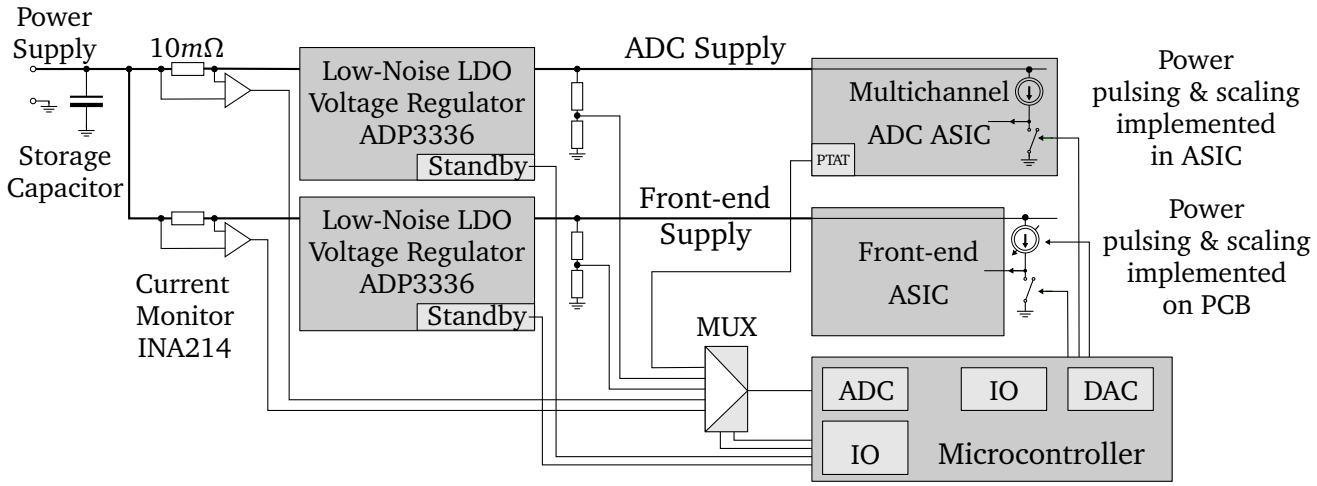

Figure 4.23: Schematic diagram of power delivery and system monitoring circuitry.

The connection between the readout system and an external host is implemented using the USB 2.0 interface. The FTDI Chip FT4232H [111] device is used as a USB to Universal asynchronous receiver/transmitter (UART) (Universal Asynchronous Receiver/Transmitter) bridge. It provides 4 independent UART interfaces, which are connected directly to ATxmega hardware UARTs.

The signals for synchronization with other detectors are available in different voltage standards (LVDS or Low Voltage Complementary Metal-Oxide Semiconductor (LV CMOS)) and on different connectors (LEMO or High-Definition Multimedia Interface (HDMI)).

Microcontroller firmware

The microcontroller firmware is written in C and built using the GNU toolchain. Its top-level architecture is shown in Figure 4.24. The firmware consists of four tasks running concurrently.

They are ordered by decreasing priority as follows: data acquisition, data transmission, monitoring system operating conditions, and user interface for configuration and calibration. The tasks are controlled by a small Real Time Operating System (RTOS), the use of which made the development of the firmware easier while keeping the trigger response time short. The abstraction layers for the drivers and the RTOS make the firmware independent of any particular platform. Such an architecture allows for cross-platform testing, and makes it easier to reuse the current firmware in future systems based on similar operating principle, but built using different hardware.

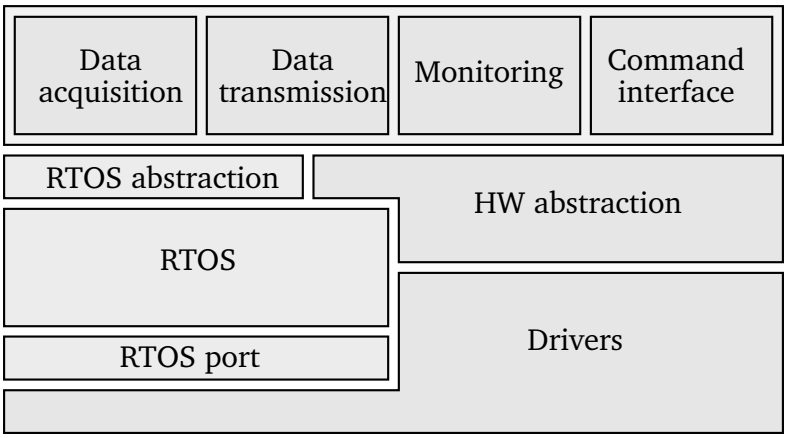

Figure 4.24: Diagram of the architecture of microcontroller firmware.

Data acquisition

The data acquisition principle is presented in Figure 4.25. The FPGA continuously accumulates

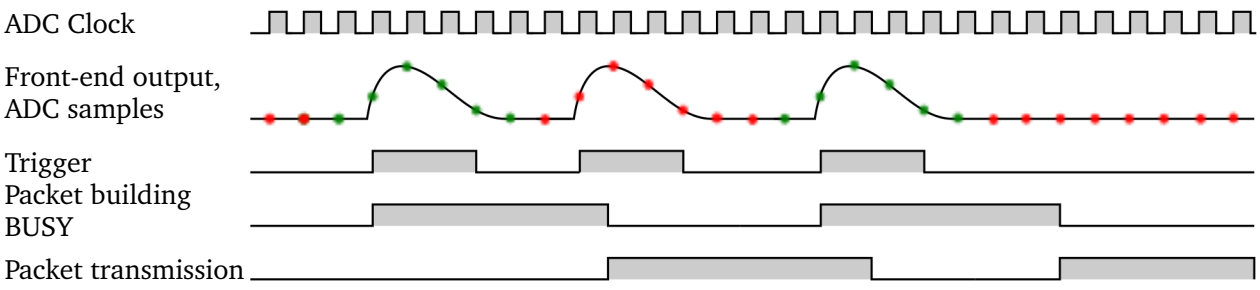

Figure 4.25: System waveforms (green dots on front-end waveform represent accepted samples while red ones are rejected).

the data in a circular buffer. The occurrence of one of trigger conditions causes the FPGA to collect a predefined number of subsequent samples (the post-trigger samples) and generates the interrupt signal for the microcontroller. Independently of what caused the trigger, this information is propagated to the output, giving the possibility of synchronization with other detector

systems, including other boards of the same type. The Busy signal can be generated to suppress accepting new triggers by other detectors.

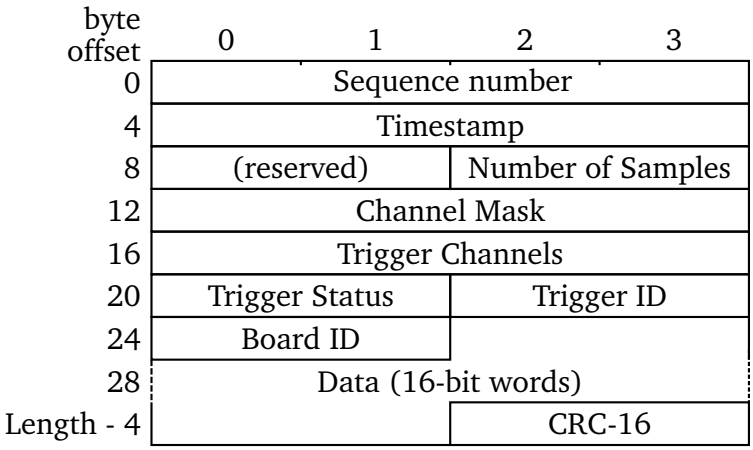

Figure 4.26: Structure of event packet.

The interrupt causes the real-time kernel to immediately switch the execution context to the data acquisition task which builds the event packet. The structure of the packet is shown in Figure 4.26. The *Sequence Number* and the *CRC-16* code are used to ensure the data integrity and to detect possible transmission errors. The precise *Timestamp* and the *Trigger ID* (optionally provided from an external source, e.g. the Trigger Logic Unit (TLU) [112]) are used for the synchronization of data when building events from multiple detectors. The *Channel Mask* and the *Number of Samples* per channel determine the interpretation of the *Data* field of the packet, and allow for suppressing channels without interesting information (i.e. all samples below threshold) in order to reduce the packet size and to increase the number of processed events per time unit. The information about the state of all trigger sources is stored in the *Trigger Info* field.

Once the packet is built, it is passed to the data transmission task, which transmits it in the background using the Direct Memory Access (DMA) transfer from the memory to the serial port. The Busy signal is cleared, which enables acceptance of a new event and processing it in the second buffer. Due to double buffering, the busy interval is shorter and the data link occupation rate can be kept close to 100%.

Communication and data transmission

From the supervising host perspective, the USB bridge is seen as four byte-oriented virtual serial port connections. Each of them can be accessed using an ordinary terminal emulator software, such as PuTTY. On the first port, a command interface to read or modify the system configuration is available. It supports Standard Commands for Programmable Instruments (SCPI)-like [113] syntax and command completion and history to facilitate direct usage by a human operator. The second port is meant for printing logs and system operating conditions. The third port is used for transmission of packets with event data. The fourth port currently remains unused, but can be potentially employed to double the data transmission rate.

The whole system was also integrated with the EUDAQ platform—a portable desktop DAQ system designed for use with the EUDET pixel detector [114]. Using EUDAQ provided a common

graphical user interface as well as data acquisition and storage infrastructure. It can be used in configurations with one or more instances of the presented system, or in heterogeneous multi-detector experiments.

4.3.2 System design

The complete detector module is composed of two PCBs (see Figure 4.27). The first PCB com-

Figure 4.27: Photograph of the complete LumiCal detector module.

prises of a silicon sensor. The kapton fanout glued on top of the sensor delivers signals from the sensor pads to the sensor edge, where connection to the PCB is ensured by means of wire bonding. The second part of the fanout, which allows matching the tracks pitch to the multi-way connector pitch, is implemented on the PCB. The significant advantages of such approach are reusability of the sensor board and direct access to all sensor pads (which can be used to measure I-V and C-V curves for each sensor pad). The drawback of this design is elongated fanout tracks, and the resulting increased capacitances (to ground and inter-strip).

The prototype of the readout system was assembled on a 6-layer PCB. The photograph of an assembled detector module is shown in Figure 4.27. To verify and to quantify the multichannel readout performance, various measurements of different system sections and the complete readout chain were executed. For the analog part, the measurements of input dynamic range, gain, noise, and their uniformities were performed. For the digital part, the data transmission rate and the event trigger rate in different readout conditions were measured. The performance of the complete readout system in self-triggering mode was verified with cosmic rays. Additionally, the measurements of power consumption and thermal system behavior in the power pulsing mode were done.

4.3.3 Input Dynamic Range, Gain and Noise

The linearity, the gain and the input dynamic range of the front-end electronics were measured in the external trigger mode with synchronous sampling, and using the calibration input signal. The measured amplitude versus input charge for one of the channels is shown in Figure 4.28a for all possible combinations of the front-end and shaper gain settings. The channel response is very linear. The non-linearity, calculated as a difference between the linear fit and the measurement points, normalized to the full scale and expressed in % is shown in Figure 4.28b. It can be observed that the front-end may be used for signals in the range 0.5 fC-10 pC.

The gain level and its distribution obtained in the high gain mode (HH) for all readout channels are presented in Figure 4.29a and Figure 4.29b, respectively. Clear pattern grouping channels with the same feedback type are visible.

The noise level and the distributions of ENC for all channels, without and with the sensor, are shown in Figure 4.29c and Figure 4.29d, respectively. The electronics noise only (without sensor) is in the range from 0.04 fC (for channels with passive feedback) up to 0.06 fC (for channels with active feedback). The obtained level is only slightly higher than the noise level measured in chapter 3.2.2. These results are caused by two factors. Firstly, as one can see, the noise level is very low in terms of LSB, and so the quantization noise contribution is significant. From the other hand, the fanout between the ASIC and the multi-way connector increase the total capacitance connected to the preamplifier input. The obtained results prove the correctness of the complete module design because no crosstalk between the digital and the analog part is observed.

The ENC level obtained with the sensor remains within range from 0.31 fC up to 0.37 fC, for passive and active feedback, respectively. After applying the common mode subtraction procedure (as described in chapter 4.2.3) the ENC stays in the range from 0.16 fC up to 0.18 fC. With such noise level, the SNR for the MIP is around 20. The noise level is significantly higher than the one obtained for the analog module. The increased ENC can be caused by the fact that the fanout between the ASIC and the sensor is much longer than in the analog prototype; more-

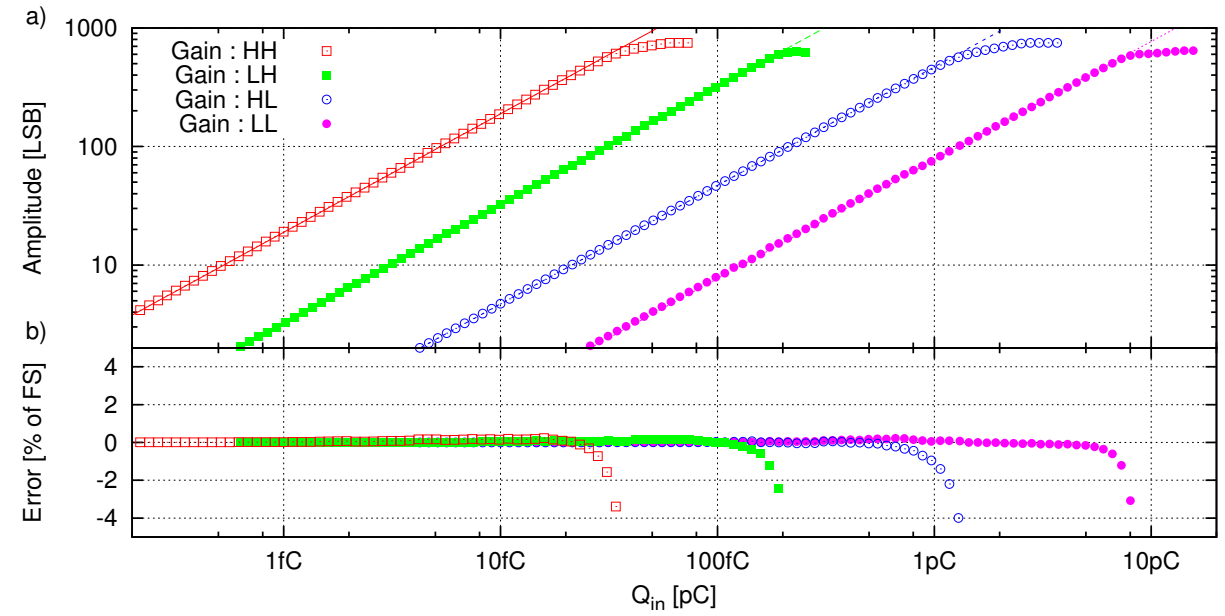

Figure 4.28: a) Measurement of the gain and the input dynamic range of the front-end ASIC. b) Non linearity of the chain transfer function.

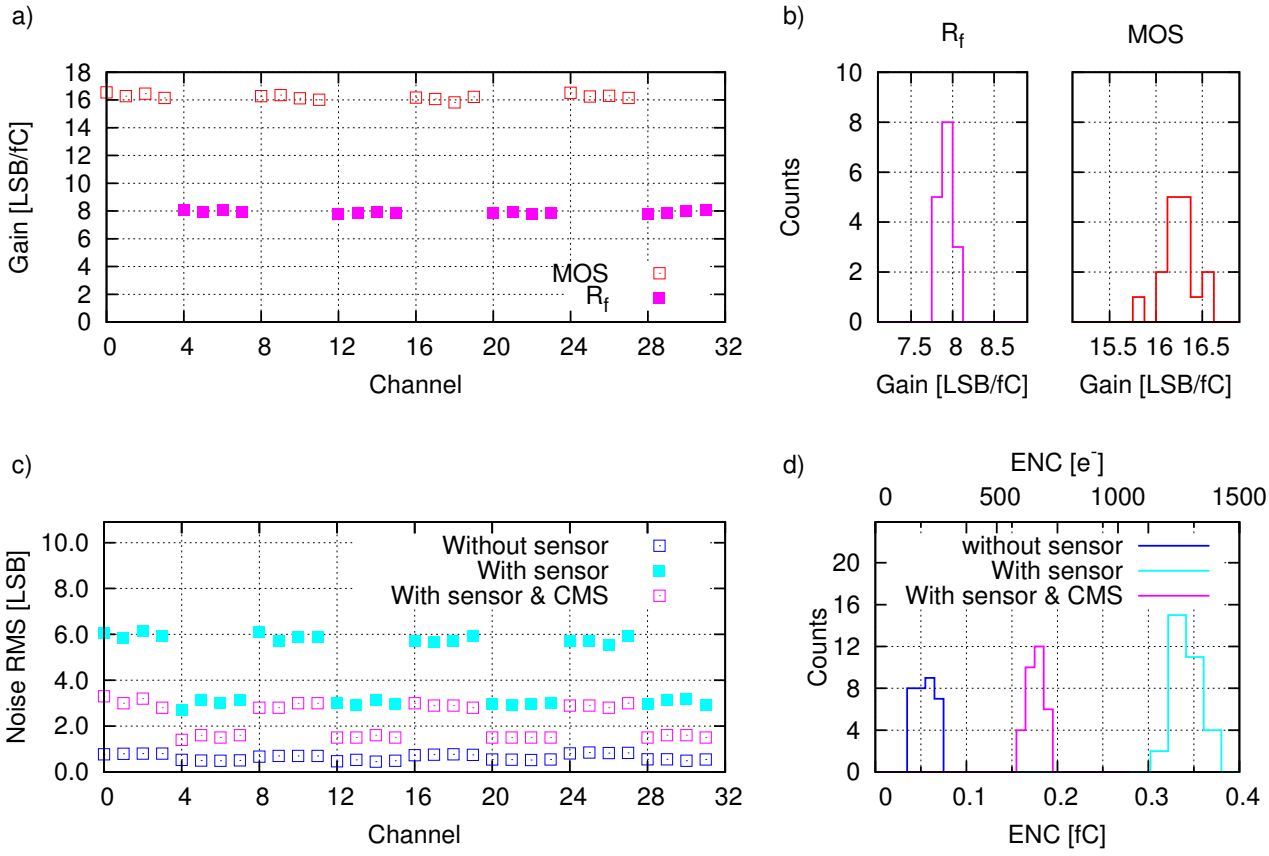

Figure 4.29: a) Channel gains in high gain mode (HH) b) Gain distributions for channels with passive (R_f) and active feedback (MOS). c) Noise level with and without sensor connected. d) Noise level distributions.

over, the fanout is interrupted by the multi-way connector. The elongated fanout, apart from having higher stray capacitance, is a good antenna. One should bear in mind that the modular construction was introduced for the flexibility purpose, and that in the final detector the readout ASICs are going to be located as close to the sensor as possible. Nevertheless, the obtained SNR is sufficient to perform valuable measurements.

4.3.4 Data transmission rate and event rate

One of the key requirements for the developed readout system was to obtain the highest rate of data transmission between the digitizer ASIC and the FPGA chip. The memory implemented inside the FPGA allows one to record an event containing up to 128 continuous samples for each channel. In order to be able to process the digital data efficiently, the ADC sampling period had to be similar or shorter than the peaking time of the front-end ASIC (∼60 ns) as described in chapter 2.8. This requirement enforces the minimum transmission rate of 170 Mbps per channel or 5.44 Gbps for the whole system of 32 channels working in parallel. The performed tests showed that the system works well for ADC sampling frequencies above 20 MHz, corresponding to the digitizer–FPGA data transfers beyond 6.4 Gbps. The efficiency of data transfer was verified by running the digitizer ASIC in the test mode, for which a known data pattern was generated in the digitizer and transferred to the Spartan FPGA. After these tests, an external 24 MHz crystal clock generator was mounted on the PCB, resulting in the default transmission rate of 192 Mbps per channel (6.14 Gbps for the 32-channel system).

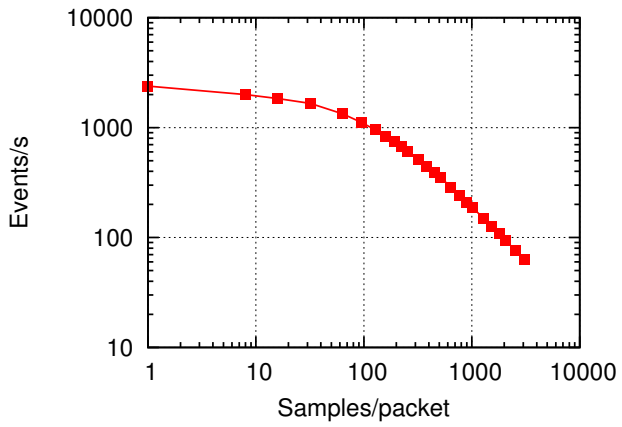

Figure 4.30: Event rate versus number of ADC samples per packet.

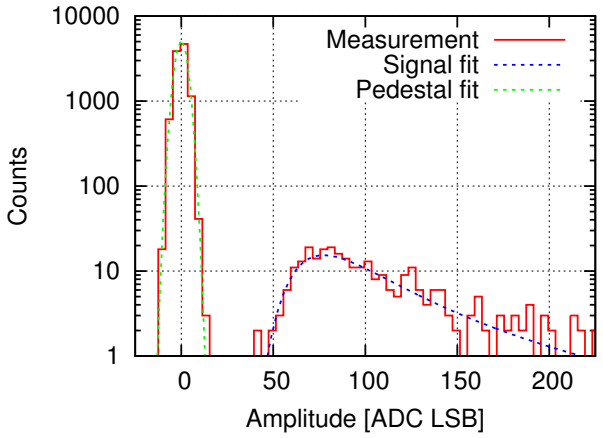

Figure 4.31: Energy deposition spectrum for cosmic particles collected from one channel.

The developed system was designed to be used in the test beams where the typical trigger rate is of the order of 100 event/s. Such trigger rate does not require high transmission speed between the readout system and the host PC and so this feature has not been of high importance. The measured event processing rate as a function of number of samples per event is shown in Figure 4.30. For event packets containing more than 200 samples the relationship is close to linear, and the event rate depends strictly on the transmission speed. It is limited by the standard USB bridge drivers which do not allow operation at baud rates higher than 4 Mbps. For smaller event packets the limitation is imposed by the cost of packet construction. For the minimum

packet size (one synchronous sample from only 1 channel) the system is capable of capturing up to 2400 events per second. The asynchronous sampling requires 3 signal samples to properly reconstruct the time of pulse occurrence and the amplitude (see chapter 2.8). In such a case, the rate is about 2000 events per second for 1 channel, and decreases to 1100 events per second when reading all channels (96 samples per packet). The same event rate per board was obtained with two boards working concurrently.

The measured event rate makes the system suitable for use with typical test beams and cosmic radiation. If needed, the transmission rate can be further increased by using specialized drivers which allow baud rates up to 12 Mbps, by enabling fourth UART, or by implementing proprietary data link utilizing signals on HDMI connector. The packet construction time can be reduced by delegating part of this process to FPGA.

4.3.5 Operation of full readout chain

To test the operation of the complete detector module in self-triggering mode, the cosmic muons were measured. The threshold levels were set to 6 RMS of noise above the baseline, for each channel independently. All channels were verified to work properly. To reconstruct the events the deconvolution algorithm was used. An example of measured spectrum is presented in Figure 4.31. To prepare this plot, only events with exactly one channel triggered were selected, and the average baseline level was subtracted. The number of entries in the pedestal peak is approximately 31 times higher than the number of entries in the signal peak, because the system was triggering acquisition when the signal level at any channel exceeded the threshold level. The measured spectrum (red curve) fits well to convoluted Landau and Gaussian distribution (blue curve), confirming the proper operation of the whole readout chain.

4.3.6 Power pulsing and thermal issues

The readout system was designed in order to allow the study of the front-end ASIC and the digitizer ASIC under pulsed power operation. The power pulsing was not applied to the FPGA and the microcontroller since these parts of the readout were designed only for testbeam purpose. In the final detector system the data concentration will be realized in an ASIC or by a newer generation, lower power, FPGA chip.

The power consumption transients were measured by switching the power “on” at time 0 and “off” 1 ms later (which reproduces the ILC beam conditions). The results are presented in Figure 4.32a. It can be seen that in the power off state the power consumption is more than 30 times lower than in the power on state. In the power off state the consumption is caused by peripheral circuits (DACs, bandgap, etc.), which are common for all channels and for which, in the present system version, the power cycling was not implemented. In the final system a much higher power-on/power-off ratio can be obtained since more channels will be integrated together and/or power cycling of peripheral circuits will be added. It was verified that the commercial voltage regulators are capable of handling sudden current changes with no effect on output voltage. The rising/falling slopes in Figure 4.32a are related to recharging the on-board decoupling capacitances.

Apart from the power-on/power-off ratio, the most important parameter in the power cycling is the time needed by the readout electronics to restart correct operation after receiving the

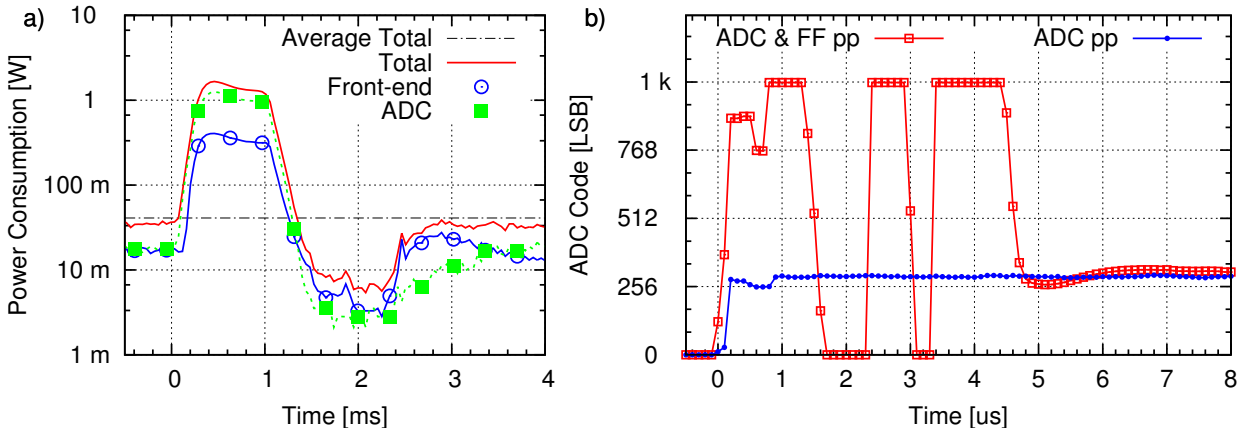

Figure 4.32: Power pulsing measurements a) transients of power consumption from voltage regulators b) transients of ADC output codes (red—both ADC and Frond-end ASIC were power pulsed, blue—only ADC was power pulsed).

power on signal. In Figure 4.32b the ADC output (codes from one of ADCs) as a function of time is presented. The ADCs were operating with sampling frequency 10 MSps and were switched on at time 0. The blue curve was obtained with the front-end working continuously, and so it shows the effect of ADC power cycling. The measurement confirms the results described in chapter 3.3.3, showing that the ADC needs fewer than 10 samples to restart correct conversion. The red curve shows the measured ADC response when power cycling was applied for the whole frond-end plus ADC chain. It is seen that less than 7 μs are needed to stabilize the baseline and to be ready to accept events. Comparing the two curves it may be concluded that the front-end ASIC needs about 7 μs to restart correct operation.

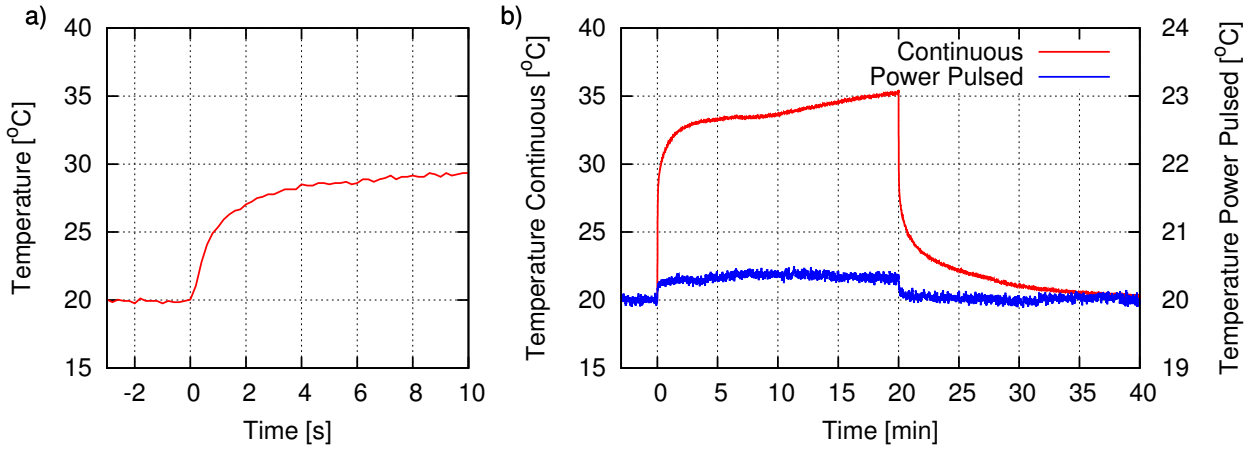

Figure 4.33: Transients of temperature (ASICs switched on at 0).

A very important aspect of the detector system is its thermal stability. The thermal behavior of the system was studied for continuous operation and in the power pulsing mode. In order to understand the thermal transient, the temperature output of the multichannel digitizer ASIC was monitored after switching the power on at time 0. The results are shown in Figure 4.33a. A fast

exponential temperature increase by ∼10 °C with time constant of about 1–2 s is observed. In Figure 4.33b, the temperature output of the multichannel digitizer ASIC is shown for continuous operation (red curve) and for the ILC-like (1 ms on, 199 ms off) power pulsing mode (blue curve), after switching the power on at time 0 (and off after 20 minutes). It can be observed that at continuous operation the ASIC temperature changes are much higher (>10 °C) than in the power pulsing mode (<0.5 °C). This drives us to the conclusion that operation with power pulsing at frequency above few Hz should not affect the thermal equilibrium of the system.

4.4 Testbeams with complete detector module

4.4.1 Testbeam setup

The testbeam setup used for the complete detector module measurements was very similar to the setup used for analog module (see chapter 4.2.2). The major differences were related to the DAQ system. The overview of the testbeam setup is presented in Figure 4.34.

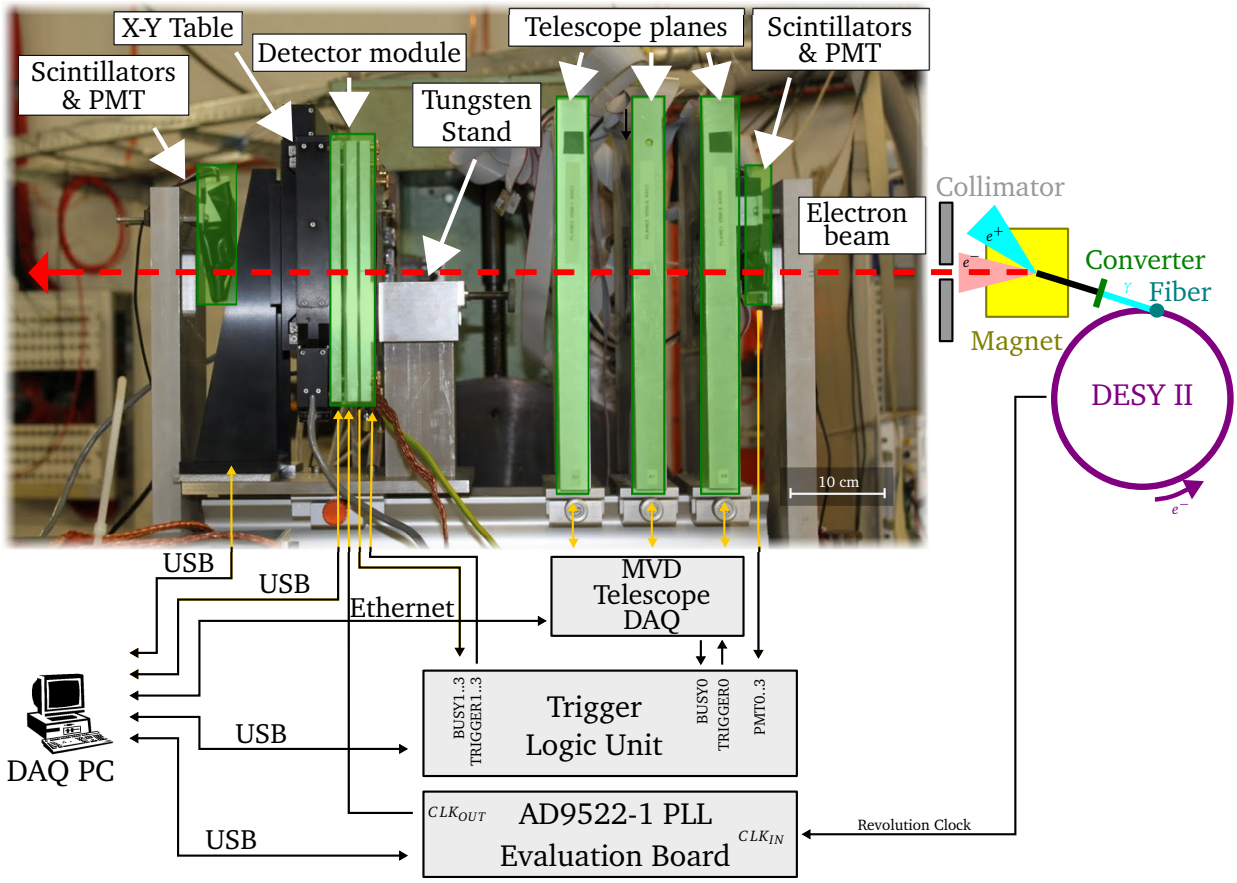

Figure 4.34: Overview of experimental setup used during complete detector module testbeam measurements.

To enable the detector module testing in both modes of operation – synchronous and asynchronous – the beam revolution clock was delivered from the accelerator complex to the test setup. Because the beam clock is too slow to be directly used by the detector module (limitation of DCM in the used FPGA), the clock is firstly multiplied by a factor of 16 by AD9522-1 PLL Evaluation Board (for more details see chapter 3.3.2). The acquired samples may always be decimated in order to reproduce the exact ILC-like data stream.

The DAQ scheme was more complex than during the first testbeam. The TLU [112] was used instead of Nuclear Instrumentation Module (NIM) module to generate and distribute information about trigger to sub-detectors. Besides acting as a coincidence unit, for each trigger the TLU provides additional trigger identification number. This number can be used later on during the data analysis to synchronize events between different DAQ systems in more robust way. A connection between the TLU supervising DAQ PC allowed for more convenient run control. At data collection up to two complete detector modules mounted one behind the other, were working simultaneously and probing the data.

Moreover, an additional precisely-aligned stand for tungsten plates were added in front of detector modules to provide the possibility of shower-development studies. The stand enabled variable tungsten thickness, ranging from one radiation length (3.5 mm) up to 14 radiation lengths (49 mm).

4.4.2 Amplitude reconstruction

The complete detector module was found to be fully operational within the described experimental testbeam setup. The data were collected in two modes of operation: synchronous and asynchronous with beam.

The example measured points collected in the asynchronous mode are presented in Figure 4.35. The on board clock generator 192 MHz (divided internally by 10 by the digitizer

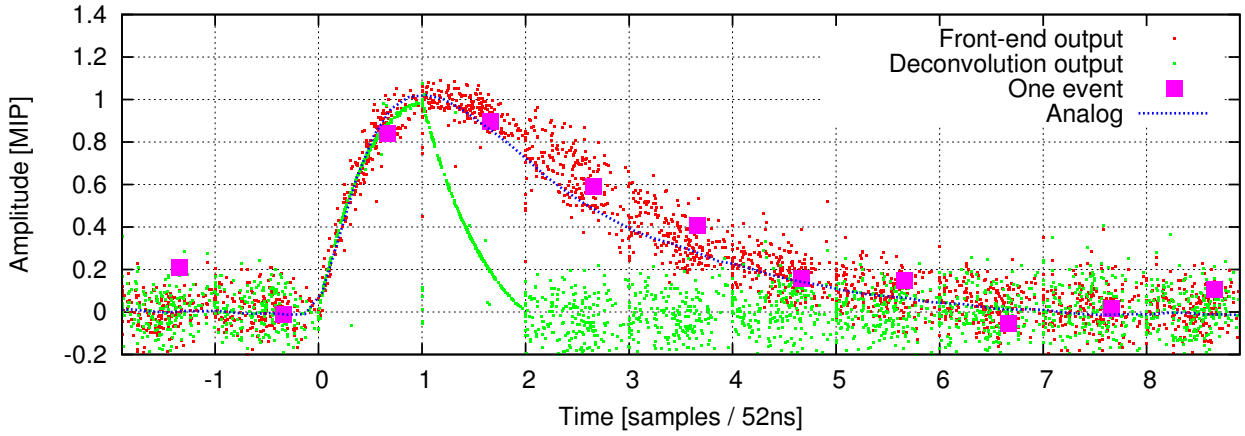

Figure 4.35: Effect of deconvolution processing (green) on input pulses (red). The pulses were time-aligned using the time information obtained from the deconvolution algorithm.

ASIC) was used as a sampling clock. The events (of the same reconstructed amplitude) are plotted in red, while the output of the deconvolution filter is shown in green. The blue waveform

obtained with analog module is shown as a reference. The events were precisely time-aligned using the information about the time obtained from the deconvolution processing algorithm (as described in chapter 2.8). One can see that the measurements with an electron beam reproduce very well the results obtained with a laser (presented in Figure 3.27). The difference in two plots is caused by the fact that for the laser measurements the signal amplitude was constant while for the testbeam measurements the signal amplitude is random, and the reconstructed amplitude needs to be used in order to select similar events.

4.4.3 Position reconstruction

Using the approach described in chapter 4.2.4, the particle impact point on the detector plane was reconstructed. In Figure 4.36 one can see the combined information from LumiCal DAQ and the telescope DAQ.

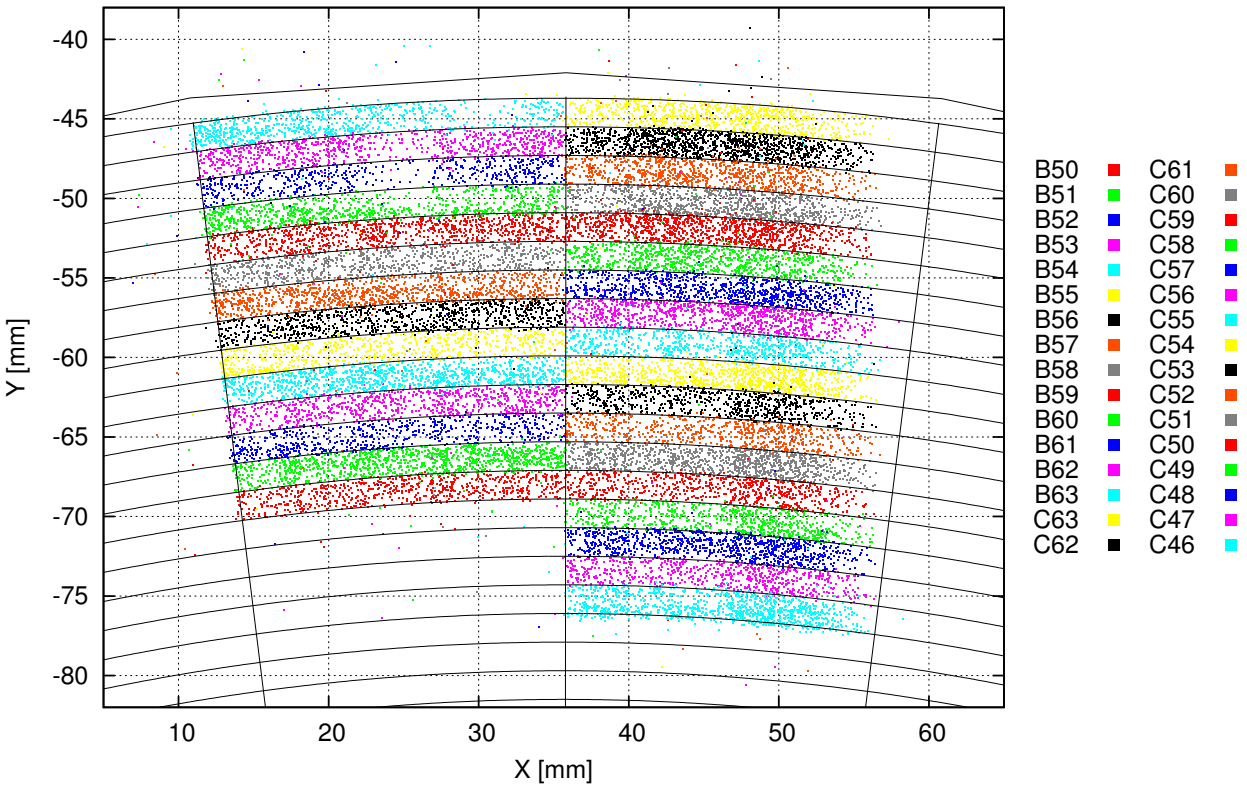

Figure 4.36: Reconstructed position of beam particle impact point combined with signals registered in LumiCal sensor pads.

The structure of the LumiCal sensor (outlined in black) is very well reflected by the reconstructed points. The lack of points close to the edge of right pads was identified to be related to the problem with the X-Y table. During the position sweeping over the whole instrumented area, the motorized table reached its limit position. Because the on-line data validation was based only on the monitoring of the number of hits in channels, this problem was discovered during off-line data analysis, and it was impossible to repeat the measurement.

4.4.4 System performance

The baseline level was estimated in the same way as it was presented for the analog module in chapter 4.2.3. The distributions of pulse heights obtained in asynchronous mode for a single channel with resistor and active feedback configurations responding to a passage of a single 4.5 GeV electron are presented in red in Figure 4.37a and Figure 4.37b, respectively. The obtained distributions follow very well the distributions obtained with the analog detector module (see Figure 4.8). Two major differences can be noticed. Firstly, the energy deposition levels

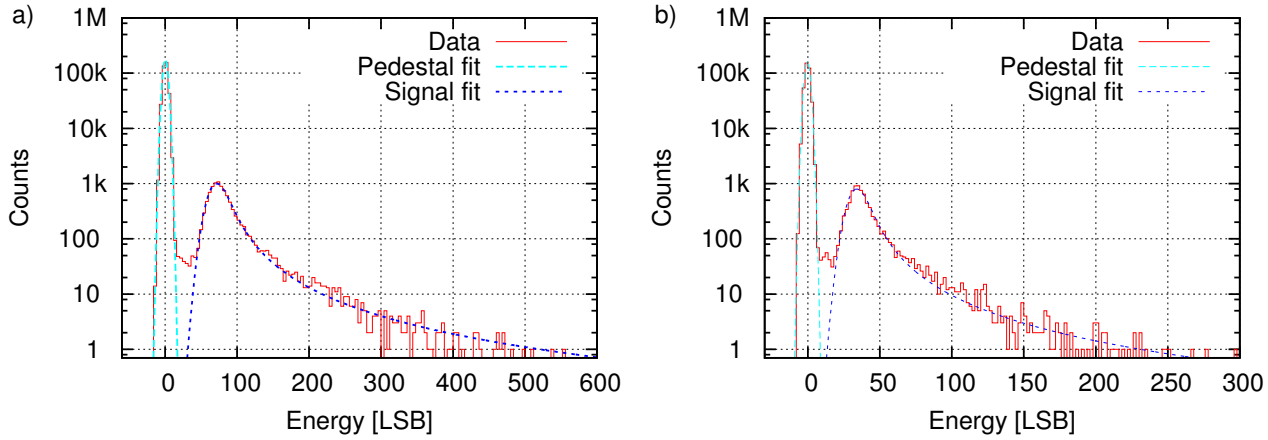

Figure 4.37: Energy deposition spectrum obtained after common mode subtraction and rejection of events with position close to pad borders in a) B58 pad (active feedback) and b) B62 pad (passive feedback) .

expressed in the LSB are much lower than for the analog module. This fact is related to the difference in the ADC resolution used to digitalize signal from the analog detector module (14 bit) and the ADC used in the complete detector prototype (10 bit). The second noticeable difference is a broader width of both – signal and pedestal – distributions. To investigate this behavior the detailed studies of the gain and the noise level were conducted for all channels. The results are summarized in Table 4.3. The obtained gains and noise level correspond very well to the measurements taken in the laboratory.

Most of the analyses performed for the analog module were also repeated for the complete detector module. The lower statistics of the collected events and worse SNR during the testbeams with the complete detector module affected the precision of the measurements. Since the obtained results agree qualitatively with the results presented in chapter 4.2, they are not presented here.

4.4.5 Response of detector module to the electromagnetic shower

During the testbeam measurements the possibility of using a complete detector module to record an electromagnetic shower was verified experimentally. Because of the stochastic character of the development of electromagnetic shower with a limited number of sensor layers (up to two in this case), only the statistical parameters can be analyzed.

Table 4.3: Gain, noise level and SNR extracted from the measured spectra for all channels in the complete detector module.

Pad	ASIC	Type	Gain [LSB / MIP]	Noise [LSB]	SNR	SNR_{CMS}
B50	ASIC0	MOS	69.4	6.3	11.0	20.0
B51	ASIC0	MOS	68.1	5.9	11.6	20.5
B52	ASIC0	MOS	68.5	5.8	11.8	20.8
B53	ASIC0	MOS	67.4	5.8	11.7	20.6
B54	ASIC0	R_f	32.6	2.8	11.5	19.8
B55	ASIC0	R_f	32.3	2.8	11.4	19.3
B56	ASIC0	R_f	32.9	2.9	11.3	19.6
B57	ASIC0	R_f	32.3	2.8	11.4	19.4
B58	ASIC1	MOS	68.8	5.6	12.3	22.2
B59	ASIC1	MOS	68.6	5.5	12.5	22.5
B60	ASIC1	MOS	68.2	5.7	11.9	21.6
B61	ASIC1	MOS	68.0	6.0	11.4	20.4
B62	ASIC1	R_f	32.1	2.9	11.0	19.0
B63	ASIC1	R_f	31.9	2.8	11.5	20.8
C63	ASIC1	R_f	32.5	2.7	12.2	21.7
C62	ASIC1	R_f	32.3	2.6	12.4	21.1
C61	ASIC2	MOS	69.2	5.4	12.9	21.6
C60	ASIC2	MOS	68.0	5.3	12.9	21.6
C59	ASIC2	MOS	67.6	5.2	12.9	21.6
C58	ASIC2	MOS	68.7	5.2	13.1	21.9
C57	ASIC2	R_f	32.0	2.5	12.8	20.8
C56	ASIC2	R_f	32.3	2.6	12.5	20.3
C55	ASIC2	R_f	32.1	2.5	12.7	20.2
C54	ASIC2	R_f	32.2	2.5	12.7	20.2
C53	ASIC3	MOS	69.5	4.9	14.2	19.7
C52	ASIC3	MOS	69.3	4.7	14.8	20.0
C51	ASIC3	MOS	68.8	4.7	14.7	20.1
C50	ASIC3	MOS	68.8	4.7	14.6	19.6
C49	ASIC3	R_f	31.9	2.3	13.7	18.7
C48	ASIC3	R_f	32.3	2.3	14.0	18.8
C47	ASIC3	R_f	32.6	2.3	14.0	19.1
C46	ASIC3	R_f	32.8	2.4	13.9	19.7

For these studies, the electron beam was directed to the center of the instrumented area (edge between pad B57 and pad C57) of the sensor plane. A similar setup was prepared for the MC simulations using GEANT4 framework by IFJ PAN group. The electron beam was modeled as a collection of electrons with parallel tracks collimated to the square shape.

Tungsten absorber plates were added in variable quantities in order to observe shower development at its subsequent phases. 3.5 mm thick tungsten plates, corresponding roughly to one radiation length, were positioned on a precisely aligned stand (see chapter 4.4.1). For each setup configuration (with variable tungsten amount in the front) 50.000 events were collected and analyzed.

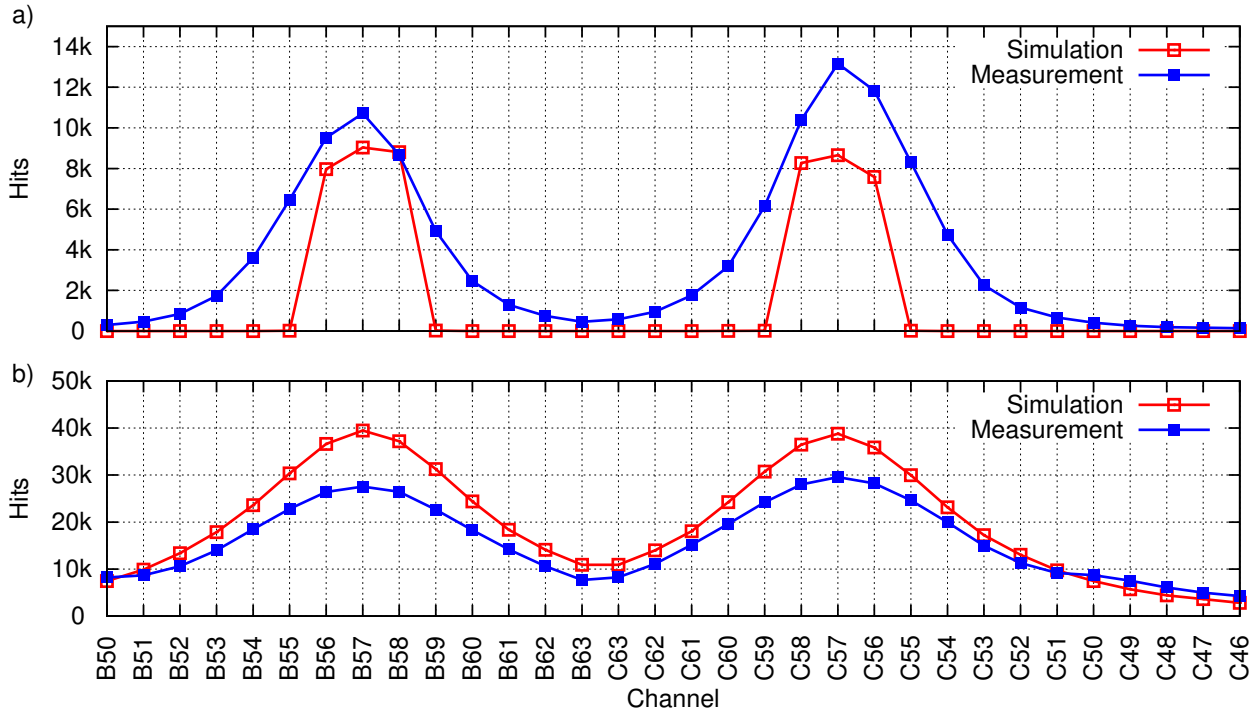

Figure 4.38: Simulated (red) and measured (blue) number of the hits recorded in the sensor pad with a) no tungsten absorber b) six radiation lengths of tungsten absorber in front of the detector module.

The numbers of hits registered in the detector channels for various absorber thicknesses are presented in Figure 4.38. One can see that more events were recorded in pad C57 than in pad B57, which shows that the beam was slightly shifted to the right of the sensor plane. Moreover, the measured distribution is much broader than the simulated one, which means that the assumption about tracks being parallel is over simplified. In the case with the tungsten absorber (Figure 4.38b), the observed distribution is much broader. This fact is related to the transverse size of the electromagnetic cascade increase, due to multiple scattering of electrons and positrons away from the shower axis, as described in chapter 1.2.3.

Example spectra of the total energy deposited in the instrumented area at different phases of shower development are shown in Figure 4.39. The measured spectra very well reproduce the results obtained in the MC simulations. A small excess of events with low energy is consistent with the hypothesis about the electrons tracks not being parallel to the detector plane. Such

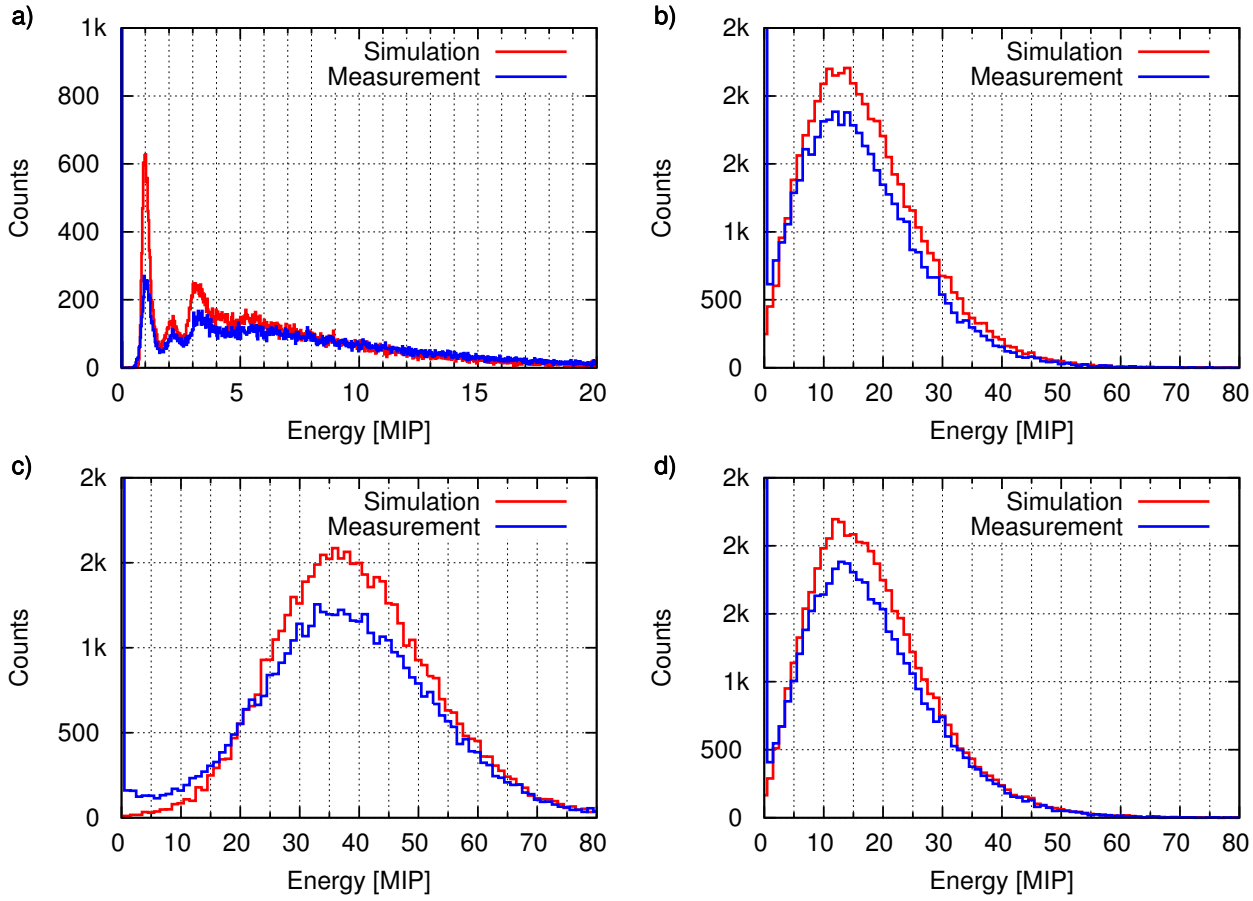

Figure 4.39: Energy deposition in the whole instrumented area with a) 1 b) 2 c) 6 d) 10 tungsten layers (each 3.5 mm thick) in the front of the sensor plane.

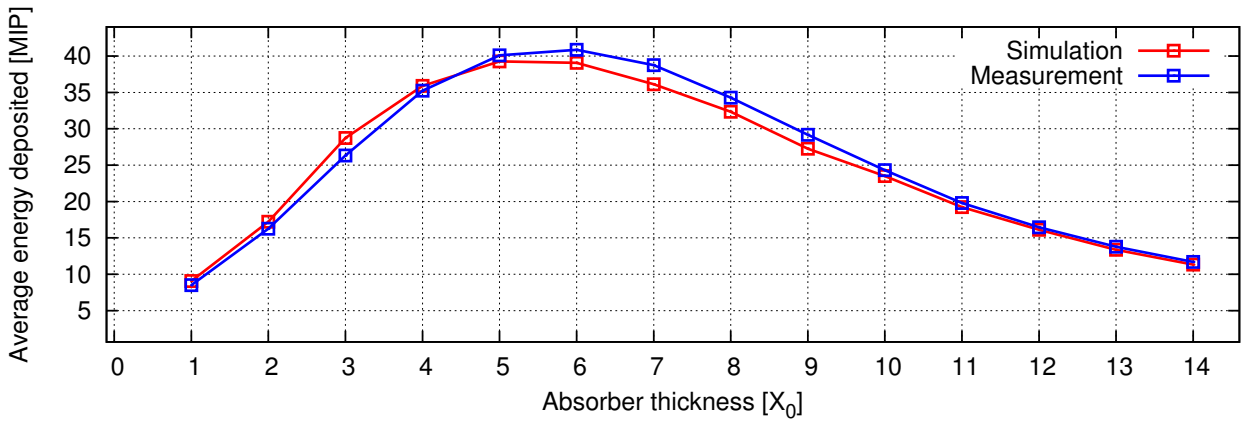

Figure 4.40: Average energy deposited in the instrumented area as a function of the tungsten absorber thickness expressed in radiation lengths.

electrons would leave less energy in the instrumented area.

The average energy deposited in the whole instrumented area as a function of the tungsten thickness is shown in Figure 4.40. The reasonable agreement with MC is found. The measured shower maximum is observed after six tungsten plates. The 3D profile of the recorded electromagnetic showers is shown in Figure 4.41.

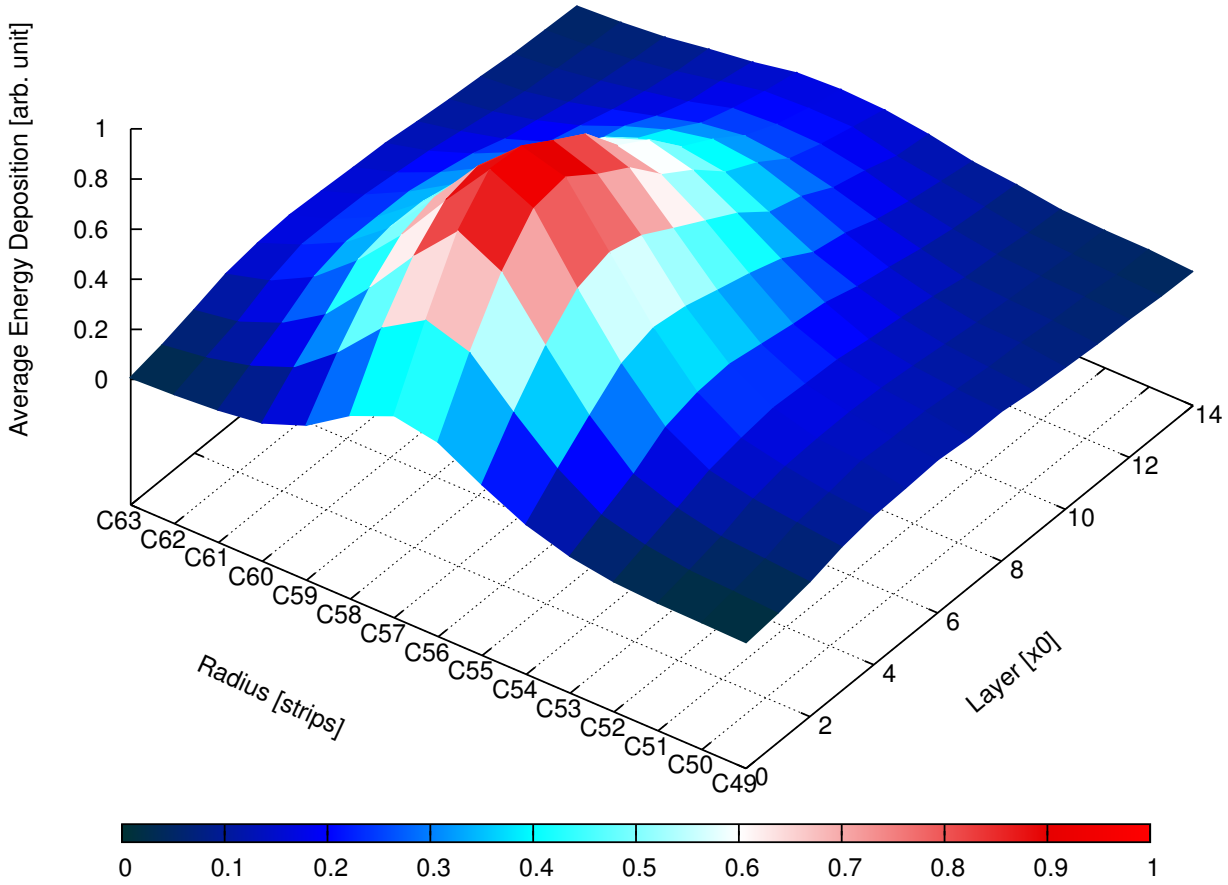

Figure 4.41: The averaged 3D profile of the recorded electromagnetic showers.

The measurements performed with the tungsten absorber in front of the complete detector module validated its usefulness in recording electromagnetic showers. Small differences between the measurements and the MC simulations were found and their possible origins were pointed out. At this phase of the LumiCal construction, this is fully tolerable and will be addressed in future studies of the FCAL collaboration, when the detector prototype with a several active planes is available.

Summary

The main objective of this dissertation was to develop a complete LumiCal detector module in order to validate the proposed detector readout architecture and enable the detector performance studies. The validation was expected to cover various design levels: starting from detector components parameterization, through the detector module construction, up to the system tests in laboratory and testbeam measurements.

The main objectives of the dissertation have been fully attained. The possibility of using the designed complex readout system to extract information from radiation sensors and to further process it with the proposed hardware and software blocks has been proven experimentally, also during the testbeams. Various works have been necessary in order to achieve the presented goals. The major conducted activities with the author's contribution are listed below:

- *Concept of readout architecture for the LumiCal detector*

  The requirements for the LumiCal detector readout were established and based on them the readout architecture was proposed (chapter 1.3.3). The author took an active part in the discussions and the determination of the LumiCal readout architecture concept [115, 48].

- *Application of Digital Signal Processing to extract information from radiation sensors*

  The author investigated the possibility of using Digital Signal Processing to extract the information about the time and the amplitude of event from the radiation sensor. Comprehensive theoretical studies, covering various aspects of the signal processing using a deconvolution-based filter, were conducted (chapter 2.8) [116]. Formulas describing the impact of various parameters (e.g. sampling frequency, ADC resolution, signal amplitude, etc.) on the amplitude and time reconstruction performance were obtained and discussed [116].

- *Parametrization of LumiCal readout chain components*

  The components of the LumiCal readout chain were designed, fabricated, and parameterized before the module construction. The author was responsible for the preparation of the test setups for the front-end and ADC converter ASICs parameterization (chapter 3.2 and chapter 3.3). The test setups, composed from the dedicated PCBs and the dedicated software, were used by the author to perform extensive measurements. The analyzed measurement data were used to improve the components design and were published in [88, 100, 98, 99, 89].

- *Experimental verification of the deconvolution based readout*

The performance of the deconvolution-based readout was verified experimentally (chapter 3.4). The author prepared the dedicated experimental test setup, which allowed him to perform the measurements using various signal sources. Additionally, the MC simulation framework, capable to generate event's waveform precisely reflecting measurements, was developed. The measured and the simulated data were carefully analyzed by the author and the performance of the time and the amplitude extraction were compared with theoretical predictions.

- *Development of the detector modules*

  Two detector modules were designed and built at subsequent project phases. The first module comprises of limited functionalities with analog signal output (as described in chapter 4.1), while the second one includes all functionalities, including data conversion, data concentration and the embedded power pulsing feature (as described in chapter 4.3). The author proposed the modules architecture, selected the necessary components and designed the dedicated PCBs. In the next step, the author developed entire firmware for the on board FPGA and a part of the firmware for on board microcontroller [117]. The developed firmware was validated in computer simulations and in hardware operation.

- *Power pulsing studies*

  The feasibility of power pulsing in the radiation detector system was investigated by the author during the module construction. The measurements of the possible reduction in power consumption, the component's wake-up times, as well as thermal response of detector components in the case of pulsed power were performed.

- *Detector modules testing and parameterization*

  The detector modules were carefully tested and parameterized in laboratory (chapter 4.3.2). The performance of all readout channels (e.g. gain, offset, noise level) was measured in all possible modes of operation. Extensive data-taking tests verified the proper architecture and design of all hardware and firmware blocks. The self-triggering feature of the developed module was proven to work as expected during test runs with cosmic particles.

- *Testbeam with the detector modules*

  The constructed detector modules were used during the FCAL collaboration testbeams. The author was responsible for the preparation and the technical coordination of the testbeam setups (chapters 4.2.2 and 4.4). He actively participated in data-taking runs during three testbeams organized on an electron beam at DESY Hamburg. Several million triggers were recorded using both detector modules.

- *Testbeam data analysis*

  The testbeam data were analyzed to understand the detector module performance. The author prepared the dedicated software which allowed him to accurately analyze all the data acquired with the LumiCal sensor. Among others, he investigated the detector's response to high energy electrons, the sensor's uniformity, the crosstalk between readout channels, and the impact of common mode disturbances on the obtained results. The performed analysis furnished ample information about the performance of the module's building blocks, as

well as about the module itself (chapter 4.2 and 4.4.4) [118]. The data obtained during runs with the tungsten absorber in front of the detector module were used to calculate the electromagnetic shower profile and to validate the MC tools used for electromagnetic shower development simulations.

The developed detector module validated the proposed detector readout architecture. In its current shape, apart from the required miniaturization, it fulfills all requirements established for the LumiCal detector at the ILC. The detector module design is very universal; it allows for various sampling schemes and sampling rates, it has power pulsing feature embedded, it can be integrated with DAQ systems commonly used by linear collider community. Moreover, the detector modules allowed to perform R&D works in the field of application of DSP for amplitude and time extraction from radiation sensor. This type of signal processing appears to be a very promising candidate for the detector systems which require precise information about time and amplitude, and where high events occupancy is expected.

During the long course of R&D work, the author gathered unique experience in development and testing of the advanced radiation-detector system. His works covered all phases of a typical HEP experiment, starting from the conceptual design, going through detailed engineering of hardware and software components, and finishing at the analysis of the data taken during the testbeam measurements.

Besides the fact that the current module is fully functional and meets all major functional requirements, some aspects may and should be improved in the future. Firstly, the module should be miniaturized in order to fulfill the tight geometrical constrains of the final detector. The usage of a newer, fabricated in a smaller feature size technology, ASICs (currently being developed by the AGH-UST group), should allow to further reduce the overall power consumption, minimize the occupied area, and increase the processing speed. Employment of a newer FPGA device will further increase the capacity of data buffers and the possible processing speed. The dedicated DSP resources available in modern FPGA devices are perfectly suitable to perform on-line computation of deconvolution equations. Faster serial interface would allow to increase the transmission rate and thus the possible trigger rate. All possible improvements should also increase the module usefulness in other applications.

Acronyms

AC	Alternating Current	49
ADC	Analog-to-Digital Converter	41
ALICE	A Large Ion Collider Experiment	16
APV	Analog Pipeline Voltage	67
ASIC	Application Specific Integrated Circuit	33
ATLAS	A Toroidal LHC Aparatus	16
BDS	Beam Delivery System	22
BOX	Buried OXide	29
BPI	Byte Peripheral Interface	94
BRAM	Block RAM	93
BSM	Beyond Standard Model	16
BeamCal	Beam Calorimeter	9
CCC	Clock & Control Card	35
CERN	Conseil Européen pour la Recherche Nucléaire	16
CLIC	Compact Linear Collider at CERN	13
CMOS	Complementary Metal-Oxide Semiconductor	28
CMS	Compact Muon Solenoid	16
CVD	Chemical Vapor Deposition	40
DAC	Digital-to-Analog Converter	60
DAQ	Data Acquisition System	43
DC	Direct Current	21
DCC	Data Concentrator Card	35
DCM	Digital Clock Manager	128
DDR	Double Data Rate	92
DEPFET	DEPleted Field Effect Transistor	28
DESY	Deutsches Elektronen-Synchrotron	21
DIF	Detetcor InterFace	35
DLL	Delay-Locked Loop	65

DMA Direct Memory Access 132
DNL Differential Nonlinearity 95
DPA Dynamic Phase Alignment 92
DSP Digital Signal Processing 14
DUT Device Under Test 92
EBI External Bus Interface 129
ECAL Electromagnetic Calorimeter 31
EMI ElectroMagnetic Interference 86
ENC Equivalent Noise Charge 56
ENOB Effective Number Of Bits 96
ESR Equivalent Series Resistance 130
FCal Forward Calorimeter 85
FEM Finite Element Method 42
FET Field Effect Transistor 29
FF Flip-Flop 65
FFT Fast Fourier Transfom 93
FIFO First In, First Out 93
FIR Finite Impulse Response 67
FPGA Field-Programmable Gate Array 92
Fermilab Fermi National Accelerator Laboratory 21
GEM Gas Electron Multiplier 48
GPIB General Purpose Interface Bus 94
GUT Grand Unified Theory 20
HCAL Hadronic Calorimeter 31
HDL Hardware Description Language 93
HDMI High-Definition Multimedia Interface 130
HEP High Energy Physics 17
HERA Hadron-Electron Ring Accelerator 16
IC Integrated Circuit 93
IIR Infinite Impulse Response 67
ILC International Linear Collider 13
ILD International Large Detector 26
INL Integral Nonlinearity 95
IO Input/Output 92
IP Interaction Point 22

KEK High Energy Accelerator Research Organization 21
LDA Link Data Agregator 35
LDO Low Drop-Out 130
LEP Large Electron Positron Collider 16
LHC Large Hadron Collider 13
LHCb Large Hadron Collider beauty 16
LSB Least Significant Bit 60
LUT Look-Up-Table 83
LV CMOS Low Voltage Complementary Metal-Oxide Semiconductor 130
LVDS Low-Voltage Differential Signaling 91
LumiCal Luminosity Calorimeter 9
MAPS Monolithic Active Pixel Sensors 28
MC Monte Carlo 25
MDAC Multiplying DAC 91
MIP Minimum Ionizing Particle 43
MOS Metal-Oxide Semiconductor 29
MPV Most Probable Value 47
MSB Most Significant Bit 61
MVD Micro Vertex Detector 115
Micromegas Micro-MEsh Gaseous Structure 48
NIM Nuclear Instrumentation Module 140
NMOS N-channel Metal-Oxide Semiconductor 28
ODR Off Detector Receiver 35
PC Personal Computer 94
PCB Printed Circuit Board 89
pCT Proton Computed Tomography 36
PFA Particle Flow reconstruction Algorithm 26
PHY PHYsical layer driver 92
PLL Phase Locked Loop 93
PMT PhotoMulTiplier 100
POSIX Portable Operating System Interface for Unix 94
PTAT Proportional To Absolute Temperature 91
PZC Pole-Zero Cancellation 88
QCD Quantum Chromodynamics 17
QED Quantum ElectroDynamics 25

RF Radio Frequency . . . 22
RMS Root Mean Square . . . 56
RPC Resistive Plate Chamber . . . 34
RTOS Real Time Operating System . . . 94
SAR Successive-Approximation-Register . . . 59
SCPI Standard Commands for Programmable Instruments . . . 132
SCRF Superconducting Radio Frequency . . . 21
SDRAM Synchronous Dynamic Random-Access Memory . . . 92
SFDR Spurious Free Dynamic Range . . . 96
SINAD Signal to Noise and Distortion Ratio . . . 96
SLAC Stanford Linear Accelerator Center . . . 21
SM Standard Model . . . 15
SNHR Signal to Non Harmonic Ratio . . . 96
SNR Signal-to-Noise Ratio . . . 55
SOI Silicon On Insulator . . . 28
SPI Serial Peripheral Interface . . . 93
SPS Super Proton Synchrotron . . . 16
SUSY Supersymmetry . . . 20
SiD Silicon Detector . . . 26
SiPM Silicon Photo Multiplier . . . 34
TAC Time-to-Amplitude Conversion . . . 64
TDC Time-to-Digital Converter . . . 63
THD Total Harmonic Distortion . . . 96
TLU Trigger Logic Unit . . . 132
TOT Time-Over-Threshold . . . 64
TPC Time Projection Chamber . . . 30
UART Universal asynchronous receiver/transmitter . . . 130
USB Universal Serial Bus . . . 94
VCO Voltage-Controlled Oscillator . . . 93
VIA Vertical Interconnect Access . . . 29
VLSI Very Large Scale Integration . . . 55
VTX Vertex Detector . . . 28

Bibliography

[1] O. S. Brüning, P. Collier, P. Lebrun, S. Myers, R. Ostojic, J. Poole, and P. Proudlock, *LHC Design Report*. Geneva: CERN, 2004. [Online]. Available: http://ab-div.web.cern.ch/ab-div/publications/LHC-DesignReport.html [Accessed: 8 July 2012]

[2] J. Brau, Y. Okada, N. Walker, and et al, Eds., *International Linear Collider Reference Design Report*. ILC Global Design Effort and World Wide Study, Aug. 2007, vol. 2: Executive Summary. [Online]. Available: http://ilcdoc.linearcollider.org/record/6321/files/ILC_RDR_Volume_1-Executive_Summary.pdf [Accessed: 1 August 2012]

[3] A. Djouadi, J. Lykken, K. Mönig, Y. Okada, M. Oreglia, and S. Yamashita, Eds., *International Linear Collider Reference Design Report*. ILC Global Design Effort and World Wide Study, Aug. 2007, vol. 2: Physics at the ILC. [Online]. Available: http://ilcdoc.linearcollider.org/record/6321/files/ILC_RDR_Volume_2-Physics_at_the_ILC.pdf [Accessed: 1 August 2012]

[4] T. Behnke, C. Damerell, J. Jaros, and A. Miyamoto, Eds., *International Linear Collider Reference Design Report*. ILC Global Design Effort and World Wide Study, Aug. 2007, vol. 4: Detectors. [Online]. Available: http://ilcdoc.linearcollider.org/record/6321/files/ILC_RDR_Volume_4-Detectors.pdf [Accessed: 1 August 2012]

[5] N. Phinney, N. Toge, and N. Walker, Eds., *International Linear Collider Reference Design Report*. ILC Global Design Effort and World Wide Study, Aug. 2007, vol. 3: Accelerator. [Online]. Available: http://ilcdoc.linearcollider.org/record/6321/files/ILC_RDR_Volume_3-Accelerator.pdf [Accessed: 1 August 2012]

[6] M. Battaglia, A. de Roeck, J. R. Ellis, and D. Schulte, *Physics at the CLIC Multi-TeV Linear Collider : report of the CLIC Physics Working Group*. Geneva: CERN, 2004.

[7] L. Linssen and et al., *Physics and Detectors at CLIC: CLIC Conceptual Design Report*. CERN, 2012. [Online]. Available: http://arxiv.org/pdf/1202.5940v1 [Accessed: 8 July 2012]

[8] E. John and W. Ian, "New physics with the compact linear collider," *Nature*, vol. 409, 2001. [Online]. Available: http://dx.doi.org/10.1038/35053224 [Accessed: 8 July 2012]

[9] A. Djouadi, "The Anatomy of electro-weak symmetry breaking. II. The Higgs bosons in the minimal supersymmetric model," *Phys.Rept.*, vol. 459, pp. 1–241, 2008. [Online]. Available: http://arxiv.org/abs/hep-ph/0503173 [Accessed: 12 July 2012]

[10] J. Ellis, M. K. Gaillard, and D. Nanopoulos, "A phenomenological profile of the higgs boson," *Nuclear Physics B*, vol. 106, no. 0, pp. 292 – 340, 1976. [Online]. Available: http://www.sciencedirect.com/science/article/pii/0550321376903825 [Accessed: 14 June 2012]

[11] S. P. Martin, "A Supersymmetry primer," 1997. [Online]. Available: http://arxiv.org/abs/hep-ph/9709356/ [Accessed: 12 July 2012]

[12] C. Adolphsen and et al., "Zeroth order design report for the next linear collider," SLAC, Tech. Rep., 1996. [Online]. Available: http://www.slac.stanford.edu/pubs/slacreports/slac-r-474.html [Accessed: 9 July 2012]

[13] R. Brinkmann, G. Materlik, J. Rossbach, and A. Wagner, "Conceptual design of a 500-GeV e+ e- linear collider with integrated x-ray laser facility. Vol. 1-2," DESY, Tech. Rep., 1997, DESY-1997-048, ECFA-1997-182. [Online]. Available: http://www.desy.de/~schreibr/cdr/cdr.html [Accessed: 8 July 2012]

[14] The JLC Group, "Kek report 92-16," KEK, Tech. Rep., 1992. [Online]. Available: http://www-jlc.kek.jp/JLC.proposal-e.html [Accessed: 8 July 2012]

[15] R. Brinkmann, K. Flöttmann, J. Roßbach, and P. S. N. W. H. Weise, "Tesla technical design report," Tech. Rep., 2001. [Online]. Available: http://tesla.desy.de/new_pages/TDR_CD/start.html [Accessed: 12 Jun 2012]

[16] S. Stapnes and et al., *CLIC Conceptual Design Report*. CERN, 2012. [Online]. Available: http://project-clic-cdr.web.cern.ch/project-CLIC-CDR/ [Accessed: 8 July 2012]

[17] P. Lebrun, L. Linssen, A. Lucaci-Timoce, D. Schulte, F. Simon, S. Stapnes, N. Toge, H. Weerts, and J. Wells, *The CLIC programme: towards a staged e+e- linear collider*. CERN, 2012, vol. 3.

[18] K. Yokoya and P. Chen., "Beam-beam phenomena in linear colliders," KEK, Tech. Rep., April 1995, KEK Preprint 91-2. [Online]. Available: http://citeseerx.ist.psu.edu/viewdoc/summary?doi=10.1.1.44.2209 [Accessed: 12 July 2012]

[19] M. A. Pons, P. Bambade, and A. Faus-Golfe, "Luminosity, beamstrahlung energy loss and beam-beam deflection for e^+e^- and e^-e^- collisions at the ilc with 500 gev and varying transverse beam sizes," LAL, Tech. Rep., Jan 2006, LAL/RT 06-01. [Online]. Available: http://democrite.in2p3.fr/docs/00/06/09/71/PDF/LALRT0601PhBambade.pdf [Accessed: 12 July 2012]

[20] K. Yokoya and P. Chen, "Beam-beam phenomena in linear colliders," in *Frontiers of Particle Beams: Intensity Limitations*, ser. Lecture Notes in Physics. Springer Berlin Heidelberg, 1992, vol. 400, pp. 415–445. [Online]. Available: http://dx.doi.org/10.1007/3-540-55250-2_37 [Accessed: 12 Feb 2012]

[21] M. Ohlerich, "Investigations of the physics potential and detector development for the ilc," Ph.D. dissertation, Brandenburgischen Technischen Universität Cottbus, 2010. [Online].

Available: http://www-library.desy.de/preparch/desy/thesis/desy-thesis-10-008.pdf [Accessed: 14 June 2012]

[22] C. Rimbault, P. Bambade, K. Mönig, and D. Schulte, "Incoherent pair generation in a beam-beam interaction simulation," *Phys. Rev. ST Accel. Beams*, vol. 9, p. 034402, Mar 2006. [Online]. Available: http://link.aps.org/doi/10.1103/PhysRevSTAB.9.034402 [Accessed: 13 Feb 2012]

[23] P. Chen, T. L. Barklow, and M. E. Peskin, "Hadron production in gamma gamma collisions as a background for e+ e- linear colliders," *Phys.Rev.*, vol. D49, pp. 3209–3227, 1994. [Online]. Available: http://arxiv.org/abs/hep-ph/9305247 [Accessed: 14 July 2012]

[24] K. Mönig, "Tests of a particle flow algorithm with calice test beam data," *LC-PHSM-2000-060*, 2000. [Online]. Available: http://tesla.desy.de/new_pages/TDR_CD/PartIII/references/ref_bs.pdf [Accessed: 28 Jul 2012]

[25] A. P. Sailer, "Studies on the measurement of differential luminosity using bhabha events at the international linear collider," Master's thesis, Humboldt-Universität zu Berlin, 2009. [Online]. Available: http://www-library.desy.de/preparch/desy/thesis/desy-thesis-09-011.pdf [Accessed: 15 May 2012]

[26] T. Abe and et al., "The International Large Detector: Letter of Intent," ILD Concept Group - Linear Collider Collaboration, Tech. Rep., 2010, FERMILAB-LOI-2010-03, FERMILAB-PUB-09-682-E, DESY-2009-87, KEK-REPORT-2009-6. [Online]. Available: http://arxiv.org/pdf/1006.3396v1 [Accessed: 12 Jun 2011]

[27] H. Aihara and et al., "Sid letter of intent," SiD Collaboration, Tech. Rep., 2009, SLAC-R-944. [Online]. Available: http://arxiv.org/pdf/0911.0006v1 [Accessed: 10 Feb 2012]

[28] J. C. Brient and H. Videau, "The Calorimetry at the future e+ e- linear collider," *eConf*, vol. C010630, p. E3047, 2001. [Online]. Available: http://arxiv.org/abs/hep-ex/0202004 [Accessed: 26 June 2012]

[29] M. Thomson, "Particle flow calorimetry and the pandorapfa algorithm," *Nuclear Instruments and Methods in Physics Research Section A: Accelerators, Spectrometers, Detectors and Associated Equipment*, vol. 611, no. 1, pp. 25 – 40, 2009. [Online]. Available: http://www.sciencedirect.com/science/article/pii/S0168900209017264 [Accessed: 26 June 2012]

[30] R. Turchetta and et al., "A monolithic active pixel sensor for charged particle tracking and imaging using standard vlsi cmos technology," *Nuclear Instruments and Methods in Physics Research Section A: Accelerators, Spectrometers, Detectors and Associated Equipment*, vol. 458, no. 3, pp. 677 – 689, 2001. [Online]. Available: http://www.sciencedirect.com/science/article/pii/S0168900200008937 [Accessed: 17 July 2012]

[31] R. Richter and et al., "Design and technology of depfet pixel sensors for linear collider applications," *Nuclear Instruments and Methods in Physics Research Section A: Accelerators, Spectrometers, Detectors and Associated Equipment*, vol. 511, no. 1–2, pp. 250 – 256, 2003, Proceedings of the 11th International Workshop on Vertex Detectors. [Online]. Available: http://www.sciencedirect.com/science/article/pii/S0168900203018023 [Accessed: 17 July 2012]

[32] J. Marczewski, K. Domanski, P. Grabiec, M. Grodner, B. Jaroszewicz, A. Kociubinski, K. Kucharski, D. Tomaszewski, W. Kucewicz, S. Kuta, W. Machowski, H. Niemiec, M. Sapor, and M. Caccia, "Soi active pixel detectors of ionizing radiation-technology and design development," *Nuclear Science, IEEE Transactions on*, vol. 51, no. 3, pp. 1025 – 1028, june 2004.

[33] K. Nakamura and et al. (Particle Data Group), "The review of particle physics," *J.Phys.*, vol. G37, 2010.

[34] C. W. Fabjan and F. Gianotti, "Calorimetry for particle physics," *Rev. Mod. Phys.*, vol. 75, pp. 1243–1286, Oct 2003. [Online]. Available: http://link.aps.org/doi/10.1103/RevModPhys.75.1243 [Accessed: 22 Feb 2012]

[35] M. Anduze and et al., "Electromagnetic calorimeter technical design report," *EUDET-Memo*, no. 0, 2009. [Online]. Available: www.eudet.org/e26/e26/e27/e43691/eudet-report-09-01.pdf [Accessed: 25 July 2012]

[36] C. Adloff and et al. (CALICE Collaboration), "Measurement of the differential luminosity using bhabha events in the forward-tracking region at tesla," *Journal of Instrumentation*, vol. 6, no. 07, p. P07005, 2011. [Online]. Available: http://stacks.iop.org/1748-0221/6/i=07/a=P07005 [Accessed: 28 Jul 2012]

[37] J. Repond and et al. (CALICE Collaboration), "Design and electronics commissioning of the physics prototype of a si-w electromagnetic calorimeter for the international linear collider," *Journal of Instrumentation*, vol. 3, no. 08, p. P08001, 2008. [Online]. Available: http://stacks.iop.org/1748-0221/3/i=08/a=P08001 [Accessed: 10 May 2012]

[38] K.Gadow and et al., "Realization and results of the mechanical and electronics integration efforts for an analog hadronic calorimeter," *EUDET-Memo*, no. 02, 2010. [Online]. Available: http://www.eudet.org/e26/e28/e42441/e68452/EUDET-Memo-2009-10.doc [Accessed: 1 July 2012]

[39] B. Vincent, "Second generation daq for calice beam tests," in *Presented during International Workshop on Future Linear Colliders*, Sep. 2011. [Online]. Available: http://ilcagenda.linearcollider.org/contributionDisplay.py?contribId=235&sessionId=12&confId=5134 [Accessed: 02 Aug 2012]

[40] L. Wolfgang, "Ilc detector r&d: Its impact," in *Presented during International Workshop on Future Linear Colliders*, Sep. 2011. [Online]. Available: http://ilcagenda.linearcollider.org/getFile.py/access?contribId=160&sessionId=38&resId=0&materialId=slides&confId=5134 [Accessed: 28 Jul 2012]

[41] T. Abe and et al., "Belle ii technical design report," Belle Collaboration, Tech. Rep., 2010. [Online]. Available: http://arxiv.org/pdf/1011.0352v1 [Accessed: 1 Aug 2012]

[42] A. Bulgheroni, "Results from the eudet telescope with high resolution planes," *Nuclear Instruments and Methods in Physics Research Section A: Accelerators, Spectrometers, Detectors and Associated Equipment*, vol. 623, no. 1, pp. 399 – 401, 2010, 1st International Conference on Technology and Instrumentation in Particle Physics. [Online]. Available: http://www.sciencedirect.com/science/article/pii/S0168900210005760 [Accessed: 1 Aug 2012]

[43] M. Szelezniak and et al., "Cmos pixel vertex detector for star," *PoS VERTEX*, no. 032, 2008. [Online]. Available: http://pos.sissa.it/archive/conferences/068/032/VERTEX%202008_032.pdf [Accessed: 17 July 2012]

[44] N. Abgrall and et al., "Time projection chambers for the t2k near detectors," *Nuclear Instruments and Methods in Physics Research Section A: Accelerators, Spectrometers, Detectors and Associated Equipment*, vol. 637, no. 1, pp. 25 – 46, 2011. [Online]. Available: http://www.sciencedirect.com/science/article/pii/S0168900211003421 [Accessed: 17 July 2012]

[45] V. Rykalin, "R&d on detector of next generation for the proton computed tomography," in *Presented during Technology and Instrumentation in Particle Physics*, 2011. [Online]. Available: http://indico.cern.ch/contributionDisplay.py?contribId=232&sessionId=13&confId=102998 [Accessed: 28 Jul 2012]

[46] E. Netter and et al., "The tumor resection camera (trecam), a multipixel imaging probe for radio-guided surgery," *Nuclear Science Symposium Conference Record (NSS/MIC), IEEE*, pp. 2573 – 2576, 2009. [Online]. Available: http://dx.doi.org/10.1109/NSSMIC.2009.5402022 [Accessed: 28 Jul 2012]

[47] A. Bell and et al., "Fast beam conditions monitor bcm1f for the cms experiment," *Nuclear Instruments and Methods in Physics Research Section A: Accelerators, Spectrometers, Detectors and Associated Equipment*, vol. 614, no. 3, pp. 433 – 438, 2010. [Online]. Available: http://www.sciencedirect.com/science/article/pii/S0168900209023936 [Accessed: 28 Jul 2012]

[48] H. Abramowicz and et al. (S. Kulis), "Instrumentation of the very forward region of a linear collider detector," *Nuclear Science, IEEE Transactions on*, vol. 51, no. 6, pp. 2983 – 2989, dec. 2004. [Online]. Available: http://ieeexplore.ieee.org/stamp/stamp.jsp?tp=&arnumber=1369422 [Accessed: 12 July 2012]

[49] "FCAL Collaboration Web Site." [Online]. Available: http://http://fcal.desy.de/ [Accessed: 28 Jul 2012]

[50] E. Caffo, M ; Remiddi, "Bhabha scattering," *Workshop on Z Physics at LEP1*, vol. 1, pp. 171–202, Sep 1989.

[51] R. Bonciani and A. Ferroglia, "Bhabha scattering at nnlo," *Nuclear Physics B - Proceedings Supplements*, vol. 181–182, no. 0, pp. 259 – 263, 2008, Proceedings of the International Workshop on e+e- Collisions. [Online]. Available: http://www.sciencedirect.com/science/article/pii/S0920563208001655 [Accessed: 8 May 2012]

[52] S. Actis, M. Czakon, J. Gluza, and T. Riemann, "Fermionic NNLO contributions to Bhabha scattering," *Acta Phys.Polon.*, vol. B38, pp. 3517–3528, 2007.

[53] A. Penin, "Two-loop photonic corrections to massive bhabha scattering," *Nuclear Physics B*, vol. 734, no. 1–2, pp. 185 – 202, 2006. [Online]. Available: http://www.sciencedirect.com/science/article/pii/S055032130501000X [Accessed: 14 June 2012]

[54] "Superconducting darmstadt linear accelerator." [Online]. Available: http://www.ikp.tu-darmstadt.de/sdalinac_ikp/ [Accessed: 28 Jul 2012]

[55] C. Grah and et al., "Polycrystalline cvd diamonds for the beam calorimeter of the ilc," *Nuclear Science, IEEE Transactions on*, vol. 56, no. 2, pp. 462 –467, april 2009. [Online]. Available: http://dx.doi.org/10.1109/TNS.2009.2013853 [Accessed: 28 Jul 2012]

[56] C. Grah, K. Afanaciev, P. Bernitt, G. Chelkov, J. Gajewski, R. Heller, H. Henschel, A. Ignatenko, Z. Krumshteyn, S. Kulis, W. Lange, W. Lohmann, M. Ohlerich, A. Rosco, A. Sapronov, R. Schmidt, and S. Schuwalow, "Radiation hard sensors for the beam calorimeter of the ilc," in *Nuclear Science Symposium Conference Record, 2007. NSS '07. IEEE*, vol. 3, 26 2007-nov. 3 2007, pp. 2281 –2284. [Online]. Available: http://dx.doi.org/10.1109/NSSMIC.2007.4436601 [Accessed: 28 Jul 2012]

[57] A. Angel, "The bean: a pulse processor for a particle physics experiment," Ph.D. dissertation, Stanford University., 2011. [Online]. Available: http://purl.stanford.edu/pj537bm6926 [Accessed: 15 Aug 2012]

[58] K. Monig, "Physics needs for the forward region," in *V. Workshop: Instrumentation of the Forward Region of a Linear Collider Detector*, 2004. [Online]. Available: http://www-zeuthen.desy.de/lcdet/Aug_04_WS/aug_04_ws.html [Accessed: 28 Jul 2012]

[59] J. Blocki and et al., "Lumical new mechanical structure," *EUDET-Memo*, no. 10, 2009. [Online]. Available: http://www.eudet.org/e26/e28/e42441/e68452/EUDET-Memo-2009-10.doc [Accessed: 1 July 2012]

[60] J. Blocki, W. Daniluk, E. Kielar, J. Kotula, A. Moszczynski, K. Oliwa, B. Pawlik, W. Wierba, L. Zawiejski, and J. Aguilar, "Redesign of lumical mechanical structure," *EUDET-Memo*, no. 06, 2010. [Online]. Available: http://www.eudet.org/e26/e28/e86887/e98740/EUDET-MEMO-2010-06.doc [Accessed: 02 Sep 2012]

[61] T. Awes, F. Obenshain, F. Plasil, S. Saini, S. Sorensen, and G. Young, "A simple method of shower localization and identification in laterally segmented

calorimeters," *Nuclear Instruments and Methods in Physics Research Section A: Accelerators, Spectrometers, Detectors and Associated Equipment*, vol. 311, no. 1–2, pp. 130 – 138, 1992. [Online]. Available: http://www.sciencedirect.com/science/article/pii/0168900292908582 [Accessed: 14 Aug 2012]

[62] W. Daniluk and et al., "Laser alignment system for lumical status report," *EUDET-Memo*, no. 14, 2008. [Online]. Available: http://www.eudet.org/e26/e28/e615/e763/EUDET-Memo-2008-14.doc [Accessed: 8 July 2012]

[63] I. Sadeh, "Luminosity measurement at the international linear collider," Master's thesis, Tel Aviv University, 2008. [Online]. Available: http://alzt.tau.ac.il/~sadeh/mscThesis.html [Accessed: 20 May 2012]

[64] D. Groom and S. Klein, "Passage of particles through matter," *The European Physical Journal C - Particles and Fields*, vol. 15, pp. 163–173, 2000, 10.1007/BF02683419. [Online]. Available: http://dx.doi.org/10.1007/BF02683419 [Accessed: 4 Sep 2012]

[65] L. Landau, "On the energy loss of fast particles by ionization," *Journal of physics*, 1944.

[66] P. Vavilov, "Ionization losses of high-energy heavy particles," *Soviet Phys. JETP*, vol. 5, pp. 749–51, Nov 1957.

[67] H. Bichsel, "Straggling in thin silicon detectors," *Rev. Mod. Phys.*, vol. 60, pp. 663–699, Jul 1988. [Online]. Available: http://link.aps.org/doi/10.1103/RevModPhys.60.663 [Accessed: 6 May 2012]

[68] H. Abramowicz, R. Ingbir, S. Kananov, A. Levy, and I. Sadeh, "Geant4 simulation of the electronic readout.constraints for the luminosity detector of the ilc." *EUDET-Memo*, no. 17, 2007. [Online]. Available: http://www.eudet.org/e26/e28/e182/e308/eudet-memo-2007-17.pdf [Accessed: 1 July 2012]

[69] H. Spieler, *Semiconductor Detector Systems*. Oxford University Press, Oct. 2005. [Online]. Available: http://www.oup.com/us/catalog/general/subject/EngineeringTechnology/ElectricalComputerEngineering/?view=usa&ci=9780198527848 [Accessed: 12 August 2012]

[70] S. Ramo, "Currents induced by electron motion," *Proceedings of the IRE*, vol. 27, no. 9, pp. 584 – 585, sept. 1939.

[71] G. Cavalleri, E. Gatti, G. Fabri, and V. Svelto, "Extension of ramo's theorem as applied to induced charge in semiconductor detectors," *Nuclear Instruments and Methods*, vol. 92, no. 1, pp. 137 – 140, 1971. [Online]. Available: http://www.sciencedirect.com/science/article/pii/0029554X71902357 [Accessed: 2 Feb 2012]

[72] W. Sansen and Z. Chang, "Limits of low noise performance of detector readout front ends in cmos technology," *Circuits and Systems, IEEE Transactions on*, vol. 37, no. 11, pp. 1375 –1382, nov 1990.

[73] J. Kaplon, "Fast bipolar and cmos rad-hard front end electronics for silicon strip detectors," Ph.D. dissertation, AGH University of Science and Technology, 2004.

[74] O. Milgrome, S. Kleinfelder, and M. Levi, "A 12 bit analog to digital converter for vlsi applications in nuclear science," *Nuclear Science, IEEE Transactions on*, vol. 39, no. 4, pp. 771–775, aug 1992.

[75] S. O. Rice, "Mathematical analysis of random noise," *Bell Systems Technical Journal*, vol. 23, pp. 282–332, 1944.

[76] J. Kalisz, "Review of methods for time interval measurements with picosecond resolution," *Metrologia*, vol. 41, no. 1, p. 17, 2004.

[77] B. Swann, B. Blalock, L. Clonts, D. Binkley, J. Rochelle, E. Breeding, and K. Baldwin, "A 100-ps time-resolution cmos time-to-digital converter for positron emission tomography imaging applications," *Solid-State Circuits, IEEE Journal of*, vol. 39, no. 11, pp. 1839 – 1852, nov. 2004.

[78] T. Bienz, "Strangeonium Spectroscopy at 11 Gev/c and Cherenkov Ring Imaging at the SLD." Ph.D. dissertation, Stanford University., 1990.

[79] V. T. Jordanov and G. F. Knoll, "Digital synthesis of pulse shapes in real time for high resolution radiation spectroscopy," *Nuclear Instruments and Methods in Physics Research Section A: Accelerators, Spectrometers, Detectors and Associated Equipment*, vol. 345, no. 2, pp. 337 – 345, 1994. [Online]. Available: http://www.sciencedirect.com/science/article/pii/0168900294910111 [Accessed: 16 May 2012]

[80] V. T. Jordanov, G. F. Knoll, A. C. Huber, and J. A. Pantazis, "Digital techniques for real-time pulse shaping in radiation measurements," *Nuclear Instruments and Methods in Physics Research Section A: Accelerators, Spectrometers, Detectors and Associated Equipment*, vol. 353, no. 1–3, pp. 261 – 264, 1994. [Online]. Available: http://www.sciencedirect.com/science/article/pii/0168900294916527 [Accessed: 18 May 2012]

[81] V. Jordanov and G. Knoll, "Digital pulse-shape analyzer based on fast sampling of an integrated charge pulse," *Nuclear Science, IEEE Transactions on*, vol. 42, no. 4, pp. 683 –687, aug 1995.

[82] R. G. Lyons, *Understanding Digital Signal Processing*. Prentice Hall, Nov. 2010.

[83] S. Gadomski, G. Hall, T. Høgh, P. Jalocha, E. Nygård, and P. Weilhammer, "The deconvolution method of fast pulse shaping at hadron colliders," *Nuclear Instruments and Methods in Physics Research Section A: Accelerators, Spectrometers, Detectors and Associated Equipment*, vol. 320, no. 1–2, pp. 217 – 227, 1992. [Online]. Available: http://www.sciencedirect.com/science/article/pii/0168900292907794 [Accessed: 8 Feb 2011]

[84] Joint Committee for Guides in Metrology, *Evaluation of measurement data — Guide to the expression of uncertainty in measurement*, Sep 2008. [Online]. Available: http://www.iso.org/sites/JCGM/GUM-JCGM100.htm [Accessed: 14 Jun 2012]

[85] V. Radeka, "Low-noise techniques in detectors," *Annual Review of Nuclear and Particle Science*, vol. 38, no. 1, pp. 217–277, 1988. [Online]. Available: http://www.annualreviews.org/doi/abs/10.1146/annurev.ns.38.120188.001245 [Accessed: 4 Sep 2012]

[86] E. Gatti and P. Manfredi, "Processing the signals from solid-state detectors in elementary-particle physics," *La Rivista del Nuovo Cimento*, vol. 9, pp. 1–146, 1986. [Online]. Available: http://dx.doi.org/10.1007/BF02822156 [Accessed: 5 Sep 2012]

[87] P. Seller, "Noise analysis in linear electronic circuits," *Nuclear Instruments and Methods in Physics Research Section A: Accelerators, Spectrometers, Detectors and Associated Equipment*, vol. 376, no. 2, pp. 229 – 241, 1996. [Online]. Available: http://www.sciencedirect.com/science/article/pii/016890029600174X [Accessed: 5 Sep 2012]

[88] M. Idzik, S. Kulis, and D. Przyborowski, "Development of front-end electronics for the luminosity detector at ilc," *Nuclear Instruments and Methods in Physics Research Section A: Accelerators, Spectrometers, Detectors and Associated Equipment*, vol. 608, no. 1, pp. 169 – 174, 2009. [Online]. Available: http://www.sciencedirect.com/science/article/pii/S0168900209013151 [Accessed: 2 July 2012]

[89] M. Idzik, K. Świentek, T. Fiutowski, S. Kulis, and P. Ambalathankandy, "A power scalable 10-bit pipeline adc for luminosity detector at ilc," *JINST*, vol. 6 P01004, 2011.

[90] W. Wierba and et al., "Silicon sensors for lumical. status report." *EUDET-Memo*, no. 12, 2008. [Online]. Available: http://www.eudet.org/e26/e28/e615/e761/EUDET-Memo-2008-12.doc [Accessed: 25 July 2012]

[91] "Hamamatsu photonics." [Online]. Available: www.hamamatsu.com/ [Accessed: 28 Jul 2012]

[92] J. Blocki, W. Daniluk, E. Kielar, J. Kotula, A. Moszczynski, K. Oliwa, B. Pawlik, W. Wierba, L. Zawiejski, and J. Aguilar, "Silicon sensors prototype for lumical calorimeter," *EUDET-Memo*, no. 07, 2009. [Online]. Available: http://www.eudet.org/e26/e28/e42441/e68451/EUDET-MEMO-2009-07.doc [Accessed: 25 July 2012]

[93] I. Levy, "Detector developement for the instruments in the forward region of future linear colliders," Master's thesis, Tel Aviv University, 2012.

[94] M. Bergholz, "I/v and c/v measurements of hamamatsu si-detectors," in *14th FCAL Workshop, DESY Zeuthen*, June 2009. [Online]. Available: https://indico.desy.de/materialDisplay.py?contribId=14&sessionId=0&materialId=slides&confId=2000 [Accessed: 28 Jul 2012]

[95] E. Beuville and et al., "Amplex, a low-noise, low-power analog cmos signal processor for multi-element silicon particle detectors," *Nuclear Instruments and Methods in Physics Research Section A: Accelerators, Spectrometers, Detectors and Associated Equipment*, vol. 288, no. 1, pp. 157 – 167, 1990, Proceedings of the Fifth European Symposium on Semiconductors Detectors. [Online]. Available: http://www.sciencedirect.com/science/article/pii/016890029090481K [Accessed: 28 Jul 2012]

[96] G. Gramegna, P. O'Connor, P. Rehak, and S. Hart, "Cmos preamplifier for low-capacitance detectors," *Nuclear Instruments and Methods in Physics Research Section A: Accelerators, Spectrometers, Detectors and Associated Equipment*, vol. 390, no. 1–2, pp. 241 – 250, 1997. [Online]. Available: http://www.sciencedirect.com/science/article/pii/S0168900297003902 [Accessed: 20 Aug 2012]

[97] H.Abramowicz, R.Ingbir, S.Kananov, A.Levy, and I.Sadeh, "Revised requirements on the readout of the luminosity calorimeter," *EUDET-Memo*, no. 8, 2008. [Online]. Available: http://www.eudet.org/e26/e28/e615/e783/eudet_memo_2008_08.pdf [Accessed: 1 July 2012]

[98] M. Idzik, K. Świentek, and S. Kulis, "Development of pipeline adc for the luminosity detector at ilc," *Proceedings of the 15th International Conference Mixed Design of Integrated Circuits and Systems MIXDES 2008, Poznan, Poland, 19-21 June*, 2008.

[99] M. Idzik, K. Swientek, and S. Kulis, "Design and measurements of 10 bit pipeline adc for the luminosity detector at ilc," *Proceedings of Topical Workshop on Electronics for Particle Physics, TWEPP-09, Paris, France*, Sep. 2009.

[100] M. Idzik, K. Swientek, T. Fiutowski, S. Kulis, and D. Przyborowski, "A 10-bit multichannel digitizer asic for detectors in particle physics experiments," *IEEE Trans. Nucl. Sci.*, 2012.

[101] M. Idzik and M. Ornat, "Design and operation of low power temperature sensor – bandgap reference circuit in submicron technology," *Proceedings of the 12th International Conference Mixed Design of Integrated Circuits and Systems MIXDES 2005*, 2005.

[102] *Xilinx Virtex-5 FXT Evaluation Kit User Guide*, Avnet, May 2008. [Online]. Available: http://www.files.em.avnet.com/files/177/xlx_v5fxt_evl-ug-rev1.pdf [Accessed: 25 April 2011]

[103] S. Kilts, *Advanced FPGA Design: Architecture, Implementation, and Optimization*. Wiley-IEEE Press, Aug. 2007.

[104] *Xilkernel v3.00.a*, Xilinx Inc., 2006. [Online]. Available: http://www.xilinx.com/ise/embedded/edk91i_docs/xilkernel_v3_00_a.pdf [Accessed: 14 August 2011]

[105] *1003.1-2008 - IEEE Standard for Information Technology - Portable Operating System Interface (POSIX(R))*, POSIX - Austin Joint Working Group, 2008. [Online]. Available: http://standards.ieee.org/findstds/standard/1003.1-2008.html [Accessed: 3 August 2011]

[106] S. Tilden and et al., "Ieee standard for terminology and test methods for analog-to-digital converters," *IEEE Std 1241-2010 (Revision of IEEE Std 1241-2000)*, pp. 1–139, 14 2011. [Online]. Available: http://ieeexplore.ieee.org/stamp/stamp.jsp?tp=&arnumber=5692956 [Accessed: 14 Jun 2011]

[107] G. Casinovi and R. J. Ho, "Computer generation of colored noise for time-domain analysis of integrated circuits," *Analog Integrated Circuits and Signal Processing*, vol. 11, pp. 205–215, 1996, 10.1007/BF00240485. [Online]. Available: http://dx.doi.org/10.1007/BF00240485 [Accessed: 10 April 2011]

[108] D. T. Rooney, D. Nager, D. Geiger, and D. Shanguan, "Evaluation of wire bonding performance, process conditions, and metallurgical integrity of chip on board wire bonds," *Microelectronics Reliability*, vol. 45, no. 2, pp. 379 – 390, 2005. [Online]. Available: http://www.sciencedirect.com/science/article/pii/S0026271404002045

[109] I. M. Gregor, *ZEUS MVD Telescope*, Aug. 2011. [Online]. Available: http://www.desy.de/~gregor/MVD_Telescope/short_intro.html [Accessed: 12 Aug 2011]

[110] Łukasz Maczewski, "Measurements and simulations of maps response to charged particles - a study towards a vertex detector at the ilc," Ph.D. dissertation, Warsaw University, 2010.

[111] *FT4232H Quad High Speed USB to Multipurpose UART/MPSSE IC*, Future Technology Devices International Ltd., 2010. [Online]. Available: http://www.ftdichip.com/Support/Documents/DataSheets/ICs/DS_FT4232H.pdf [Accessed: 13 August 2011]

[112] D. Cussans, "Description of the jra1 trigger logic unit (tlu), v0.2c," *EUDET-Memo*, Sep. 2009. [Online]. Available: http://www.eudet.org/e26/e28/e42441/e57298/EUDET-MEMO-2009-04.pdf [Accessed: 12 Aug 2011]

[113] *Standard Commands for Programmable Instruments (SCPI)*, SCPI Consortium, May 1999. [Online]. Available: www.ivifoundation.org/docs/scpi-99.pdf [Accessed: 16 Aug 2011]

[114] "Eudaq web page." [Online]. Available: http://eudaq.hepforge.org/ [Accessed: 28 Jul 2012]

[115] M. Idzik, K. Swientek, S. Kulis, W. Dabrowski, L. Suszycki, B. Pawlik, W. Wierba, and L. Zawiejski, "The concept of lumical readout electronics," *EUDET-Memo*, no. 13, 2007. [Online]. Available: http://www.eudet.org/e26/e28/e182/e281/eudet-memo-2007-13.pdf [Accessed: 1 July 2012]

[116] S. Kulis and M. Idzik, "Triggerless readout with time and amplitude reconstruction of event based on deconvolution algorithm," *Acta Physica Polonica B, Proceedings Supplement*, vol. 4, no. 1, pp. 49–58, 2011.

[117] S. Kulis, A. Matoga, M. Idzik, K. Swientek, T. Fiutowski, and D. Przyborowski, "A general purpose multichannel readout system for radiation detectors," *Journal of Instrumentation*, vol. 7, no. 01, p. T01004, 2012. [Online]. Available: http://stacks.iop.org/1748-0221/7/i=01/a=T01004

[118] S. Kulis and et al., "Test beam studies of the lumical prototype," *EUDET-Memo*, no. 09, 2010. [Online]. Available: http://www.eudet.org/e26/e28/e86887/e105930/EUDET-Memo-2010-09.pdf [Accessed: 25 July 2012]

List of Figures

List of Tables